Petrology of the Kula Volcanic Field

Western Turkey

A thesis presented to the Faculty

of the State University of New York

at Albany

in partial fulfillment of the requirements

for the degree of

Master of Science

School of Science and Mathematics

Department of Geological Sciences

Julie M. Dyer

1987

State University of New York at Albany

College of Science and Mathematics

Department of Geological Sciences

The thesis for the master's degree submitted by

Julie M. Dyer

under the title

Petrology of the Kula Volcanic Field, Western Turkey

has been read by the undersigned. It is hereby recommended

for acceptance by the Faculty with credit to the amount of

six semester hours.

(Signed) _Stephen E. DeLong_____

(Date) _5/8/87_____

(Signed) _W S Pfeiss_____

(Date) _11 May 1987_____

(Signed) _George N. Putman_____

(Date) _5/11/87_____

Recommendation accepted by the Dean of Graduate Studies for

the Graduate Academic Council.

(Signed) _____

(Date) _____

```
VLADIMIR:   I don't understand.
ESTRAGON:   Use your intelligence, can't you?
  (Vladimir uses his intelligence.)
VLADIMIR:   I remain in the dark.
ESTRAGON:   This is how it is.

            Samuel Becket,
            Waiting for Godot
```

TABLE OF CONTENTS

ABSTRACT

The Kula volcanics are a small Pleistocene to Recent volcanic field located on the north shoulder of the Gediz graben, approximately 120 km east of İzmir. The field consists of a mixture of flows, small cones and pyroclastic deposits erupted during three periods of volcanic activity beginning about one million years ago. The volcanics range in composition from basanites to trachybasalts, commonly porphyritic with abundant clinopyroxene, olivine and amphibole phenocrysts. The lavas also host a wide variety of megacrysts, crustal xenoliths and hydrous mantle-derived nodules. These volcanics unconformably overlie Neogene lacustrine sedimentary rocks and the metamorphic basement rocks of the late Poterozoic-Eocene Menderes Massif.

Results of analyses of up to 24 lava samples and 4 hydrous ultramafic nodules for whole rock major elements, selected trace elements and Rb/Sr isotopes are presented. Paragenetic models utilizing a least-squares subtraction program for major elements suggests that fractional crystallization processes can explain compositional variations between products erupted from the same cone during a single eruptive period , but not between different cones or different eruption periods. Trace element concentrations do not seem to support the major element fractionation models, which suggests a more complex origin for the lavas. Variations in trace element and Rb/Sr

isotopic values support the hypothesis that the Kula source region has undergone a recent enrichment in incompatible elements, similar to recently proposed models of paragenesis for ocean island basalts. This enrichment is thought to be related to a change from a compressional to extensional tectonic regime in western Turkey during Neogene time. Further isotopic analyses will be necessary to adequately test this hypothesis.

LIST OF FIGURES

LIST OF TABLES

INTRODUCTION

The observations and conclusions presented in this thesis are the result of both field and laboratory research on the Kula volcanic field of western Anatolia. This study was carried out under the direction of Dr. Stephen E. DeLong at the State University of New York at Albany as part of a Master's degree program. Field work was undertaken in Turkey during September and October of 1979, and consisted primarily of sample collection from the Kula volcanic field, as well as from a number of less extensive Neogene-Recent(?) volcanic fields (Figure 1). These samples were augmented by a smaller collection made available to me at Albany; these specimens were previously collected by A.M.C. Şengör. The bulk of this thesis is concerned exclusively with the Kula volcanic rocks, which comprise the largest Recent volcanic field in western Anatolia; its extent is estimated at 360 km^2 (Erinç, 1970). These volcanic rocks overlie Neogene lacustrine-derived sedimentary rocks and Pre-Cambrian to Eocene metamorphic rocks of the Menderes Massif. The regional terrane is dominated by a north-south series of roughly east-west trending grabens, which contain Pliocene-Recent sediments.

Objectives of this study were to determine the chemical character of the Kula volcanic rocks (as well as that of other young volcanics in western Anatolia), model their paragenesis, and to evaluate the volcanism in terms of the regional tectonic evolution. Study procedure involved initial petrographic examination and description of each

2
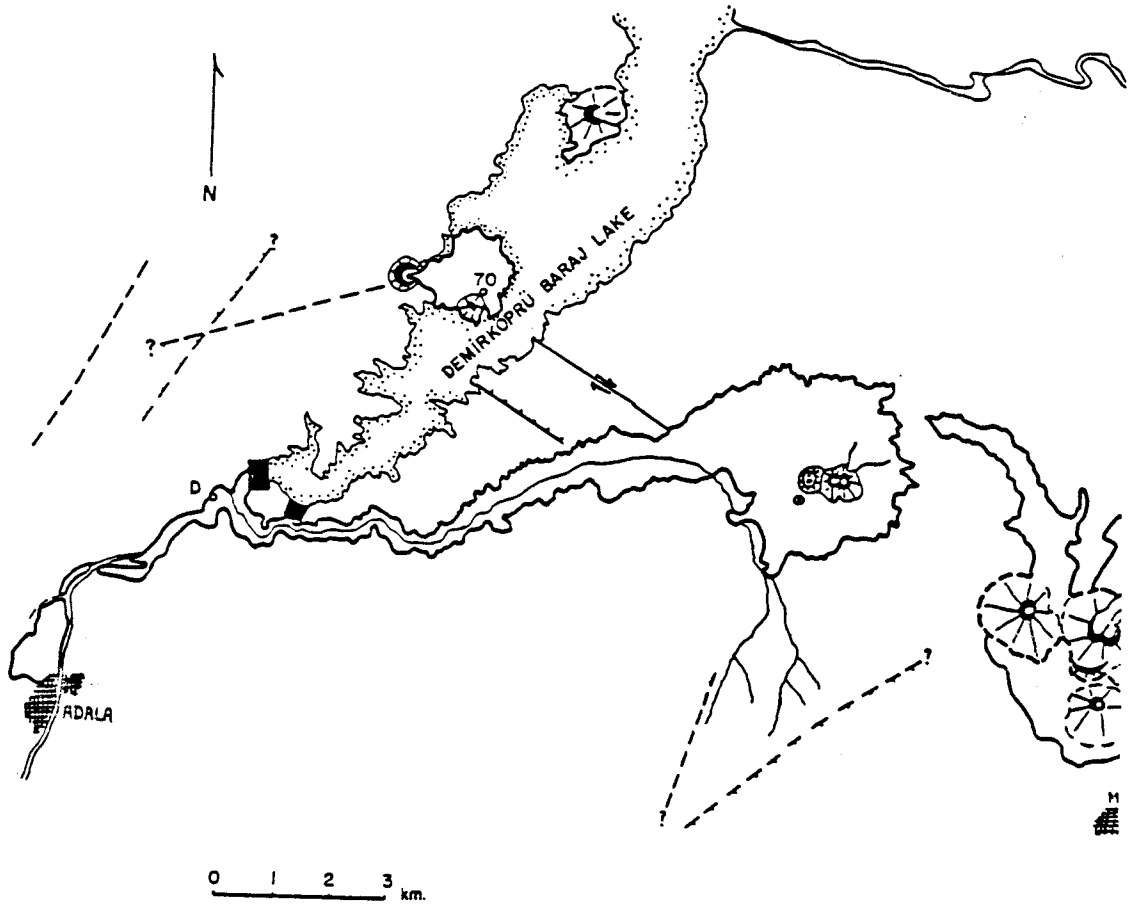
Figure 1a. See text next page.

Third period cone and flow

Second period cone

First period flow and injection site
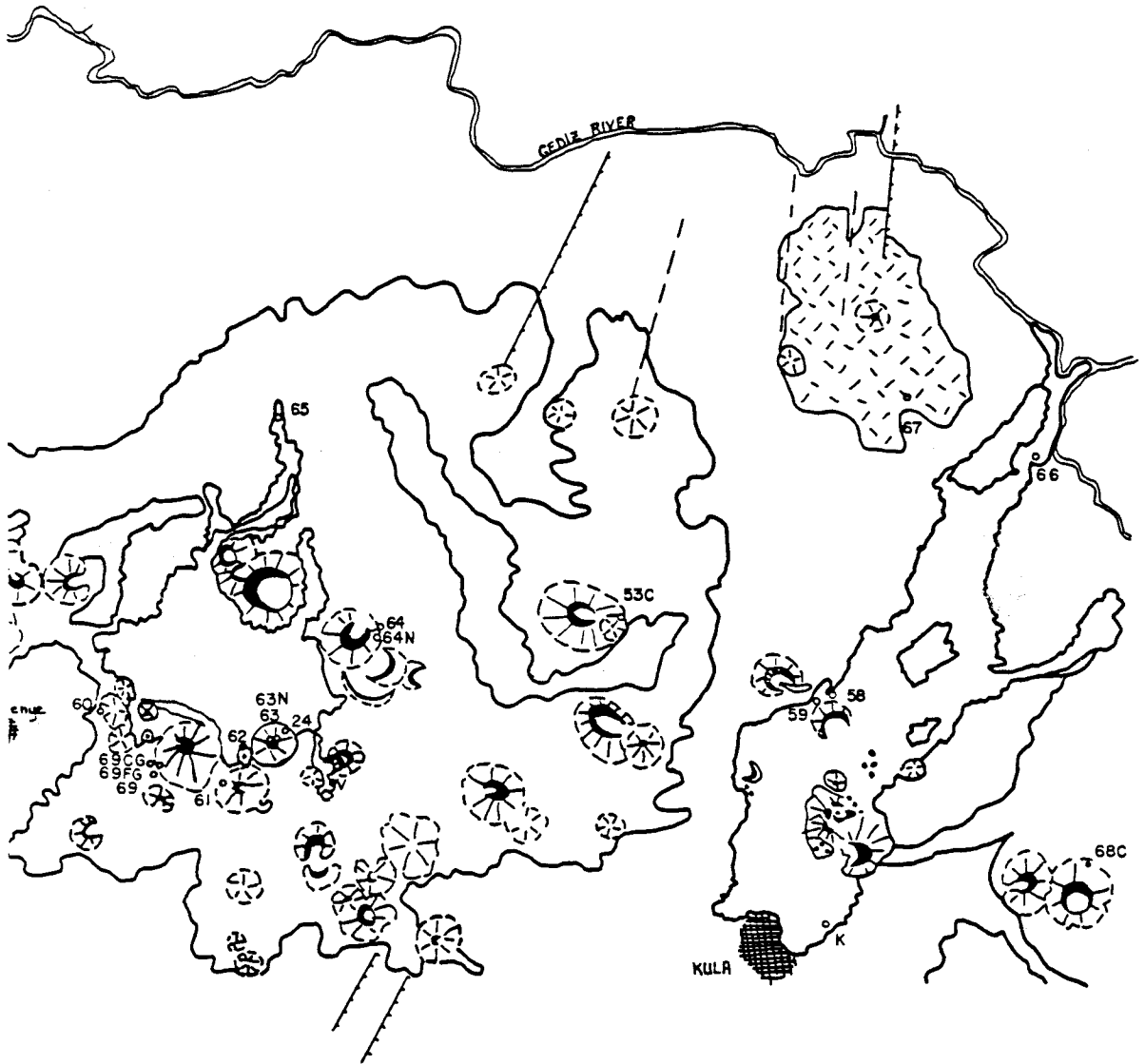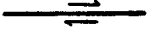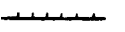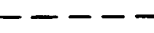
—⇌— Strike-slip fault with motion

⊥ Normal fault with hachure toward downthrown block

— — — — Possible strike slip fault

- - - - - Possible normal fault

70
∘ Sample site with number

4

Figure 1a-b.   Location of samples included in this study
from the Kula volcanic field.   The base map for Fig. 1a
is modified from Erinç, 1970.   Figure 1b shows continu-
ation of geology east of Fig. 1a (although at a different
scale), and is taken from the 1 : 50,000 scale
sheet topographic map.   Geologic contacts were ascertained
by members of M.T.A..   Inset shows Kula's geographic
position within western Anatolia.
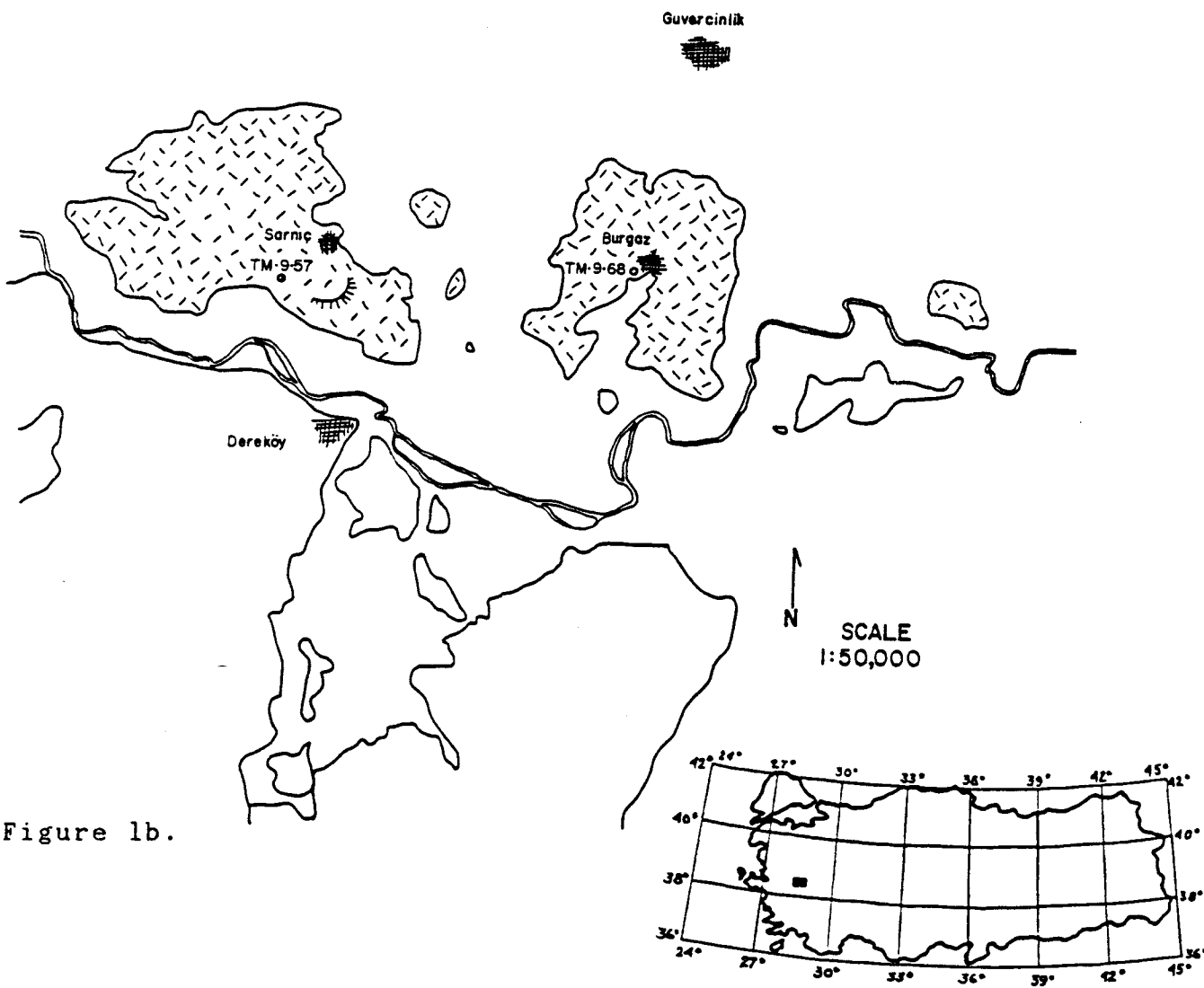
Figure 1b.

sample. Most samples were subjected to further analysis, including whole rock major chemistry determination on fused glass beads using an electron microprobe and whole rock trace element analysis by XRF on pressed powder pellets. Selected samples were analyzed by electron microprobe to determine phenocryst and groundmass phase compositions. Certain samples were analyzed by spark source mass spectrometer by Dr. Richard Arculus for REE abundances, rubidium-strontium isotopic data were determined by Dr. Stephen Moorbath, and water content determined by Peter Lyman at S.U.N.Y.A.. Twelve of thirty two trace element determinations were run by Dr. Stephen E. DeLong. These data allowed chemical characterization of the lavas as well as providing constraints on various petrogenetic models. Petrographic study of other Neogene-Recent(?) volcanic rocks from Western Anatolia, a survey of literature on western Anatolian volcanism, and use of tectonic models of evolution for the eastern Mediterranean region (models largely developed by faculty and students of this department) allowed speculation on the interdependence of magmatism and tectonic evolution in western Anatolia.

PREVIOUS WORK

Early descriptions of the Kula basalt field were made by Hamilton and Strickland (1841), and Hamilton (1842), who described the generalized geology of the Kula area, including the volcanics. The former reference contains a map of the region. Tchihatcheff (1867) and Texier (1882) also described the generalized geology of the area, based largely on the earlier two works. The only major petrological investigation of the Kula volcanics was undertaken by Henry S. Washington, who in the spring of 1892 spent eight days in the eastern portion of the volcanic field, where he sampled flows and sketched a map of cones and flows in the vicinity of the town of Kula. From this field work and subsequent laboratory investigation he wrote his Ph.D. (1893), which was later published (1894a). He also published two short articles on petrographic classification and petrology of the Kula basalts (1894b and 1900). Washington considered the rocks unique and as such classified them as "Kulaites", defined as basalts with hornblende as a phenocryst phase in excess of augite or olivine.

In 1913, Philippson published a short paper dealing with the development of the western Anatolian graben system, which mentions the basalts as spatially associated with the faults. Cavet and Jaoul (1946) produced a geologic map of the volcanic field and the immediate surrounding region.

Recent work on the Kula volcanic field centers on the work of Sırrı Erinç (1955, 1970), whose careful and accurately

6

detailed map of geomorphology of the basalt field (1970) provided the base map used in this study. Other investigators include Borsi et al. (1973), who radiometrically dated the earliest Kula volcanism at 1.1 m.y.b.p. (K-Ar), as well as dating many of the other young volcanic rocks in western Turkey. Members of the Mineral Research and Exploration Institute of Turkey (M.T.A.) have much unpublished data on the volcanic rocks of western Anatolia, including Kula, as part of a regional study of western Anatolian magmatism and stratigraphy.

GEOLOGICAL SETTING AND TECTONIC EVOLUTION

The Kula basalts are the most recent products of a history of abundant volcanic activity in western Turkey (Figure 2). This widespread volcanism is associated with a complex sequence of collisional and collision-related tectonic events. The tectonic evolution of Turkey has been treated in detail by a number of authors including Ketin (1959, 1966), McKenzie (1972), Dewey et al. (1973), Brinkmann (1976), Dewey and Şengör (1979), Şengör and Kidd (1979), and Şengör and Yilmaz (1981). Therefore the tectonic evolution of Turkey will not be treated in detail in this thesis, except to summarize briefly the tectonic history with emphasis on western Anatolia, as hypothesized by Şengör and Dyer (1979), Şengör and Yilmaz (1981), and Şengör (personal directive, 1981).

During Permian time, the present day area of Turkey formed a portion of the northern Gondwana-Land continental margin (pre-Permian history is complex, conjectural and will not be treated here). South-dipping subduction of the Paleo-Tethyan ocean disrupted this margin. Paleo-Tethys closed during the Jurassic, and gave way to the opening of northern and southern branches of the Neo-Tethyan ocean, which widened until early Cretaceous. Elimination of these two branches of Neo-Tethys began during late Cretaceous time along two northerly-dipping subduction zones. The present day Black Sea was formed as a marginal basin behind the Pontide island arc, which developed in front of the northern subduction

8

Figure 2. Tertiary-Recent volcanism of western Turkey
modified after Ercan (unpublished M.T.A. report).
Paleogene volcanism is shown in green, Neogene volcanism
in red, and Quaternary volcanic centers in blue. Alkaline
volcanism is illustrated in a stippled pattern, color
without stippled pattern denotes calc-alkalic volcanism.
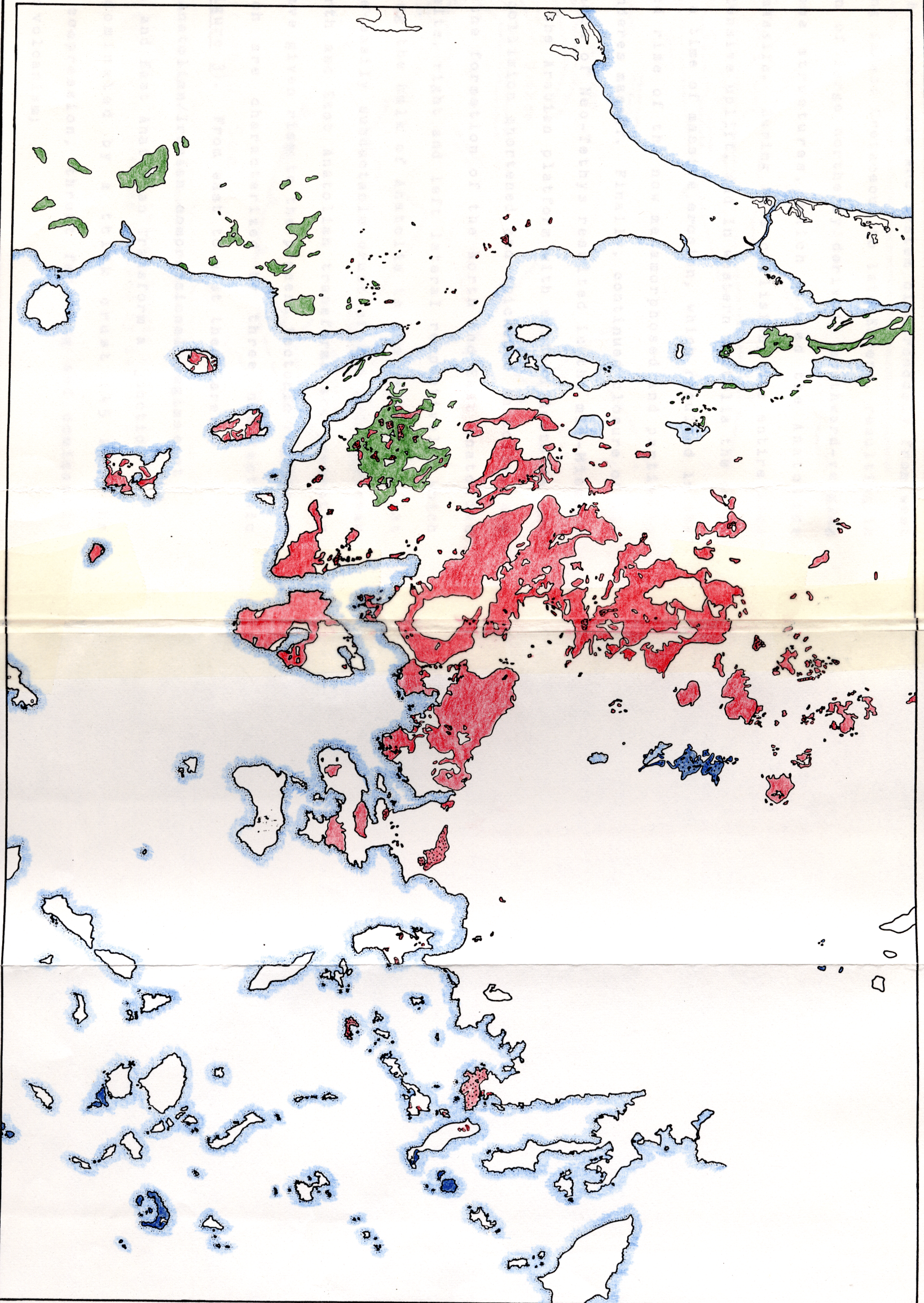
zone. The Anatolide-Tauride platform, a fragment of Gondwana, as well as other smaller continental fragments, collided with the Pontide arc system diachronously from west to east during latest Cretaceous to late Eocene, resulting in the formation of large northerly derived, southward-verging Tauride nappe structures, which buried the Anatolide metamorphic massifs. During this collision, the entire area underwent extensive uplift, and in western Anatolia the early Tertiary was a time of massive erosion, which resulted in the unroofing and rise of the now metamorphosed and partially anatectic Menderes massif. Finally, continued closure of the southern branch of Neo-Tethys resulted in the mid-Miocene collision of the Arabian platform with eastern Anatolia and Iran. This collision shortened and thickened Anatolia, and resulted in the formation of the North and East Anatolian transform faults, right and left lateral respectively, which began ejecting the bulk of Anatolia to the west-southwest onto the more easily subductable crust of the Mediterranean Sea. The North and East Anatolian transforms are presently active and have given rise to the present tectonic regimes in Turkey, which are characterized by three neo-tectonic provinces (Figure 3). From east to west these are:

1. The east Anatolian/Iranian compressional regime east of the North and East Anatolian Transform a junction which is dominated by a thick crust (45 km?) in north-south compression, thrust faulting and dominantly calc-alkaline volcanism;
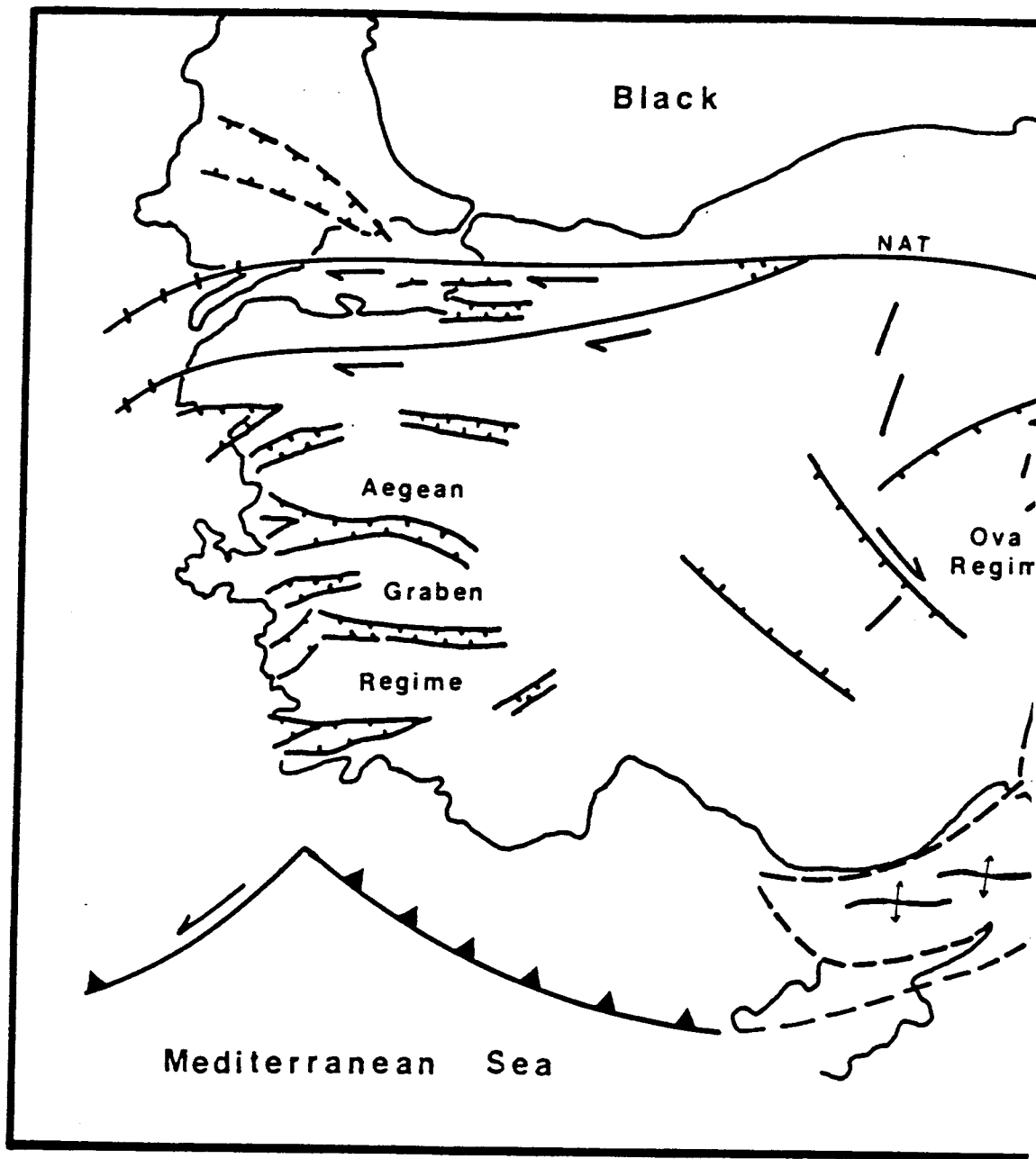
Figure 3. Schematic tectonic map (after Şengör and Yilmaz, 1981) with neotectonic provinces as defined by Şengör and Dyer (1979).

Sea

East

Anatolian

Compressional

Regime

ɪe

EAT

BS

ZS

DST

Arabian

Plate
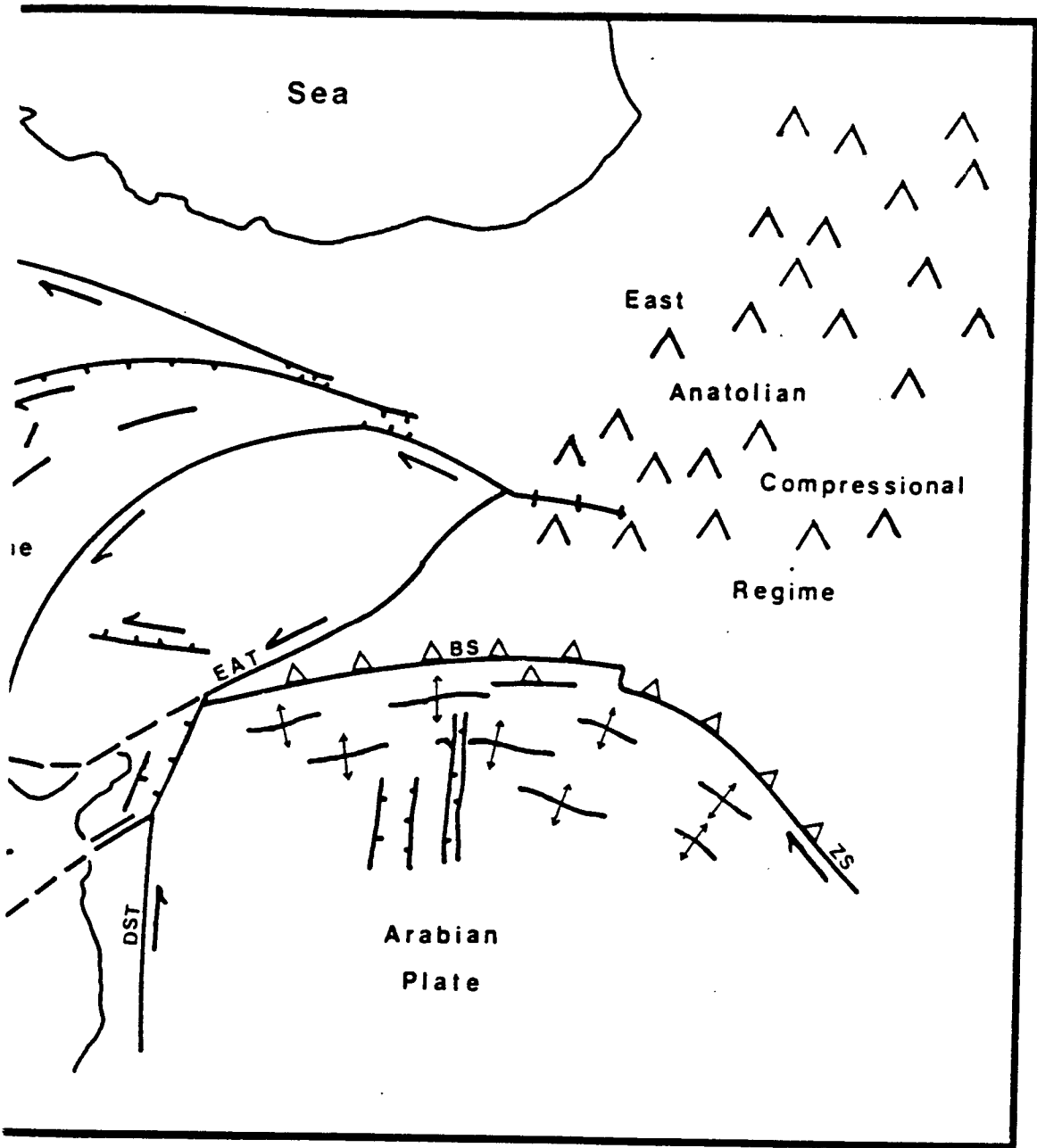
BS: Bitlis suture
EAT: East Anatolian transform
DST: Dead Sea transform
NAT: North Anatolian transform
ZS: Zagros suture

2. The central Anatolian "ova" regime, characterized by increasing westward crustal extension, large oblique fault-bounded equant depressions (faults are northwest and northeast trending conjugate sets), and both calc-alkaline and alkaline volcanism, with extensive ignimbrite deposits; and,

3. The Aegean extensional regime or Aegean graben regime, characterized by greater than 30% north-south extension along east-west trending grabens and northwest and northeast trending conjugate fault pairs with associated highly alkaline basalts.

These regimes are a result of continued northward convergence of the Arabian platform, coupled with increasing westward crustal extension within the transform bounded wedge-shaped Anatolian block as it escapes to the west.

In the Kula region, as well as much of western and central Anatolia, the onset of extension disrupted an environment consisting of wide-spread lacustrine sedimentation. Crustal extension may have initially increased the extent of the lakes, but continued extension resulted in the formation of the east-west graben terrane during Pliocene time, which probably caused drainage of the lakes into the Aegean basin to the west. Volcanism has been widespread in Turkey from Cretaceous to Recent time. Subduction-related volcanism related to both subduction and collision outcrops throughout much of the Anatolide-Tauride platform. Superimposed on these volcanics in western Anatolia

and intimately associated with these volcanics in eastern Turkey are Miocene to Recent volcanics, which are associated with faults formed under crustal extension. These volcanics have a wide variety of chemistries, but may be generally described as decreasing in volume and increasing in basicity and alkalinity with decreasing age. As a result of steady increase in crustal extension west of Karliova (junction of the North and East Anatolian Transform faults), a diachronous volcanism exists in Turkey. Because of this, the evolution of volcanism with increasing crustal extension should be able to be studied in Turkey by traveling from east to west between the two bounding transforms.

In addition, there is also a north-south trend in Turkish volcanism, characterized by decreasing age of volcanic rocks from north to south. This is a function of the southerly-migrating zones of subduction and collision with time, as opposed to the later east-west trend of chemical change with increasing crustal extension.

STRATIGRAPHY - General Statement

Quaternary plateau basalts and lava-tephra cones of the Kula volcanic field overlie the early Tertiary Menderes metamorphic massif, which forms the basement of Kula, and the Neogene sedimentary and volcanic cover (Philippson, 1913; Erinç, 1970). Immediately to the south of the Kula volcanics, outcrops of Menderes metamorphics predominate, except for the Neogene to Recent terrestrial sediments associated with the roughly east-west trending Gediz graben. To the north lies terrane dominated by Neogene terrestrial sediments and Miocene-Quaternary(?) volcanic rocks.

Kula volcanism has been subdivided into three eruptive stages of decreasing age, based on both geomorphological (Erinc, 1970) and chemical criteria, although the various states of preservation of second stage cinder cones suggest that eruptions continued intermittently over an extensive period, and therefore the separation of second and third stage activity may be somewhat artificial.

Stratigraphy developed in this study is largely compiled from units defined by earlier workers. The study of country rock surrounding the volcanics served limited petrologic purpose considering the scope and time limitations of the project.

Menderes Massif

The Menderes massif is an early Tertiary metamorphic complex which consists of rocks ranging in age from late Proterozoic to Eocene (Dürr, 1975; Gutnic et al., 1979;

Şengör and Yilmaz, 1981). Menderes rocks form the basement of the Kula volcanics, and consist of a concentric structure composed of three major lithotypes. The core rocks of the massif consist of strongly foliated granitic and augen. gneisses of conjectural anatectic origin. The rocks possess a strong north-northeast trending lineation. A number of different dates of formation for the core rocks have been proposed (see Dürr et al., 1978); recent consensus agrees on a pre-Caledonian origin. Şengör and Yilmaz (1981) have proposed, on the basis of Menderes-Taurus autochthon correlation (see Dürr, 1975; Gutnic et al., 1979) that the core represents a remobilized Baikalian age basement. Menderes core rocks are exposed in the western portion of the Kula volcanic field; fine exposures of biotite-quartz-feldspar metablastic augen gneiss outcrop along the western shore of Demirköprü Baraj Gölü (fig. 4).

The core rocks are surrounded by a Paleozoic sequence of mica schists, phyllites and other pelites (Schieferhulle of Dürr, 1975). These rocks outcrop in the volcanic field east of Demirköprü Baraj Gölü. This envelope is in turn surrounded by an outer envelope of Permo?- Triassic to Upper Cretaceous marbles and quartzites, intercalated with metapelites and metabauxites (Marmorhulle of Dürr, 1975). These outer units were metamorphosed to the greenschist facies during the early Tertiary, according to Ketin (1966) and Dürr (1975), with grade of metamorphism decreasing away from the core rocks. Rocks of the outer envelope are exposed in the central and

Figure 4. Biotite-quartz-feldspar augen gneiss core rocks of the Menderes Massif, exposed in the western end of the volcanic field.

eastern portions of the Kula volcanic field, and xenoliths of marble, quartzite and metapelite are common in the scoriaceous volcanic rocks (Fig. 5).

Neogene Sedimentary Rocks

Descriptions of Neogene rock of the Kula region are based on the personal communications of E. Gunay in the field (1979), the work of Ercan et al. (1978), and on my observations made in the Kula region between the towns of Salihli in the west and Uşak in the east.

Miocene rocks consist of a basal ophiolitic conglomerate consisting of blocks of ophiolitic and metamorphic rock. Overlying the conglomerates is a thick (up to 1800 m near Uşak; Ercan et al., 1978) sequence of interbedded lacustrine, debris flow and volcanic derived material of upper Miocene to Pliocene age. These consist of interbedded conglomerate, sandstone, clay marl, tuff, agglomerate and limestone. Age is distinguished on the basis of fossil assemblages (see for example, Ercan et al., 1978). In very general terms, Miocene rocks are typically orange to dark yellow in color, Pliocene rocks are paler yellow to grey or off-white. Dip of the strata progressively decreases in a Neogene - Quaternary stratigraphic section northeast of Salihli from 30°N dip in middle Miocene rocks to dips of 5°N or less in upper Pliocene and Quaternary rocks and sediment. This is evidence for rotation of normal fault bounded blocks in the western Anatolian graben system, and may indicate that the normal faults bounding the blocks are listric, as suggested by

Figure 5.   Example of common upper crustal xenolith in
third period scoria.   Photograph is of Menderes Massif
quartzite in Kula Devit scoria.

Şengör (1978) and by McKenzie (1978).

Kula Basalts

The Kula volcanic rocks overlie rocks of the Menderes metamorphic massif and Pliocene sedimentary rocks, when they have been erupted onto a prominent erosion surface of possible Pliocene age (Erinç, 1955). The volcanic-sedimentary rock contact is characterized by a distinctive red baked horizon in the Pliocene sediments (Fig. 6).

The Pleistocene-Recent Kula volcanics occupy an area of approximately 52 by 18 km on the north-east sholder of the Gediz graben, between the villages of Adala in the west and Kula in the east, although eruptive centers extend a few kilometers east of Kula. The volcanism has been subdivided into three periods of activity by morphology and state of cinder cone preservation. This subdivision has been either previously noted or described by Hamilton and Strickland (1836), H.S. Washington (1893, 1894a, 1894b, 1900), Philippson (1913), and Erinç (1970).

First Period Basalts

The earliest Kula volcanic rocks consist of alkaline plateau-type flood basalts, that have been radiometrically dated (K-Ar) by Borsi et al. (1972) at 1.1 m.y.b.p. They are the most widespread basalts of the Kula sequence, with total estimated coverage in excess of 230 km^2 (Erinç, 1970). In the field, these rocks typically form erosion resistant caps on the underlying Pliocene sedimentary rocks, and dip slightly to the north (Figure 7). The flows have very

Figure 6. Contact between first period Kula flood
basalt and underlying Neogene lacustrine sedimentary
rocks. Note the prominent red baked horizon.

Figure 7. Typical morphology of first period plateau
basalts, which form erosion-resistant cuestas on the
underlying poorly-indurated Neogene sedimentary rocks.
Note the slight northward tilt of the basalt flows, a
result of continuing rotation of the strata along normal
listric fault surfaces.

discontinuous outcrop due to a large amount of denudation resulting from continued uplift of the Gediz graben shoulders. Eruption centers are uncertain, but magma probably emanated from west-northwest trending fissures which extended from Catallarepe to Kula (Erinç, 1970), following the strike of the postulated Catallarepe-Kula-Menye fault. One flow identified in the field is approximately 10 to 20m thick, and generally massive, although well-developed columnar jointing was observed at a few localities. The rock is medium to light grey on a fresh surface, weathers tan and is typically fine-grained and non-vesicular. Phenocrysts are not abundant in hand specimen and consist primarily of stumpy black euhedral augite. Large yellowish-green anhedral olivine grains can be observed, although they are less common than augite. Large, presumably xenocrystic inclusions of quartz are also present.

Second Period Basalts

Discrimination between second and third period basalts is some what subjective due to the fact that both periods consist of mixed cinder or tephra and lava cones with associated lava flows that form a continuum from severely eroded and vegetated to perfectly preserved. In this thesis, cones have been classified roughly in accordance with Erinç's (1970) geomorphological study of the volcanic field. Unvegetated or sparsely vegetated cones and flows have been classified as third period, whereas all heavily vegetated cones and flows have been classified as second period,

regardless of their state of preservation (Figs. 8a & b). In contrast to the quiescent style of fissure eruption that characterizes the first period activity, second period volcanics are explosive. Erinç (1970) notes that second period activity seems to start with flows and progresses with time to a more violent eruptive style. Extensive ash and cinder deposits were formed during second period activity, although the total area coverage of 130 km^2 (Erinç, 1970) is less than that of the first period. Erinç (1970) has classified fifty-seven small lava and tephra cones as second period, which are aligned in a general east-west trend along a series of enechelon north-northeast trending faults. This alignment has also been pointed out by Cavet and Jaoul (1946).

Outcrops of unweathered second period rocks suitable for geochemical analyses are difficult to find, therefore sampling is undoubtably biased toward the better preserved second period rocks. The rocks are quite variable in appearance, and may be oxidized or non-oxidized, vesicular to non-vesicular, porphyritic to phenocryst-poor (no aphyric samples were found). Color ranges from dark grey to light greyish-pink in hand specimen, often exhibiting a slightly mottled look. Inclusions of many types are common, with a large proportion of small (generally less than 2 cm), rounded hornblende-rich ultramafic xenoliths. Phenocrysts observed in hand specimen consist of black, augite euhedra, black elongate amphibole and anhedral dull yellow-green olivine

Figure 8a. Photographs 8a and 8b show the range of
preservation of cinder cones classified as second
period. 8a shows a cone in the central portion of
the field, northeast of Kara Devit, with heavily
vegetated flanks, as well as a collapsed and eroded
crater. 8b shows a younger second period cone with
a well preserved crater and more sparse vegetation
on the western shore of Demir Köprü Baraj Gölü.
The range of preservation suggests that this eruptive
period was sporadically active over a substantial
period of time. Second period volcanic rocks also
have the widest range of chemical composition.

Figure 8b. Photographs 8a and 8b show the range of
preservation of cinder cones classified as second
period. 8a shows a cone in the central portion of
the field, northeast of Kara Devit, with heavily
vegetated flanks, as well as a collapsed and eroded
crater. 8b shows a younger second period cone with
a well preserved crater and more sparse vegetation
on the western shore of Demir Köprü Baraj Gölü.
The range of preservation suggests that this eruptive
period was sporadically active over a substantial
period of time. Second period volcanic rocks also
have the widest range of chemical composition.

which sometimes has a granular appearance.

One rounded, black, coarse-grained, oblate hornblendite ultramafic nodule was found in second period float. In hand specimen it appears to be composed of an interlocking mosaic of large prismatic hornblende grains; interstices between the crystals are filled with a black glass containing innumerable tiny gas bubbles.

Third Period Basalts

Cinder cones and lavas of the third (final) period are defined as those which have a pristine appearance (e.g., well preserved craters on cinder cones, glassy surface in places on flows) and which lack substantial vegetative cover (Fig. 9). Third period activity appears to have begun as explosive volcanism similar to terminal second period eruptions. The most recent activity, however, consists of long (up to 15 km), thin aa flows. The flows emanate from the flanks of cones or from fissures at the base of cones. These volcanics are the most areally restricted. Erinç (1970) has classified thirteen cones and their associated flows as third period. Washington (1894b) noted that there are three major period cones; most of the others classified by Erinç are parasitic cones closely associated with the main three. Each of these major period cones sits in a Neogene sedimentary basin, separated from each other by ridges of metamorphics, first noted by Washington in 1894. These basins are probably the geomorphological expression of intersecting fault sets; either intersections of east-west

Figure 9. Kara Devit and parasite cone. The large
third period cinder cone and lava cone from the
central volcanic field. Aa flows emanated from fis-
sures at the base of the cone, also forming the
parasite cone in the right foreground. Note the fresh
appearance and lack of vegetation on the third period
volcanics.

and north-northwest trending fault traces, or north-northwest and north-northeast trending fault traces, all of which are presently active in western Anatolia. The east-west trending faults which form the prominent graben terrane are the youngest structures, and can be seen to cross-cut the other trends in the Kula region.

PETROGRAPHY AND ROCK CLASSIFICATION

Rock Classification

Difficulties in classification of volcanic rocks have been both bemoaned and obfuscated by many, to which I add my personal tooth-gnashing. Classification by mode is misleading in any rock with a glassy groundmass, yet these classifications are in wide use. Alternatively, to use a scheme such as that of Baker (1969), which employs the Differentiation Index to set limits for various rock types, implies to me an acceptance of fractional crystallization in controlling compositional variation within a suite of rocks. For classification purposes in this thesis, major element chemistry in conjunction with Nockolds' (1978) descriptions is used. This incorporates both modal assemblage and groundmass components in the classification.

The Kula volcanics appeared unique to H.S. Washington, and in his 1894 study of the volcanics he proposed that they be given the name Kulaite, the definition being "a subgroup of the basalts which is characterized by the presence of hornblende as an essential constituent, which surpasses the augite in quantity and importance." He identified leucite-bearing and nepheline-bearing varieties of Kulaite. Although Kulaite has made its way into a few learned papers (e.g., Coombs and Wilkinson, 1969), the term is not in common use. Washington himself mentioned (1900) that "the closest analogues of the Kula rocks are to be found among the nepheline-tephrites and nepheline-basanites", which are where

many of them are classified in this thesis. In view of the
fact that some of the Kula rocks are not hornblende-bearing;
while in others the hornblende has completely (magmatically)
altered to an assemblage of anhydrous phases and therefore is
no longer strictly present; and in the desire to remove
another confusing term from the igneous petrology literature,
the term Kulaite will not be used here. Although these rocks
have some unusual characteristics, which will be described
later, the volcanics can be adequately described as a
basanite to trachybasalt suite. Nockolds (1978) defines
basanites as having olivine and calcic plagioclase as
essential consituents, normally with abundant clinopyroxene.
In addition a basanite should contain greater than 5 or 10
percent normative nepheline, depending on the classification
used. All of the Kula volcanics contain greater than 10%
normative nepheline, and differ from the petrographic
description given only in containing kaersutitic amphibole as
an additional mafic phase. The amphibole-rich basalts are
similar to many authors' descriptions of trachybasalts (e.g.,
Baker, 1979), although no modal sanidine is present, which
Nockolds (1978) considers a further essential constituent.
In light of their similar major element chemistry, however, I
have classed hornblende-bearing samples with the
trachybasalts.

Terminology

Authors who have described rock suites that have
similarities to Kula, in particular Binns (1969), Binns et

al. (1970), Best (1970, 1974), Irving (1974), Stuckless and Irving (1976), and Wass (1979), refer to phenocrysts as phases which have crystallized in the magma which encloses them, xenocrysts as accidental inclusions which may or may not have a genetic relationship to their enclosing magma, and megacrysts as grains of uncertain origin, which the aforementioned authors believe may represent high pressure crystallates of the enclosing magma. Megacryst assemblages may consist either of different phases or of similar phases of different composition compared to the phenocryst assemblages.

Kula volcanic rocks often pose problems in classification of the prequench generation of minerals. Inclusions such as quartz or ferrohypersthene are obviously xenocrystic; anorthoclase, plagioclase, spinel and gehlenite fit the definition of megacryst - not present as a phenocryst phase in the samples and of uncertain relationship to their enclosing magmas. However, the classification of clinopyroxene, hornblende and olivine in the Kula volcanics is sometimes problematic. Zoned euhedral titanaugite and kaersutite occur as phenocryst phases, yet large, unzoned grains of both minerals are common, with and without various alteration features. The composition of these phases is commonly identical to coexisting phenocrysts. Unzoned anhedral-subhedral cores are commonly mantled by zoned phenocrystic rims. It is difficult to decide which material should be classified as megacrystic or phenocrystic (or even

xenocrystic) when a single grain may be both phenocrystic and megacrystic, when both zoned and unzoned grains are commonly mechanically broken, and when both types may be of similar size and appearance. Olivine poses the same problem, as nearly all grains have one or more of the following features: rounding and embayment of grains by the melt, signs of strain such as undulatory extinction, or euhedral terminations at one end with the other end deeply embayed. Many olivines are unzoned, and the rest have slight zonation undetectable by optical examination. These could be interpreted as either xenocrystic or megacrystic olivines, yet they have the same composition as olivines which lack these features.

In the following text, minerals which are described as zoned and/or euhedral are considered phenocrysts; others, with exception of phases totally foreign to the nature of the magma, are considered megacrystic and their possible relations to their enclosing lava will be treated in a later section.

Petrography - General Statement

Kula volcanics are characterized by high alkali and alumina content, combined with relatively high magnesia. The suite of samples collected indicates that the volcanic field is relatively homogeneous in composition both within and among the three periods of activity. The rocks are silica-undersaturated and usually contain a glassy groundmass rich in nepheline and/or leucite, though these phases are often modally occult. The rocks are phenocrysts-bearing to various

degrees, with phenocryst assemblages dominated by olivine-clinopyroxene in the basanites or clinopyroxene-hornblende in the trachybasalts.

In the following text, one detailed description is provided for each textural and/or compositional rock type. A summary of the major petrographic characteristics of the Kula volcanics can be found in Table 1.

Petrography of Representative Lavas

Hornblende-bearing trachybasalts, example TM-9-68

TM-9-68 was collected from the first period plateau basalts. The sample is non-vesicular, tan weathering, medium gray on a fresh surface with sparse black augite phenocrysts set in a fine-grained groundmass. The basalt is typically massive, although first period basalts may show localized development of columnar jointing.

In thin section, zoned titaniferous to titanaugites are the most prominent phenocrysts. Glomeroporphyritic titaniferous augite clots are common. The augite is pale tan in color and non-pleochroic, with weak to moderately strong oscillatory and sector zoning. Simple and multiple twinning is fairly common. Rare phenocryst cores are pale green in color, surrounded by pale tan rims, intensifying toward the edge of the crystal. Clusters of fine-grained blocky magnetite are commonly observed in the cores.

Olivine is invariably rounded, embayed or broken; it is colorless, unzoned, devoid of inclusions and typically has a thin pale orange iddingsite rim. Plagioclase is not present

TABLE 1. Petrography of the Lavas and Nodules

	TM-9 57	TM-9 58	TM-9 59	TM-9 60	TM-9 61	TM-9 62	TM-9 63	TM-9 64	TM-9 65	TM-9 66	TM-9 67I	TM-9 67II	TM-9 68	TM-9 69	TM-9 70
CLINOPYROXENE	a	c	c	a	c	c	a	a	c	c,m	c	c	a	c,x	a
glomerophyric	-	+				-	-	+	-	+	+	+	+	+	+
twinned	-	-		+	+			+	-	+	-	+	+	+	
sieved cores	+			+	-		+	-			-	-	-		
green cores	+	-		+	-		-	+			-	-	-	+	-
OLIVINE	c	c	r	c	c	c	r		a	c	a	c	r	c	c
resorbed	-	-	+	-	+	+	-	+	+		+	+	+	+	-
altered	-		+	+	-	+	-		-			-	-	+	
reaction rim		cpx					hbl							+	
AMPHIBOLE		a	r	?	a	c	a	c,m	a	a	a	a,x	a	c	a
not altered			+		+	+	+							+	
zoned						+	+							+	
twinned			-												
fresh cores								+		+					
oxidized rim	-	-	+	+	+			+	+	+	+	+	+		+
opx alteration	+	+		+	+			+	+	+	-	+	+		+
granular alt.		-							-	+	+	+			
GLASS	cl	cl	br	cl	cl	br	lbr		cl	cl	cl	cl	cl		lbr
PLAGIOCLASE	g	g		g	g	?	?		g,m	g	g	g,m	g	?	g
APATITE	g			g	g			m							
SPINEL GROUP	g	g		g	g			g	g	g	g	g	g	?	g
LEUCITE	gl								g	g					
NEPHELINE	gl								g	g					g
ANACITE															
GEHLENITE															
TI-MICA															
SPHENE															
ORTHOPYROXENE	x														
ANORTHOCLASE															
QUARTZ				x											
CARBONATE													x		
K-SPAR				x											

TABLE 1. Petrography of the Lavas and Nodules

	V	23L	K1	D1a	D2	D4	D5	53C1	53C2	68C1	68C2	68C3	TM-9 63N	TM-9 64N	TM-9 69FG	TM-9 69CG
CLINOPYROXENE	c	c	c	c	c,x	c	a	a,m	a	a,x	a	a	a	c	a	c
glomerophyric	+	-	-	+	+	-	+	+	+	-	+	+				
twinned	+	-	-		-	-	-	+	+	+	+	-				
sieved cores	-	-			-	-	-	+	+	-	+	-				
green cores	-	+		-	+	-	-	+	-	-						
OLIVINE	c,m	c,m	c	c	nc	r	c	nc	nc			c				c
resorbed	+	+	-	+	+	+	+	+	-	+	+					
altered										+						-
reaction rim	hbl	cpx, hbl			cpx			hbl	cpx	cpx	cpx					
AMPHIBOLE	a,m	a,m	a	a,m	a,m	a	a	a,m	a	a			a	a	a	a
not altered	+	+						+	+	+			+	+	+	+
zoned	+	+											+	+		
twinned	-								-							
fresh cores	+	+	+	+				+	+							
resorbed	+	+	-	-		+		+	+	+						
oxidized rim	+	+	+	+		+	+	+	+							
opx alteration	-	+	+				+		+							
granular alt.			+	+	+											
GLASS	br	br	lbr	cl	cl	lbr	cl	?		cl	cl	lbr	or	b/c	or	
PLAGIOCLASE	g,m	g	g	g,m	g,m	g	g	g,m	g	g,m,x	g	g	c	g		
APATITE	g	g	g	g,m	g,m	g	g	g	g,m	g	g	g	r	a	r	a
SPINEL GROUP	g,m	g,m	g	g	g	g	g	g	g	g	g	g	r	r	r	c
LEUCITE	g	g	g	?	g	g	g	?	g					r		
NEPHELINE																
ANALCITE												g				
GEHLENITE								m								
TI-MICA									m	m				a		c
SPHENE						x?			m					r		
ORTHOPYROXENE																
ANORTHOCLASE	m	m			m	m			m	m						
QUARTZ		x	x		x				x							
CARBONATE																
K-SPAR	?								x?							

a=abundant, c=common, nc=not common, r=rare, m=megacryst, x=xenocryst, g=groundmass phase, hbl=amphibole, cpx=clinopyroxene, cl=colorless, lbr=light brown, br=brown, or=orange, b/c=brown and colorless, +=commonly observed, -=present but not common, ?=positive identification not made.

as a phenocryst phase. Abundant fine-grained aggregates of iron ore, clinopyroxene, orthopyroxene, calcic plagiocalse and nepheline can be observed that maintain the euhedral outline of former amphibole.

Mesostasis is composed of fine-grained titanaugite, titanomagnetite, plagioclase, colorless glass, apatite and minor olivine. Sinuous veinlets of carbonate are rarely observed. The colorless glass is alkali-rich and in places analyzes as either leucite or nepheline. Calcic plagioclase (labradorite) clubs or laths are aligned, defining a flow foliation. Twinning is poorly developed, and the often club-shaped grains give the texture the look of eel grass. Alkali feldspar may be occult in the groundmass as a low relief phase with undulatory extinction, but was never optically identified.

This sample is typical of first period and most third period flows, except that in the latter leucite is present as an optically identifiable phase in the mesostasis, and hornblende may be present in either altered or unaltered form. The main characteristic of both first and third period samples is the presence of abundant groundmass plagioclase, usually with a flow fabric (trachytic) (Fig. 10).

Porphyritic hornblende-bearing trachybasalts, example V

This sample is a porphyritic third period flow of small areal extent issued from a parasitic cone at the base of Kara Devit, in the center of the volcanic field.

The sample consists of black, unweathered highly
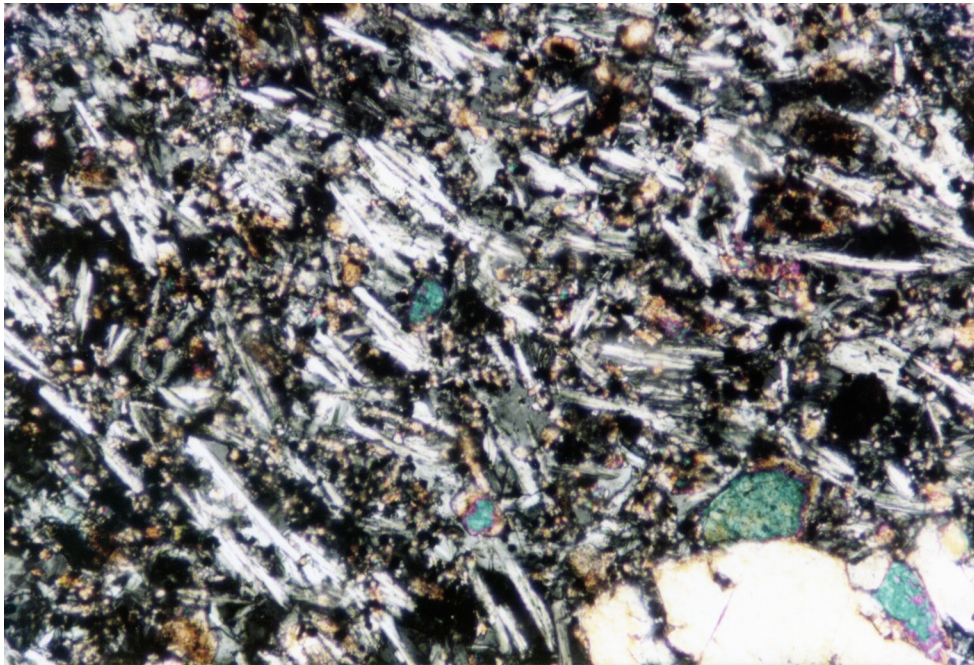
Figure 10. Third period hornblende-bearing trachy-
basalt $D_{1(a)}$, showing trachytic texture of the
groundmass. In certain samples, poorly developed
crystal form and lack of twinning in plagioclase micro-
lites may be indicative of high pH_2O in the magma
until the actual subaerial eruption. Field of view:
1.38 mm

vesicular lava, rich in black hornblende grains. In thin section, kaersutite is the most abundant phenocryst phase, followed by titaniferous to titanaugite and olivine. The groundmass consists of pale brown glass which contains spherical titanaugite, plagioclase and apatite microlites, very fine-grain titanomagnetite, euhedral kaersutite and titanaugite microphenocrysts, and round to faintly octagonal inclusion-filled leucite.

The predominant phenocryst phase is kaersutite, which occurs from 0.05 mm microphenocrysts to large 0.5 cm phenocrysts or megacrysts. Multiple generations of kaersutite are present; some of them may be xenocrystic to the enclosing basalt. Evidence for this is the wide variety of kaersutite texture, which ranges from euhedral zoned phenocrysts, to unzoned kaersutite with opacitized rims, to complete break-down of the amphibole to anhydrous phases. Pleochroic colors vary with extent of oxidation or alteration. Concentric zoning occurs in unaltered phenocrysts (Fig. 11), some kaersutites consist of a rounded core surrounded by an euhedral rim. Rarely, cores consist of pale plum-brown glass with microlite and oxide inclusions surrounding a gas bubble, in turn mantled by euhedral zoned kaersutite. Apatite is a common inclusion in unzoned amphibole.

Clinopyroxene forms abundant small phenocrysts. Concentric but not sector zoning is common. Both green pheochroic cores and sieve texture are common, the latter consisting of plum-brown glass, small vesicules, opaque
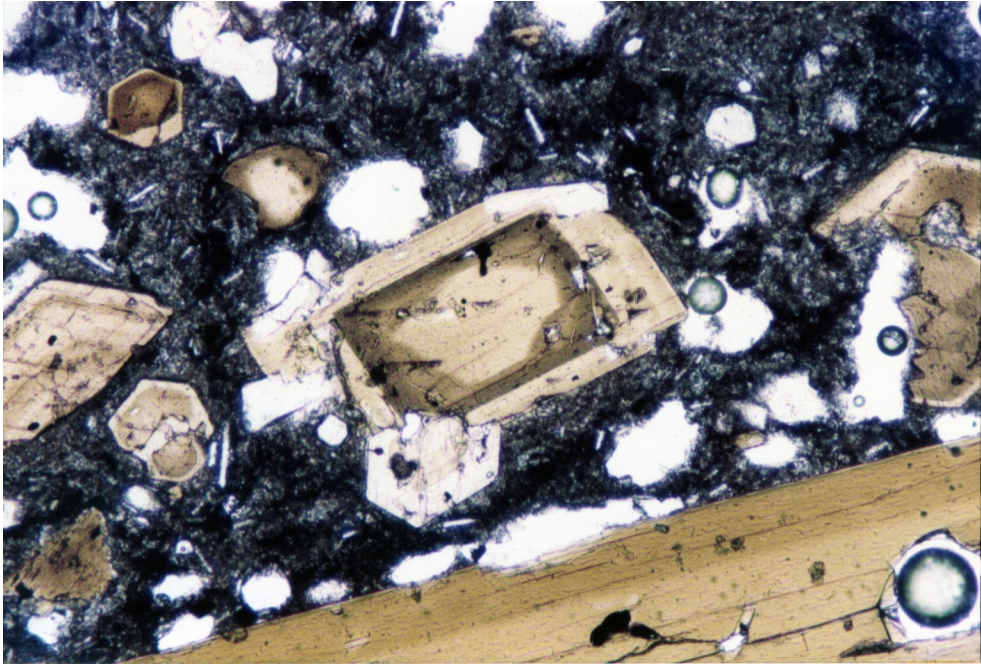
Figure 11. Third period porphyritic hornblende-
bearing trachybasalt, V. Kaersutite phenocryst shows
oscillatory zoning with an inner core of Mg-rich
kearsutite mantled by Fe-rich kearsutite with a Mg-
rich rim. Field of view: 1.38 mm.

inclusions and recrystallized clinopyroxene in the core of many clinopyroxenes. Recrystallized clinopyroxene is the same composition as outer quench pyroxene rims. Although many phenocrysts are euhedral, some show signs of resorption, and many are mechanically broken, especially larger grains. Glomeroporphyritic clots are common, typically made up of smaller grain sizes.

Olivine also exhibits multiple habits. The phenocrysts examined are either unzoned (Fo $_{86}$), or slightly zoned (Fo 86-84). Olivines can be euhedral, embayed with no other alteration, or can be surrounded by rims of kaersutite and/or titanaugite (Fig. 12). The latter type of olivine commonly has very irregular, serrated contacts with the cpx/hbl rim, and shows evidence of strain, such as undulatory extinction and possible sub-grain formation. These olivines may be xenocrystic to their host basalt.

Sample V and rocks similar to it typically carry a variety of megacrystic and xenocrystic inclusions. Anorthoclase, plagioclase (oligoclase to andesine), and plum-gray spinel can be observed, usually with rounded or embayed margins. Rare plagioclase megacrysts have euhedral kaersutite either included in or embaying the feldspar rim. Rare corroded gabbro xenoliths, quartz and iron-rich pyroxene grains are probable accidental inclusions of Menderes basement lithologies.

Non-hornblende-bearing basanites, examples TM-9-57 and 68C$_3$

These rocks vary in hand specimen from black and highly
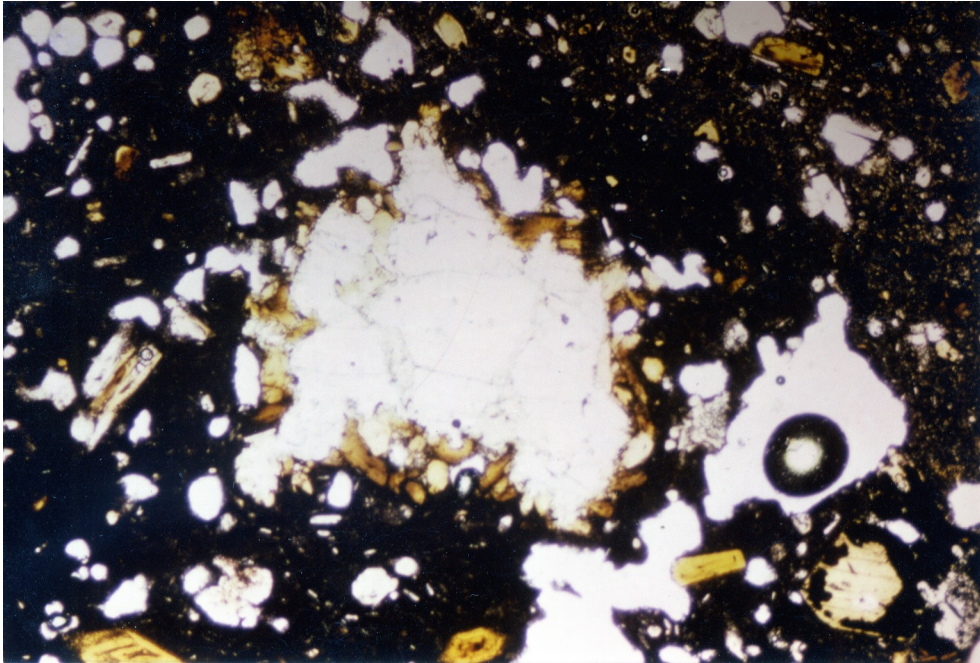
Figure 12. Third period porphyritic hornblende-
bearing trachybasalt, V. Kaersutite in reaction with
olivine (Fo_{86}) megacryst. Olivine shows un-
dulatory extinction and may be a xenocryst unrelated
to the enclosing magma. Some olivine with similar
Fo content in the same thin section are not armored
with kaersutite, indicating complex olivine-amphibole
stability relationships. Field of view: 3.4 mm.

vesicular to mottled pinkish-gray non-vesicular varieties. They contain abundant phenocrysts of black clinopyroxene and less abundant yellow-green olivine.

In thin section titaniferous to titanaugite is the predominant phenocryst phase. The euhedral to subhedral grain size is variable and can be quite large, up to .5 cm. Both concentric and sector zoning is common and complex, with zones often accentuated by drastic changes in both color and optical properties. Phenocryst cores are generally colorless to pale tan, with $2V_z = 58\text{-}60^\circ$, although rounded to euhedral, apple to olive green pleochroic cores are not uncommon. Pyroxene rims are pale tan to purplish brown with lower $2V_z$ and z c. One dark purplish groundmass grain in TM-9-57 was observed to have parallel extinction and a positive uniaxial figure, most likely a result of high (over 5%) TiO_2 content. Both glomeroporphyritic and single phenocrysts can be observed; single grains are generally large in size. Some phenocryst cores show extensive sieving and recrystallization, surrounded by homogeneous quench rims. Oxides are abundant inclusions in the cores, particularly sieve-textured cores. Some resorption is common in the large grains.

Olivine is euhedral to anhedral, colorless, with minor iddingsite rims. No zoning can be optically determined. Grains commonly appear mechanically broken, but lack reaction relationships that are observed in some of the other lava types.

Groundmass consists of microphenocrysts of titanaugite and olivine set in a colorless to light brown glass, which is alkali-rich and heterogeneous on the scale of a thin section. Calcic plagioclase laths are in general poorly developed and sparse, considering alkali and alumina contents. In 68C$_3$, light brown alkali-rich glass surrounds inclusion-riddled colorless, isotropic round blobs which analyze as analcite and appear to be primary.

Common in these rocks, as well as the other types, are rings of clinopyroxene (non-titaniferous) microphenocrysts which surround irregularly-shaped turbid dark brown to pale brown glass. Some of these can be demonstrably related to reaction with and assimilation of quartz xenocrysts by the magma (Fig. 13a & b).

Xenoliths are not as common as in porphyritic hornblende-bearing lavas. One unusual kaersutite and titaniferous augite xenolith was found. This xenolith shows the effect of possible thermal metamorphism under hydrous conditions; by replacement of titaniferous augite by kaersutite with development of a granoblastic polygonal texture (Spry, 1969, see Fig. 50).

Nodule Petrography

TM-9-69CG

TM-9-69 was collected from third period float west of Kara Devit, and was most likely erupted from Kara Devit or one of its parasite cones. The 10 by 15 cm hand specimen is dark brown in color, and is composed of large equidimensional
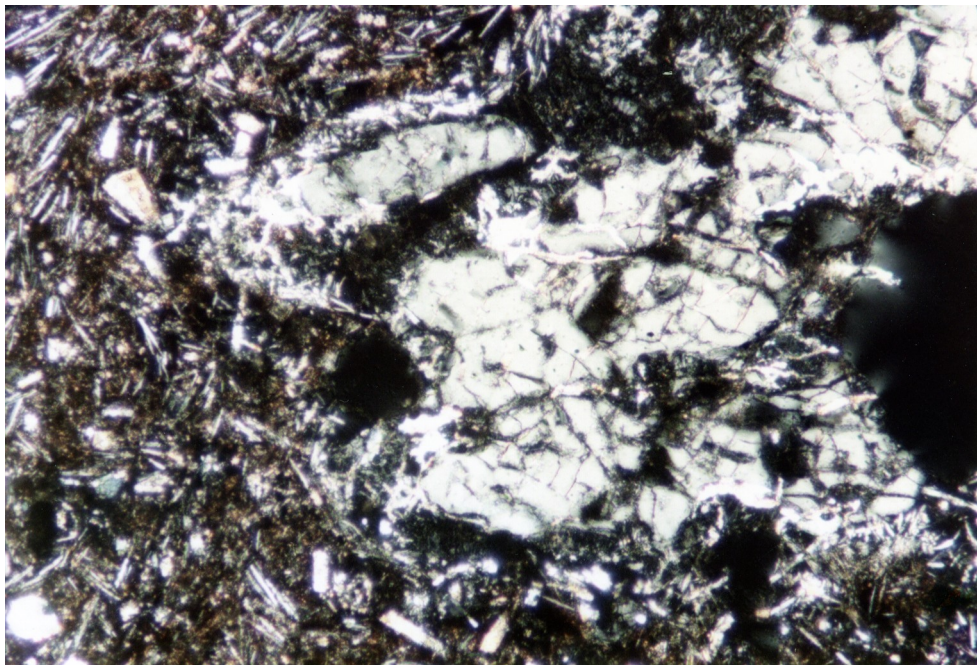
Figure 13a. Quartz xenocryst with partially melted rim and clinopyroxene quench rim, hornblende-bearing trachybasalt, K_1. Field of view: 1.38 mm.
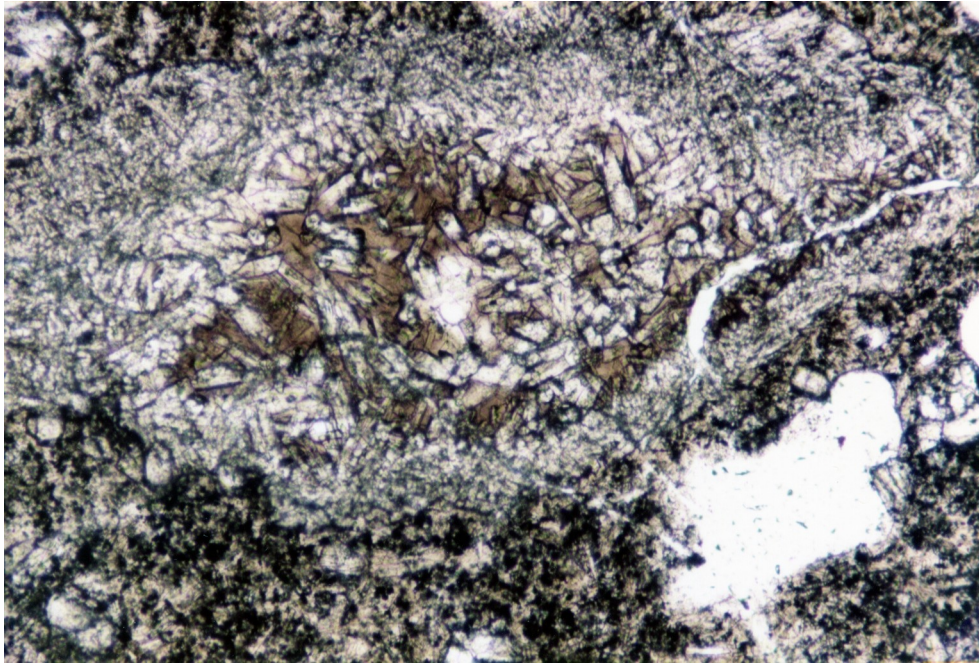
Figure 13b. Oscellar structure hypothesized to have
formed by total partial melting of a quartz xenocryst,
quenched to glass on eruption. Clinopyroxene microlites
which surround the glass become systematically enriched
in SiO_2 and depleted in TiO_2 and Al_2O_3 as the glass is
approached. From $53C_2$, field of view: 1.38 mm.

grains of amphibole and mica. In places, very fine grained green clinopyroxene are observable as inclusions within the large equidimensional grains.

In thin section, oikocrysts of titaniferous ferroan pargasite and titaniferous phlogopite to 1-2 cm in diameter poikilitically enclose clinopyroxene, olivine and apatite. Clinopyroxenes and olivines are typically anhedral and are unzoned; clinopyroxenes have ragged borders and contain patches of amphibole, suggesting replacement of earlier pyroxene by amphibole. The clinopyroxenes also contain fine-grained spinel inclusions. Olivine is unaltered except for ubiquitous thin orange iddingsite rims. Apatite is an essential constituent of this rock, and reaches lengths of 0.5 cm or greater. It occurs as anhedral to subhedral grains in association with clots of anhydrous phases, or as subhedral grains totally enclosed by oikocryst phases. The apatites are characterized by innumerable fine grained elongate opaques oriented coincident with the "c" crystallographic direction of the apatite (Fig. 14).

Grains enclosed by phlogopite are typically more altered than phases enclosed by amphibole. Grain boundary geometries and appearance of the mica suggest that it may be secondary after amphibole.

TM-9-64N

TM-9-64N was collected in second period float near outcrop of TM-9-64. It consists of a strongly oblate spheroid approximately 14x5cm. In hand specimen the sample
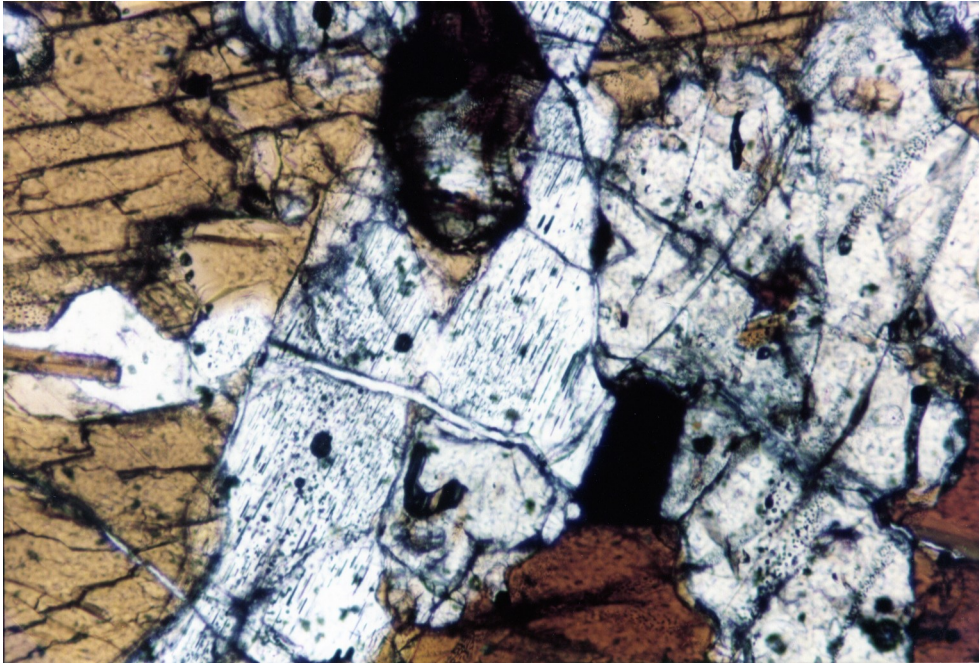
Figure 14. Nodule TM-9-69CG. Apatite grain containing crystallographically oriented iron-rich rods. Apatite megacrysts similar to this have been observed in a third period trachybasalt flow (D_2). Field of view: 1.38 mm.

elongate, loosely interlocking black amphibole crystals averaging 1 cm in length. Vesicles and irregular holes are interstitial to the crystals.

In thin section zoned kaersutite is irregularly surrounded or replaced by pale tan to dark red-brown pleochroic titanbiotite, unzoned kaersutite and zoned tit naugite (Fig. 15). Interstitial to these grains is a vesicle-filled, heterogeneous, dark brown to colorless glass which encloses abundant euhedral to subhedral apatite grains (Fig. 16) which contain inclusions of both glass and opaques. Sphene occurs rarely as pale yellow anhedral grains in close association with the kaersutite. The relationship between glass and crystalline phases is obscure from petrographic examination. The titanbiotite appears, at least in part, to be secondary after amphibole, but prior to incorporation of the nodule in its enclosing magma. The unzoned kaersutite and zoned clinopyroxene are interpreted as phases crystallized after incorporation into the magma under decreasing pressure and volatile content conditions.

TM-9-69FG

This 12x7 cm nodule was collected from the same third period float as TM-9-69CG. In hand specimen it is brown with irregularly distributed red oxidized patches. One side of the nodule is covered with an amphibole selvage reminiscent of nodule TM-9-64N. It is made up predominantly of fine-grained amphibole with lesser areas of gray-blue clinopyroxene. The nodule has local areas of high gas bubble
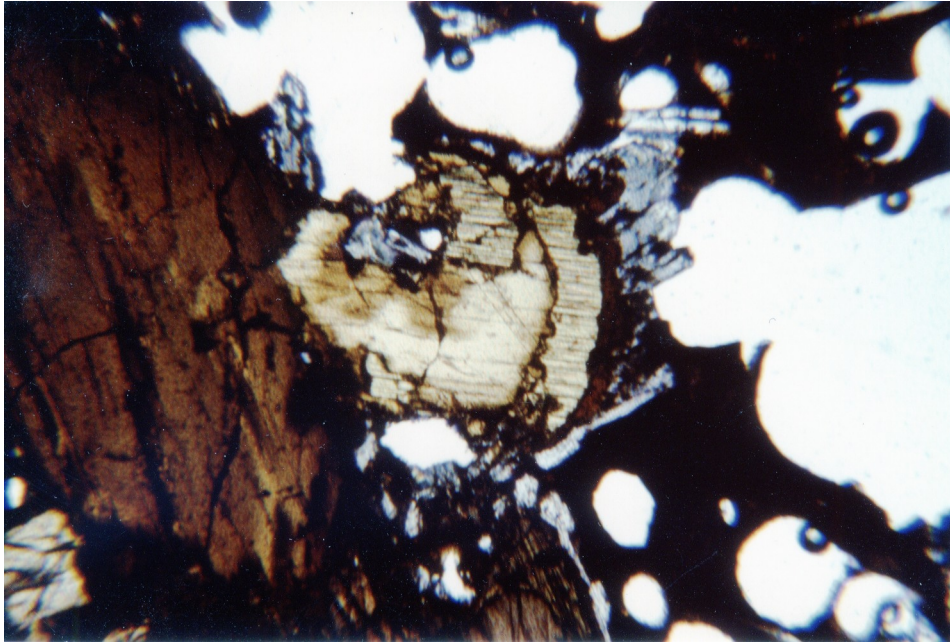
Figure 15.   Typical mineral zonation in nodule TM-
9-64N.   Core amphibole is kaersutite, zoning outward to
ferroan pargasite.   The amphibole is successively
mantled by titanbiotite, kaersutite and titanaugite.
This is interpreted to be a result of increasing pH_2O
in the melt, stablilizing mica;   thereafter the corona
follows a progressive decrease in pH_2O, possibly
recording ascent of the nodule to the surface.   Field of
view: 1.38 mm.
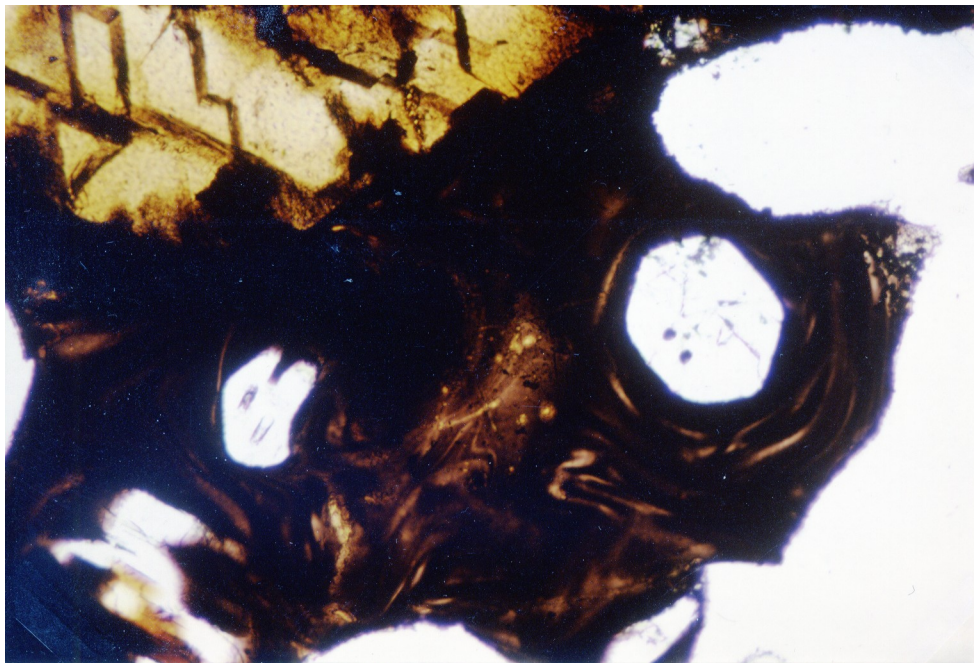
Figure 16. Heterogeneous brown to colorless glass
with apatite crystals, nodule TM-9-64N. Apatites
sometimes enclose rounded to euhedral opaque grains
distinct in appearance from the opaque rods observed
in nodule TM-9-64N. Field of view: 1.38 mm.

content, but most of it is quite dense.

In thin section roughly equidimensional (0.5 mm) kaersutite and clinopyroxene are the predominant phases, with clinopyroxenes tending to form discrete clumps or stringers surrounded by and in places invaded by kaersutite (Fig. 17). Fine grain euhedral to anhedral opaques are common. Anhedral apatite is also present. In the vesicular areas gas pockets are often separated by pale orange glass. This glass is sporadically present at 120° grain boundaries throughout the nodule, and is possibly a decompression related melt phase. Near the edge of the nodule a black oxidation rim surrounds most of the grains.

TM-9-63N

TM-9-63N is a small 5x3 cm nodule collected from a locally inclusion-rich area in outcrop near the crater lip at the summit of Kara Devit. It resembles TM-9-69FG in appearance, but has no kaersutite selvage.

In thin section the texture also resembles TM-9-69FG. Differences include a slightly more elongate kaersutite habit, lack of apatite, and most significant, the presence of intermediate plagioclase interstitial to kaersutite and clinopyroxene. TM-9-63N is the only plagioclase-bearing nodule recovered, suggesting that it may have been derived from shallower depth than the other nodules. This nodule also contains thin films of pale orange glass around vesicles distributed throughout the nodule; an area of elongate kaersutite grains shows a distinct preferred orientation in

one area of the nodule (Fig. 18).
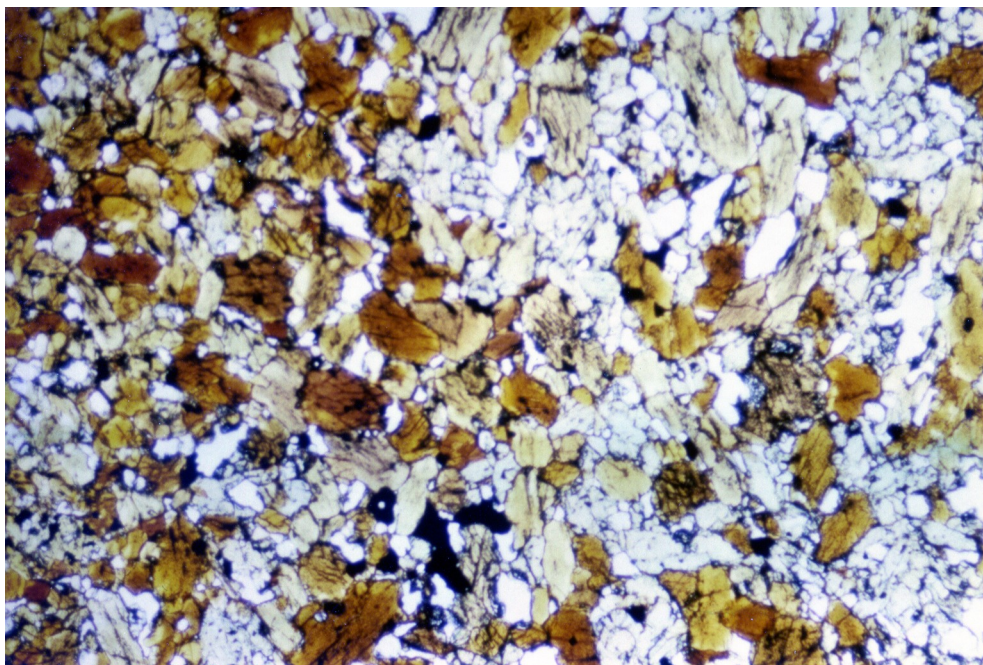
Figure 17. Nodule TM-9-69FG, showing typical tex-
tural relation of clinopyroxene and amphibole.
Sub-equant grains of similar size suggest recryst-
allization of both this nodule and large portions of
TM-9-63N, which has a similar appearance. Kaersutite
appears to be secondary after clinopyroxene, although
recrystallization(?) has obscured relationships.
Field of view: 3.4 mm.
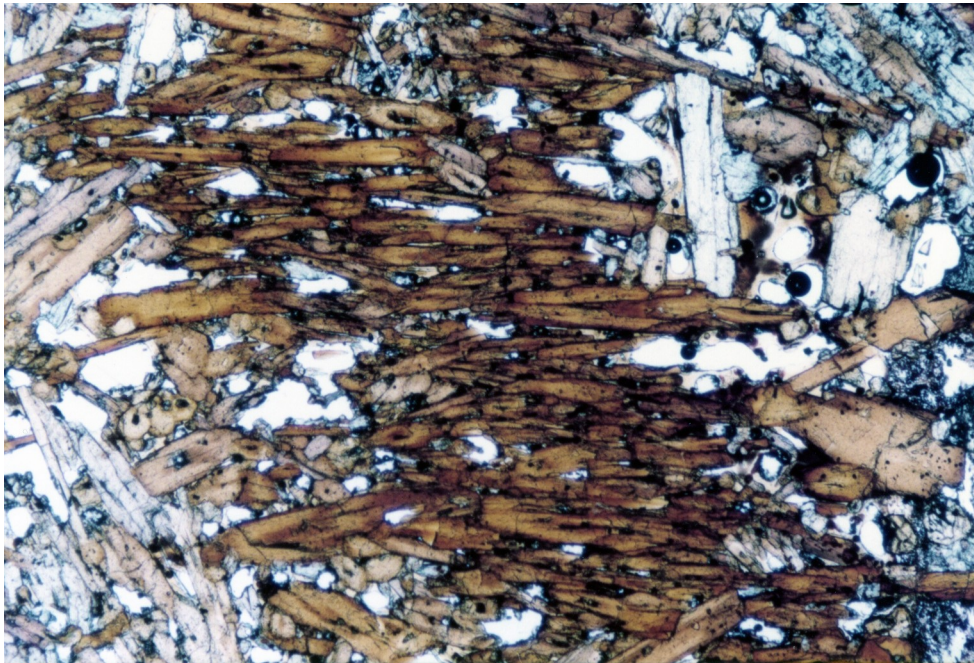
Figure 18. Zoned kaersutite vein in nodule TM-9-63N.
The origin of the preferred orientation is unknown
but may involve crystallization in a non-hydrostatic
stress field. The elongate nature of the kaersutite
of this area contrasts with the more equant grains in
rest of the nodule. Field of view: 3.4 mm.

MAJOR ELEMENT CHEMISTRY

Analytical Technique

Major element composition was determined by electron microprobe analysis on fused glass beads. Lava samples were ground to approximately 400 mesh using a steel mechanical jaw crusher, roller mill and tungsten carbide mixer mill. Sample passes through the steel rooler mill and time in the mixer mill were kept to a minimum in an attempt to reduce contamination. Glass beads were prepared by fusion of unfluxed sample splits on Mo strips under 40 psi Ar atmosphere to reduce alkali loss. Fused beads were ground in an agate mortar with reagent grade acetone and refused to ensure homogenity. Whole rock analyses reported are averages of three determinations on the same bead.

Analyses were done using the Harvard University automated ARL-EMX electron microprobe at an accelerating potential of 15 kv and a sample current of 20 nanoamps. Counts were corrected for dead time, drift and background. Matrix corrections were calculated online according to Bence and Albee (1968).

Ultramafic nodule powders were prepared by hand using a hammer and steel plate, percussion mortar (stainless steel) to reduce sample to sand size, followed by grinding to at least 100 mesh using an alumina mortar and pestle.

Results

Analyses of 24 lava samples and 4 ultramafic nodules from the Kula volcanic field, and their C.I.P.W. normative

mineralogy are presented in Table 2.

The Kula basanite-trachybasalt suite is characterized by relatively minor variations in major element chemistry, excepting Na_2O and K_2O, of lava erupted both within and among eruptive periods, over a time interval of approximately 1.1 m.y. The rocks are peraluminous, highly alkaline, undersaturated with respect to SiO_2, and plot in the strongly alkaline field as defined by Saggerson and Williams (1964) on a $Na_2O + K_2O$ versus SiO_2 variation diagram (Fig. 19). The rocks fall above but near the Tristan da Cunha trend of Baker (1964). Note that the range of SiO_2 for the entire suite is less than five weight percent. Normative felspar plots (Fig. 20) can be used to distinguish sodic and potassic alkaline rock series as defined by Coombs and Wilkinson (1969). The plot shows that Kula volcanic rocks have both sodic and potassic affinities, which Washington (1894) noted in his classification of both nepheline and leucite Kulaite. Third period volcanics are potassic, first and second period rocks have both sodic and potassic members. The samples form a trend which is nearly perpendicular to other reported trends, with the Kula trend characterized by variations in Ab:Or ratio at roughly constant An. Other suites maintain either a roughly constant or slightly increasing potassium:sodium ratio with decrease in An:alkali ratios. Many of these trends have been explained by fractional crystallization models, which may suggest either that the Kula rocks are fractionating different phases than most

Table 2. Kula Major Element Chemistry - lavas

	First Period			Second Period								
	TM-9-57	TM-9-67I	TM-9-68	68C3	68C2	53C2	68C1	53C1	TM-9-64	TM-9-67II	TM-9-61	TM-9-58
SiO2	46.77	48.73	47.72	46.70	46.27	45.46	45.86	46.26	45.80	49.47	48.29	48.36
TiO2	2.12	2.02	2.17	2.19	2.10	2.19	2.25	2.32	2.19	1.90	1.93	1.90
Al2O3	16.95	17.92	18.18	16.98	17.07	16.02	16.35	16.32	16.80	18.28	18.20	18.36
Cr2O3	0.03	---	---	---	0.02	---	0.04	0.02	0.02	0.01	0.01	0.04
FeO*	8.55	7.69	8.25	8.42	8.38	9.00	9.04	8.89	9.11	7.55	7.83	7.16
MnO	0.16	0.13	0.13	0.19	0.18	0.12	0.19	0.14	0.18	0.16	0.16	0.14
MgO	6.70	4.84	4.59	6.84	6.75	6.13	6.09	6.07	5.54	4.55	4.54	5.87
CaO	9.28	7.45	8.54	8.96	9.57	10.23	10.59	10.37	10.15	7.63	7.54	7.62
Na2O	6.01	5.93	5.14	5.32	5.91	4.91	5.78	4.84	4.97	6.68	7.21	5.45
K2O	1.52	3.31	2.83	2.66	1.04	2.40	1.16	2.30	1.46	1.66	1.14	3.13
P2O5	1.12	0.74	0.70	0.92	1.22	1.13	1.19	1.02	1.18	0.61	0.65	0.51
total	99.21	98.76	98.25	99.18	98.51	97.59	98.54	98.55	97.40	98.50	97.50	98.54

C.I.P.W. normative mineralogy (wt%)

	TM-9-57	TM-9-67I	TM-9-68	68C3	68C2	53C2	68C1	53C1	TM-9-64	TM-9-67II	TM-9-61	TM-9-58
or	8.98	19.56	16.72	15.72	6.15	14.18	6.86	13.59	8.63	9.31	6.74	18.50
ab	18.90	17.22	17.23	12.27	21.15	10.87	17.30	12.65	19.47	28.05	28.21	15.88
an	14.78	12.50	18.18	14.60	16.98	14.59	15.24	16.01	19.22	14.99	13.93	16.45
ne	17.31	17.86	14.23	17.74	15.63	16.62	17.12	15.33	12.23	15.42	17.77	16.38
di	19.26	15.87	15.92	19.16	18.12	23.24	23.85	23.21	18.99	15.29	15.60	14.48
ol	10.11	7.33	7.14	10.24	10.50	7.94	7.71	7.63	8.52	7.06	7.13	9.37
ap	2.65	1.75	1.66	2.18	2.89	2.68	2.82	2.42	2.79	1.44	1.54	1.21
mt	3.45	3.09	3.32	3.41	3.39	3.62	3.64	3.58	3.68	3.04	3.16	2.89
il	4.03	3.84	4.12	4.16	3.99	4.16	4.27	4.41	4.16	3.61	3.67	3.61
100 Mg / Mg+.75Fe*	65	60	57	66	66	62	62	62	59	59	58	66

* = Fe2+ + Fe3+

Table 2. Major Element Chemistry - lavas

	Third Period TM-9-63	V	TM-9-70	TM-9-23L	K1	TM-9-66	Dl(a)	TM-9-62	D5	TM-9-59	D2	D4
SiO2	48.05	47.57	47.76	48.16	48.74	49.57	48.27	48.46	49.00	47.86	47.98	48.58
TiO2	1.97	1.89	1.99	1.95	1.77	1.82	1.99	1.92	2.04	2.04	1.93	1.93
Al2O3	17.73	17.80	17.37	17.96	17.89	17.97	17.93	18.43	18.34	18.57	18.26	18.24
Cr2O3	0.06	--	0.02	0.02	0.02	0.02	--	0.02	0.01	0.04	0.02	--
FeO*	7.74	7.73	7.70	7.85	7.42	7.34	7.69	7.52	7.73	7.15	7.67	7.61
MnO	0.16	0.14	0.16	0.18	0.18	0.16	0.16	0.13	0.17	0.13	0.19	0.19
MgO	6.30	6.20	6.02	6.00	5.94	5.79	5.66	5.47	5.41	5.38	5.34	5.33
CaO	8.27	8.20	8.04	8.19	7.49	7.65	7.89	7.39	7.80	7.67	7.80	7.56
Na2O	5.35	5.93	5.79	5.62	5.91	5.34	5.75	5.47	5.77	5.28	6.01	5.93
K2O	3.07	3.43	3.26	3.39	3.63	3.45	3.36	3.24	3.23	3.31	3.46	3.29
P2O5	0.58	0.86	0.78	0.79	0.76	0.75	0.81	0.46	0.63	0.81	0.87	0.77
total	99.28	99.75	98.89	100.11	99.75	99.86	99.51	100.13	98.51	98.27	99.53	99.43

C.I.P.W. normative mineralogy (wt%)

	TM-9-63	V	TM-9-70	TM-9-23L	K1	TM-9-66	Dl(a)	TM-9-62	D5	TM-9-59	D2	D4
or	18.14	20.27	19.27	20.03	21.45	20.39	19.86	19.15	19.09	19.56	20.45	19.44
ab	13.46	9.42	12.43	11.87	12.95	17.64	13.79	16.21	15.95	15.97	12.41	15.71
an	15.30	11.82	11.78	13.77	11.57	14.87	13.19	16.17	14.60	17.19	12.63	13.44
ne	17.23	22.08	19.81	19.33	20.08	14.92	18.89	16.29	17.81	15.55	20.83	18.67
di	17.63	18.69	18.51	17.48	16.60	14.63	16.64	14.09	16.11	12.51	16.45	15.37
ol	9.46	8.99	8.59	9.13	9.17	9.43	8.61	9.05	8.33	8.98	8.18	8.51
ap	1.37	2.04	1.85	1.87	1.80	1.78	1.92	1.09	1.49	1.92	2.06	1.82
mt	3.13	3.12	3.12	3.16	3.00	2.97	3.09	3.03	3.12	2.89	3.09	3.06
il	3.74	3.59	3.78	3.70	3.36	3.46	3.78	3.65	3.87	3.87	3.67	3.67

| 100 Mg / Mg+.75Fe* | 66 | 66 | 65 | 65 | 66 | 65 | 64 | 64 | 62 | 64 | 62 | 62 |

* = Fe2+ + Fe3+

Table 2. Major element chemistry - nodules

	TM-9-63N	TM-9-64N	TM-9-69CG	TM-9-69FG
SiO_2	42.94	40.61	41.40	38.43
TiO_2	3.81	4.19	2.60	3.58
Al_2O_3	16.33	15.89	12.01	14.55
Cr_2O_3	0.04	0.02	0.06	0.06
$FeO*$	8.54	10.00	8.30	11.09
MnO	0.15	0.15	0.13	0.24
MgO	10.01	10.57	16.52	10.06
CaO	11.94	11.87	13.59	16.75
Na_2O	2.29	2.23	1.41	1.65
K_2O	1.22	1.51	1.42	0.90
P_2O_5	na	na	0.44#	na
total	97.27	97.04	97.44	97.31

C.I.P.W. normative mineralogy (wt.%)

	TM-9-63N	TM-9-64N	TM-9-69CG	TM-9-69FG
or	7.21	5.60	0.00	0.00
ab	6.47	0.00	0.00	0.00
an	30.67	28.89	22.25	29.64
ne	6.99	10.22	6.46	7.56
lc	0.00	2.61	6.58	4.17
cs	0.00	0.00	2.68	9.16
di	22.58	23.78	26.53	19.07
ol	12.97	14.34	24.35	16.83
mt	3.10	3.62	3.00	4.02
il	7.23	7.96	4.94	6.80
ap	na	na	1.02#	na
en	44.5	43.6	45.2	40.6
fs	5.5	6.4	4.8	9.4
wo	50.0	50.0	50.0	50.0
fo	89.1	87.2	90.4	81.3
$\frac{100Mg}{Mg+.75Fe*}$	73	65	78	62

$* = Fe^{2+} + Fe^{3+}$
na = not analyzed or calculated
# = P_2O_5 determined by modal point count (2000 pts.).
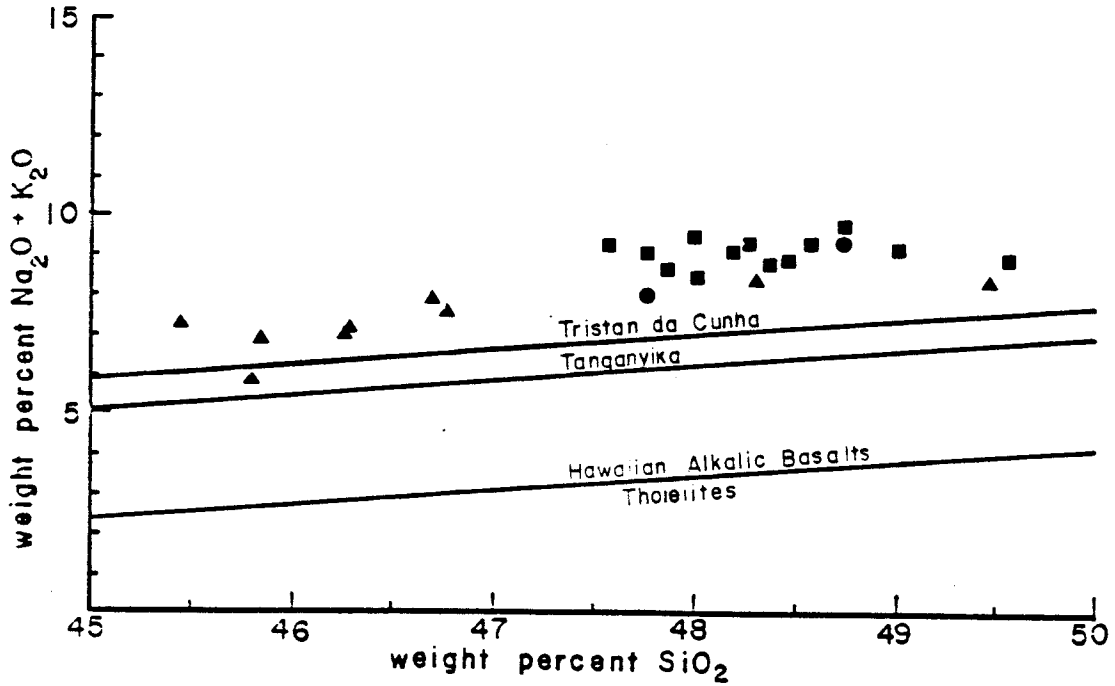
Figure 19. Alkali-silica variation diagram for the
Kula lavas. Alkaline-subalkaline division line
from MacDonald, 1968; alkaline-highly alkaline field
from Saggerson and Williams, 1964. The Tristan trend,
taken for comparison, is from Baker, 1964. Filled
circles = first period lavas, filled triangles =
second period lavas, filled squares = third period
lavas. These symbols will be used throughout the
text with the above connotation unless otherwise noted.
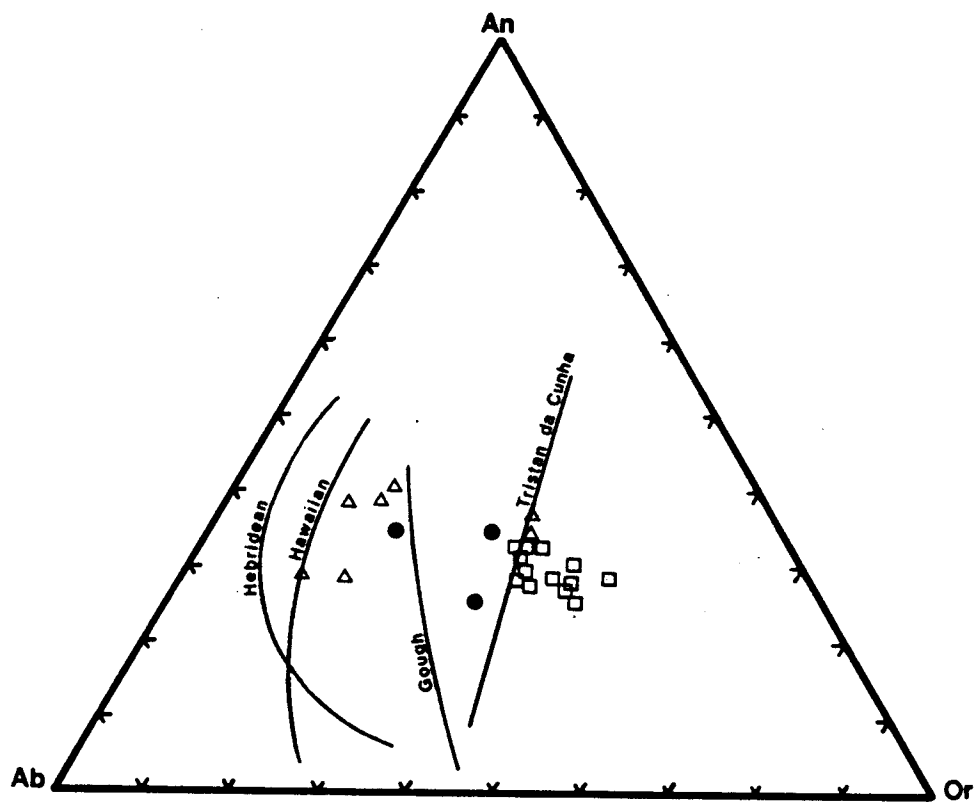
Figure 20. Normative feldspar plot of Kula lavas. Other oceanic island suite trends taken from Coombs and Wilkerson (1969). Solid circles=first period, triangles=second period, squares=third period lavas.

alkalic suites, or that a process other than fractional crystallization is responsible for variations in alkalis and lime.

Figures $\underline{21}$ and $\underline{22}$ show Kula major chemistry data plotted on magnesia variation diagrams. Linear trends are calculated least-square best-fit slopes. As was evident in SiO_2 content, the variation of MgO in the volcanic suite is limited, only 2.3 weight percent. If MgO content of the phenocryst phases is subtracted from the whole rock total, variation is even smaller. Major element variation of first period volcanics will not be discussed because of the lack of samples on which to define a trend; however first period samples generally resemble third period basalts in major element chemistry. Second period rocks show sympathetic increase in CaO and FeO with decreases in SiO_2, Al_2O_3, and Na_2O, at high MgO contents. K_2O is highly variable and seems to form two different trends. None of the observed phenocryst phases can account for this depletion in sodium and aluminum, although anorthoclase, which occurs as a megacryst in some samples could be a possible fractionating phase at high pressure, in conjunction with magnesian olivine. Binns (1970) noted anorthoclase megacrysts from alkaline volcanic rocks of New South Wales, Australia, but to my knowledge no mention of anorthoclase has appeared in high-pressure experimental literature. Plagioclase has been found to become increasingly sodic with increased pressure but rare earth data indicates lack of plagioclase fractionation. At
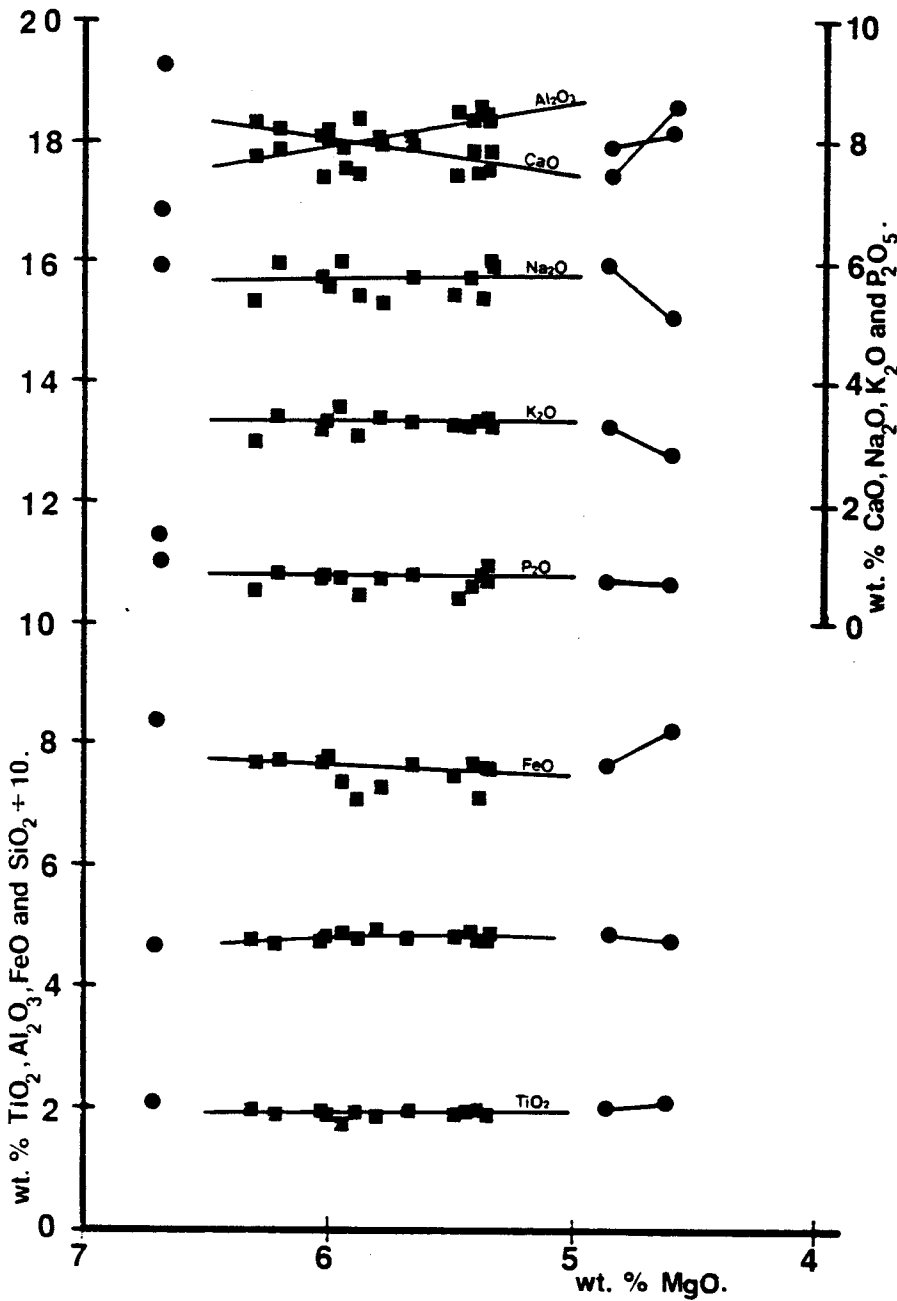
Figure 21. Oxide versus magnesia variation plot for first and third period lavas. Symbols as in Figure 19. Trends are compatible with limited clinopyroxene and amphibole fractionation; however, note the intersection of third period CaO, Na$_2$O, FeO, TiO$_2$ and P$_2$O$_5$ with second period trend (fig. 21) at approximately 5 wt.% MgO and the extrapolated intersection at approximately 7 wt.% MgO. The shape of this plot resembles a mixing line; third period volcanics might be generated by mixing of a liquid parental to the second period lavas with an evolved alkalic melt.

Too few samples of first period basalts were analyzed to note anything other than they span the same ranges of oxide composition as the other period lavas.

Figure 25a-d. Clinopyroxene, amphibole and olivine mineral chemistry plotted in atom weight percent on an Mg-Fe-Ca ternary
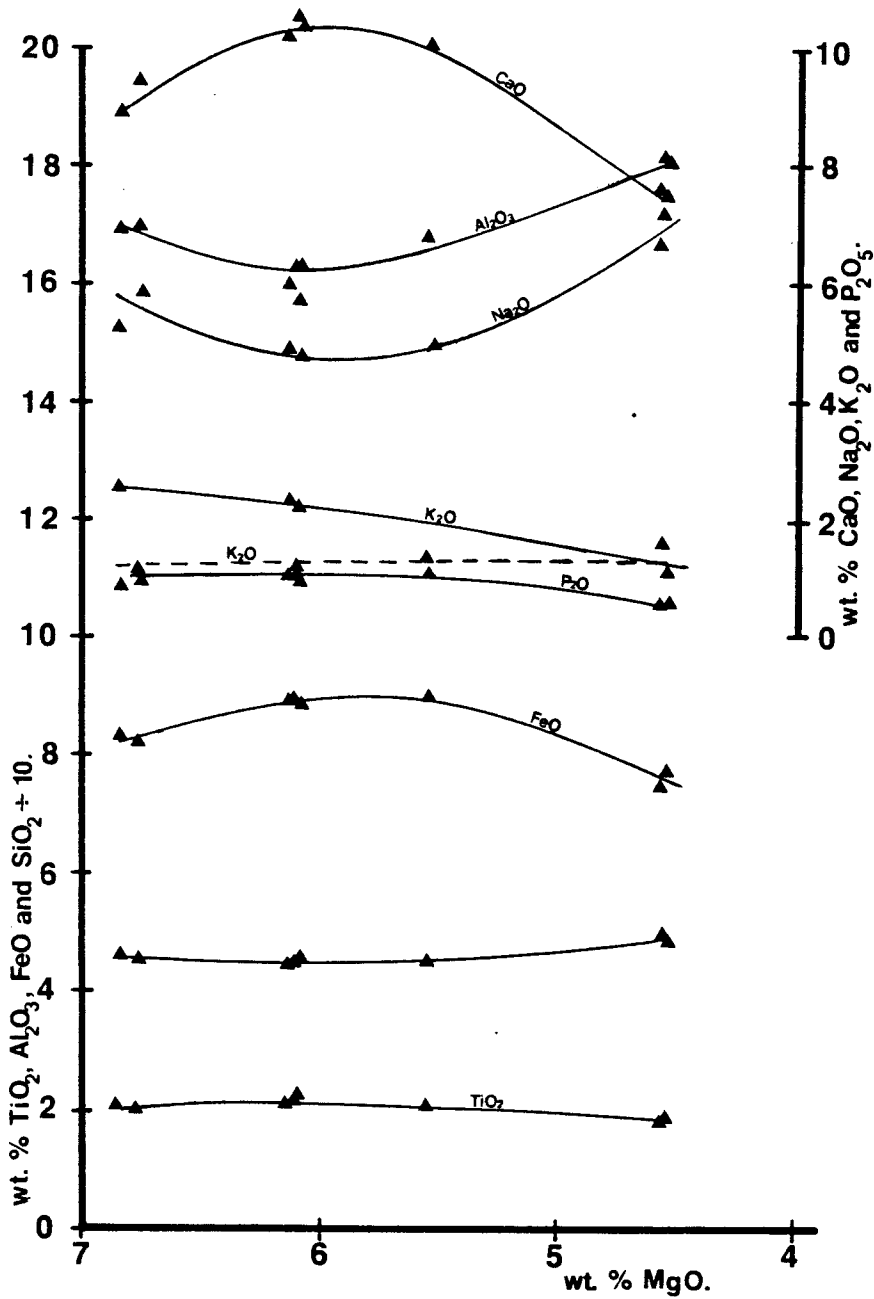
Figure 22. Oxide versus magnesia variation plot for second period lavas Symbols as in Figure 19. Trends from 7-6 wt.% MgO may be recording high pressure fractionation trends. Oxide trendsfor MgO contents of less than 6% seem to suggest amphibole and clinopyroxene control of fractionation, reasonable given the modal phenocryst assemblage.

5.9 - 5.8 weight percent MgO, these trends show a sharp reversal; CaO and FeO decrease sympathetically with SiO_2, Al_2O_3 and Na_2O increase. This may possibly record the effect of clinopyoxene and kaersutite fractionation, which is supported by the appearance of modal hornblende in samples with less than 5.9 weight percent MgO. As previously mentioned, K_2O in the second period volcanics is extremely variable, even in samples from the same cone and for samples with otherwise similar major element chemistry and petrographic characteristics. Fractionation of observed phenocryst phases will result in an increase of K_2O in the residual liquids. If either anorthoclase or biotite megacrysts represent high pressure fractionating phases, there should be indications of this reflected in the barium trace element concentrations, since barium should substitute for potassium in early-formed potassic minerals (Taylor, 1965). No evidence of sympathetic K_2O and Ba fluctuation has been observed. It is possible that potassium fluctuations may be inherited from source heterogeneities, perhaps controlled by differing hornblende:phlogopite ratios in the source rock.

Third period volcanics differ from most second period rocks in that they contain higher total Al_2O_3, SiO_2 and alkalies, lower CaO, FeO, MgO, TiO_2, and P_2O_5. Variation in MgO in the third period samples is 0.97 weight percent; with the exception of Al_2O_3 and CaO, major element oxide concentrations are nearly constant. This pattern is

compatible with limited fractonation of clinopyroxene and hornblende, probably at moderate pressure, since plagioclase is not present as a phenocryst phase.

Qualitatively, from the presence of phenocrysts, coupled with variation diagrams and simple graphical calculations using one sequence of third period flows D_1-D_5 (Fig. 23, after Cox et al., 1979), it can be hypothesized that third period volcanics may be related by removal of titaniferous augite and kaersutite in approximately a 25:75 ratio. Graphical treatment of first and second period samples from different cones, and second period samples from the same cone do not suggest the simple fractionation relations of the D_1-D_5 flows. These graphical results compare favorably with more quantitative methods of fractionation modelling in a later section.

Kula lavas, when plotted on an AFM diagram (Fig. 24), show a cluster of points, with a lack of iron enrichment compared to alkalic lavas of Hawaii and Gough Island (Kuno, 1968). Evidence (see trace elements) does not suggest removal of a significant amount of magnetite. The position of the cluster, compared to the alkalic liquid trends of the oceanic island magmas, looks suspiciously like it may be the result of some sort of mixing process. Note the position of the ultramafic nodules as possible indication of an origin as slightly accumulative primitive Kula magmas.
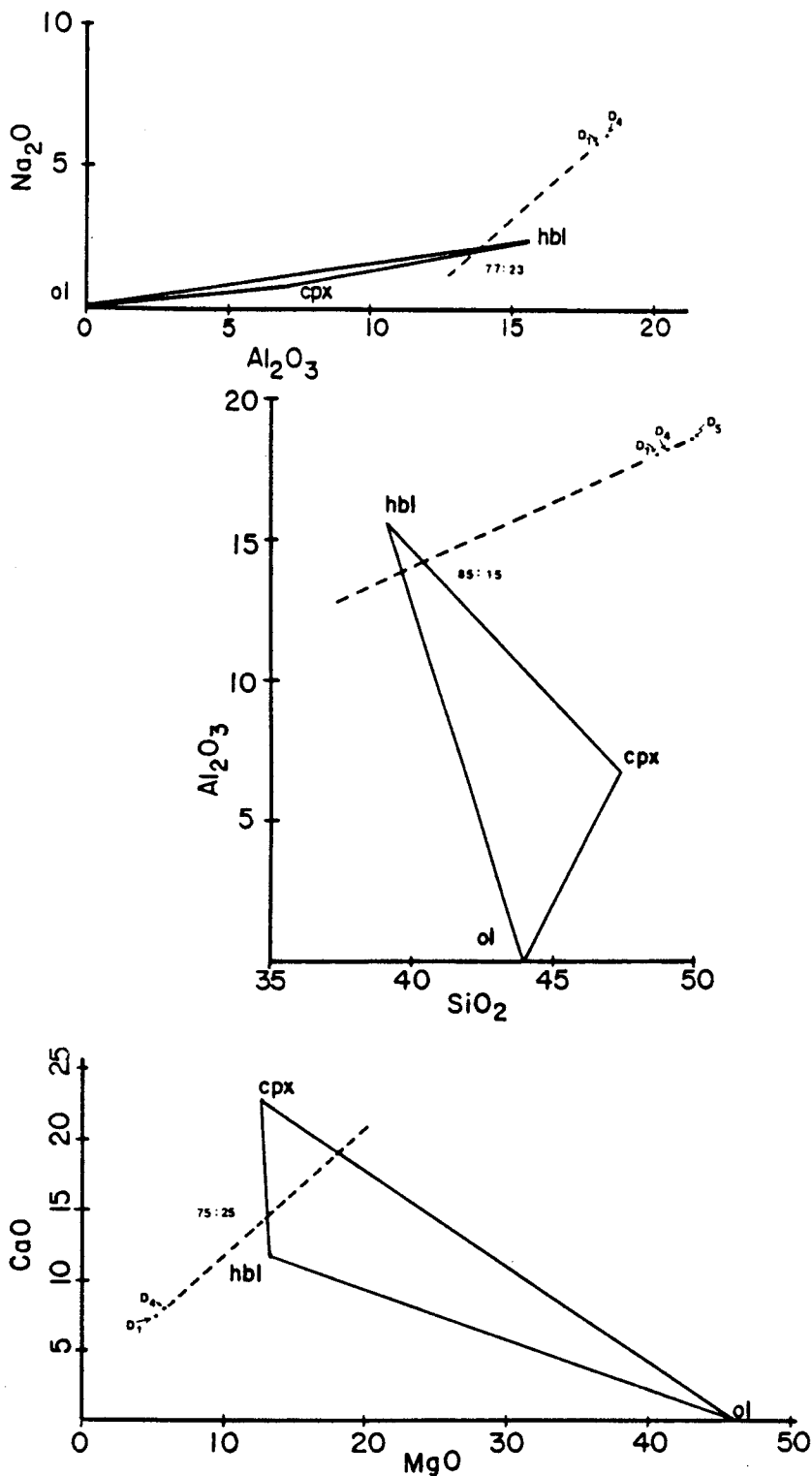
Figure 23. Extraction diagram for lavas D1a-D4, with whole rock compositions normalized to 100%. Olivine and clinopyroxene compositions are mineral analyses from sample D2; hornblende is un unzoned core analysis from third period lava V. Although the very similar oxide concentrations between the samples does not allow very precise determination of the ratio of the extracted phases, it appears that the lavas can be related by the separation of kaersutite and titanaugite from D1a to produce D4.
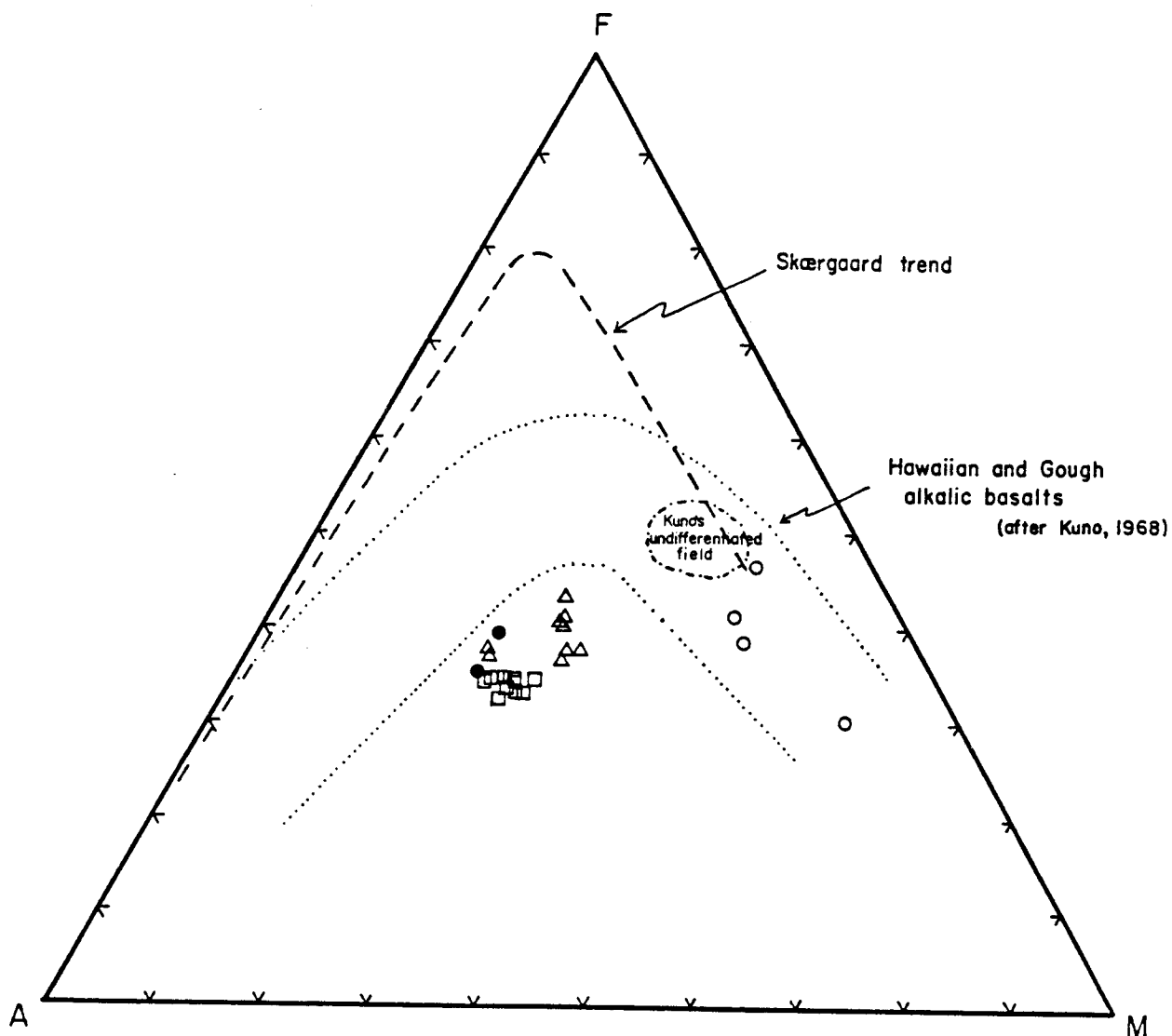
Figure 24.   AFM data for Kula lavas and ultramafic
nodules. Skaergaard tholeiitic and Kuno's (1968)
alkalic trends shown for comparison.   Despite their
alkaline nature, the Kula samples plot in a region
typically occupied by suites of calc-alkaline affinity.
Open circles=nodules, filled circles=first period lavas,
triangles=second period lavas, squares=third period
lavas.

MINERAL CHEMISTRY

Mineral chemistry was obtained by ARL electron microprobe analysis at Harvard University under the same operating conditions described in the section on major element analytical technique. All analysis were performed on polished thin sections of optical thickness (approximately 30). Both cores and rims of phenocryst and megacryst phases were analyzed; if strong zoning was present in a grain, the nature of the zonation was determined. Beam size was broadened for phases with high volatile and/or alkali content. When a large number of analyses exist for a particular phase, selected representative analyses appear in the table. Appendix I contains a complete compilation of mineral chemistry data.

Clinopyroxene

Clinopyroxene is the most abundant ferromagnesian mineral in the Kula volcanics, subordinate to kaersutite only in the more hornblende-rich trachybasalts. Clinopyroxene occurs as phenocrysts, glomerocrysts, megacrysts, xenocrysts, and as a groundmass constituent. Kula pyroxenes characteristically contain large percentages of calcium and aluminum, many contain significant amounts of other components including sodium, titanium, ferric iron and chronium. The high proportion of non-pyroxene quadrilateral components causes most mineral analyses to plot outside the pyroxene quadrilateral (Fig.25), even after correction for the calcium tschermaks molecules (Fig.26 after Kushiro, 1962). Four types of calcic clinopyroxene are found in the Kula lavas and

b. SECOND PERIOD
ol. cpx and hbl atom %

▲ core
△ rim
▲ Fe-rich
⊕ xenocryst

d. NODULES

olivine, clinopyroxene and
hornblende mineral chemistry

atomic %

clinopyroxene

amphibole

olivine

● 69CG
▲ 43N
□ 95FG
○ 54N

a. FIRST PERIOD
ol. cpx and hbl atom %

● core
○ rim
⊕ xenocryst

c. THIRD PERIOD
ol. cpx and hbl atom %

■ core
□ rim
▣ Fe-rich
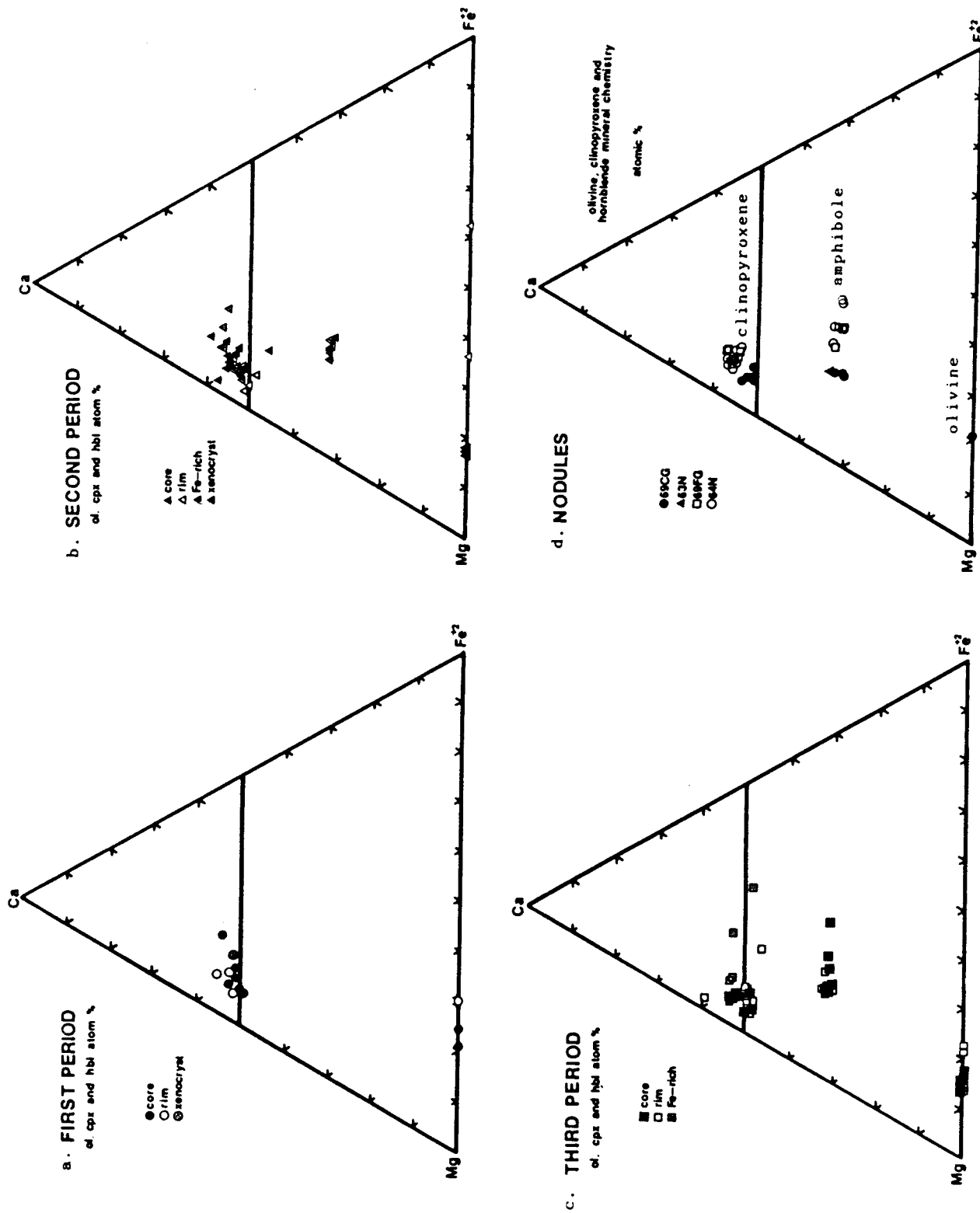
Figure 25a-d. See text on following page.

a.   First period clinopyroxene and olivine analyses (no
unaltered amphibole observed).   The high proportion of non-
quadrilateral clinopyroxene components is evident from the
tendency of points to plot above the 50 atom percent line for Ca.
Although clinopyroxene core analyses seem to delineate a
fractionation trend,   petrographic analysis indicates a more
complex relationship between the core compositions.   This is true
for clinopyroxene cores of the other two periods as well.
    b.   Second period clinopyroxene, amphibole and olivine
mineral chemistry. Note similarities between first and second
period clinopyroxene trends.
    c.   Third period clinopyroxene, amphibole and olivine
chemistry.   The clinopyroxene trend appears to be slightly more
magnesian than in the first two eruptive stages.
    d.   Mineral chemistry of nodule clinopyroxene, amphibole
aned olivine.   Note the compositional overlap between nodule and
lava phases.
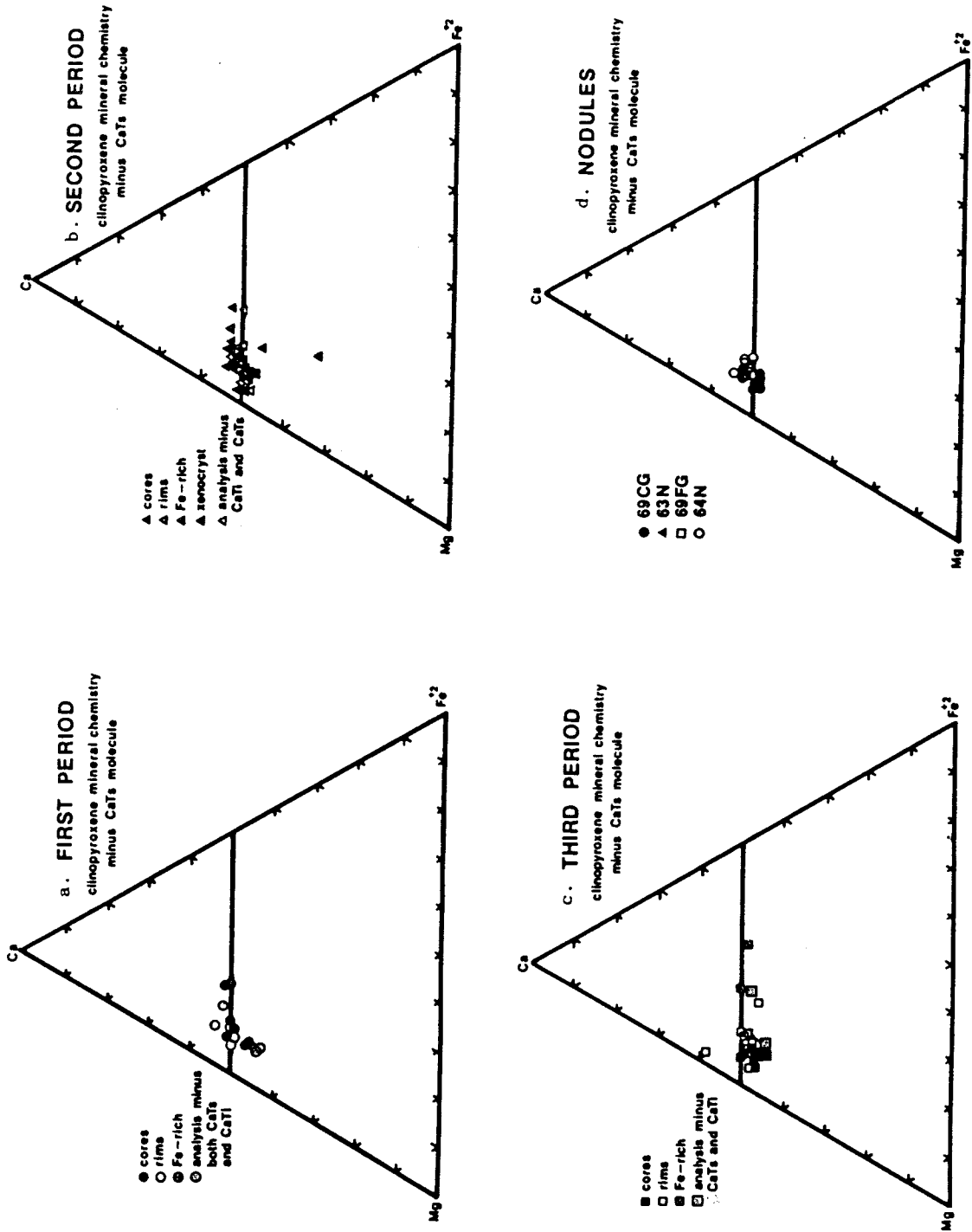
Figure 26. Kula clinopyroxene analyses recalculated (after Kushiro, 1962) to correct for the calcium tschermaks molecule. Many of the analyses still plot outside of the pyroxene quadrilateral, indicating significant amounts of non-quadrilateral components in the pyroxenes.

nodules; non-aluminous salite to ferrosalite, aluminous diopside, aluminous sodian augite and aluminous titanaugite, listed in order of increasing abundance. Characteristics of each type are discussed below.

Non-aluminous Clinopyroxene

Non-aluminous clinopyroxenes are not common and consist of two types: xenocrysts or xenoliths, and microphenocrysts and microlites which form ocellar-like structures around xenocrysts or turbid glass. The xenocrysts and xenoliths occur as colorless to pale green non-pleochroic anhedral grains, some of which have metamorphic texture and are associated with plagioclase, potassium feldspar and/or quartz in crustally-derived xenoliths. These pyroxenes can be classified as salites and ferrosalites, and are characteristically high in SiO_2, 50.0 to 54.5 wt. %; very low TiO_2, 0.04 to 0.31 wt. %; and low Na_2O, 0.16 to 0.47 wt. %.

Microphenocrysts can be classified as salites, have high SiO_2 content, 50-54 wt.%; very low calculated ferric iron, 0.0 to 0.27 wt.%; and TiO_2 less than 1.00 wt.%, which increases away from the contact of xenocryst or glass with the clinopyroxene (see Fig. 13). Al_2O_3, 0.08 to 4.50 wt.%, also increases away from this contact. Analyses of both xenolithic / xenocrystic and microlitic non-aluminous clinopyroxenes are presented in Table 3, analyses 1-3.

Aluminous Diopside

Aluminous diopside is also not common in the Kula volcanics. It occurs as phenocryst cores in second period volcanic rocks, and as the only clinopyroxene of ultramafic

Table 3. Clinopyroxene Mineral Chemistry - Non-aluminous cpx,
Al-diopside and Na- augite

	1	2	3	4	5
SiO2	50.64	51.21	54.41	46.05	43.03
TiO2	0.30	0.31	0.04	1.50	2.07
Al2O3	0.70	1.21	0.85	12.77	13.96
Cr2O3	0.04	0.22	0.12	--	0.03
FeO*	18.37	9.72	3.56	2.87	7.12
MnO	0.90	0.21	0.06	0.07	0.04
MgO	7.04	11.71	16.16	12.43	8.96
CaO	21.95	24.37	25.25	24.68	24.01
Na2O	0.47	0.26	0.16	0.27	0.27
K2O	--	--	--	--	--
P2O5	0.03	0.01	0.03	0.06	--
total	100.43	99.24	100.63	100.70	99.49

Number of ions on the basis of six O

	1	2	3	4	5
Si	1.672	1.971	1.945	1.979	1.614
Al	0.328	0.029	0.054	0.022	0.386
	(2.000)	(2.000)	(2.000)	(1.998)	(2.000)
Al	0.218	0.015	0.003	0.000	0.231
Ti	0.041	0.001	0.009	0.009	0.059
Fe3+	0.048	0.043	0.049	0.013	0.058
Mg	0.673	0.409	0.663	0.876	0.501
Fe2+	0.041	0.556	0.260	0.096	0.116
	(2.021)	(2.049)	(2.000)	(2.000)	(2.005)
Cr	0.000	0.001	0.007	0.004	0.000
Ca	0.961	0.916	0.992	0.984	0.965
Na	0.020	0.036	0.020	0.012	0.020
				(2.000)	(2.016)
Mg	40.2	21.7	34.6	44.8	30.
Fe*	2.4	29.6	13.6	4.9	10.2
Ca	57.4	48.7	51.8	50.3	59.1

Table 3. Clinopyroxene Mineral Chemistry - Non-aluminous cpx, Al-diopside and Na-augite

	6	7	8	9	10
SiO2	51.02	51.08	47.63	47.98	48.20
TiO2	0.86	0.60	1.84	1.48	1.82
Al2O3	4.45	3.39	8.09	5.41	6.46
Cr2O3	0.06	0.07	0.01	0.00	0.00
FeO*	5.13	10.71	9.90	14.06	7.94
MnO	0.12	0.54	0.30	0.64	0.21
MgO	13.95	10.65	9.52	7.84	10.58
CaO	23.25	21.29	21.48	20.18	22.43
Na2O	0.63	1.96	2.00	1.96	1.58
K2O	--	--	--	--	--
P2O5	0.01	0.02	--	--	.07
total	99.48	100.31	100.77	99.55	99.38

Number of ions on the basis of six O

	6	7	8	9	10
Si	1.885	1.901	1.762	1.830	1.805
Al	0.115	0.099	0.239	0.170	0.196
	2.000	2.000	2.000	2.000	2.000
Al	0.079	0.050	0.114	0.073	0.089
Ti	0.024	0.017	0.052	0.043	0.052
Fe3+	0.033	0.156	0.166	0.157	0.119
Mg	0.769	0.591	0.525	0.446	0.591
Fe2+	0.127	0.179	0.141	0.292	0.130
Cr	0.002	0.003	0.000	0.000	0.000
Ca	0.921	0.849	0.852	0.825	0.900
Na	0.046	0.142	0.144	0.145	0.115
	2.035	2.010	2.006	2.006	2.030
Mg	42.3	36.5	34.6	28.5	36.4
Fe*	7.0	11.0	9.3	18.7	8.0
Ca	50.7	52.5	56.1	52.8	55.6

Table 3. Clinopyroxene Mineral Chemistry -- Titanaugite

	11	12	13	14	15
SiO2	47.99	48.01	44.33	45.49	49.49
TiO2	2.02	1.86	3.05	2.94	1.45
Al14545	8.40	6.36	8.68	8.65	6.38
Cr2O3	0.50	0.02	--	0.09	0.45
FeO*	5.24	7.13	8.32	6.54	4.80
MnO	0.10	0.21	0.19	0.15	0.11
MgO	13.36	12.65	10.91	11.84	14.32
CaO	22.02	22.98	22.93	23.59	22.79
Na2O	0.98	0.60	0.57	0.52	0.82
P2O5	0.03	0.04	0.04	0.02	0.01
total	100.66	99.91	99.03	99.84	100.63

Number of ions on the basis of 6 0

	11	12	13	14	15
Si	1.763	1.784	1.675	1.693	1.802
Al	0.238	0.217	0.326	0.307	0.199
(Σ)	2.000	2.000	2.000	2.000	2.000
Al	0.126	0.062	0.061	0.072	0.075
Ti	0.056	0.052	0.087	0.083	0.040
Fe3+	0.029	0.095	0.134	0.106	0.090
Mg	0.732	0.701	0.615	0.657	0.777
Fe2+	0.132	0.128	0.130	0.099	0.057
(Σ)	2.091	2.000	2.042	2.030	2.022
Cr	0.015	0.000	0.000	0.003	0.013
Ca	0.867	0.915	0.928	0.941	0.889
Na	0.043	0.044	0.042	0.038	0.058
(Σ)					2.053
Mg	42.3	40.2	36.7	38.7	45.1
Fe*	7.6	7.3	7.7	5.8	3.3
Ca	50.1	52.5	55.5	55.5	51.6

Table 3. Clinopyroxene Mineral Chemistry - Titanaugite

	16	17	18	19	20
SiO2	46.14	42.93	45.83	47.46	50.17
TiO2	2.00	3.45	2.81	2.30	1.52
Al2O3	8.74	11.78	9.23	8.21	5.00
Cr2O3	--	--	--	0.26	0.10
FeO*	8.08	8.66	6.91	4.91	5.05
MnO	0.11	0.12	0.11	0.12	0.16
MgO	11.08	9.45	12.13	13.07	14.47
CaO	23.17	22.29	22.23	22.21	22.59
Na2O	0.66	0.95	0.73	0.71	0.59
P2O5	0.10	0.11	0.09	0.07	0.07
total	99.99	99.74	100.11	99.32	99.72

Number of ions on the basis of 6 O

	16		17		18		19		20	
Si	1.719		1.612		1.699		1.759		1.849	
Al	0.282	2.000	0.389	2.000	0.302	2.000	0.241	2.000	0.151	2.000
Al	0.102		0.133		0.101		0.118		0.066	
Ti	0.057		0.098		0.079		0.065		0.043	
Fe3+	0.116		0.131		0.097		0.039		0.041	
Mg	0.615		0.529		0.670		0.722		0.795	
Fe2+	0.136	2.028	0.142	2.034	0.118	2.066	0.114	2.066	0.115	2.066
Cr	0.000		0.000		0.000		0.008		0.003	
Ca	0.925		0.897		0.882		0.882		0.892	
Na	0.048		0.070		0.053		0.052		0.043	
Mg	36.7		33.7		40.1		42.0		44.1	
Fe*	8.1		9.0		7.0		6.6		6.4	
Ca	55.2		57.2		52.9		51.4		49.5	

Table 3. Clinopyroxene Mineral Chemistry -- Titanaugite

	21	22	23	24	25
SiO_2	46.24	42.83	45.15	46.14	42.59
TiO_2	2.81	4.41	3.10	2.88	4.89
Al_2O_3	8.93	11.81	10.11	8.78	10.63
Cr_2O_3	0.03	0.02	0.00	0.00	0.02
$FeO*$	6.51	7.05	8.62	6.27	6.14
MnO	0.16	0.12	0.14	0.14	0.14
MgO	12.16	10.70	9.64	11.38	10.86
CaO	21.40	21.45	22.53	22.98	23.15
Na_2O	0.94	0.80	1.19	0.99	0.63
P_2O_5	0.15	0.11	.03	0.16	0.09
total	99.31	99.30	100.51	99.71	99.14

Number of ions on the basis of 6 O

	21	22	23	24	25
Si	1.723	1.608	1.680	1.717	1.603
Al	0.277	0.392	0.321	0.284	0.397
Al	0.115	0.130	0.123	0.102	0.075
Ti	0.079	0.125	0.087	0.081	0.139
Fe^{3+}	0.072	0.071	0.111	0.093	0.092
Mg	0.676	0.599	0.535	0.631	0.610
Fe^{2+}	0.132	0.151	0.158	0.103	0.103
Cr	0.000	0.000	0.000	0.000	0.000
Ca	0.855	0.863	0.898	0.917	0.934
Na	0.068	0.059	0.086	0.072	0.046
Mg	40.7	37.1	33.6	38.2	37.0
Fe*	7.9	9.4	9.9	6.2	6.2
Ca	51.4	53.5	56.5	55.5	56.8

Bracket sums:
- Si + Al (tetrahedral): 21 = 2.000, 22 = 2.000, 23 = 2.000, 24 = 2.000, 25 = 2.000
- octahedral + M2 group: 21 = 2.078, 22 = 2.079, 23 = 2.016, 24 = 2.013, 25 = 2.013 / 1.999

Key to Clinopyroxene Analyses

1. Non-aluminous clinopyroxene core from third period trachybasalt Kl, analysis px-1.

2. Non-aluminous clinopyroxene xenocryst from first period trachybasalt TM-9-67I.

3. Non-aluminous clinopyroxene from second period porphyritic trachybasalt 68C, analysis 68-11.

4. Aluminous diopside from second period basanite 53C1; analysis 53C2-A, core.

5. Aluminous salite from second period basanite 53C1; analysis 53-6.

6. Aluminous salite from nodule 69CG.

7. Sodian augite from first period basanite TM-9-57.

8. Sodian augite from second period basanite 53C1, analysis 53-2 core.

9. Sodian augite from third period trachybasalt D-2, analysis.

10. Sodian augite from nodule TM-9-63N.

11. Titanaugite from first period trachybasalt TM-9-67I, core analysis.

12. Titaniferous augite, same grain as analysis 10, outer core analysis.

13. Titanaugite, same grain as analysis 10, rim analysis.

14. Titanaugite from first period basanite TM-9-57. Recrystallized pyroxene in sieve-textured core.

15. Titaniferous augite, same grain as analysis 13. Unrecrystallized pyroxene immediately adjacent to sieve-textured core.

16. Titanaugite from second period porphyritic trachybasalt 68C, analysis 68-4 core.

17. Titanaugite, same grain as analysis 15, outer core.

18. Titanaugite, same grain as analysis 15, rim.

19. Titanaugite, third period porphyritic trachybasalt V, analysis Vpx core.

20. Titaniferous augite, same grain as analysis 18, Vpx rim.

21. Titanaugite, third period trachybasalt K, analysis Px-3, core.

22. Titanaugite, same grain as analysis 20, px-3, rim.

23. Titanaugite, from TM-9-69FG nodule interior.

24. Titanaugite rimming kaersutite, nodule TM-9-64N. Analysis 1.5 core.

25. Titanaugite rimming kaersutite, nodule TM-9-64N, rim analysis.

nodule TM-9-69CG. Aluminous diopside phenocryst cores are colorless and non-pleochroic. They are neither zoned nor twinned, and characteristically have no chromium, moderate TiO_2, 1.5 to 2.0 wt.%; low Na_2O, 0.3 wt.%; high CaO, 24.0 to 25.0 wt.%; and very high Al_2O_3, 12.0 to 14.0 wt.%. SiO_2 is low and varies from 43 to 46 wt. %. Aluminous diopside from nodule TM-9-69CG contrasts with the phenocrystic diopside, containing high SiO_2, 50.0 to 51.0 wt.%; moderate Al_2O_3, approximately 4.5 wt.%; and low TiO_2, less than 1.0 wt.%. They are pale green and non-pleochroic, subhedral to anhedral in shape, and are enclosed poikilitically by ferroan pargasite and titaniferous phlogopite, which can be seen replacing the clinopyroxene along the margins of the diopside as well as by patchy replacement in the interior of the grains. Fine-grained blocky opaques, probably titanomagnetite, are common inclusions in the diopsides. The grains are unzoned and untwinned. Analyses of aluminous diopside are listed in Table 3, analyses 4-6.

Aluminous Sodian Augite

Sodian augite is common in all periods of Kula volcanism, and typically forms euhedral to anhedral cores in both phenocrysts and grains of hornblende nodule TM-9-64N. Some sodian augite cores are extremely embayed, and all grains have a mantle of titanaugite. Grains may be apple-green in color and non-pleochroic, or pleochroic with γ = olive-green, $\beta = \alpha$ = light olive to gray-green. Pleochroism increases in intensity with increasing iron content. These pyroxenes may contain either no inclusions (Figure 27a & b), or contain
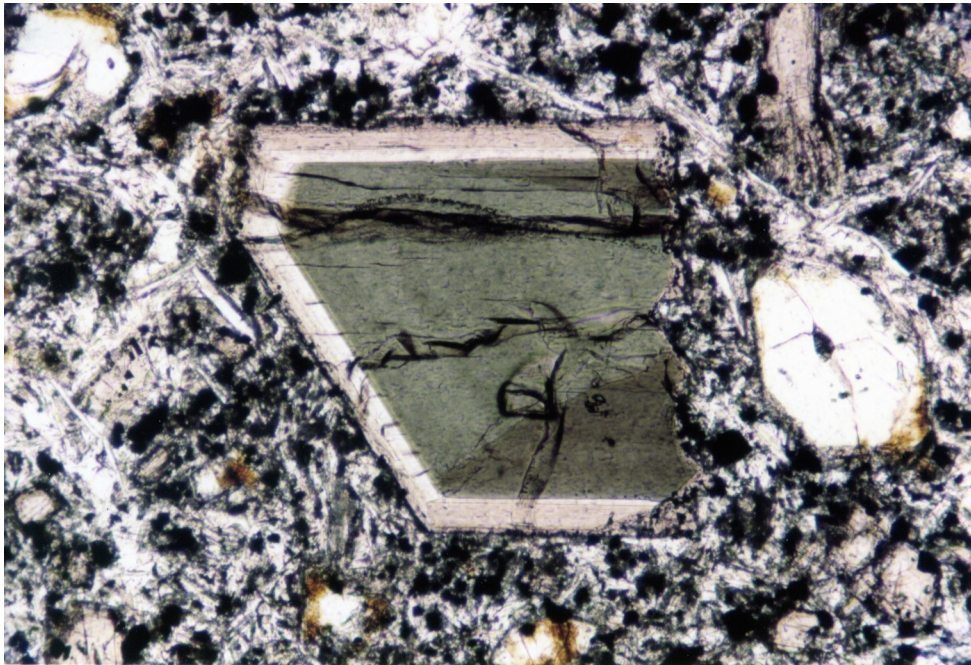
Figure 27a-b. Contrasting sodian augite habits.
Fig. 27a (above): Euhedral sector-zoned sodian core
mantled by titanaugite quench margin, suggesting rapid
disequilibrium crystallization. Because low-pressure
titanaugite quench margin is absent along broken grain
margins, the breakage must have occurred during an
explosive eruption. From TM-9-57. Field of view: 1.38
mm.
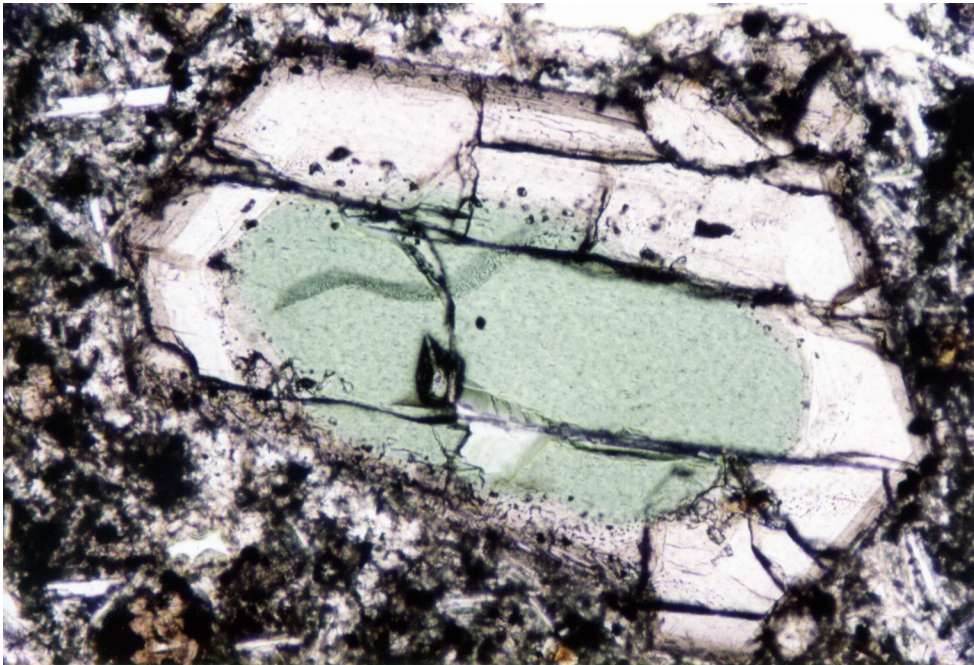
Figure 27b. Unzoned sodian augite core, rounded and
mantled with titaniferous augite and titanaugite
quench margin. Rounded nature of the sodian core as
well as the composition of the mantling titaniferous
augite suggests that the sodian augite may have been
entrained into the host basanite at moderate depth,
perhaps indicative of contamination of the Kula melts
by more evolved melts(?) during ascent. From TM-9-57.
Field of view: 1.38 mm.

inclusions of spinel minerals such as those observed in basanite TM-9-57; some cores are characterized by an unusual sieve texture. The grains are untwinned and very rarely show concentric zoning (Figure 28). Boundaries with mantling titanaugite are always sharp. As well as being rich in Na_2O, to 2.00 wt. %, these pyroxenes contain substantial amounts of FeO (total), 9.90 to 14.06 wt.%; Al_2O_3, 3.39 to 9.69 wt.%; and low Cr_2O_3, from 0.00 to 0.07 wt.%. Analyses of sodian augite are given in Table 3, analyses 7-10.

Titanaugite

Titanium-rich augite is the dominant clinopyroxene of all three periods of volcanism, and occurs abundantly in all volcanic samples, as well as in all ultramafic nodules except TM-9-69CG. Both titaniferous augite (1.0 to 2.0 wt.% TiO_2, Deer et al., 1978) and titanaugite (greater than 2.0 wt.%, Deer et al., 1978) occur; the more titanium-rich compositions typically form quench margins on phenocrysts and groundmass grains. They will both be referred to as titanaugite in the remainder of the text. The highest observed TiO_2 content occurs in hornblende TM-9-64N, where a quench pyroxene has a TiO_2 content of 5.5 wt.%. Titanaugite varies in color from pale brown and non-pleochroic, through pleochroic mauve to pale brownish-yellow, to a spectacular γ = deep purplish-pink, β = pink, α = yellowish pink, $\gamma > \beta > \alpha$. Often there is a sharp color change at the core-quench rim boundary, the rim typically a deeper color. Titanaugite always mantles cores of sodian augite and aluminous diopside, with a sharp boundary between different compositions. The majority of
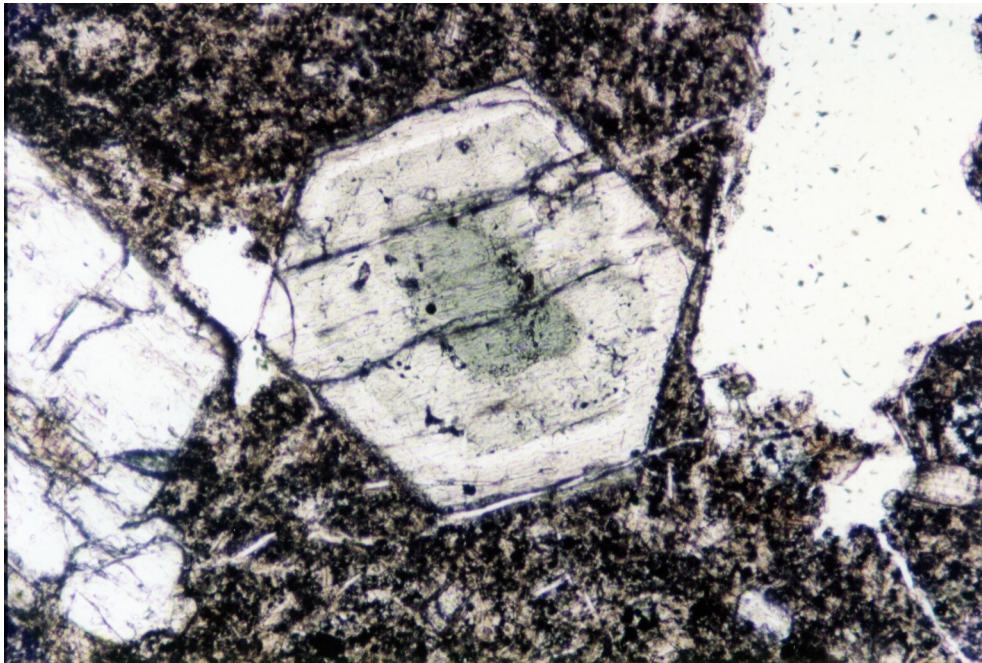
Figure 28. Concentric-zoned clinopyroxene with rounded sodian augite core similar to Fig. 27b and a euhedral sodian mantle. This also appears to suggest some sort of contamination of the Kula magmas with a more evolved composition. From $53C_2$. Field of view: 1.38 mm.

titanaugites are zoned; both oscillatory and sector zoning is common, often in the same grain. Study of compositional variation between zones was not systematically undertaken. Large phenocrysts (rarely small phenocrysts) commonly show sieve texture in the core, characterized by gas bubbles, plum-colored glass with microlites of quench clinopyroxene, opaque inclusions and recrystallized titanaugite (Fig. 29). The sieving is interpreted as a partial melting texture due to decompression, and similar textures in titanaugites have been observed by Wass (1979) and others, with the same interpretation. Less commonly, clusters of opaque blocky grains are clustered in the core with no accompanying sieving. Titanaugites commonly are twinned on (100), in some grains, mantles of multiple-twinned pyroxene occurs on unzoned cores. In rocks that have a glassy groundmass, titanaugites with a hollow "swallow-tail" form of hourglass zoning are common in the groundmass. Both this type of hourglass zoning and multiple twinning have been cited by authors as evidence of extremely fast growth (e.g., Buerger, 1945; Wass, 1973) but relations may be more complex (see for example, Walker et al., 1976). Most of the phenocrysts are euhedral with grain size up to 0.5cm, although certain of the largest grains have partially resorbed borders. Many grains have been mechanically broken, but show no evidence of resorption. In the mesostasis, euhedral microphenocrysts are common, as well as round blobs and microliths. Analyses of titanaugites are listed in Table 3, analyses 11-25. Aluminous pyroxenes have been inferred by many authors (Kuno,
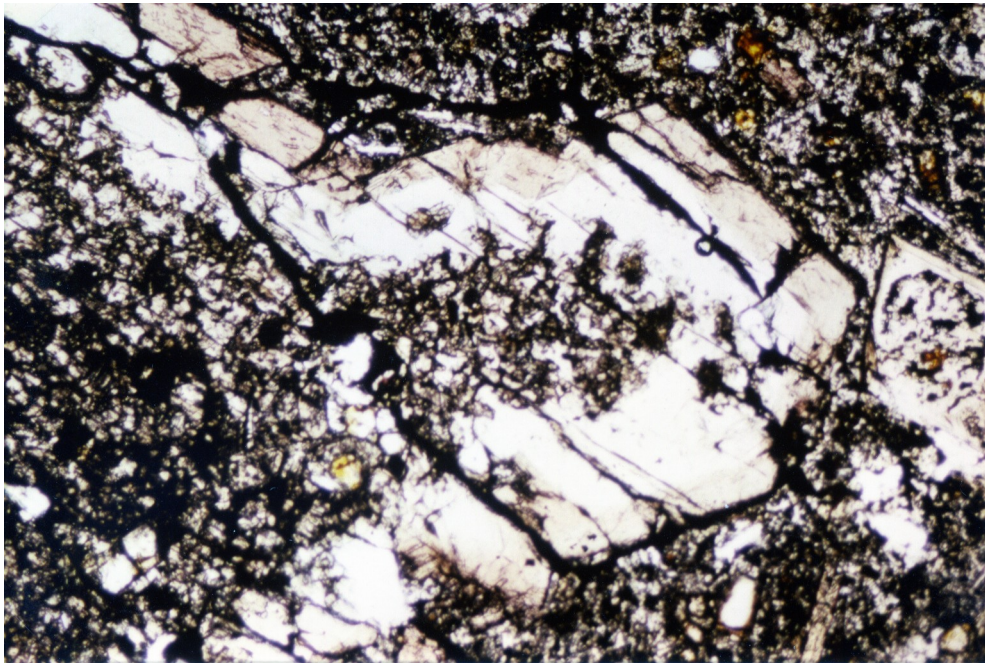
Figure 29. Sieve texture in clinopyroxene core, first period basanite TM-9-57. Recrystallized pyroxene in the core has the same composition as the quench rim. The texture is interpreted to be a result of partial melting due to decompression.

1964; Thompson, 1974; Green and Hibberson, 1970; Ringwood, 1976) to be derived from moderate to high pressure because of the reaction, plagioclase + olivine = spinel + pyroxene with increased pressure. In the Kula clinopyroxenes, the Al_2O_3 content of the titanaugite quench margins is typically higher than that of the core clinopyroxene. This relationship has also been reported by Wass (1979), and is coupled with a sympathetic increase in TiO_2. Although the total content of Al_2O_3 does not seem to be indicative of a high pressure origin in itself, the comparison of Al^{IV} to Al^{VI} coordination (Aoki and Kushiro, 1968) does seem to depend on pressure (Fig. 30). This ratio is calculated by assuming perfect stoichiometry and assigning tetrahedrally coordinated aluminum to correct any silica deficiency in the z site. Excess aluminum is assumed to be octahedrally coordinated in the M2 site. Figure 30 shows that the quench titanaugites and non-aluminous salites fall in the field of low pressure igneous rocks, while the nodule clinopyroxenes as well as many of the phenocryst and megacryst cores fall in the field of granulites and inclusions in basaltic rocks. Wass (1979) suggests that this ratio, if quantified, could be a useful geobarometer; however this is unlikely because of secondary controls on pyroxene alumina content, which include bulk composition of the melt, activity of SiO_2, and oxygen fugacity, although, as Wass points out, in a given basaltic host aluminum coordination seems to be a good relative indcator of pressure. Aside from crustal-derived inclusions, there are no obvious xenocrystic clinopyroxenes

eclogites

granulites and inclusions in basaltic rocks

Al^{VI}(atomic proportion)

.30

.20

.10

igneous rocks

0   .10   .20   .30   .40   .5 0

Al^{IV} (atomic proportion)
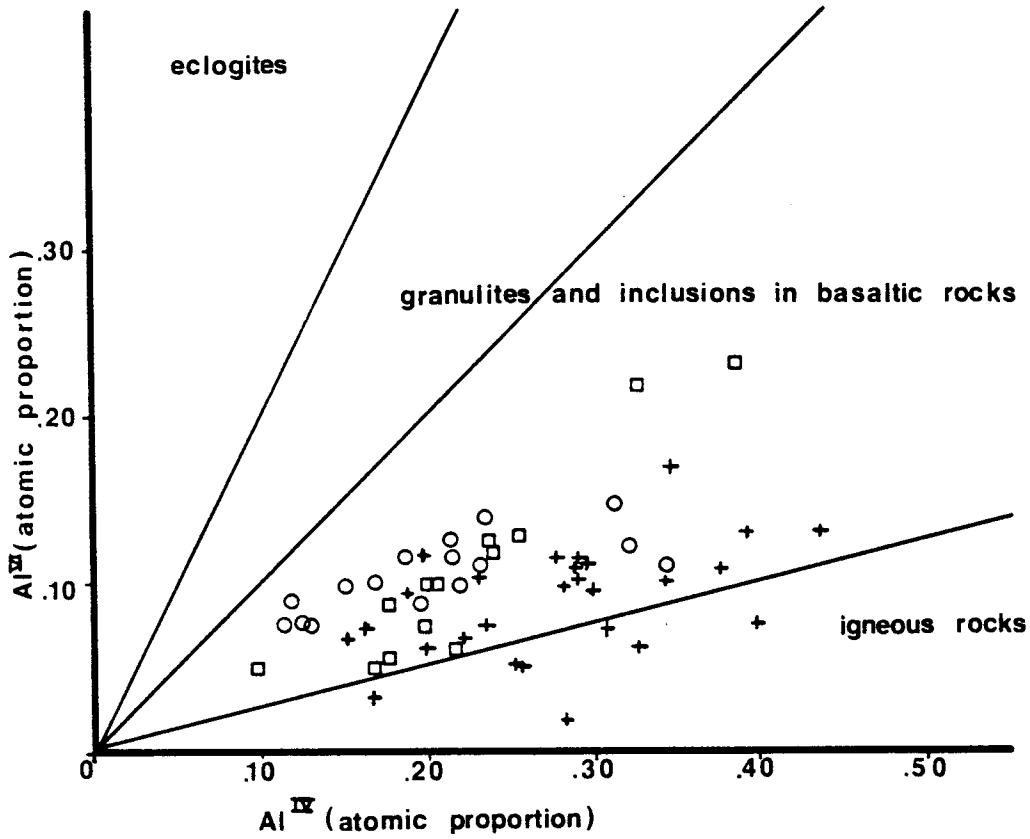
Figure 30. Relative proportion of Al in the tetrahedral site (Al^{IV}) and Al in the octahedral site (Al^{VI}) in Kula clinopyroxenes, after Aoki and Kushiro, 1968. Crosses = quench clinopyroxene, squares = phenocryst and megacryst cores, circles = nodule cores.

in the Kula rocks. Except for large titanaugite cores, the pyroxenes are characteristically low in chromium. Calculated stoichiometry of sodian aluminous clinopyroxenes indicates that these pyroxenes contain a substantial amount of ferric iron, which suggests that sodium is largely present in the acmite rather than jadeite pyroxene molecule. If the calculated amount of ferric iron is correct, then these Fe^{+3}-rich augites may represent crystallates from an evolved liquid at considerable depth. Common rimming of embayed sodian pyroxene by chromian Mg-rich titaniferous augite suggests that the titanaugite crystallized from a more primitive liquid which thermally resorbed sodian augite prior to nucleation of titanaugite.

Olivine

Olivine is generally not a prominent phenocryst phase, particularly in the hornblende-rich trachybasalts. Olivine is confined to the phenocryst generation when hornblende is abundant, otherwise it occurrs as both phenocrysts and sparse round grains in the groundmass. In the nodules, olivine occurs only in nodule TM-9-69CG, poikilitically enclosed by ferroan pargasite and phlogopite. Euhedral olivine is rare in any Kula volcanic rock. Grains are commonly rounded and embayed by the melt, armored by titanaugite and/or kaersutite, mechanically broken and/or show euhedral terminations in conjunction with deep embayment in the same grain. Rarely, olivine shows sign of strain, such as undulatory extinction or subgrain formation. Figure 12 shows olivine (Fo^{86}) from third period sample V, with undulose extinction, armored by kaersutite. The paragenesis of these olivines is unclear, but some of the grains are probably xenocrystic.

In hand specimen, olivine occurs as large, anhedral, dull yellow-green grains often with granular texture. In thin section olivine is colorless, has poor cleavage and is usually inclusion-free. Pale brown, microlite-filled glass commonly forms rounded blobs in grains or occurs as elongate rods in the core of the grains. Composition of the glass is the same as that in the groundmass, and the glass is probably a result of corrosion of olivine by the melt. Olivine is typically fresh, with no secondary alteration, and commonly

has a thin, pale orange iddingsite rim in unoxidized lava samples. Heavily oxidized lavas contain olivine with both heavy iddingsite rims and development of hematite(?) overgrowths. Nodule TM-9-69CG contains olivine that has a green alteration as well as iddingsite rims, although these features in no way obscure the nature of the primary olivine.

Unlike clinopyroxene, olivine shows slight difference in composition between the three eruptive periods. Those from first period flood basalts have a range of composition from Fo_{84} to Fo_{78} cores to Fo_{75} to Fo_{69} rims. One groundmass grain has a composition of Fo_{63}. Second period flows contain olivines with Fo_{83} to Fo_{81} core compositions with little or no zoning (less than 1% Fo zoning). Third period rocks have Fo_{86} to Fo_{82} core compositions, with little or no zoning in samples which contain unaltered kaersutite. Samples such as D-2, in which only anhydrous hornblende pseudomorphs remain, are more strongly zoned from a Fo_{85} core to a Fo_{77} rim. From these analyses it appears that a slight increase in Mg content of olivine is correlative with decreasing age of eruption, and that the presence of kaersutite controls olivine stability. Nodule TM-9-69CG contains unzoned olivine of uniform Fo_{79} composition, more iron-rich than olivine core compositions in the lavas, with the exception of the first period basalts. If it is assumed that most of the olivine in the Kula basalts crystallized from the Kula magmas, it becomes difficult to relate nodule TM-9-69CG by cumulate processes to second or third period volcanism. Nodule TM-9-

69CG was found among third period float, probably erupted from the nearby Kara Devit cone. Major element chemistry of both olivines from the volcanics and the ultramafic nodule are listed in Table 4.

Although olivine invariably shows some degree of resorption by, or reaction with the melt, they are not believed to be xenocrystic inclusions. Experiments by Watson (1979) on forsterite olivine in equilibrium with a synthetic (Fe-free) basalt melt, indicate that the CaO content of olivine is linearly dependent on the CaO content of the melt from which it crystallized. Watson indicates that one use of this relationship might be the ability to discriminate between xenolithic and cognate olivine. Figure 31 shows Ca content of Kula olivine cores and rims plotted against Ca content of the whole rock, together with Watson's experimentally determined values for olivine in equilibrium with melt. The magnesium-rich olivine cores plot fairly close to the experimentally determined values, while rims and small groundmass grains fall substantially off the line. The wide scatter of the rims and groundmass grains might be attributable both to higher FeO content in these grains and to secondary fluorescence of calcium in the groundmass phases, factors which Watson notes as affecting the data. The correlation of the olivine compositions with the experimentally determined points is evidence that these cores crystallized either from the enclosing magma, or from a magma of similar Ca content. However, the increase of Ca in

Table 4. Olivine Mineral Chemistry

	1	2	3	4	5	6	7	8	9	10
SiO2	39.87	36.75	39.55	39.57	40.35	40.03	39.81	38.84	39.24	39.07
TiO2	.03	.07	.03	.04	.04	.05	.05	.04	.04	.10
Cr2O3	--	.02	--	--	.04	.05	.01	.04	.01	--
FeO*	14.11	30.86	17.57	17.58	13.23	14.05	14.50	21.29	19.11	18.88
MnO	.22	.89	.35	.33	.23	.27	.25	.56	.36	.42
MgO	43.84	30.52	42.55	42.46	46.72	45.79	45.61	39.31	40.46	40.95
CaO	.27	.47	.21	.21	.20	.27	.23	.30	.07	.08
Na2O	.04	.05	.02	.05	--	.01	--	--	--	.04
total	98.38	99.63	100.28	100.24	100.81	100.52	100.46	100.38	99.29	99.54

Number of ions on the basis of 4 oxygens

	1	2	3	4	5	6	7	8	9	10
Si	1.013	1.005	1.003	1.003	0.997	0.997	0.994	1.002	1.011	1.004
Al	0.000	0.000	0.000	0.000	0.000	0.000	0.000	0.000	0.000	0.000
Ti	0.001	0.001	0.001	0.001	0.001	0.001	0.001	0.001	0.001	0.002
Fe*	0.300	0.706	0.373	0.375	0.273	0.293	0.303	0.460	0.412	0.406
Mg	1.660	1.244	1.608	1.604	1.721	1.699	1.697	1.512	1.554	1.569
Mn	0.005	0.021	0.008	0.007	0.005	0.006	0.005	0.012	0.008	0.009
Ca	0.007	0.014	0.006	0.006	0.005	0.007	0.006	0.008	0.002	0.002
Na	0.002	0.003	0.001	0.002	0.000	0.000	0.000	0.000	0.000	0.002
total	2.987	2.995	3.000	2.998	3.002	3.003	3.005	2.996	2.988	2.995
	Fo84	Fo63	Fo81	Fo81	Fo86	Fo85	Fo85	Fo77	Fo79	Fo79

* total iron
1 includes 0.04 wt% Al2O3

Key to Olivine Analyses

1. Chrysolite from first period trachybasalt TM-9-68, core of phenocryst.

2. Hyalosiderite, groundmass grain from first period trachybasalt TM-9-68.

3. Chrysolite from second period basanite 53Cl, core analysis of phenocryst.

4. Crysolite, rim of grain in analysis 3.

5. Chrysolite outer core from third period porphyritic trachybasalt V, (grain V-7).

6. Chrysolite rim of grain in analysis 5.

7. Chrysolite core from third period trachybasalt D2, analysis D2-4.

8. Chrysolite rim from grain in analysis 7.

9. Chrysolite core from nodule 69CG.

10. Chrysolite rim from grain in analysis 9.
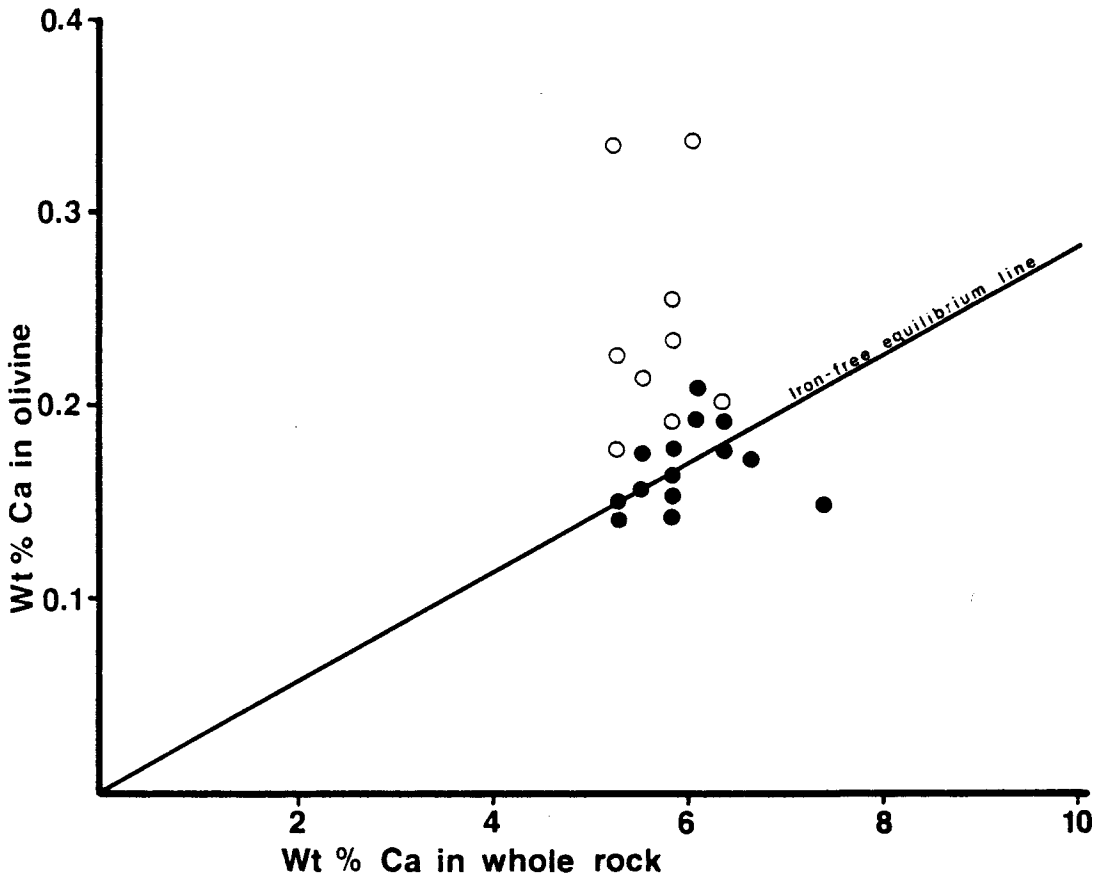
Figure 31. Calcium content of olivine as a function of Ca concentration in coexisting liquid, after Watson, 1979. Filled circles = core analyses, open circles = rim analyses.

groundmass olivine might be a function of increasing calcium K_D with decreasing pressure of crystallization. Although Watson notes that there seems to be a positive correlation between iron content and CaO content in olivines, olivine from nodule TM-9-69CG combines relatively high iron content (Fo_{79}) with low CaO content. This may indicate either that the olivine is a cumulate phase from a CaO-poor, Fe-rich melt, or that these olivines crystallized at higher pressure than the olivines from the basalts. Stormer (1973) has proposed, from consideration of molar volume data, that CaO content of olivine may have a pressure dependence.

Kaersutite and Ferroan Pargasite

Amphibole is a predominant phase in the trachybasalts, commonly the most abundant phenocryst phase. It is generally confined to the phenocryst generation, although in porphyritic trachybasalts hornblende may occur as microphenocrysts.

Hornblende is not always obvious in hand specimen because of breakdown to anhydrous phases. However, where unaltered, hornblende occurs as elongate black prismatic crystals, in contrast to the stumpy black titanian clinopyroxenes. Small hornblende-rich clots are common inclusions in second and third period basalts.

The ultramafic nodules are extremely rich in hornblende (Fig. 32), which occurs in a variety of textures. In TM-9-69CG, hornblende occurs as large (to 2 cm) cinnamon-brown oikocrysts of ferroan pargasite which enclose olivine and
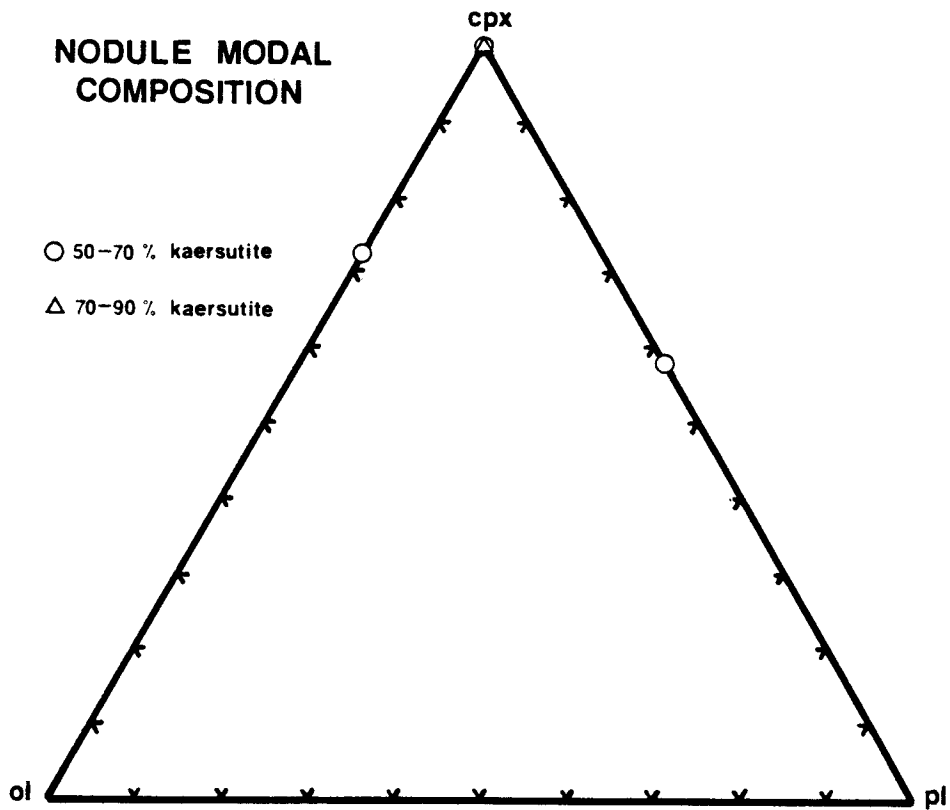
Figure 32. Modal composition of Kula ultramafic nodule. Note the preponderance of hydrous phases in the mode.

clinopyroxene. In TM-9-64N, large (to 1.5 cm) black prismatic kaersutite crystals interlock to form a massive hornblendite nodule. Both TM-9-69FG and TM-9-63N consist of fine-grained granular cinnamon-brown grains, which analyze as kaersutite. In addition, TM-9-69FG is partially coated with what Wilshire and Trask (1971) and other authors have referred to as kaersutite selvages, which consist of a thin veneer of usually preferentially oriented kaersutite which forms a coating on the nodule surface. These selvages have been hypothesized by Wilshire and Trask (1971), Lloyd and Bailey (1976), Wilshire et al. (1980), Boettcher and O'Neil (1980) and others to be evidence of metasomatic veining of the upper mantle. Their descriptions involve kaersutite selvages on anhydrous blocks (e.g., spinel lherzolite). At Kula the selvages surround amphibole bearing nodules.

In the lavas, hornblende occurs as euhedral zoned or unzoned phenocrysts, unzoned megacrysts, and partially to completed altered aggregates of anhydrous phases. Hornblende can appear mechanically broken, but not to the extent of clinopyroxenes and olivine. The anhydrous aggregates can be easily identified as relict hornblende due to the preservation in thin section of the complete breakdown process, as well as the characteristic euhedral outline which is usually perfectly preserved.

Unaltered hornblendes are typically strongly pleochroic, with γ = varying deep red to orange or yellow brown, β = slightly paler color similar to , and α = pale yellow or

orange brown; $\gamma > \beta >> \alpha$. 2V is 70°(-), and (z∧C) extinction angles are small, generally less than 10°. Unaltered hornblende generally has sharp euhedral crystal outlines, although severely rounded but otherwise unaltered grains can be observed in some samples. Zoning (concentric) is common in euhedral hornblende, and is distinguished by color oscillations from light to darker brown colors that correspond to changes in iron content. Simple twinning on (010) is common.

Hornblende in both lavas and ultramafic nodules can be classified according to Leake (1978) as either kaersutite or ferroan pargasite. Compositions are plotted on a Ca-Mg-Fe ternary diagram in Figure 33. Kaersutite is the dominant phase, ferroan pargasite is found only in nodule TM-9-69CG and as rare grains in the second period flows. Ferroan pargasite is similar in optical and chemical properties to the kaersutite, but does not contain sufficient titanium (0.5 atoms per formula) to be classified as kaersutite, although it is titaniferous. Analyses of Kula kaersutites and ferroan pargasites are listed in Table 5.

Hornblende Alteration

As previously mentioned, the hornblendes show a breakdown process to anhydrous phases that can be observed in thin section. There are three main types of alterations: rounding and/or embayment of hornblende by the melt, opacitite rims, and a gradual breakdown of hornblende to two types of anhydrous assemblages.
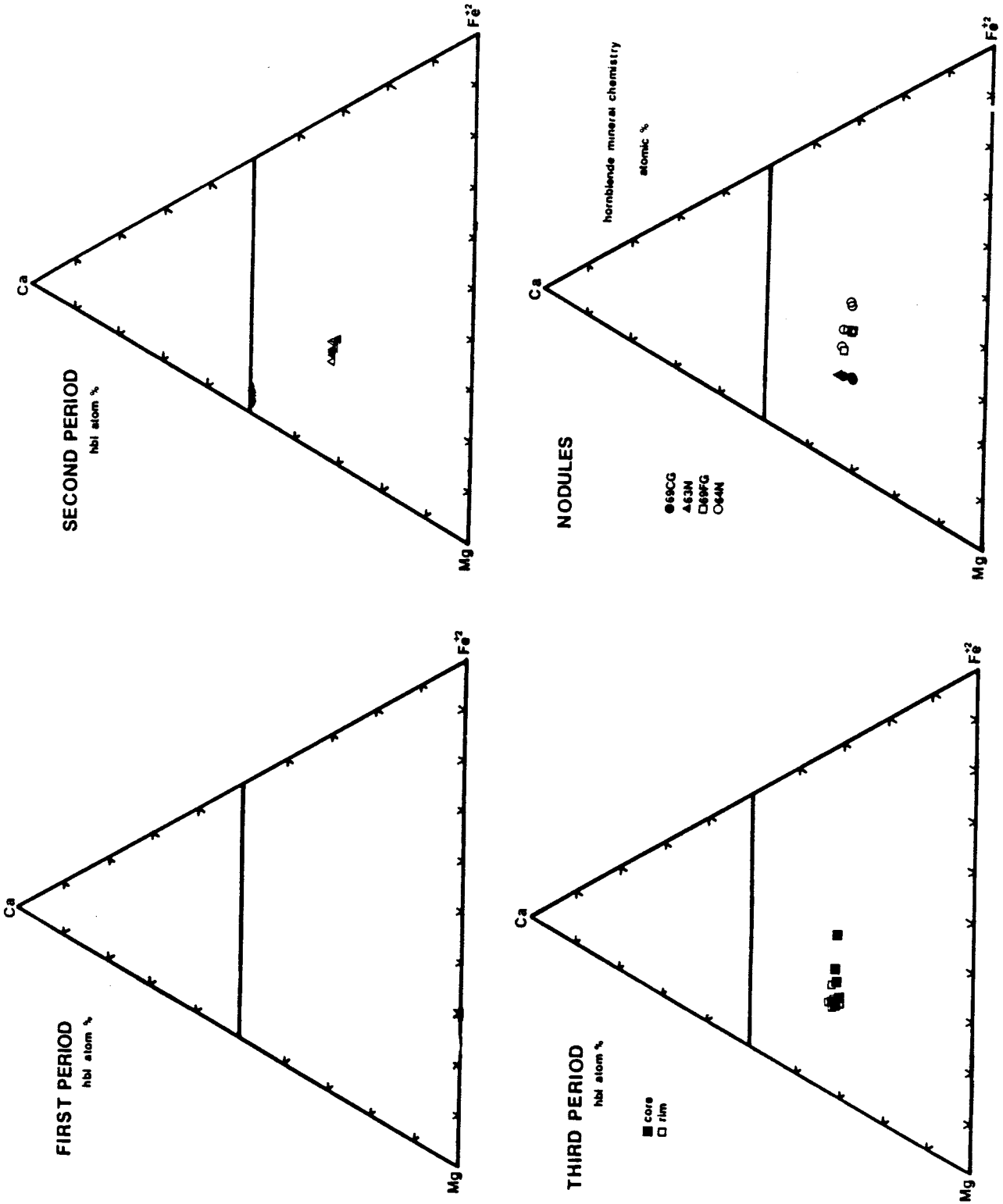
Figure 33. Amphibole compositions plotted in the Ca-Mg-Fe ternary system (taken from the general diagram in figure 25).

Table 5 — Amphibole Mineral Chemistry

	1	2	3	4	5
SiO2	39.34	39.34	39.53	40.16	39.30
TiO2	5.31	4.32	4.92	5.00	5.05
Al2O3	15.54	15.22	14.93	14.94	15.04
Cr2O3	0.01	0.02	0.03	0.04	0.02
FeO*	10.14	11.68	11.55	10.50	11.01
MnO	0.12	0.12	0.12	0.07	0.12
MgO	12.42	11.89	12.06	12.30	11.93
CaO	11.66	11.23	11.89	11.84	11.84
Na2O	2.81	2.72	2.78	2.61	2.59
K2O	1.39	1.45	1.41	1.45	1.45
P2O5	0.07	0.13	0.05	0.07	0.04
Cl-	0.03	0.02	0.03	0.02	0.02
F-	0.29	0.38	0.16	--	0.22
total	99.14	98.52	99.46	99.00	98.64

Number of ions on the basis of twenty-four (O, OH, F, Cl)

	1		2		3		4		5	
Si	5.750	8.000	5.826	8.000	5.793	8.000	5.861	8.000	5.793	7.999
Al	2.249		2.173		2.206		2.138		2.206	
Al	0.428		0.484		0.372		0.432		0.407	
Ti	0.583		0.481		0.542		0.548		0.559	
Mg	2.705		2.624		2.634		2.675		2.621	
Fe*	1.239	7.852	1.447	7.942	1.415	7.9000	1.281	7.807	1.357	7.842
Mn	0.014		0.015		0.014		0.008		0.014	
Na	0.173		0.164		0.132		0.148		0.129	
Ca	1.826		1.782		1.867		1.851		1.870	
K	0.259		0.273		0.263		0.269		0.272	

na = not analyzed
* = total iron

Table 5 - Amphibole Mineral Chemistry

	6	7	8	9	10
SiO2	39.54	38.35	39.75	39.98	38.58
TiO2	5.36	4.57	5.05	5.01	4.58
Al2O3	14.50	14.84	13.87	14.73	14.42
Cr2O3	0.02	0.03	0.04	0.00	0.02
FeO*	9.24	15.04	9.14	10.66	12.73
MnO	0.08	0.23	0.11	0.11	0.16
MgO	13.33	9.84	13.82	12.69	11.09
CaO	11.75	11.41	11.69	11.77	12.02
Na2O	2.45	2.53	2.62	2.65	2.50
K2O	1.61	1.56	1.54	1.64	1.66
P2O5	0.09	0.10	0.12	0.10	0.05
Cl-	0.02	0.05	0.02	0.03	na
F-	0.45	0.25	1.27	0.16	na
total	99.13	98.79	99.03	99.54	97.83

Number of ions on the basis of twenty-four (O, OH, F, Cl)

	6	7	8	9	10
Si	5.812 (8.000)	5.767 (7.999)	5.859 (8.000)	5.830 (8.000)	5.792 (7.999)
Al	2.187	2.232	2.140	2.169	2.207
Al	0.326	0.398	0.270	0.363	0.345
Ti	0.592	0.516	0.559	0.549	0.517
Mg	2.921	2.205	3.036	2.758	2.481
Fe*	1.136 (7.836)	1.891 (7.952)	1.127 (7.898)	1.3000 (7.876)	1.598 (7.923)
Mn	0.009	0.029	0.013	0.013	0.020
Na	0.148	0.118	0.144	0.160	0.065
Ca	1.851	1.838	1.846	1.839	1.934
K	0.301	0.299	0.289	0.305	0.304

na = not analyzed
* = total iron

Table 5 -- Amphibole Mineral Chemistry

	11	12	13	14	15
SiO2	39.32	39.68	38.54	40.12	40.55
TiO2	3.09	5.57	4.91	3.33	3.49
Al2O3	14.32	14.94	15.02	14.79	15.21
Cr2O3	0.04	0.03	0.01	0.00	0.10
FeO*	15.35	7.93	10.91	12.99	8.56
MnO	0.32	0.13	0.09	0.22	0.11
MgO	9.70	13.08	12.33	11.36	13.96
CaO	11.28	12.16	12.30	11.47	12.41
Na2O	3.06	2.95	2.37	2.77	2.37
K2O	1.71	1.48	1.83	1.85	2.07
P2O5	0.00	0.06	0.01	0.00	0.03
Cl-	na	na	na	na	na
F-	na	na	na	na	na
total	98.19	98.08	98.34	98.89	98.86

Number of ions on the basis of twenty-four (O, OH, F, Cl)

	11	12	13	14	15
Si		5.804	5.709	5.932	5.894
Al		2.195 7.999	2.290 7.999	2.067 7.999	2.105 8.000
Al		0.381	0.332	0.510	0.501
Ti		0.612	0.547	0.370	0.381
Mg		2.851	2.722	2.503	3.024
Fe*		0.970 7.841	1.351 7.935	1.606 7.989	1.040 7.344
Mn		0.016	0.011	0.027	0.013
Na		0.094	0.047	0.163	0.066
Ca		1.905	1.952	1.817	1.933
K		0.276	0.345	0.348	0.383

na = not analyzed
* = total iron

105

Key to Amphibole analyses

1. Kaersutite megacryst core, second period basanite 53Cl, analysis 53-1.

2. Ferroan pargasite outer core from grain in analysis 1.

3. Kaersutite rim from grain in analysis 1.

4. Kaersutite core, second period porphyritic trachybasalt 68Cl, analysis 68-20.

5. Kaersutite rim of grain in analysis 4.

6. Kaersutite core from third period porphyritic trachybasalt V, analysis V-8.

7. Kaersutite outer core, same grain as analysis 6.

8. Kaersutite rim, same grain as analysis 6.

9. Kaersutite phenocrysts armoring olivine megacryst, porphyritic trachybasalt V, analysis V-13.

10. Kaersutite core, nodule TM-9-64N.

11. Ferroan pargasite rim, same grain as analysis 10.

12. Kaersutite from nodule TM-9-63N.

13. Kaersutite from margin of nodule TM-9-69FG.

14. Ferroan pargasite from interior of nodule TM-9-69FG.

15. Ferroan pargasite form nodule TM-9-69CG.

The first type of alteration, resorption by the melt, does not alter the chemistry of the unresorbed hornblende, although these grains commonly have more intense pleochroic colors than unembayed hornblendes. This alteration is indicative of either thermal or chemical disequilibrium of the hornblende with the enclosing melt. Figure 34 is an example of a rounded hornblende, found in second and third period flows.

The second form of alteration consists of formation of heavy opaque or "opacitite" rims on the border of hornblende grains. These opaque borders may occur either on otherwise unaltered hornblende, or in conjunction with both of the other types of alteration. Unaltered portions of the hornblende commonly have deepened pleochroism. Kuno (1950) attributed this type of alteration to a severe increase in fO_2/fH_2 and decrease in fH_2O during eruption of calc-alkaline magma from Hakone Volcano, Japan. The alteration of hornblendes in the alkaline Kula rocks may have been caused by a similar process.

The third and most pervasive form of hornblende alteration involves breakdown of hornblende to anhydrous phases consisting of clinopyroxene, orthopyroxene, plagioclase, nepheline, and oxides. Alteration initiates at the hornblende rim and progresses inward. A thin rim of blocky oxides, probably magnetite or titanomagnetite surrounds a zone consisting of crystallographically(?) controlled oriented club to lath-shaped small grains, with
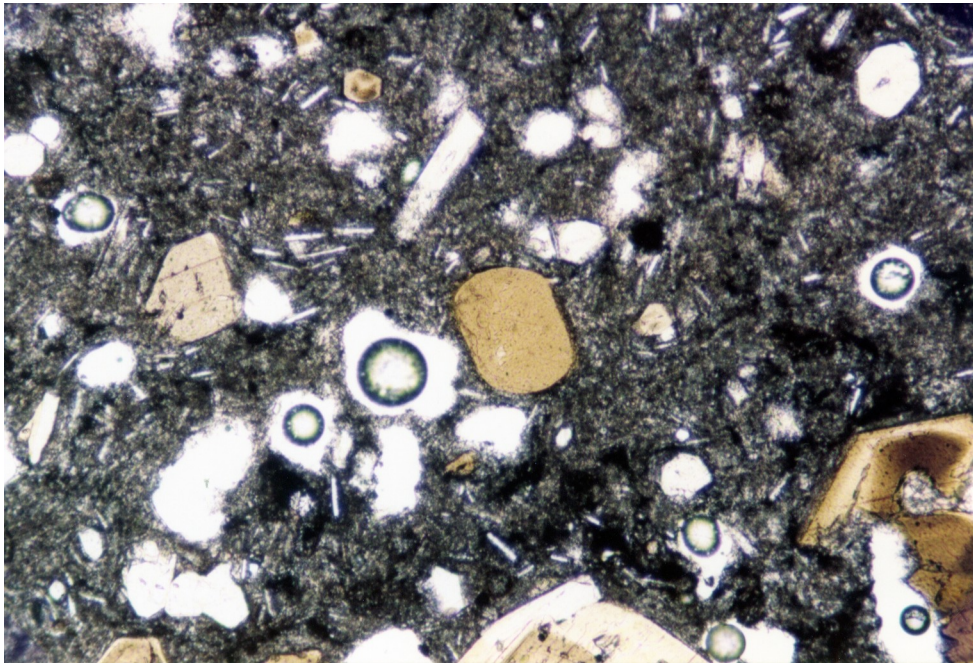
Figure 34.   Rounded kaersutite megacryst, third period
porphyritic trachybasalt, V.   This is probably due to
thermal disequilibrium.   The variety of amphibole tex-
tures in this sample implies a complex history for the
magma.   Field of view: 1.38 mm.

interstices filled with a low relief, low birefringence material. Clinopyroxene is also present. The club-shaped brown aggregates, as Washington (1894a) termed them, are strongly pleochroic olive green to brownish-red orthopyroxene, probably iron-rich. Orthopyroxenes observed in optic plane section (010) show that the pyroxenes are usually oriented in patches with their 'c' crystallographic axes parallel to the 'c' axis in the original hornblende. Other patches of orthopyroxene are oriented at angles of approximately 60° to the laths or clubs parallel to 'c'. These 60° angles are particularly well-developed at both the edges and pinacoids of the original hornblende crystals, with laths parallel to 'c' predominating in the central portions of the grains. The whole arrangement resembles a lattice. Throughout the alteration process the original grain outline of the hornblende is preserved. The outer margin may or may not have an opacitite rim. Often a core of corroded hornblende is preserved.

In more extensively altered specimens, the crystallographic orientation of the initial alteration products is destroyed and the final alteration assemblages consists of a granular aggregate of blocky titanomagnetite, clinopyroxene, feldspar, nepheline and orthopyroxene (not pleochroic), which still maintains the original outline of the hornblende. Feldspar and nepheline often core the aggregate.

This type of alteration, from oriented orthopyroxene-

dominated aggregate to granular clinopyroxene-dominated
aggregate is interpreted to be of magmatic origin, related to
the loss of volatiles from the magma sometime prior to
eruption.   Other authors (e.g., Garcia, 1979) have noted
similar hornblende breakdown assemblages in calc-alkaline
rocks, and have interpreted the anhydrous assemblage to have
been formed by magmatic processes, although I have not found
mention of the oriented orthopyroxene alteration type in
recent literature.   The Kula samples indicate that both the
oriented orthopyroxene and the granular aggregates are part
of a continuous process.   Often the oriented orthopyroxene
assemblage is found as cores, with granular aggregate
material forming the rim of a former hornblende.   A sequence
of photomicrographs which show the alteration process is
presented in Figure 35.

Vesicular, glass rich samples are consistently more rich
in unaltered hornblende than are the nonvesicular samples.
Two samples from near Kula Devit crater and from the distant
tip of the same flow both show the same type of hornblende
alteration, suggesting that no further alteration occurs
subsequent to eruption, although the sample from the tip
shows slightly more prominent opacitite rims, consistent with
the hypothesis that this form of alteration does occur during
subaerial eruption.   These observations suggest that in the
vesicular samples (volatile-rich), hornblende remained stable
until the magma was erupted, when the subsequent rate of
quenching determined presence (slow-quenching) or absence

Page 111 is missing from all copies of the submitted thesis; however no material appears to have been lost; probably this page was intended for the caption to Figure 35a-f, which can be found on page 115 after those six photos.
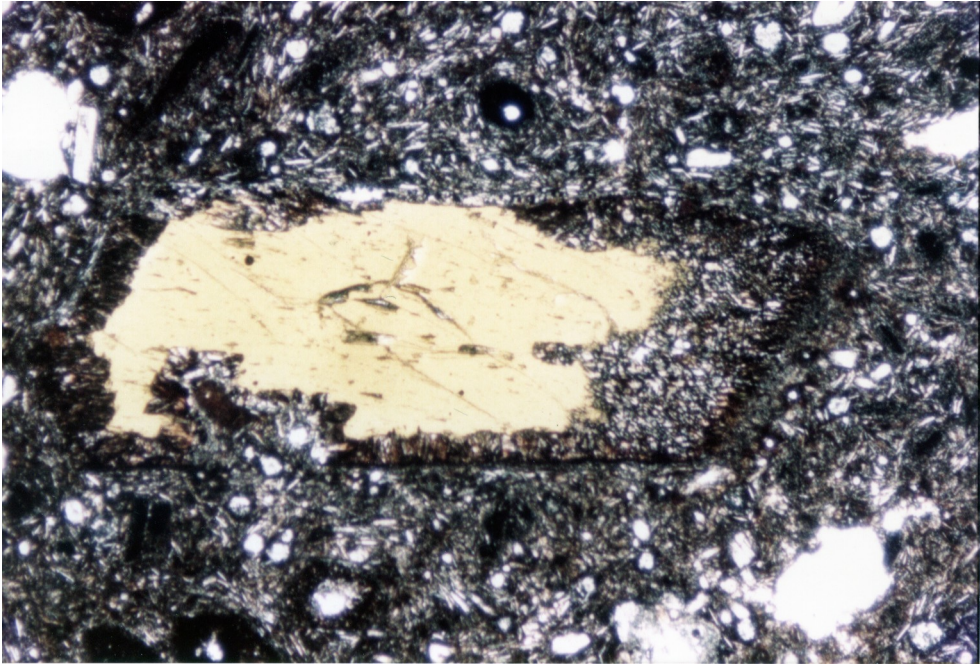
Figure 35a.
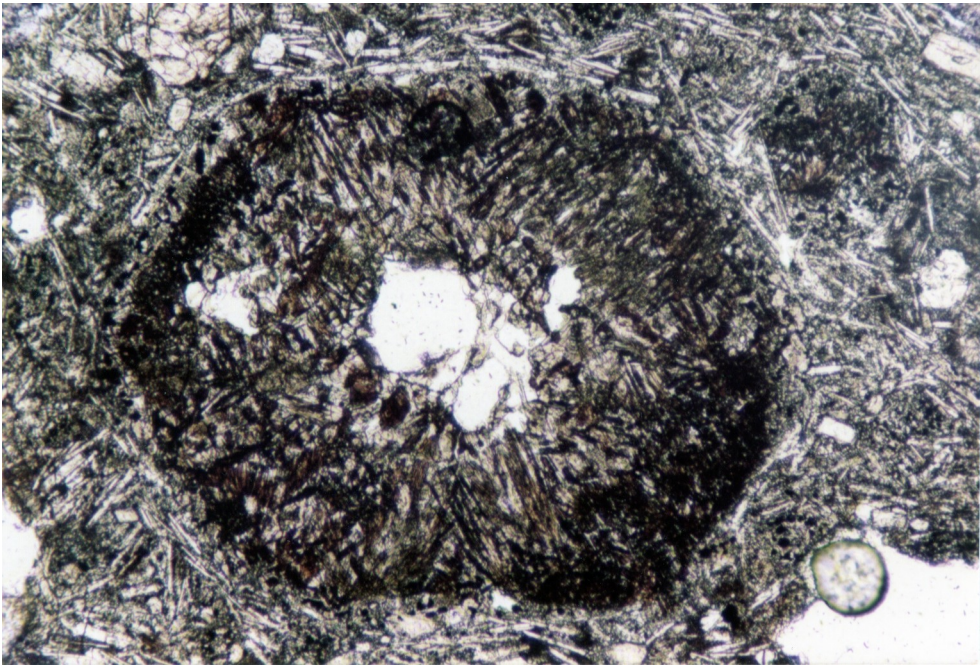
Figure 35b.
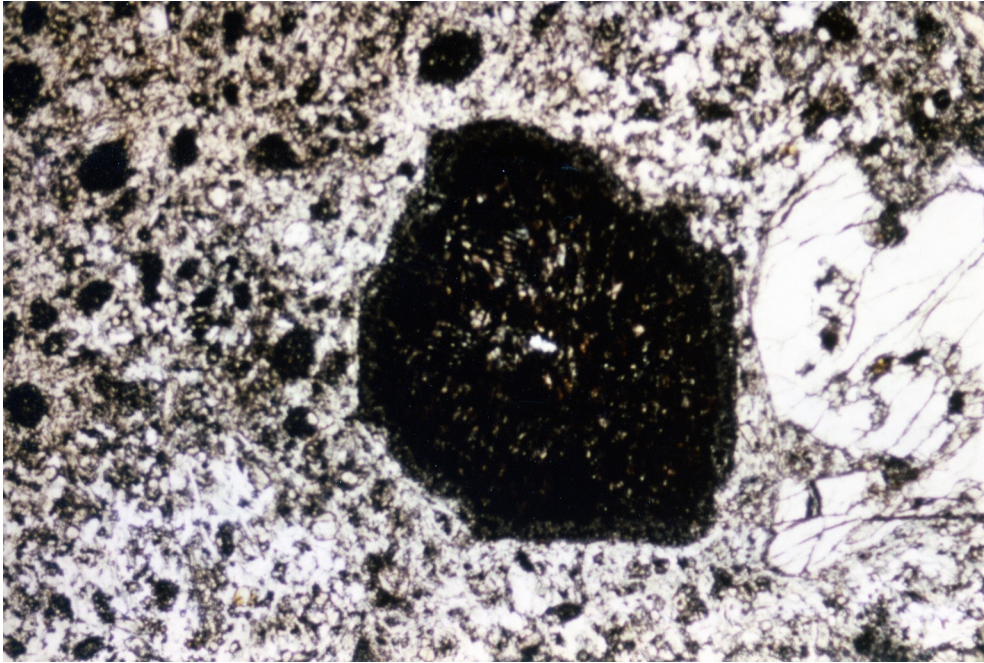
Figure 35c.
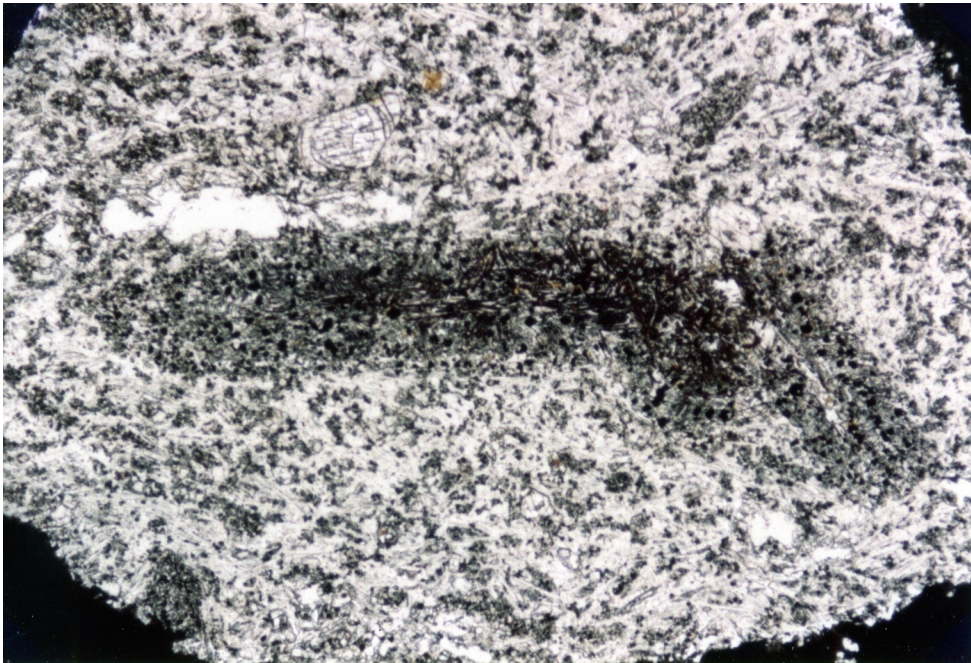
Figure 35d.
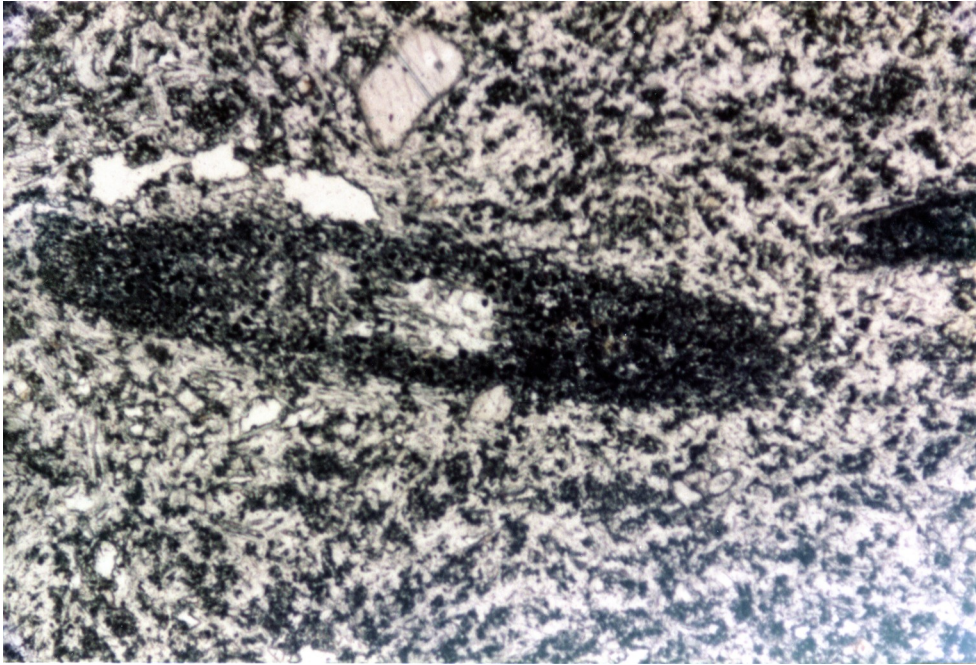
Figure 35e.
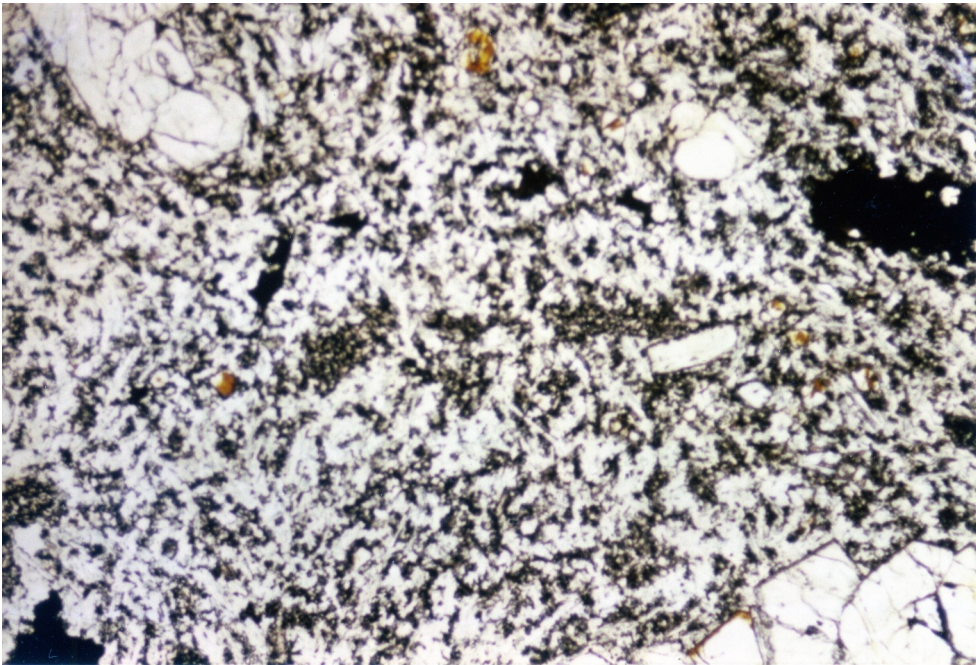
Figure 35f.

Figure 35a-f. Progressive alteration of amphiboles in
Kula lavas: a. Initiation of lattice-work breakdown
of kearsutite to oriented orthopyroxene structure, with
core kaersutite preserved, sample K_1, 3.4 mm. field
of view. b. Complete alteration of amphibole to oriented
orthopyroxene structure, TM-9-70, 1.38 mm. field of view.
c. Oriented orthopyroxene structure with rim of granular
aggregate breakdown, TM-67I, 3.4 mm. field of view. d.
Granular aggregate structure with some orthopyroxene
remaining in the core of the grain, TM-9-68, 3.4 mm.
field of view. e. Complete breakdown of amphibole to
blocky granular aggregate. Note not uncommon core of
feldspar and nepheline, TM-9-68, 1.38 mm. field of view.
f. Disaggregation of granular breakdown products into
the surrounding mesostasis of sample TM-9-68, 3.4 mm.
field of view.

(fast-quenching) of an opacitite rim. The depth at which volatile loss occurs may be indicated by the extent of hornblende alteration, with shallow volatile loss indicated by minor alteration to the oriented orthopyroxene, and deep loss indicated by the granular type of alteration.

Apatite

Apatite occurs in three forms in the Kula volcanic rocks: as microlites in the groundmass of the lavas, as xenocrysts and as a constituent of the ultramafic nodules.

Apatite microlites are recognized in the mesostasis by their high relief and untwinned form relative to plagioclase and by parallel extinction and negative elongation relative to clinopyroxene. This form of apatite occurs in all of the eruptive periods. Rare xenocrysts are present as large (to 1 mm) rounded or embayed grains. They are colorless, but may contain either dust-like opaque inclusions or elongate iron-rich rods which are aligned with their long axis parallel to the "c" axis of the host apatite. Apatite in the ultramafic nodules occurs as three varieties. Anhedral to subhedral, colorless, inclusion-free, fine-grained apatite occurs in nodule TM-9-69FG. In hornblendite nodule TM-9-64N, elongate colorless crystals cut through large kaersutite grains, or occur in water-clear euhedral to subhedral shapes in turbid brown glass in the interstices between the hornblende grains (see Fig. 16). Apatites of this form may have inclusions of round oxides(?) or glass. In TM-9-69CG, apatite forms subhedral to anhedral grains either poikilitically enclosed

by ferroan pargasite or titanphlogopite, or along the hornblende grain boundaries (Fig.36). These apatites contain the same oriented iron-rich oxide rods as those found in the xenocrystic apatite. Apatite analyses are listed in Table 6.

Phosphorus ranges from 0.46-1.22 wt% P_2O_5 in the Kula volcanic rocks. Experiments to determine phosphorus solubility in a variety of natural rock compositions as a function of SiO_2, pH_2O, and pressure were conducted by Watson (1980). His experiments demonstrate that apatite solubility is positively correlated with increasing temperature, and negatively correlated with increasing SiO_2 content, pressure and pH_2O. SiO_2 content seems to be the most influential factor, and in magmas of 50.0 wt% or less SiO_2 at upper mantle pressures, apatite solubility is so great (3.0-4.0 wt%) that even under lower temperature hydrous conditions, which could reduce solubility to 1.0-2.0 wt%, few basic magmas reach apatite saturation. The phosphorus contents in the Kula basanites and trachybasalts, when compared with their low SiO_2 content, virtually preclude them from ever having been saturated with apatite, since apatite crystallization can never reduce the phosphorus content of a magma below the saturation concentration (Watson, 1980). Thus, rare apatite megacrysts in the lavas are not likely to have crystallized from their enclosing magma at any depth, and probably have an origin similar to the apatite of the ultramafic nodules. Watson (1980) notes two conditions that may promote apatite saturation in a basic magma; high P_2O_5
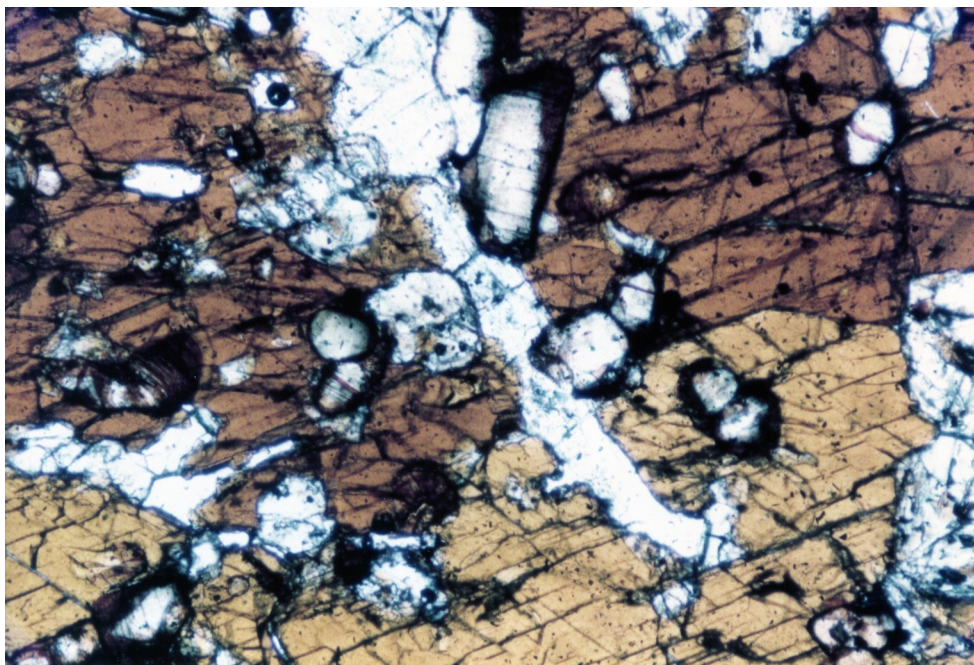
Figure 36. Apatite grain, nodule TM-9-69CG. Note anhedral shape, the cross-cutting relation of apatite with respect to ferroan pargasite grain boundaries, and the presence of oriented opaque rods within the apatite grain. Field of view: 3.4 mm.

Table 6 -- Apatite analyses

	1	2	3	4	5
SiO_2	.74	3.35	.33	.36	.38
TiO_2	.05	.02	.01	.03	--
Al_2O_3	.23	1.00	--	--	.05
$FeO*$	.81	.55	.43	.18	--
MnO	.21	.05	.07	.04	--
MgO	.54	.30	.14	.12	.21
CaO	47.31	47.81	49.72	52.52	47.63
Na_2O	.40	.35	.11	--	.14
K_2O	--	.12	--	--	--
P_2O_5	40.19	38.59	40.95	39.12	40.52
$Cl-$	1.31	.23	.37	na	.48
$F-$	2.84	2.52	5.15	na	3.52
total	94.62	94.89	97.29	92.38	92.93

1. Fine-grained wormy (myrmekitic) groundmass apatite in second period porphyritic trachybasalt 68C1, analysis 68-10.

2. Apatite megacryst in third period trachybasalt D-2, analysis D1-R core.

3. Rim composition of grain in analysis 2.

4. Apatite with appearance similar to analysis 1, surrounding severely altered kaersuite in third period porphyritic trachybasalt V, analysis V-12.

5. Apatite from nodule TM-9-69CG (contains oriented iron-rich inclusions).

content attained by fractional crystallization, or solidus depression due to the presence of volatiles. The occurrence of abundant apatite in the nodules could be explained by both of these factors if the nodules are orthocumulates of Kula magmas, or if the apatite is formed by a metasomatic migratory fluid.

Spinel

Spinel occurs as rare rounded plum-grey megacrysts in the lavas, and in the ultramafic nodules. Compositionally they are Al-rich, Cr-poor Fe-pleonaste (see analyses, Table 7), with low TiO_2 and low calculated ferric iron. Pleonaste of this composition could be derived from a crustal environment, where it is common in thermally or regionally metamorphosed silica-poor argillaceous rocks (Deer et al., 1966). However, spinel that appears optically identical to megacrysts in the lavas occurs in hornblendite TM-9-64N, suggesting that the megacryst origin is igneous. Binns (1970) has recognized compositionally identical spinel megacrysts in alkaline lavas from New South Wales, Australia, which he hypothesizes to be of high-pressure origin. He reports that Yoder and Tilley (1962, p. 499) found a "plum-colored spinel" in experimental runs on an Oahu nephelinite at 31.4 and 40 kb. Haggerty (1978) notes that spinels in volcanic rocks contain a wide range of Al/Cr ratios, which he suggests are depth-dependent. Spinels derived from shallow depth are enriched in Cr^{+3} because of the incorporation of aluminum in plagioclase. With increasing pressure, plagioclase becomes unstable and

Table 7.   Spinel Analyses

	1	2	3
SiO_2	0.13	0.11	52.55
TiO_2	0.30	0.20	0.80
Al_2O_3	63.14	62.87	22.88
$FeO*$	22.22	24.96	6.86
MnO	.13	.12	.20
MgO	13.75	11.52	2.29
Cr_2O_3	.06	.06	.02
CaO	.01	.01	3.63
Na_2O	.02	--	4.02
K_2O	--	--	4.58
P_2O_5	--	.02	.99
$Cl-$	--	--	.22
$F-$	--	--	.30
total	99.76	99.85	99.34

Number of ions on the basis of six O

	1		2	
Si	0.027		0.023	
Al	15.714		15.827	
Cr	nc	15.789	.015	15.897
Fe^{3+}	nc		nc	
Ti	0.048		0.032	
Mg	4.326		3.666	
Fe^{2+}	3.923		4.458	
Mn	0.023	8.282	0.022	8.148
Ca	0.002		0.002	
Na	0.008		0.000	

nc = not calculated
* = total iron

Key to spinel analyses

1. Ferroan-pleonaste megacryst from porphyritic
    trachybasalt V.   Analysis V-1.

2. Ferroan-pleonaste megacryst from porphyritic
    trachybasalt V.   Analysis V-2.

3. Glass inclusion in ferroan-pleonaste megacryst V-1.

Al/Cr ratios gradually increase to a maximum value at the garnet-spinel lherzolite field boundary, where spinel becomes unstable. Haggerty also remarks that low pressure spinel is typically rich in TiO_2 and Fe^{+3}, and has an inverse spinel structure, whereas high pressure spinels have normal structure, with low TiO_2 and Fe^{+3}. Haggerty's observations support a moderate pressure origin of between 15 and 20 kb (40 to 65 km) for the Kula spinel megacrysts. However, it should be noted that hard constraints of the above observations are few, and it is not known to what extent the bulk composition of the melt will affect the Al content of the coexisting spinel.

Feldspar

Plagioclase is the only feldspar observed in most of the Kula samples. Plagioclase does not occur as a phenocryst phase, but is present in the mesostasis in nodule TM-9-63N, and as rare megacrysts and small xenoliths. Anorthoclase is a rare megacryst phase, and potassium feldspar was only observed in rare crustal xenoliths. Table 8 contains selected feldspar analyses, and Figure 37 shows Kula feldspar compositions plotted on an An-Or-Ab ternary diagram.

Groundmass plagioclase occurs with two textural forms. The first type is commonly observed in samples that have a high proportion of glass, and consists of poorly formed, club-shaped grains with indistinct twinning. The second type is more common, and consists of fluidally arranged small laths (to approximately 0.10 mm) with generally well defined

Table 8. Feldspar analyses

	1	2	3	4	5	6	7	8	9	10
SiO2	50.60	51.15	52.03	50.64	57.59	64.46	64.79	45.88	55.52	52.70
TiO2	.16	.15	.17	.25	.11	--	.05	.02	.07	.11
Al2O3	31.25	30.78	30.82	30.51	26.56	22.42	21.66	34.09	27.32	28.86
Cr2O3	.01	--	.03	--	.02	--	.01	--	.01	.02
FeO*	.57	.50	.68	.61	.30	.12	.14	.20	.20	.49
MnO	.02	.02	.01	.02	--	--	--	.01	.01	.02
MgO	.04	.03	.04	.09	.08	--	--	--	--	.04
CaO	14.24	13.01	12.96	13.75	8.79	3.55	2.47	17.82	9.61	12.67
Na2O	3.50	3.84	3.72	3.30	5.95	8.83	7.30	1.55	5.80	4.06
K2O	.17	.32	.38	.30	.86	1.34	3.72	--	.52	.34
P2O5	.01	--	.01	.05	.05	--	--	--	.02	.07
total	100.58	99.80	100.87	99.52	100.32	100.72	100.15	99.59	99.08	99.38

Number of ions on the basis of 8 oxygen

	1	2	3	4	5	6	7	8	9	10
Si	2.299	2.333	2.349	2.323	2.582	2.835	2.877	2.123	2.525	2.412
Al	1.674	1.654	1.641	1.650	1.404	1.163	1.134	1.860	1.465	1.557
Ti	0.005	0.004	0.006	0.009	0.004	0.000	0.002	0.001	0.002	0.004
Fe*	0.021	0.019	0.026	0.023	0.011	0.004	0.005	0.008	0.008	0.019
Mg	.001	0.001	0.000	0.006	0.005	0.000	0.000	0.000	0.000	0.003
Mn	--	--	--	0.001	--	0.000	0.000	0.000	0.000	0.001
Na	0.308	0.338	0.326	0.293	0.517	0.753	0.628	0.139	0.511	0.360
Ca	0.692	0.636	0.627	0.676	0.422	0.167	0.118	0.884	0.468	0.621
K	0.009	0.019	0.022	0.018	0.049	0.075	0.211	0.000	0.030	0.020
total	5.009	5.003	4.999	4.999	4.995	4.998	4.974	5.015	5.010	4.996
An	69	64	64	70	43	17		86	46	62

* = total iron

Key to Feldspar Analyses

1. Labradorite microphenocryst core, TM-9-57.

2. Labradorite rim of analysis #1 microphenocryst, TM-9-57.

3. Labradorite microlite, 53C1.

4. Bytownite groundmass lath, 68C3.

5. Andesine, anorthosite xenolith, 68C1.

6. K-rich oligoclase megacryst, V.

7. Anorthoclase megacryst, V.

8. Bytownite, clinopyroxene-plagiovlase crustal xenolith, TM-9-67I.

9. Andesine, nodule TM-9-63N.

10. Labradorite groundmass lath, D2.
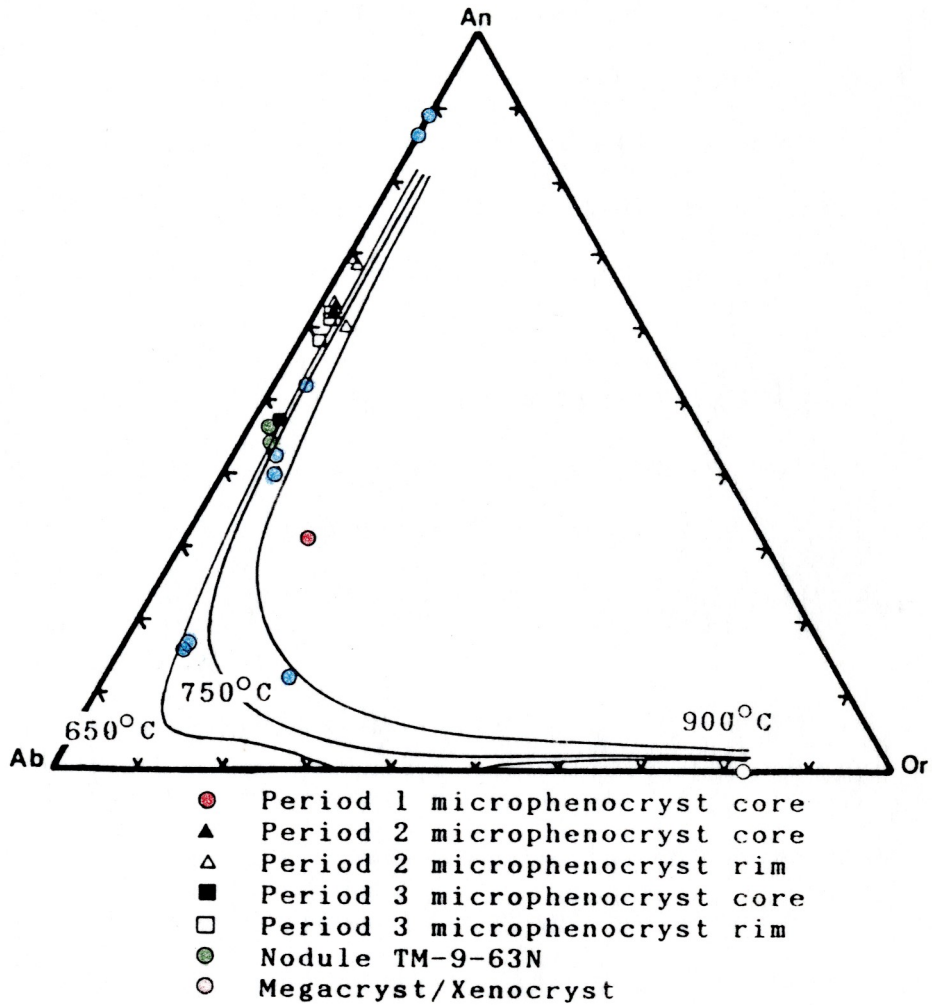
Figure 37. Kula feldspar mineral chemistry plotted on the
An-Ab-Or ternary diagram (in mole percent). Experimental
temperature curves after Seck (1971).

twinning. Both forms analyze as calcic labradorite with more sodic labradorite rims.

Megacrystic plagioclase is invariably rounded and embayed by the enclosing melt; some show severe sieving, which is interpreted as a partial melting texture. The megacrysts are unzoned except at the rim where there may be a thin zone of quench plagioclase which is the same composition as the groundmass grains. They are typically middle to calcic andesine in composition. One rounded andesine grain was observed to contain two euhedral hornblende crystals grown in the rim (Fig. 38).

TM-9-63N is the only plagioclase-bearing nodule. The plagioclase, An 44-46, occurs as oikocrysts which surround or partially enclose titaniferous, sodian augite and kaersutite. Twinning is only locally developed, and an undulatory extinction is common.

Both the megacrystic and nodule plagioclase are believed to be cognate to the basalts, and to have a similar origin, although the textural differences between the two suggest slight differences in environment of crystallization. Both trace element and rare earth element data suggest that either very little or no plagioclase fractionation has occurred; petrographic observation also supports this suggestion. The megacrysts and plagioclase-bearing nodule are tentatively interpreted as samples of trapped magma which crystallized at fairly shallow crustal levels, and which were entrained into the lavas during a later magma pulse. The more sodic nature
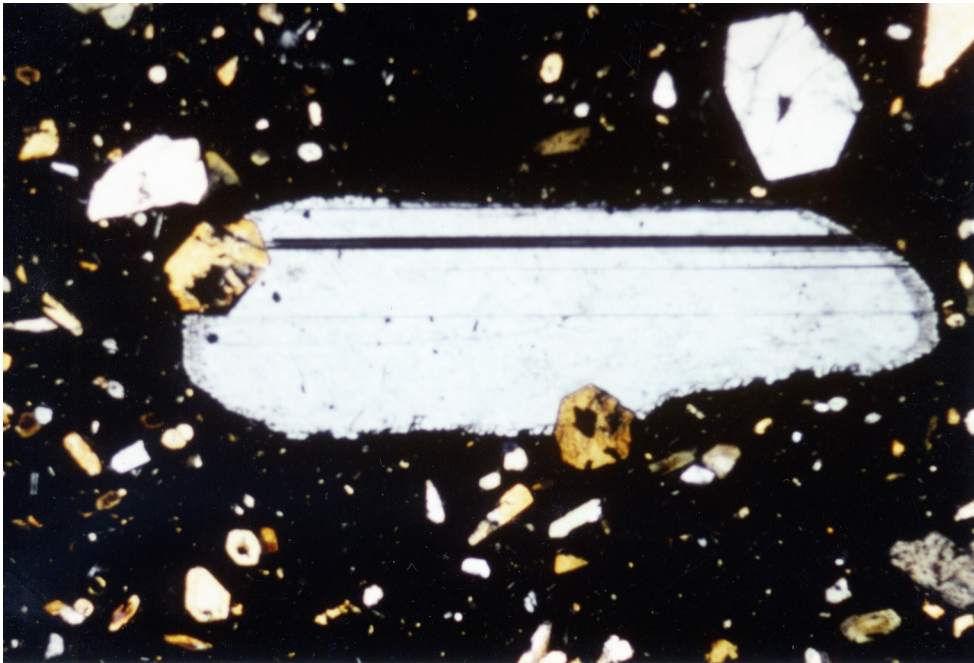
Figure 38.   Kaersutite euhedra in an unzoned megacryst;
third period trachybasalt V. This relationship in-
dicates the presence of an amphibolitic gabbro related
to the magmas, presumably at shallow depth.   The lack
of Europeum anomalies in the rare earth patterns may
indicate that this amphibolite body is not represented
by complimentary rocks at the surface.   Field of view:
3.4 mm.

of these plagioclases also suggests a closed system equilibrium crystallization, rather than a fractionated cumulate phase which might be expected to be more calcic than the groundmass plagioclase.

Anorthoclase is a megacryst phase which occurs as rare, colorless, extremely rounded grains which show only faint signs of the characteristic fine cross-hatching. An analysis is given in Table 8. Anorthclose megacrysts have been reported by Binns (1969) and Binns et al. (1970) to occur in alkaline rocks from New South Wales, Australia, and have been proposed to be a high pressure crystallizing phase. However, no corroborative experimental work is known of by either Binns or me. The presence of anorthoclase crystallizing at depth in the Kula magmas could explain some of the second period major element chemistry, but it is not certain what sort of physical or chemical parameters are necessary to promote anorthoclase crystallization, other than relatively high temperatures (Deer et al., 1966).

Feldspathoids and Related Phases

Kula volcanic rocks contain both nepheline and leucite. Analcite and gehlenite will also be discussed in this section. Analyses for these phases appear in Table 9.

Leucite

Leucite can be optically identified only in the third period trachybasalts. In the second and first period rocks leucite is occult in the groundmass glass. The grains are small (.05 mm), colorless, and generally have indistinct rounded margins; only rarely is there a hint of the more

129

Table 9 -- Feldspathoids and Related Phases

	1	2	3	4	5
SiO2	54.52	54.68	52.22	50.55	50.46
TiO2	0.21	0.09	0.96	0.21	0.13
Al2O3	23.32	23.43	20.57	21.30	30.01
FeO*	0.21	0.25	4.27	0.43	0.49
MnO	--	--	0.15	--	--
MgO	--	--	2.10	0.07	--
CaO	0.14	--	2.43	2.22	0.34
Na2O	0.18	0.44	0.94	0.55	16.15
K2O	20.83	16.80	15.27	18.41	2.99
P2O5	0.08	--	0.43	1.39	--
total	99.61	95.70	99.34	95.13	100.58

Number of ions on the basis of six oxygens (anal. 1 and 3)

	1		3	
Si	1.990		1.930	
Ti	0.006		0.027	
Al	1.004		0.896	
Fe*	0.006	1.021	0.132	1.272
Mn	--		0.005	
Mg	--		0.116	
Ca	0.005		0.096	
Na	0.013		0.067	
K	0.970	0.983	0.720	0.787
	3.994		3.989	

* = total iron

130

Table 9 - Feldspathoids and Related Phases

	6	7	8	9	10
SiO2	53.34	35.09	34.81	58.39	55.75
TiO2	0.16	0.14	0.04	0.13	0.23
Al2O3	27.81	19.39	21.20	23.83	24.89
FeO*	0.67	4.59	4.07	0.65	0.77
MnO	0.02	0.08	0.07	0.02	--
MgO	0.02	2.72	2.39	0.33	0.18
CaO	0.23	35.00	35.01	1.07	2.90
Na2O	13.71	2.10	2.28	5.07	4.95
K2O	2.15	0.33	0.35	0.74	0.66
P2O5	--	0.05	0.04	0.17	0.42
total	98.10	99.49	100.26	90.40	90.81

Number of ions on the basis of 14 oxygen (anal. 7 and 8)

	7		8	
Si	3.224		3.161	
Ti	0.010		0.003	
Al	2.100	6.065	2.270	6.072
Fe*	0.353		0.309	
Mn	0.006		0.005	
Mg	0.372		0.324	
Ca	3.445	3.858	3.407	3.849
Na	0.374		0.401	
K	0.039		0.041	
	9.923		9.921	

* = total iron
1 = analysis 10 contains 0.02 wt% Cl5-4 and 0.03 wt% F5-4

Key to Feldspathoid and Related Phases Analyses

1. Leucite glass from first period trachybasalt TM-9-67I.

2. Leucite glass from first period trachybasalt TM-9-68.

3. Leucite from groundmass of porphyritic trachybasalt V.

4. Leucite from third period trachybasalt TM-9-70.

5. Nepheline glass from first period basanite TM-9-57.

6. Nepheline glass from first period basanite TM-9-57.

7. Gehlenite from aluminous salite megacryst in second period basanite 53C1.

8. Gehlenite from another area of megacryst in analysis 7.

9. Analcite spherule from second period basanite 68C3.

10. Analcite spherule from second period basanite 68C3.

characteristic octagonal outline (Fig. 39). Microlite inclusions are invariably present, arranged in a concentric pattern. Most inclusions are silicates; oxide inclusions are less common. No complex twinning was observed under cross-nicols, most of the grains are completely isotropic. Analyses of both leucite glass and leucite are presented in Table 9.

Nepheline

Nepheline is optically identifiable only when it occurs as a breakdown product of kaersutite. Otherwise it occurs only as an isotropic, colorless, groundmass glass. Microprobe analysis confirmed the presence of nepheline in first and second period samples, although the high sodium content of the lavas suggests it should also be present in the third period rocks. Washington (1894) was also mystified at the lack of modal nepheline in such sodic rocks, and reports negative results in staining for nepheline in third period samples.

Gehlenite

Gehlenite was observed in second period basanite $53C_1$, where it occurs in an ash inclusion with aluminous salite. The gehlenite borders and replaces(?) the clinopyroxene with an unusual texture consisting of crystallographically oriented(?) fine grained brown material which forms a lattice-like framework with gehlenite occupying the interstices (Fig. 40). The associated salite is slightly zoned and highly aluminous, with a high proportion of Al^{VI},
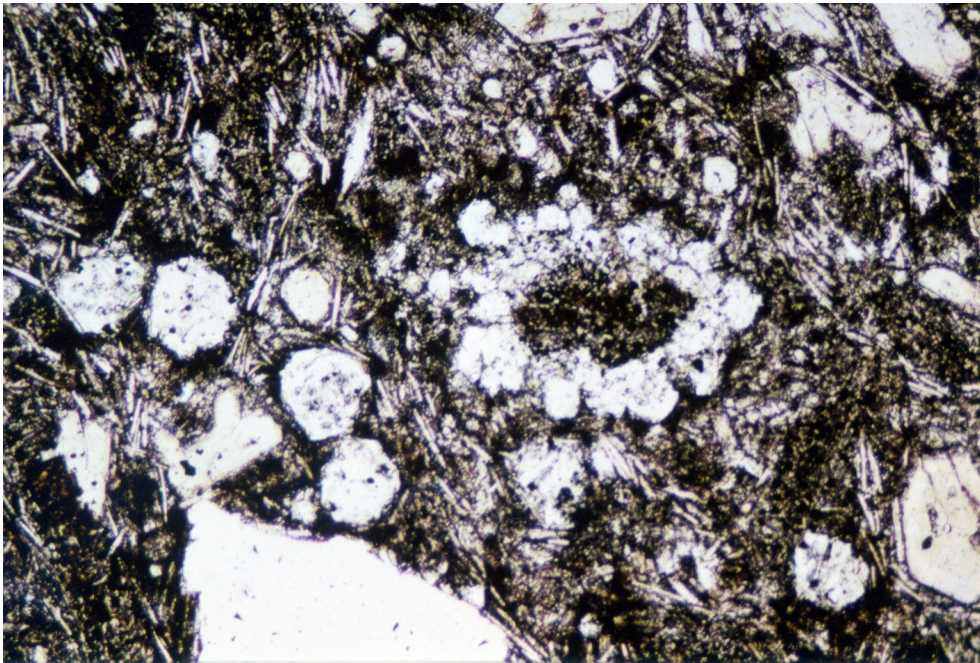
Figure 39. Leucite grains in the mesostasis of third
period trachybasalt TM-9-70. Grains occur either as
discrete crystals or as circular clusters (left center).
The typical octagonal morphology is usually not well
developed. Numerous microlites are invariably present
as inclusions. Field of view: 1.38 mm.

gehlenite

high aluminum
clinopyroxene

grunge

finer grain
clinopyroxene &
grunge

1.3 mm
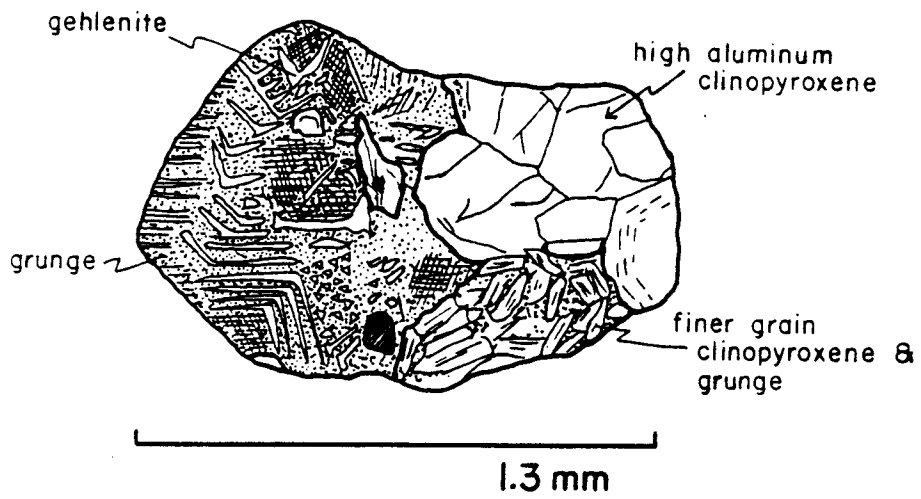
Figure 40. Gehlenite-bearing aluminous salite mega-
cryst in second period basanite $53C_1$.

suggestive of a high pressure origin (see analyses, Table 3). The origin of the gehlenite is unclear, although textural relations indicate that the pyroxene is reacting to form gehlenite, similar to Chinner and Schairer's (1962) documentation of a reaction aluminous clinopyroxene + liquid = melilite in olivine diabase contaminated by limestone at Scawt Hill, Northern Ireland (Tilley and Harwood, 1931). Yoder (1979) maintains that except under very low pressure conditions (e.g., Scawt Hill), CO_2 released by limestone assimilation will react with melilite to form diopside and calcite. Addition of $CaCO_3$ does not seem to favor melilite formation under most conditions. The isolated occurrence of highly aluminous salite reacting to gehlenite is evidence that this reaction is not an effect of limestone assimilation, in which case the reaction would be expected to be more generally observable, and in conjunction with clinopyroxene of known low pressure origin. Bowen (1928) and Yoder (1979) have stated that high alkali content is necessary for melilite crystallization. Yagi (1963) and Velde and Yoder (1976) have also noted that iron enrichment may also promote melilite crystalliztion in an alkaline magma. The Kula gehlenite may have been formed either by extensive crystallization of an alkali-rich magma under moderate pressure, or by the introduction of a highly alkaline and/or iron-rich melt into a less alkaline melt or crystal aggregate.

Analcite

Analcite was identified in one sample; second period basanite $68C_3$ where it occurs as approximately 0.15 mm circular colorless blobs in a light brown glassy mesostasis. The analcite is isotropic and contains abundant microlite inclusions (which may be clinopyroxene) as well as blocky opaque grains (Fig.41). Although it has been suggested (John Bender, personal communication, 1981) that the grains may be leucite altered to analcite, the very fresh, glassy nature of the rock and peculiar round nature of the grains suggests that they are indeed primary. The textures strongly resemble those described by Philpotts (1976), who used them as strong evidence for silicate liquid immiscibility.

As previously mentioned, $68C_3$ was the only lava containing the analcite. If it is indeed an example of liquid immiscibility, its relation to the paragenesis of the Kula volcanic field is uncertain at present.

Oxides

Oxides occur in the groundmass of all Kula lavas, and as a minor consituent of the nodules. Titanomagnetite is typically the only oxide phase in the lavas, and occurs as blocky fine-grained (0.05 mm or less) euhedra in the mesostatis, and as inclusions in the third period leucite grains. Titanomagnetite is also one of the breakdown products of kaersutite. Magnetite is the common oxide phase in the nodules; ilmenite has also been identified as discrete grains in one nodule. There are no magnetite-ilmenite
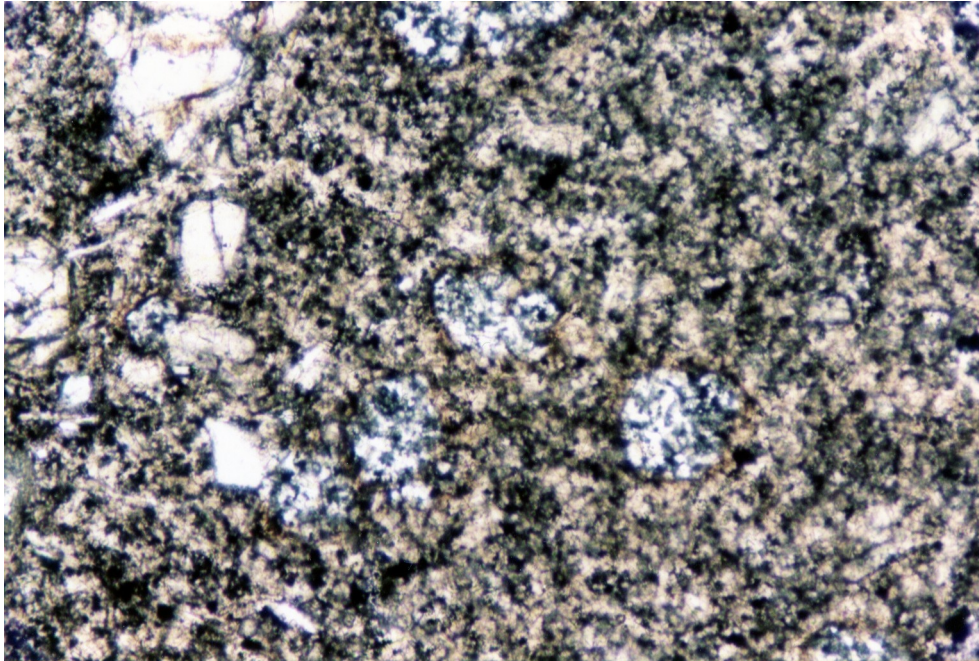
Figure 41. Analcite in second period basanite $68C_2$ groundmass. The fresh appearance of these colorless, round grains within the surrounding non-devitrified groundmass glass suggests that these grains may be primary analcite, not pseudo-leucite. The characteristic assemblage of leucite inclusions is not present within the analcite grains, which contain only minute blocky oxide inclusions. Field of view: 1.38 mm.

exsolution relations within single grains. Inclusions of oxides in silicate phases are rare, with the exception of sieve-textured clinopyroxene cores and in the aluminous salites of nodule TM-9-69CG. The abundance of oxides can be related to the color of the mesostasis glass. Abundant oxides are associated with colorless glass; as oxides become less abundant, the coexisting glass becomes a deep brown. As Washington (1894) points out, this suggests that the oxides are not an early crystallizing phase.

Because titanomagnetite is the only oxide present in the lavas, determination of temperature and fO_2 for equilibrated oxide pairs (Buddington and Lindsley, 1964) is not possible.

Work on ilmenite-absent suites by Verhoogen (1962) has shown, from thermodynamic calculations, that the assemblage magnetite + sphene is more stable at low temperatures and high fO_2 than the assemblage diopside + ilmenite. Carmichael and Nichols (1967), and Mitchell (1973) have examined ilmenite stability and sphene-magnetite relationships in terms of fO_2 and activity of SiO_2 in undersaturated rocks. Thermodynamic arguments imply that an assemblage consisting of ol + mt_{ss} + pf is stable under fO_2 conditions imposed by the FMQ buffer, while the association mt_{ss} + sph requires higher fO_2 conditions. Formation of sphene depletes the magnetite solid solution in Ti, and ilmenite may be completely absent.

These calculations are of relevance to the genesis of the Kula magmas because of the presence of the association sph +

mt in nodule TM-9-64N, which is considered to be genetically related to the basalts. Presence of Ti-poor magnetite in the nodules, in conjunction with a Ti- rich silicate phase, is indicative of high fO_2, at least in the environment of nodule origin. The change in composition from magnetite in the nodules to titanomagnetite in the lavas may be the result of cooling rate changes (equilibrium versus disequilibrium crystallization), a change in SiO_2 activity (Carmichael, 1974), or changes in fO_2 resulting from volatile release during breakdown of kaersutite, and subsequent eruption. Analyses of oxides are presented in Table 10.

Titanbiotite

Titanbiotite occurs in hornblendite nodule TM-9-64N and as rare megacrysts in the second and third period lavas. It is always associated with kaersutite, either rimming kaersutite grains or as irregular patches within kaersutite, which it appears to be replacing (Fig. 42). Grains are pleochroic deep brown parallel to cleavage, pale tan perpendicular to cleavage. An analysis is given in Table 11.

Titanphlogopite

Titanphlogopite occurs only in nodule TM-9-69CG, as oiko-crysts enclosing anhydrous phases. It also forms irregular patches in the ferroan pargasite oikocrysts, suggesting that the titanphlogopite was formed by replacement of ferroan pargasite. Anhydrous phases are more severely altered and embayed when surrounded by the mica, which is pleochroic deep orange-brown parallel to cleavage, pale yellow perpendicular

Table 10. Opaque Mineral Chemistry

	1	2	3	4	5	6	7	8	9	10	11
SiO2	.52	.27	.18	.13	1.34	.12	.08	.21	.10	19.19	.08
TiO2	24.00	.13	22.09	60.82	.17	13.32	23.00	.32	48.84	8.21	.07
Al2O3	1.29	.63	5.15	--	1.34	9.32	3.30	1.72	.75	11.88	--
Cr2O3	--	.12	.11	.13	.13	.11	.09	.08	.03	.70	--
FeO*	61.87	77.47	66.30	30.50	74.04	67.35	65.93	87.69	44.39	33.05	75.09
MnO	.70	.16	.88	.63	.20	.59	.81	.16	.86	.34	.01
MgO	2.26	.09	2.69	6.23	.13	5.23	2.68	.23	3.62	21.74	--
CaO	2.55	.25	.13	.02	.60	--	.08	.36	.07	5.32	--
Na2O	--	.05	--	--	.08	.01	--	.05	.04	.11	.08
K2O	--	.07	--	--	--	.10	--	.11	.01	--	--
P2O5	1.93	.12	.02	.01	.13	.08	--	.11	.07	.07	--
total	97.67	79.50	97.28	98.47	78.16	96.23	95.98	91.03	98.78	100.50	75.33

Key of opaque analyses

1. Titanomagnetite, first period trachybasalt TM-9-68.

2. Opaque in xenocryst, first period trachybasalt TM-9-67I.

3. Titanomagnetite, first period basanite TM-9-57.

4. Titanomagnetite, fine grain plagioclase xenolith in second period porphyritic trachybasalt 68C1.

5. Opaque in core of clinopyroxene from second period porphyritic trachybasalt 68C1.

6. Titanomagnetite inclusion, opaque + glass + gas inclusion in zoned kaersutite, third period porphyritic trachybasalt V.

7. Titanomagnetite inclusion in apatite megacryst from third period trachybasalt D-2.

8. Opaque from nodule TM-9-63N.

9. Titanomagnetite from nodule TM-9-69FG.

10. Inclusion in olivine (Fo79) from nodule TM-9-69CG.

11. Opaque inclusion from nodule TM-9-69CG.
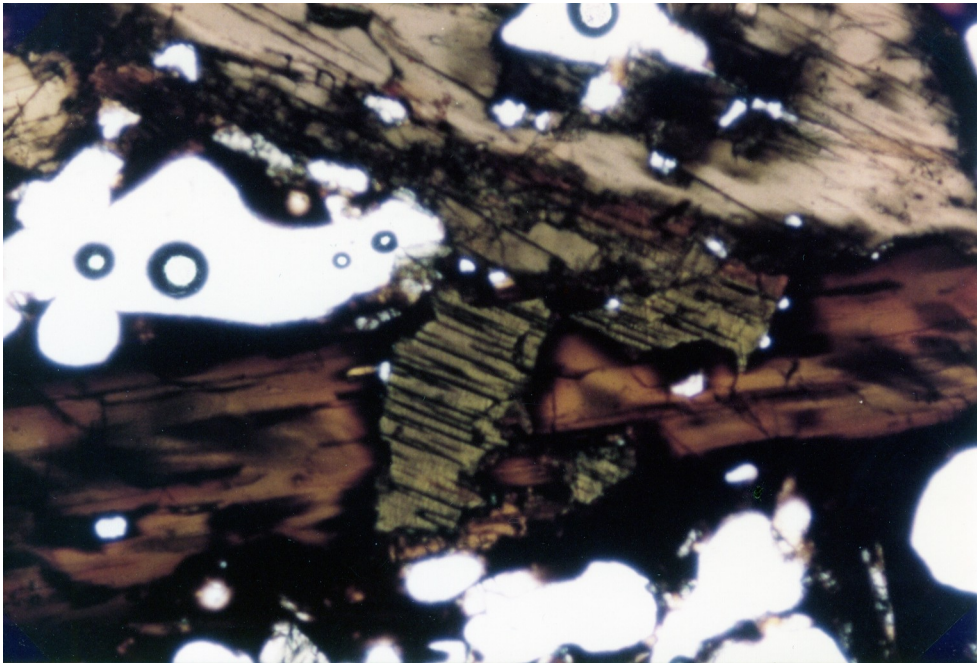
Figure 42. Titanbiotite crosscutting kaersutite in
nodule TM-9-64N. This texture suggests that mica is
replacing as well as mantling amphibole. Field of
view: 3.4 mm.

Table 11.   Mica and sphene mineral chemistry

	1	2	3	4
SiO2	35.63	36.07	36.79	31.25
TiO2	5.13	4.61	4.07	37.08
Al2O3	16.33	16.54	17.29	1.43
Cr2O3	0.01	0.00	0.01	0.01
FeO*	14.91	15.26	8.79	0.79
MnO	0.16	0.22	0.05	0.04
MgO	13.28	13.39	18.68	0.02
CaO	0.00	0.00	0.00	26.52
Na2O	0.75	0.69	0.79	0.06
K2O	9.00	8.93	9.05	0.00
P2O5	0.00	0.00	0.01	0.22
total	95.20	95.71	95.53	97.41

1. Titaniferous biotite, patch in kaersutite, TM-9-64N.
2. Titaniferous biotite, mantle on karsutite, TM-9-64N.
3. Titaniferous phlogopite oikocryst, TM-9-69CG.
4. Sphene bleb on edge of kaersutite, TM-9-64N.

to cleavage. An analysis appears in <u>Table 11</u>, and is similar to secondary phlogopite analyses reported by Boettcher and O'Neil (1980) and Delaney et al. (1980).

Sphene

Sphene occurs as irregular fine grained pale yellow blobs in nodule TM-9-64N. its petrogenetic significance is discussed with the oxide phases. An Analysis is given in <u>Table 11</u>.

Xenocryst Phases

Orthopyroxene

Ferrohypersthene (<u>Table 12</u>) was identified in both first and second period lavas, but is extremely rare. High iron and low alumina content suggest that these grains are of crustal origin. The grains are pleochroic olive-green to brownish-pink, with irregular spongy-textured rims mantled by titanaugite microphenocrysts. Iron-rich orthopyroxene also occurs in a fine grained granulite xenolith in $68C_1$ coexisting with andesine and oxide.

Clinopyroxene

Clinopyroxene xenocrysts are discussed under non-aluminous clinopyroxenes.

Feldspar

Feldspar xenocrysts(?) are discussed under the section on feldspar mineral chemistry.

Quartz

Quartz occurs in crustal xenoliths, or more commonly as single xenocrysts in second and third period lavas (rarely in

Table 12. Orthopyroxene (xenocryst) mineral chemistry

	1	2
SiO2	53.32	53.39
TiO2	0.43	0.30
Al2O3	6.44	1.47
Cr2O3	0.05	0.04
FeO*	18.84	19.48
MnO	0.67	0.79
MgO	21.62	21.06
CaO	1.51	1.51
Na2O	0.20	0.03
K2O	0.02	0.01
P2O5	0.05	0.03
F-	0.14	0.03
Cl-	0.02	0.02
total	103.33	98.16

1 = Aluminous orthopyroxene from plagioclase-rich xenolith, 68Cl.
2 = Aluminous orthopyroxene from plagioclase-rich xenolith, 68Cl.

first period lavas).   Grains often have spongy margins (melting texture) of very low relief isotropic glass, surrounded by a rim of clinopyroxene microlites.

Former quartz xenocrysts can often be identified by the presence of colorless to turbid brown glass, surrounded by clinopyroxene microlites and microphenocrysts which change in composition from titanaugite (aluminous) to salite (non aluminous) as the former quartz xenocryst is approached.

Carbonate

One rounded xenolith(?) of carbonate was identified in first period lava TM-9-68.   The carbonate has an unusual fibrous texture and is of uncertain origin, although Anita Crews (personal communication, 1982) has informed me that the inclusion does not have a sedimentary texture.

TRACE ELEMENT GEOCHEMISTRY

Analyses for Zr, Nb, Sr, Rb, Ni, Cr, V, Co, Y, Zn, Cu, and Ba were obtained on all basalts and nodules for which major element data are known. Sample powders were prepared in the manner described under whole rock chemistry analytical technique. Two samples, TM-9-57 and TM-9-67I, were prepared twice, using both preparation techniques (tungsten carbide mixer mill VS. the alumina mortar and pestle); both types were then analyzed to assess the effect of sample preparation technique on trace element concentrations. Sample TM-9-64N was run at the beginning and end of the run as a monitor of machine drift.

Pelletized samples were prepared in a manner similar to the process described by Schroeder et al. (1980), under vacuum in a 33 mm evacuated die. A highly polished steel pellet was placed in the die, polished side up, and a tightly fitting brass tube of 4 mm wall thickness was placed over the steel pellet. A small amount of rock powder was added until the steel pellet was completely covered, and this powder was tamped gently to form a cohesive disk. The brass tube was then carefully removed. Any errant rock powder which fell into this void was removed using a vacuum tweezer (Fullam no. 1585). Boric acid was sprinkled into the die, filling the void and covering the rock powder. A second steel pellet and a steel shaft were inserted into the die, and the whole apparatus was then placed in a hydraulic press (Spex no. O-30), where the sample was pelletized under vacuum at a force

of 10 tons for approximately 15 seconds.   Analyses were performed using the Woods Hole Oceanographic Institute Philips AXS automated spectrometer with a PW 1140 100 kv generator and standard 4 position sample turret. A W-target X-ray tube was used and Ce, Fe and Ti peaks counted to obtain on-line overlap correction data for Ba, Co and V peaks respectively (Schroeder et al., 1980).   All intensities are corrected on-line for interfering intensities. Intensity data was corrected for mass adsorption effects using an off-line correction program at S.U.N.Y.A. Peak and background intensity data for U.S.G.S. standards used were obtained from Brian Schroder (W.H.O.I.) for current machine operating conditions to calculate standard curves. Precision and accuracy of all trace element data is believed to be in the 1-5% range (Schroeder et al., 1980). Error bars in graphs represent 5% precision and accuracy.

In addition to these analyses, concentrations of La, Ce, Pr, Nd, Sm, Eu, Gd, Tb, Dy, Ho, Er, Tm, Yb, Hf, Pb, Th, U, Y, Sn, Cs, and Ba were determined on splits of whole rock powders using spark source mass spectrometric techniques. The samples for which data are currently available were analyzed by Dr. Richard Arculus with facilities at Australian National University, using the methods described by Taylor and Gorton (1977).

Effect of Preparation Technique on Trace Element Concentration

Samples TM-9-57 and TM-9-67I were analyzed twice; one

pellet was prepared using the roller mill-tungsten carbide mixer mill method, the other pellet was prepared using a steel percussion mortar and alumina mortar and pestle. In addition, a single pellet of TM-9-64N was run twice as a check on deviation for multiple analyses on a single sample, and two different pellets of TM-9-69CG (prepared in exactly the same way) were run to check on intra-pellet variation when the same preparation technique was used. Due to the limited number of analyses, this is by no means a definitive or quantitative examination, merely a qualitative indicator of the possible consequences of using different techniques.

Table 13 lists trace element concentrations and inter-sample variation for Kula lavas. Note that the analyses on TM-9-64N do not exceed 2% difference except for Co and Cr. Analyses of different pellets of TM-9-69CG show analytical variation of less than 5% except for Nb and Y, both elements of low concentration in this sample. In contrast, samples prepared using different techniques have a wider range of variation, and excepting Cr, element show synpathetic variations dependent on the sample preparation technique used. Obviously, more analyses of each pellet under carefully controlled conditions are necessary for any of these results to be statistically valid; however one striking difference in trace element concentration with different sample preparation technique is obvious. Co, used as a binder in the tungsten carbide mixer mill, increased in concentration by 30% in the samples prepared using the mixer

Table 13. Trace Element Geochemistry-Lavas

	TM-9-57	TM-9-67I	TM-9-68	68C3	68C2	53C2
Rb	66.2	78.5	76.5	61.0	39.6	48.3
Sr	1109.0	812.1	844.2	910.6	1053.8	1178.5
Ba	na	na	na	902	1031	965
Zr	246.9	248.3	203.3	238.6	299.7	284.2
Nb	123.2	100.0	80.5	91.3	103.7	90.5
Y	25.1	27.8	24.7	28.2	28.0	30.0
V	184.8	148.8	172.6	174.4	178.2	195.8
Cr	92.5	49.6	40.0	71.5	67.5	46.1
Ni	76.9	39.0	20.2	71.6	71.3	43.1
Co	39.7	32.5	32.8	34.5	29.6	36.8
Cu	43.2	38.6	24.9	26.2	24.2	25.7
Zn	66.3	69.3	64.6	63.6	63.6	72.2

	68C1	53C1	TM-9-64	TM-9-67II	TM-9-61	TM-9-58
Rb	48.4	52.3	27.8	61.0	84.2	77.6
Sr	1258.7	1173.1	1402.8	894.6	1000.1	827.3
Ba	1088	1079	na	na	na	na
Zr	245.7	286.2	244.8	271.0	250.8	205.0
Nb	89.6	90.3	130.2	112.6	104.0	96.1
Y	31.1	29.5	25.4	24.7	26.5	22.1
V	196.4	202.4	212.6	148.0	162.9	156.8
Cr	42.5	51.5	51.3	41.3	26.1	73.7
Ni	42.9	44.4	35.8	35.9	36.4	63.2
Co	29.9	32.5	33.7	33.9	31.2	45.7
Cu	28.1	25.5	33.8	36.7	28.6	38.4
Zn	73.0	73.9	80.0	69.6	70.2	72.7

All analyses by X.R.F., samples prepared using tungsten carbide technique.

Table 13. Trace Element Geochemistry-Lavas

	TM-9-63	V	TM-9-70	23L	K1	TM-9-66
Rb	80.7	72.7	78.6	74.7	80.3	85.0
Sr	877.6	873.6	845.8	884.8	862.2	820.8
Ba	na	954.6	na	1045	1008	na
Zr	213.8	265.1	213.4	278.2	269.1	203.4
Nb	106.8	95.0	104.1	95.8	92.4	91.5
Y	23.2	25.4	23.2	25.5	24.0	25.7
V	173.9	168.7	166.7	160.7	137.0	151.2
Cr	60.4	52.4	73.5	51.3	50.6	59.9
Ni	68.8	60.6	73.3	56.6	65.6	74.7
Co	59.5	32.8	46.4	29.4	33.0	59.7
Cu	29.7	21.8	31.6	24.0	28.4	38.4
Zn	103.4	60.1	78.2	61.8	60.4	75.0

	D1a	TM-9-62	D5	TM-9-59	D2	D4
Rb	73.7	82.3	75.6	71.0	74.0	74.5
Sr	934.9	840.0	946.0	894.7	952.2	954.8
Ba	1005	na	1002	na	1007	1010
Zr	290.1	214.6	297.6	208.5	302.0	302.9
Nb	98.3	103.9	103.2	103.8	100.4	103.5
Y	25.8	23.2	25.8	23.6	26.0	26.4
V	143.7	161.5	147.6	184.1	142.6	140.4
Cr	35.7	63.3	36.1	59.8	36.2	42.3
Ni	47.2	55.1	44.2	46.9	44.4	51.9
Co	25.6	78.4	29.2	63.7	24.6	29.6
Cu	17.6	45.6	19.9	44.7	23.4	19.0
Zn	54.3	73.7	58.8	65.5	56.5	60.7

All analyses by X.R.F., samples prepared using tungsten carbide technique.

Table 13. Trace Element Geochemistry-Lavas

	D1a	D2	D4	D5
U	2.26	2.04	2.39	2.06
Th	7.59	7.03	8.39	7.91
Pb	5.77	5.14	6.83	7.04
Hf	4.44	4.01	5.05	4.30
Yb	2.20	1.98	2.14	1.87
Tm	0.32	0.29	0.31	0.27
Er	2.18	2.10	2.16	2.03
Ho	0.88	0.78	0.85	0.81
Dy	5.79	4.94	5.54	6.12
Tb	1.07	0.86	0.78	0.93
Gd	6.42	5.64	5.02	5.13
Eu	2.32	2.00	2.04	2.04
Sm	7.45	6.48	6.93	6.65
Nd	39.3	33.90	39.30	38.55
Pr	11.2	8.60	11.30	10.05
Ce	119.4	80.93	104.63	101.83
La	57.1	45.39	57.54	54.37
Ba	1154	735	948	951
Cs	1.34	1.03	1.26	1.41
Sn	2.23	1.94	2.04	2.20
Y	25.5	19	26.9	25.1

Analyses by spark source mass spectrometer,
samples prepared using tungsten carbide technique.

mill. Less dramatically, use of the steel roller in conjunction with the mixer mill appears to result in systematic increases in Ni, V, Y, and Zn concentrations, and systematic dilution of Zr, Nb, Sr, and Rb concentrations relative to the alumina mortar and pestle technique, regarded by many geochemists to be a technique resulting in far less contamination (J. Bender, personal communication, 1981). However, it could be possible that the alumina mortar affected Zr, Nb, Sr and Rb concentrations. These possible contaminant-induced variations should be carefully considered when deciding what preparation method to employ when high accuracy is desired, or when certain elements are of special importance. As a result of my use of both methods, as well as the collection of trace element data under two possibly different machine operating conditions (some data were obtained by S.E. DeLong from the same machine in 8/78, although standard curves should correct for machine drift.), precision and accuracy of the data may differ, possibly resulting in looser constraints on interpretations using trace element data.

Trace Element Geochemistry - Data

Trace element concentrations for Zr, Nb, Sr, Rb. Ni, Cr, V, Co, Y, Zn, Cu, and Ba done by XRF analysis, and U, Th, Pb, Hf, Cs, Sn, Y, La, Ce, Pr, Nd, Sm, Eu, Gd, Tb, Dy, Ho, Er, Tm, and Yb by spark source analysis, are presented in Table 13. Kula volcanic rocks are characterized by low to moderate concentrations of compatible elements such as Ni, Cr, and Co,

.pn 153 and high concentrations of REE and other incompatible elements. In general, concentrations of compatible elements decrease with decreasing Mg number (Mg/Mg+Fe), while incompatible elements tend to have less correlation with Mg number. Elements of the first and third period volcanic rocks tend to show similar trends; trace elements of the second period volcanic rocks follow first and third period trends for most elements, but show significant difference for Rb, Sr, and V. Trace element concentrations are plotted against Mg number in Figure 43. Kesson (1973), Sun and Hanson (1975), Frey et al. (1978), and numerous other authors use Mg number as both an indicator of fractionation processes and as one criterion in the recognition of primary (direct partial melt) basaltic magmas are in equilibrium with an upper mantle source region (olivine composition of $Fo_{89}-Fo_{90}$, Irving and Green, 1976). It is interesting to note that if Kesson's method (1973) of linear extrapolation of trace element trends into the primary field (Mg numbers in the range 66-75) to obtain estimates of primary trace element abundances is valid, trace element abundances of Ni and Cr in "primary" Kula basalt is lower than most authors (e.g., Wass, 1980; Bender, personal communication, 1981) maintain are necessary for primary upper mantle-derived magmas. It is also apparent from Figure 43 that third period hornblende-bearing trachybasalts are as primitive as the second and first period non-hornblende bearing basanites, at least using Mg numbers as a discriminant.
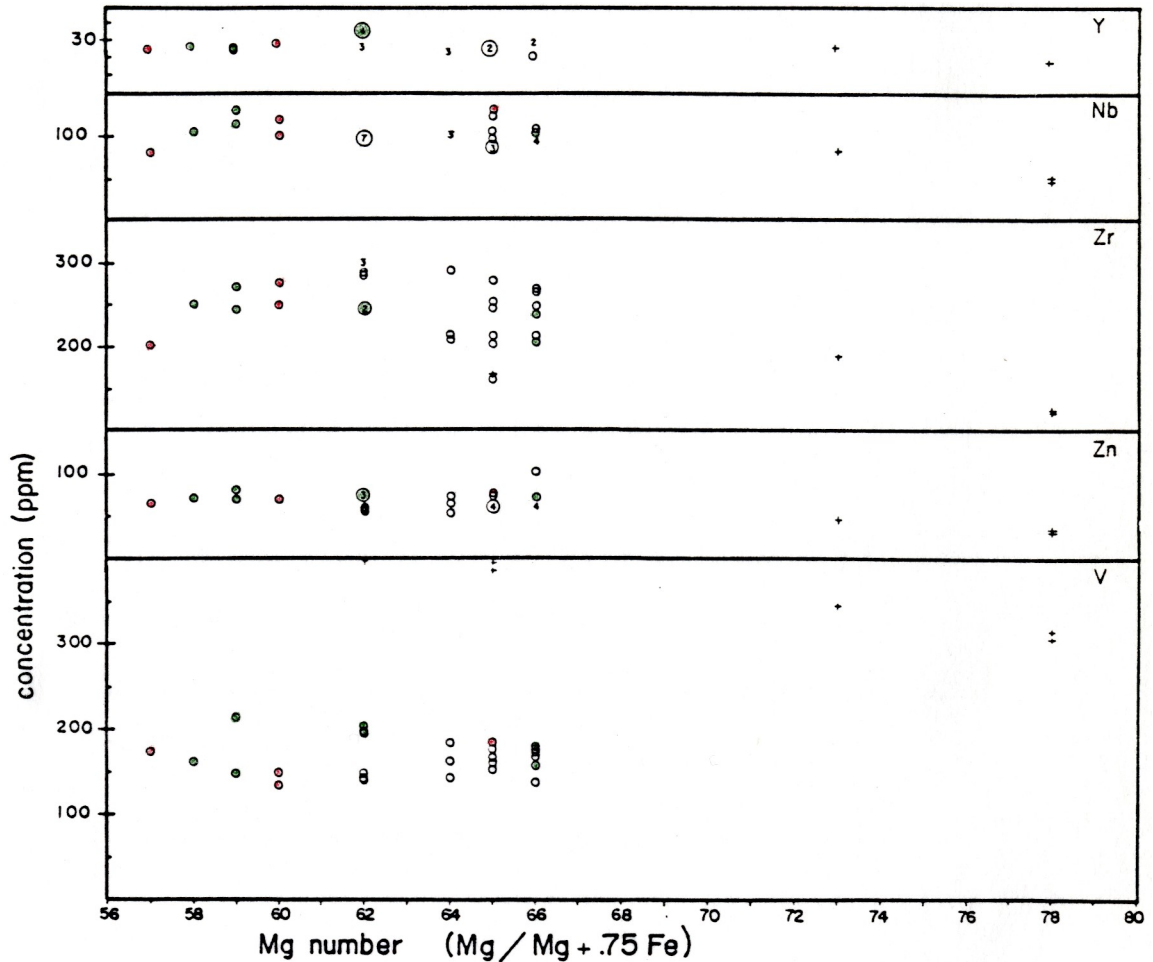
Figure 43. Kula lava and nodule trace element concentrations plotted against Mg number (Mg/ Mg + .75Fe). Nodules plot as crosses, lavas as circles, with red=first period, green=second period, white=third period. Numbers indicate a number of samples which plot at the same point. Large open circles around numbers indicate that a nodule plots at that value also.
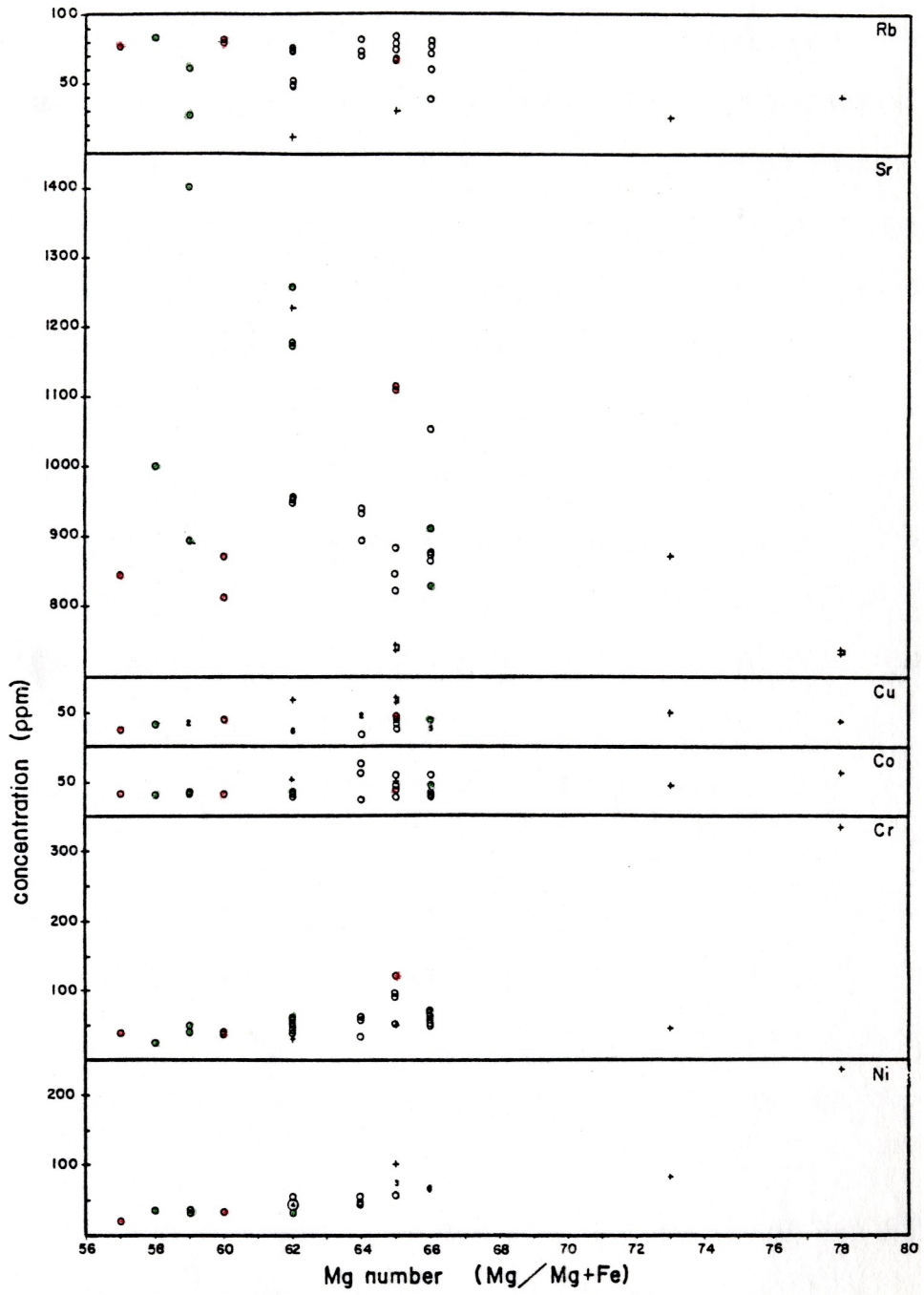
The trace element concentrations of the Kula volcanics are similar to basanites and trachybasalts erupted in continental rift environments (see, for example Brown and Carmichael, 1969; Kesson, 1973; Evans and Nash, 1979), although for equivalent Mg number, Kula volcanics tend to be more depleted in Ni and Cr, and more enriched in Rb. The volcanic rocks most closely similar to both Kula major and trace element composition are from the Korath Range basanite-tephrite series of the northern Kenya Rift (Brown and Carmichael).

Four third period chondrite normalized rare earth element (REE) patterns are presented in <u>Figure 44</u>. All four samples show strong light REE enrichment (La/Yb = 23-29), high total REE abundances and small positive Eu anomalies. REE patterns also show a slight enrichment of the heavy rare earth Yb, which may be indicative of either hornblende as a fractionating phase or of its presence in the source (Arculus, personal communication, 1981). The presence of crossing patterns and an unexplained dysprosium anomaly in two of the samples (D_2 and D_5), suggest that complex processes may be responsible for the paragenesis of this series of flows.

The nodules show a range of trace elements distinct from their enclosing lavas, and from each other. Nodule TM-9-69CG is depleted in high field strength ions (Nb, Zr and Y) relative to the other nodules and the lavas, slightly depleted in LIL elements (Rb and Sr) relative to the lavas,
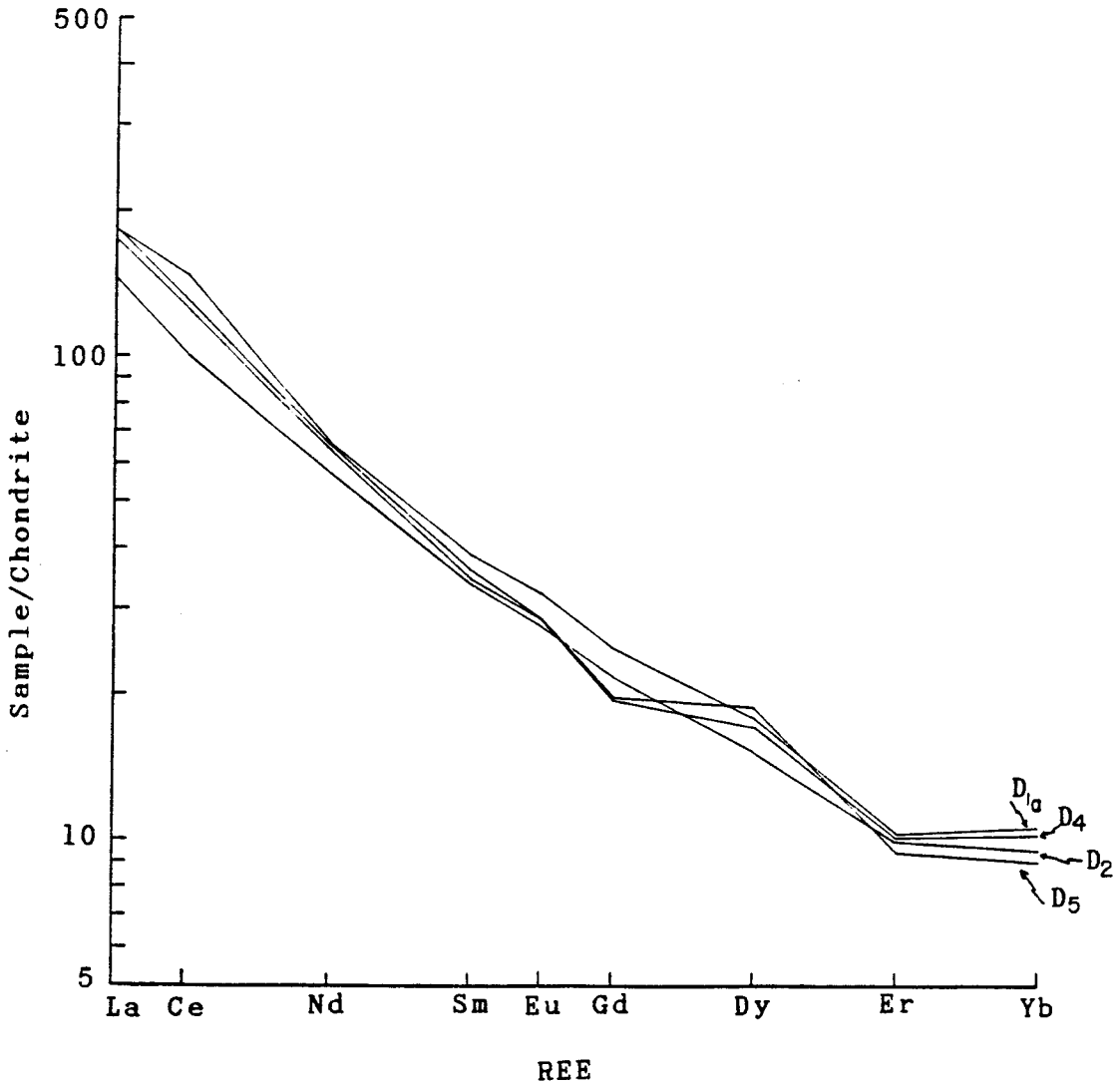
Figure 44. Chondrite-normalized rare earth element concentrations for a series of third period trachy-basalts; $D_{1(a)}$, D_2, D_4 and D_5.

and is enriched in the compatible elements (Ni, Cr, V and Co) relative to the lavas. Nodules TM-9-64N and TM-9-63N have roughly similar trace element concentrations; and are slightly depleted in Nb, Zr, Rb, and Sr, similar in Cr and Y, slightly enriched in Ni and enriched in V relative to the lavas. Nodule TM-9-69FG has trace element concentrations virtually indistinguishable from the lavas, with the exception of Rb (depleted in nodule relative to lava) and V (enriched in nodule relative to lava). The nodule trace element concentrations suggest that all of the nodules are of igneous origin, but that they have somewhat different relationships to the lavas and to each other. Nodule trace element concentrations are given in Table 14.

Table 14. Trace Element Geochemistry-Nodules and Lavas

	TM-9-63N	TM-9-64N	TM-9-1 64N	TM-9-69FG	TM-9-69CG	TM-9-2 69CG	TM-9-57a	TM-9-671a
Rb	25.3	31.9	32.6	12.8	41.6	43.1	67.7	82.3
Sr	871.3	739.8	745.7	1228.0	731.9	739.3	1140.0	870.1
Zr	189.8	167.3	166.4	247.7	122.0	126.5	255.0	278.7
Nb	82.9	87.9	87.3	97.3	45.1	50.5	130.4	119.8
Y	26.6	25.0	25.6	31.6	17.1	14.6	22.3	22.9
V	345.3	386.1	392.4	396.8	315.2	306.9	176.4	132.0
Cr	46.6	44.6	50.4	31.8	333.8	335.7	99.1	40.1
Ni	82.7	101.7	102.4	43.8	237.7	236.9	72.6	34.1
Co	44.7	51.8	49.9	53.2	60.8	59.0	27.8	22.3
Cu	48.1	62.0	70.6	68.9	32.8	32.6	43.2	41.6
Zn	47.9	61.2	61.5	74.1	34.2	35.3	66.3	65.9

1 = duplicate analysis of same pellet
2 = analysis on separate pellet

Analyses by X.R.F., samples prepared using alumina mortar and pestle.

STRONTIUM ISOTOPE GEOCHEMISTRY

Whole rock rubidium-strontium isotope data were determined for nine lava and four nodule samples by Dr. Stephen Moorbath of Oxford University. Because of the young age of the volcanics (< 1.1 m.y.), no age corrections are necessary, and all $^{87}Sr/^{86}Sr$ values are initial ratios.

The data (Table 15) show a narrow overall range in $^{87}Sr/^{86}Sr$ values from .70306 to .70397 in the lavas, and from .70302 to .70341 in the nodules, with small but distinct differences for both intra and interperiod samples. Correlations of lava and nodule $^{87}Sr/^{86}Sr$ with major and trace element data were searched for, but no distinct relationships were observed (Figs. 45,46). Second period samples have distinctly higher $^{87}Sr/^{86}Sr$ than do first and third period lavas and mafic nodules, which are fairly closely grouped. Noudle TM-9-69FG contains unsupported strontium (Fig. 47), which suggests either that radiogenic strontium has been added to this sample, or that rubidium has been preferentially leached from it. The low $^{87}Sr/^{86}Sr$ values are among the lowest recorded for intraplate continental alkaline volcanism, and fall within the range of oceanic island basalts. These low ratios, combined with the lack of correlations between the ratios and other chemical data, as well as the existence of a pre-Cambrian to Paleozoic basement of feldspathic gneisses, indicates that these rocks probably suffered little or no crustal contamination. Thus, although crustal xenoliths and xenocrysts are not uncommon in

160

Table 15. Rubidium-strontium isotope geochemistry.

Sample	Rb ppm[1]	Sr ppm[1]	Rb/Sr[2]	Rb87/Sr86[2]	Sr87/Sr86[3,4]	
TM-9-57	75	1308	0.058	0.168	0.70324	0.00003
TM-9-67I	92	1034	0.089	0.257	0.70311	0.00005
TM-9-68	85	1050	0.081	0.234	0.70326	0.00005
53C1	52.7	1184	0.045	0.130	0.70359	0.00007
68C2	50.7	1226	0.042	0.122	0.70397	0.00007
23L	73.8	884	0.084	0.084	0.70316	0.00006
V	73.9	886	0.084	0.243	0.70321	0.00008
K1	79.9	859	0.093	0.269	0.70324	0.00007
D1a	75.4	954	0.079	0.229	0.70306	0.00007
TM-9-63N	27	1057	0.026	0.075	0.70302	0.00004
TM-9-64N	29	729	0.040	0.116	0.70307	0.00005
TM-9-69FG	7	1181	0.006	0.017	0.70334	0.00006
TM-9-69CG	45	860	0.053	0.153	0.70341	0.00005

1 Rb and Sr contents only accurate to ca. 5% (X.R.F.)
2 Average errors on 87Rb/86Sr ratios ca. 1% (X.R.F.)
3 Normalized to 86Sr/88Sr = 0.1194 and Eimer and Ameud 87Sr/86Sr = 0.70800
4 2 sigma (95%) errors
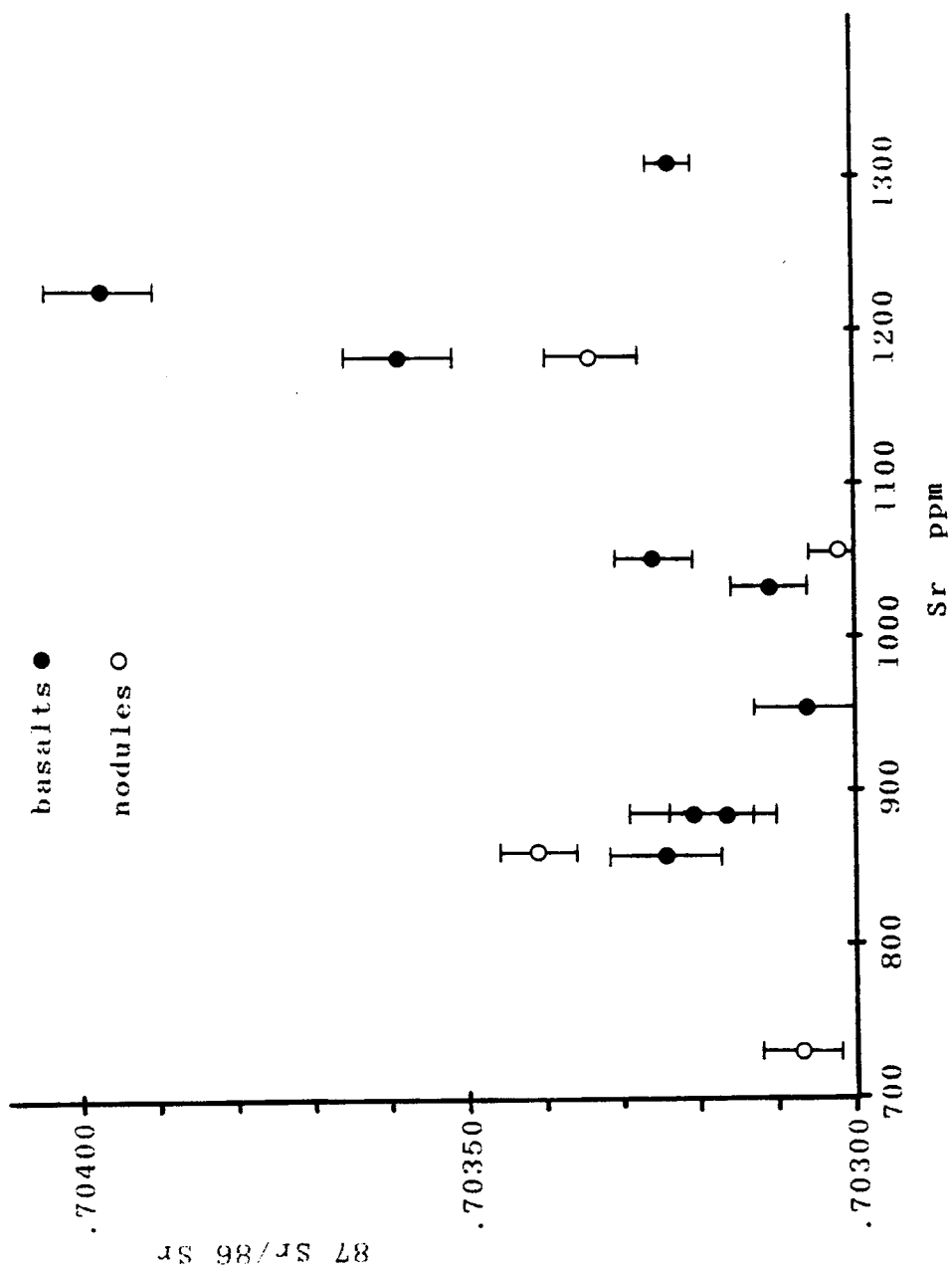
Figure 45. 86Sr/87Sr versus Sr concentrations for Kula lavas and nodules.

163
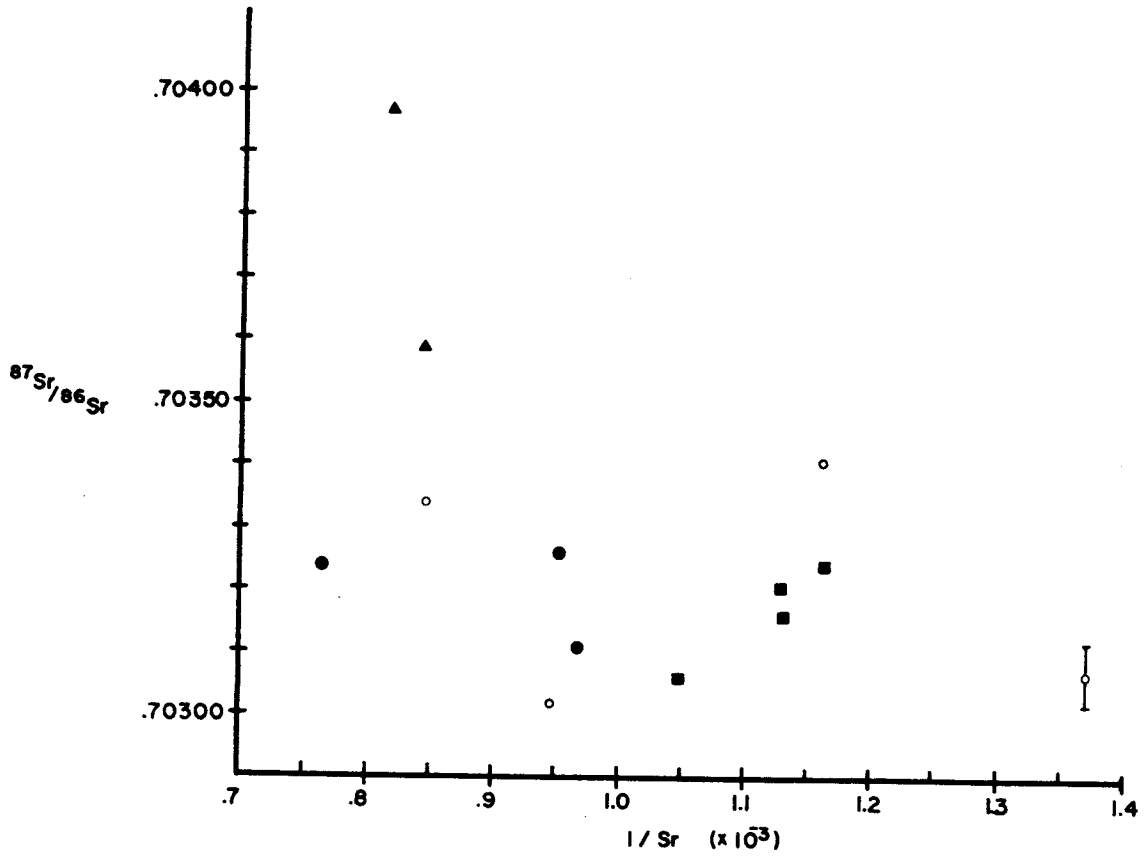
Figure 46. $^{86}Sr/^{87}Sr$ versus 1/Sr variation diagram.
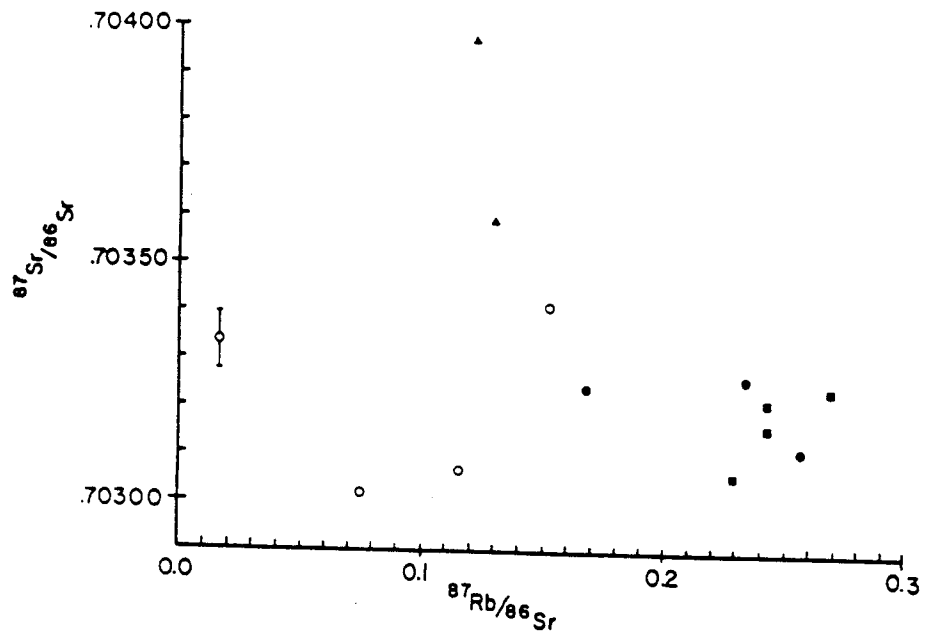
Figure 47.   86Sr/87Sr versus 87Rb/87Sr variation
diagram.   Note the position of nodule TM-9-69FG to the
left of the geochron.

the basalts, it appears little of this material was assimilated by them. The lack of contamination suggests a relatively rapid rate of ascent of magmas through the crust.

Most of the ultramafic nodules are isotopically identical (within error) with certain lavas, although not necessarily with the enclosing lava. TM-9-63N, isotopically identical to TM-9-67I and D_1, is isotopically distinct from the volcanic center from which the nodule was obtained (Kula Devit, of which samples V and 23L are parasite cones). Only nodule TM-9-69CG is isotopically dissimilar to all of the basalts analyzed, falling in $^{87}Sr/^{86}Sr$ value between the second period and the combined first and third period lavas. Petrographic and chemical data suggest that nodules with the possible exception of TM-9-69CG might be genetically related to the Kula lavas as either cumulates, conduit platings, or as pods of trapped magma not necessarily related to their enclosing lavas.

Heterogeneity of the upper mantle is now fairly widely accepted, and numerous authors (e.g., Kesson, 1973; Schilling, 1973; Lloyd and Bailey, 1975; Sun and Hanson, 1975; O'Nions et al., 1976; Frey et al., 1978) have cited heterogeneity of the mantle source in explaining chemical and isotopic differences in rocks from a single volcanic field when crustal contamination is not suspected. If metasomatic enrichment of the mantle source by KREEP components is a necessary prerequisite for alkaline magmatism, as has been suggested by Boettcher and O'Neil (1980), Windom and

Boettcher (1980), Menzies and Murthy (1980a,b), Lloyd (1981), and others, then the small differences in the isotopic composition of the Kula lavas might be explained by the existence of localized magma conduit systems fed by pulses of isotopically distinct partial melts from heterogeneous mantle source material. Patchy distribution of a rubidium-rich phase; phlogopite for example, that is not in isotopic equilibrium with associated anhydrous phases, could by preferential entry into partial melts, cause variations in the isotopic compositions of the resultant magma (Pushkar and Stoeser, 1975). The $^{87}Sr/^{86}Sr$ of the lavas would thus depend on the mineralogy of the source, the $^{87}Sr/^{86}Sr$ ratios of the minerals and the amount of partial melt (Faure, 1977). Phlogopite and other hydrous or LIL-enriched phases may have been introduced via the aforementioned mantle metasomatic event, prior to or synchronous with the melting event that resulted in the Kula magmatism.

DISCUSSION

Lavas of the Kula volcanic field are characterized by relatively small ranges in composition over an eruptive history of 1.1 m.y. Differences in the $K_2O:Na_2O$ ratio in first and second period lavas, which seem to define separate trends in the second period volcanic rocks on variation diagrams, suggest that separate sodic and potassic series exist, possibly a result of heterogeneous source material. Complex paragenetic relationships are also suggested by zoning and mantling relations in the phenocryst population, existence of a variety of megacryst phases, significant variation in strontium isotope ratios, variations in trace element concentrations for non-cumulative samples of the same Mg number (particularly common for the incompatible trace elements), and crossing rare earth patterns in a sequence of flows from a single cone.

Although crustal xenocrysts or xenoliths are not uncommon in the lavas, lack of plagioclase phenocrysts implies a short residence time of the magmas under low pressure conditions, and although strontium concentrations are high, strontium isotopes indicate that it is non-radiogenic strontium. Although crustal contamination of the Kula magmas cannot be conclusively ruled out, available data suggest that contamination is insignificant. Unfortunately, Nd isotopic data, which would be a sensitive indicator of the presence of a crustal component do not yet exist for these rocks.

This section will discuss processes that might be

167

involved in the production of observed petrographic and chemical variations within the three periods of activity. It will be assumed that each period underwent similar evolution (although MgO variation diagrams indicate that this is a simplification), which is supported by similar lava compositions in each period of activity. It will also be assumed that the upper mantle is the only source for the Kula magmas, based on the lack of evidence for crustal contamination.

Lavas related by Different Percentages of Partial Melting

It is unlikely that intra-period variations in major and trace element chemistry can be explained by variation in amount of partial melting. This can be seen by examination of compatible trace element concentrations. For any trace element with a bulk distribution coefficient significantly greater than one (D = (concentration of element in source)/(concentration of element in liquid) >> 1), the concentration of that element will be buffered at a constant level of concentration of the liquid for large variations in percent of partial melt (Arth, 1976; Cox et al., 1979). Ni, for almost any hypothetical upper mantle source material, will have a D >> 1. Thus, if the Kula basalts are related to different percentages of partial melt of a single source, nickel concentrations should be roughly constant in the lavas. Positive correlation between Mg number and Ni contents (as well as Cr, also with a D>>1) does not support a hypothesis of partial melting variations. Alternatively,

fractional crystallization processes will result in rapid depletion of elements of large D, if common ferromagnesian phases such as olivine, clinopyroxene, or hornblende make up the fractionating assemblage, along with only slight enrichment of incompatible phases for large variations in crystallization.

Fractionation Models

The presence of phenocrysts in the Kula volcanic rocks suggests that fractionation processes must, at least in part, be responsible for chemical variations within each period of volcanism. An attempt was made to model these variations using a least-squares subtraction program (Bryan et al., 1969). This program computes the weight fractions of specified mineral phases that must be removed or added to a model parental magma, to produce a daughter magma. The difference of calculated and observed daughter oxides is squared, and the results summed for all oxides to give a sum of squares of residuals, which is then used in evaluatinge the validity of the proposed model. Sums of squared residuals greater than one were considered not to be realistic solutions. Phenocryst and megacryst compositions of kaersutite, ferroan pargasite, titanaugite, sodian augite, aluminous diopside, olivine, plagioclase, anorthoclase and titanomagnetite were used to model fractionating phases. Results of selected fractionation models are presented in Table 16.

The most plausible solutions were obtained by modelling

Table 16. Major element fractionation models.

	MODEL #1		MODEL #2		MODEL #3	
	OBS	CALC	OBS	CALC	OBS	CALC
SiO2	48.86	48.91	48.86	48.85	48.86	48.84
TiO2	1.94	1.83	1.94	1.90	1.94	1.92
Al2O3	18.34	18.13	18.34	18.29	18.34	18.30
FeO*	7.65	7.65	7.65	7.75	7.65	7.74
MgO	0.19	0.16	0.19	0.16	0.19	0.16
MgO	5.36	5.35	5.36	5.37	5.36	5.34
CaO	7.60	7.77	7.60	7.62	7.60	7.65
Na2O	5.96	5.93	5.96	5.96	5.96	5.96
K2O	3.31	3.45	3.31	3.48	3.31	3.48
P2O5	0.77	0.85	0.77	0.85	0.77	0.85
r2	.1171		.0509		.0492	

	MODEL #4		MODEL #5		MODEL #6	
	OBS	CALC	OBS	CALC	OBS	CALC
SiO2	48.86	48.84	49.20	49.14	48.74	48.96
TiO2	1.94	1.93	1.95	1.88	2.08	1.79
Al2O3	18.34	18.33	18.71	18.73	18.91	17.97
FeO*6	7.65	7.66	7.64	7.64	7.28	7.46
MnO 8	0.19	0.16	0.13	0.16	0.13	0.18
MgO 4	5.36	5.37	5.55	5.61	5.48	5.99
CaO 6	7.60	7.64	7.50	7.59	7.81	7.46
Na2O2	5.96	5.96	5.55	5.81	5.38	5.93
K2O 6	3.31	3.49	3.29	3.35	3.37	3.64
P2O54	0.77	0.85	0.47	0.63	0.82	0.76
r2	.0399		.1161		1.7672	

Model #1 = D1 - hbl = D4
Model #2 = D1 - (hbl + cpx) = D4
Model #3 = D1 - (hbl + cpx + ol) = D4
Model #4 = D1 - (hbl + cpx + ol + timag) = D4
Model #5 = TM-9-63 - (hbl + cpx + ol + timag) = TM-9-62
Model #6 = K1 + hbl = TM-9-59

Table 16. Major element fractionation models.

	MODEL #7		MODEL #8		MODEL #9	
	OBS	CALC	OBS	CALC	OBS	CALC
SiO2	48.74	48.88	48.74	48.70	48.74	48.71
TiO2	2.08	1.90	2.08	2.29	2.08	2.32
Al203	18.91	18.18	18.91	18.63	18.91	18.69
FeO*	7.28	7.58	7.28	7.46	7.28	7.26
MnO	0.13	0.18	0.13	0.18	0.13	0.18
MgO	5.48	6.03	5.48	5.44	5.48	5.51
CaO	7.81	7.35	7.81	7.46	7.81	7.90
Na20	5.38	5.97	5.38	5.92	5.38	5.92
K20	3.37	3.68	3.37	3.66	3.37	3.66
P205	0.82	0.76	0.82	0.74	0.82	0.73
r^2	1.6478		.5569		.5060	

	MODEL #10		MODEL #11		MODEL #12	
	OBS	CALC	OBS	CALC	OBS	CALC
SiO2	47.69	47.81	46.95	46.92	46.95	46.93
TiO2	1.89	1.99	2.35	2.42	2.35	2.31
Al203	17.84	17.87	16.56	16.78	16.56	16.56
FeO*	7.75	7.74	9.02	8.42	9.02	9.03
MnO	0.14	0.16	0.14	0.19	0.14	0.19
MgO	6.22	6.11	6.16	6.40	6.16	6.18
CaO	8.22	8.02	10.52	10.52	10.52	10.57
Na20	5.94	5.40	4.91	5.26	4.91	5.02
K20	3.44	3.11	2.33	2.06	2.33	2.46
P205	0.86	0.58	1.04	0.87	1.04	0.87
r^2	.5515		.7024		.0598	

	MODEL #13	
	OBS	CALC
SiO2	41.86	42.01
TiO2	4.32	4.27
Al203	16.38	16.20
FeO*	10.31	10.45
MgO	0.15	0.16
MgO	10.89	10.72
CaO	12.23	11.96
Na20	2.30	2.44
K20	1.56	1.49
P205	0.00	0.02
r^2	.2115	

Model #7 = K1 + hbl - cpx = TM-9-59
Model #8 = K1 + hbl - (cpx + ol) = TM-9-59
Model #9 = K1 + hbl - (cpx + ol + timag) = TM-9-59
Model #10 = TM-9-63 + hbl -(cpx + ol + timag) = V
Model #11 = 68C3 + hbl + cpx - (ol + phlog) = 53C1
Model #12 = 68C3 + cpx + timag - (hbl + ol) = 53C1
Model #13 = TM-9-63N + hbl + phlog - Na cpx = TM-9-64N

different lava flows from the same volcanic center. Flows within each of the three main third period centers give excellent fits for fractionation models using the observed phenocryst/megacryst assemblage contained in these flows.

Models 1 through 4 show different combinations of possible fractionating phases for deriving sample D_4 from sample D_1. These samples were collected from a sequence of flows which emanate from the large third period cone just northeast of Demir Kopru Baraj Golu. The combinations of D_1-hbl, D_1-(hbl+cpx), D_1-(hbl+cpx+ol), and D_1-(hbl+cpx+ol+timag) all result in excellent fits producing the daughter "liquid" D_4. The best fit is obtained by fractionating hornblende, clinopyroxene, olivine, and titanomagnetite. This is also the most appealing model because these phases are present in the basalts in roughly similar proportions to the model (number 4). Approximately 4% crystallization is necessary to derive D_4 from D_1. Separation of these same phases provides a good fit for deriving TM-9-62, scoria from a small parasite cone of Kara Devit, from TM-9-63, a sample of scoriaceous lava from the main cone of Kara Devit. In this case 7.9% crystallization of TM-9-63 is required (model 5).

Models 6 through 9 attempt to relate lave K_1 to scoria TM-9-59, both from the kula Devit third period cone. Interestingly, all four models necessitate the addition of hornblende to derive sample TM-9-59 from K_1. Addition of hornblende alone, model 6, cannot adequately account for the major element variation, and neither can hornblende-

clinopyroxene (model 7). Addition of 13% hornblende coupled with 7.2% fractionation of clinopyroxene + olivine + titanomagnetite (model 9) provides a relatively good fit. Addition of hornblende is also necessary in deriving sample V, another parasitic cone of Kara Devit, from TM-9-63 (model 10). Assimilation of hornblende by at least some of the Kula magmas is supported by petrographic evidence in V, 23L and K$_1$, where more than one generation of hornblende crystals is evident. Large, partially resorbed or altered hornblendes can be are observed coexisting with fresh, small euhedral hornblende grains, implying addition of the resorbed hornblende to the magma prior to the appearance of hornblende on the liquidus.

Although fractionation processes, along with hornblende assimilation, seem adequate in accounting for major element variations within the third period volcanic rocks, neither intra-cone nor inter-cone chemical variations of second and first period volcanic rocks could be successfully modelled using observed phenocryst or megacryst phases. Low residuals invariably required geologically unrealistic addition and/or subtraction of phases. Models 11 and 12 derive sample 53C$_1$ from sample 68C$_3$, two different second period cones. Although residuals are less than one, a model which necessitates the addition of hornblende and subtraction of phlogopite seems worthy of great skepticism (model 11), and there is no petrographic evidence of clinopyroxene and titanomagnetite addition in 53C$_1$ (model 12), despite the

spectacularly low residual value.

Likewise, attempts to model derivation of TM-9-67I, a first period sample with Mg number = 60 from TM-9-57, a first period sample with Mg number = 65, result in lowest residuals greater than one, with one model requiring the addition of large amounts of both hornblende and anorthoclase.

A major problem in trying to model the major element chemistry of second and first period volcanic rocks using fractionation models, is the inability of any reasonable model to explain variations in the K_2O, Na_2O, and P_2O_5 contents of the lavas. This problem is evident in comparing the major element chemistry of samples $68C_2$ and $68C_3$. These two basanites were collected from the same volcanic center, and both samples contain only small phenocrysts of olivine and clinopyroxene. They both have Mg nubmers of 66 and relatively similar major element compositions, with the exception that $68C_3$ contains 2.66 wt% K_2O, while $68C_2$ contains only 1.04 wt% K_2O. No fractionation models could successfully relate the two samples, therefore other processes must be hypothesized to explain these variations. None of the ultramafic nodules could be related to the Kula lavas by fractionation modelling. The enriched nature of the nodules had suggested that they might be samples of the Kula magmas trapped at varying pressures and temperatures. It was, however, possible to derive TM-9-63N from TM-9-64N by subtraction of hornblende and addition of clinopyroxene. Alternatively TM-9-64N can be derived from TM-9-63N by

subtraction of clinopyroxene and addition of hornblende (indicative of a metasomatic enrichment event? - model 13). Inability to model nodule-lava pairs may indicate any of the following:

1. The nodules are accidental inclusions genetically unrelated to the Kula basalts.

2. Nodule-lava pairs may be related by an untried fractionation model.

3. The nodules may be cumulates related to the Kula lavas, which contain a large percentage of former intercumulate liquid.

4. The nodules may represent cumulates or conduit platings which have experienced a metasomatic subsequent to their initial crystallization.

5. The nodules may represent the product of small percentages of partial melting of garnet or spinel lherzolite present as a network of veins in the mantle source region of the Kula basalts.

Trace element abundances were evaluated using a Rayleigh fractionation model, $C_L/C_O = F^{(D-1)}$, to see if major element fractionation models could account for trace element concentrations. <u>Table 17</u> illustrates the measured and calculated trace element concentrations for Rb, Sr, K, Ni and Cr for major element fractionation models 4 and 5 respectively. The proportions of crystallizing phases were used to calculate bulk distribution coefficients. Mineral/liquid distribution coefficients for hornblende, .pn

Table 17. Rayleigh fractionation models: comparison of observed and calculated trace element abundances for Models 4 and 5.

	Model #4				Model #5	
Element	Dla	MEAS. D4	CALC. D4	TM-9-63	MEAS. TM-9-62	CALC. TM-9-62
Rb	73.7	74.5	76.1	80.7	82.3	87.6
Sr	934.9	954.8	962.2	877.6	840.0	939.4
K*	2.79	2.73	2.85	2.55	2.68	2.72
Ni	47.2	51.9	42.9	68.8	55.1	54.6
Cr	35.7	42.3	21.2	60.4	63.3	20.1
		F = .962			F = .921	

* All concentrations in ppm except K, given in weight percent.

clinopyroxene and olivine are from Arth (1976) for Rb, Sr, and K, and from Cox et al. (1979) for Ni and Cr. Magnetite/liquid distribution coefficients are from Lindstrom (1976) as reported in Irving (1978).

A comparison of the tables indicates serious discrepancies between measured and calculated trace element abundances for certain elements. Calculated abundances of the compatible elements Ni and Cr in model 4 decrease, as would be expected in fractionation of ferromagnesian phases. Measured abundances, however, show an increase in Ni and Cr in D_4, relative to the hypothesized parental composition D_1, along with increases in the incompatible elements Rb and Sr. Model 5 shows the same problem with Cr concentration, and Sr in the measured samples decreases in the daughter sample TM-9-62, when calculation suggests that Sr concentrations should increase.

The cause of these discrepancies is not immediately apparent. Even if mineral/melt distribution coefficients are not specifically appropriate to the Kula mineral and melt compositions, experimental data in all known literature suggests that for the phases fractionated in the major element models, trace elements should vary in the direction of the calculated values. It may be possible that although the residuals are extremely small, and agree with petrographic observation, an incorrect combination of fractionating phases has been modelled. This is somewhat unlikely, as a large number of petrographically reasonable

variations were tested. In model 5 the depletion of Sr in the daughter magma suggests removal of a phase with a high mineral/melt distribution coefficient for strontium, for example, plagioclase or apatite. However, rare earth element patterns for D_1 and D_4 show no suggestion of a negative europium anomaly that would be present if significant plagioclase fractionation had taken place. In fact all of these patterns suggest that D_4, with lower total REE concentrations, could have generated D_1 by fractionation, opposite to relations derived by major element modelling. Lastly, Watson's experimental work on basic magmas suggests that apatite fractionation could not occur.

Other possible explanations involve more complex hypotheses of magma evolution, source heterogeneities, and/or magma mixing.

In conclusion, although fractionation of observed phenocryst and megacryst phases can adequately account for major element variation in flows with similar alkali content (but not flows with substantially different alkali content), calculated trace element abundances differ significantly from measured abundances, evidence that fractionation processes alone cannot explain the chemical variations in the Kula lavas.

Magma Mixing or Assimilation

The inability to successfully model both major and trace element data by fractionation models is not surprising when petrographic observations are considered. In every period of

activity, abrupt changes in clinopyroxene phenocryst composition are common, with cores of iron-rich sodian augite or highly aluminous salite or diopside mantled with titaniferous augite. Complex zoning is a common feature. Iron-rich clinopyroxenes mantled by titanaugite in basanitic lavas have been reported from eastern Australia by Wilkerson (1975), France (Wass, 1979), and Tahiti (Peter Robinson, personal communication, 1981). Wass (1979) suggests that these pyroxenes represent a high pressure differentiation trend, and that the pyroxenes are cognate to their enclosing magma. Crystallization of magnetite at low pressure, or spineliferous magnetite at high pressure was invoked to explain the high magnesium content of the mantling titan-augite. Crystallization of titanomagnetite could adequately explain variations in Mg as well as Ti, Al and Si in the Kula quench clinopyroxenes, but high vanadium contents in the Kula lavas do not indicate significant crystallization of spinel-iferous magnetite at depth. Oxide inclusions are typically absent from the phenocryst phases, with the exception of sieve-textured cores, where the formation of oxides may be due to depressurization effects rather than a feature of primary crystallization from a melt. Although the Kula Fe-rich clinopyroxenes may be a high pressure phase, it may be possible that they represent crystals from an evolved magma, perhaps ponded at the base of the crust, which mixed with a more primitive magma pulse prior to eruption. The often rounded or embayed appearance of the Fe-rich core (Fig. 48)
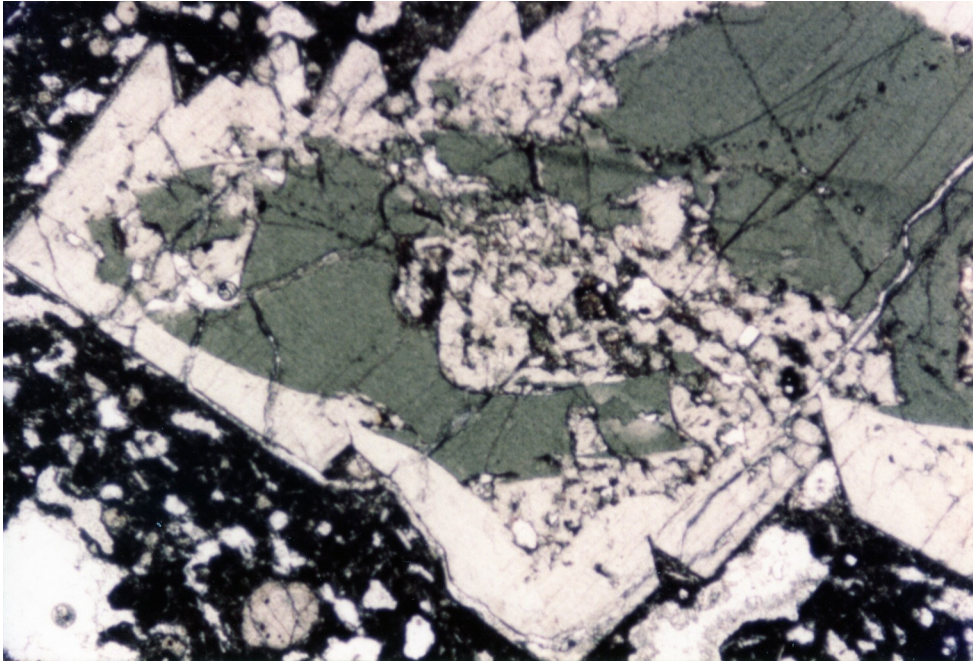
Figure 48. Sodian cored titanaugite from second period
cone 68C. The embayed nature of the sodian core suggests
thermal and/or chemical disequilibruim of the core in the
Kula magmas.

suggests conditions of disequilibrium "stewing" of a grain in a more primitive (or higher temperature) liquid, rather than armoring of a euhedral crystal with material of different composition, which might be expected if the mechanism Wass suggests is operative (although this type of overgrowth is also present in the Kula clinopyroxenes). Similar relationships can be observed in kaersutite phenocrysts. Cores or zones of kaersutite phenocrysts (typically the larger ones) are characterized by highly iron-enriched compositions, mantled by more magnesium-rich rims.

In addition to these petrographic observations, the consistent requirement of phase addition for low residual fractionation models (see models 6-12; many models not included in this text also required significant addition of material) suggest that processes such as magma mixing or assimilation may be important.

If magma mixing is responsible for chemical variations in the Kula suite, it should be possible to test the hypothesis by the use of mixing equations (Langmuir et al., 1978). One test for the applicability of this method is shown in Figure 49. Element-element variation plots, which for mixing relationships should be linear, are approximately so; but most plots show significant scatter (greater than analytical uncertainty). Individual sample also do not maintain the same relative relationship to each other, a requirement of any mixing model. Thus, the data do not seem to be consistent with a mixing model according to model
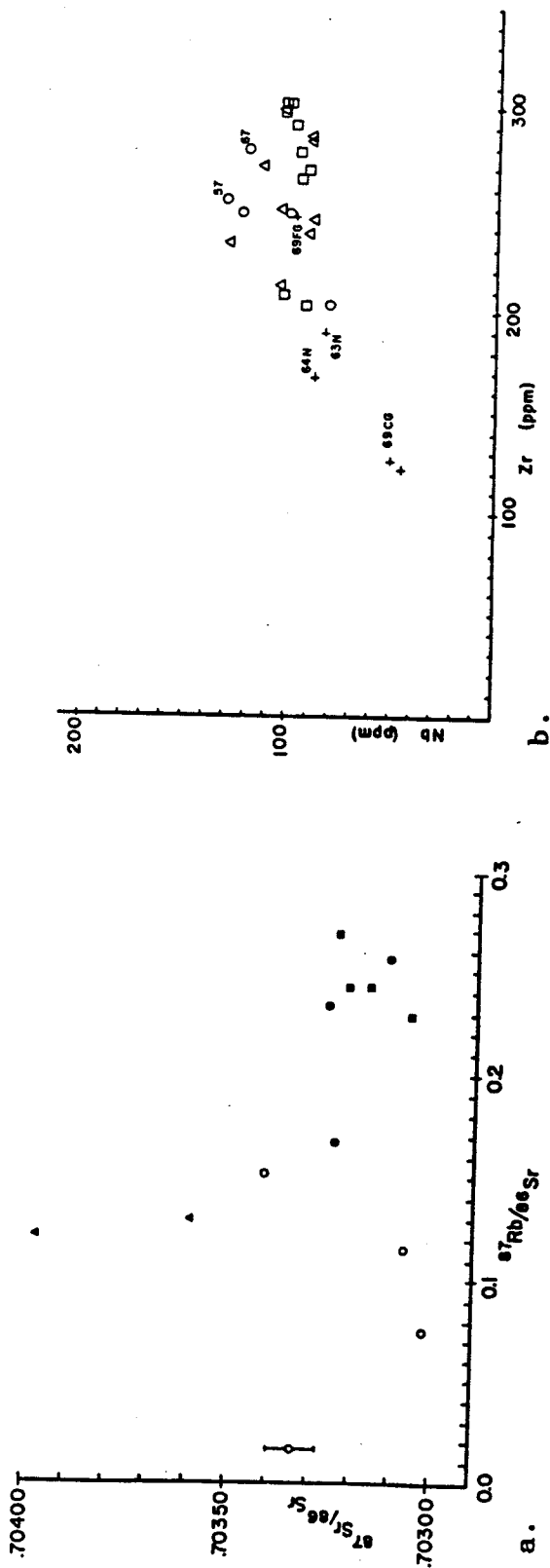
Figure 49a-c. Ratio/ratio and element/element/element trace element varation diagrams for Kula lavas and nodules. The large amount of scatter, nonlinear nature of some of the diagrams and individual samples that do not always maintain the same relative relationship with respect to each other suggests either that mixing is not an important process in the genesis of the Kula suite, or that mixing relations are obscured by the effects of other processes. 49b.&c.: 1st period=open circles, 2nd period=triangles, 3rd period=squares, nodules=crosses. Filled circles=Al mortar duplicate analyses. 49a.:filled circles=1st period, triangles= 2nd period, squares=3rd period, nodules=open circles.
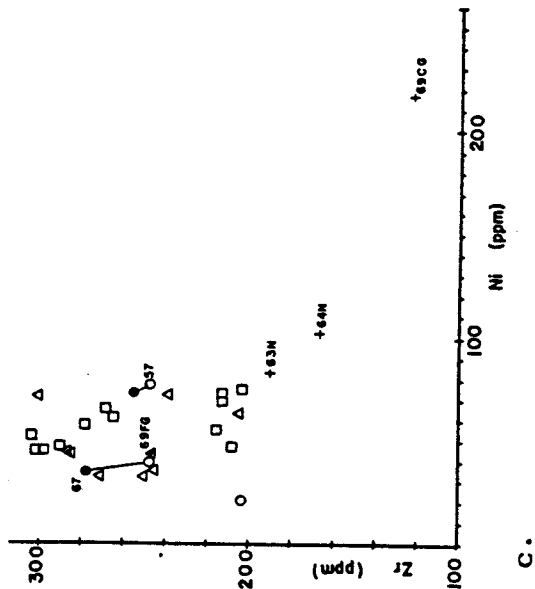
requirements (Langmuir et al., 1978). These authors note, however, that alkali basalts from Iceland and the Reykjanes ridge consistently fell off mixing curves, and that they consider source heterogeneity to be a preferable model for these magmas.

Assimilation of earlier generated Kula magmas, crystallized within a network of conduits, by later magmas might produce the observed petrographic features within the suite. Although not modelled in a quantitative manner, the following features suggest that some assimilation has taken place:

1. In certain third period samples, large unzoned megacrysts of kaersutite partially broken down to an assemblage of fine-grained anhydrous phases coexisting with zoned, euhedral and unaltered phenocrysts and microphenocrysts of kaersutite.

2. In all periods of activity, iron-rich rounded clinopyroxene cores mantled by titaniferous augite occur in the lavas. This feature could result from assimilation as well as from magma mixing.

3. Olivine, clinopyroxene and kaersutite grains are often mechanically broken. Some grains show severe embayments on one side, with the rest of the grain remaining perfectly euhedral. This could suggest initial assimilation, followed by ripping up of larger clots, and subsequent disaggregation of clots in the host magma.

4. Megacrysts of clinopyroxene and/or kaersutite are

common inclusions in the lavas. The composition of the megacrysts is the same as phenocrysts phases, but the megacrysts commonly have textures suggesting that they have undergone thermal metamorphism (Fig. 50).

5.   Kaersutite or ferroan pargasite megacrysts, particularly in second period lavas, commonly contain large apatite laths. Phosphorus contents in the host magma are too low (Watson, in press) for apatite saturation to have occurred, therefore the kaersutites must be foreign to their host magma.

6.   Least-squared fractionation models for major elements often require addition of phases to produce low residuals.

7.   Trace element abundances calculated for low residual subtraction models are not in accord with measured abundances.

It must be noted, however, that even large amounts of assimilation cannot account for the variation in K_2O and Na_2O in first and second period lavas. Assimilation by itself will also not explain isotopic variations in rocks of so young an age. Therefore, these differences are most likely reflections of source rock heterogeneity, although assimilation might be responsible for much of the scatter in trace element variation diagrams.

Paragenesis and Source of the Kula Volcanic Rocks

Paragenesis of alkali-rich basalts has long been a subject of active controversy among igneous petrologists; from the limestone assimilation hypothesis of Daly (1910)
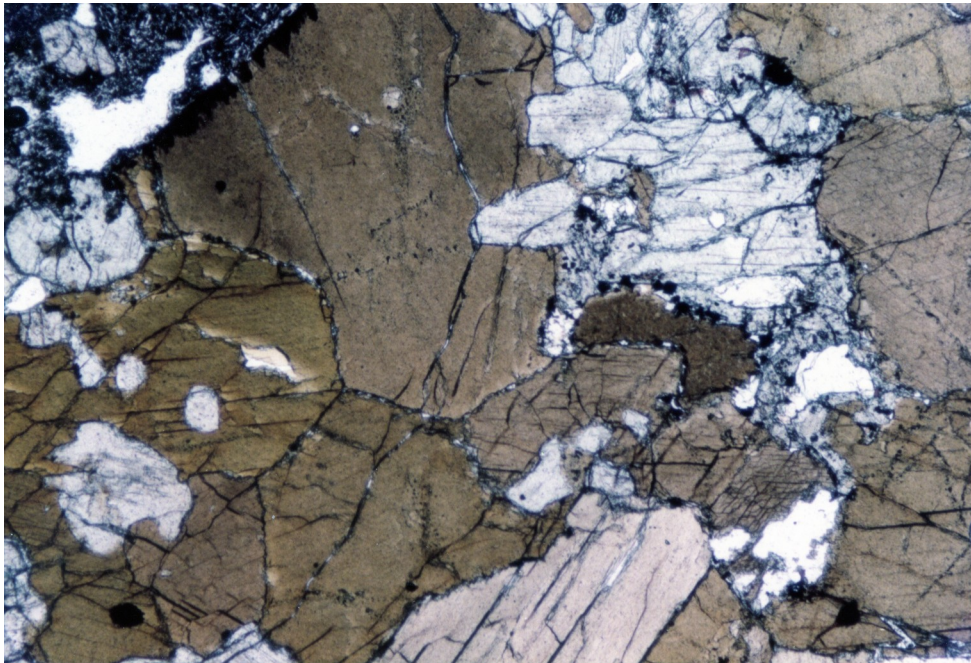
Figure 50.   Titanaugite-kaersutite megacryst
(megalith?) inclusion in second period lava 68C3.
The margin of the megacryst with the enclosing lava
can be seen in the top left hand corner of the photo.
In many places 120 degree grain boundaries in the
kaersutite grains suggest that the megacryst has under-
gone thermal metamorphism.

versus Bowen's fractional crystallation models (1928), to more recent models largely dominated by partial melting and fractionation modelling. Most of these models postulate a mantle origin for the parental magmas. Green and Ringwood (1967) showed that approximately 15% partial melting of a hypothetical upper mantle composition, "pyrolite," could account for the major element chemistry of an alkali-rich basalt, but not the abundances of incompatible trace elements. Green (1971), invoked "wall rock reaction" as a process by which to enrich selectively incompatible elements in magmas. Other workers used natural compositions as experimental material. Griffin and Murthy (1969) observed that partial melts of anhydrous lherzolites, common xenoliths in alkalic basalts, could account for major but not trace element abundances of basalts. These authors and others (e.g., Oxburgh, 1964) hypothesized the existence of minor phases in the source, such as amphibole or mica, enriched in necessary minor and trace elements.

Kay and Gast (1973) were able to successfully model both major and trace element chemistry of highly potassic basalts, nephelinites and alkali basalts without resorting to a minor phase or wall rock reaction argument by small amounts (.5 - 2%) of partial melting of hydrous garnet peridotite that contained two to five times chondritic abundance of REE. Although this model can successfully account for the chemical character of alkali-rich basalts, a number of authors have questioned the ability of such small percentages of partial

melt to segregate from the parent rock. Yoder (1978) maintains that small stress differences will result in magma segregation, but more recent studies by experimental structural geologists (Van der Molen and Patterson, 1979) on partially melted garnite suggests that in a deforming substance, liquids tend to remain along grain boundaries for low melt fractions.

An alternative to low percentages of partial melting is partial melting of an upper mantle source enriched in incompatible elements. A number of recent hypotheses require some sort of enrichment event, or metasomatism prior to or simultaneous with generation of alkalic magmas. Lloyd and Bailey (1975) made an impressive argument for light element enrichment of the source in explaining regional uplift, petrographic features of ultramafic inclusions in the lavas and chemical characteristics of the highly potassic volcanics of the East African Rift and sodi-potassic rocks of the Eifel volcanic field in Germany. Evidence supporting source enrichment of alkali-rich magmas has steadily accumulated during the past decade (see for example Best, 1974; Frey and Green, 1974; Francis, 1976; Boettcher et al., 1977; Frey et al., 1978; Boettcher and O'Neil, 1980; Menzies and Murthy, 1980a,b,c).

An enriched mantle source can explain the LIL enriched nature of alkali-rich basalts without recourse to prohibitively small percentages of partial melt at variance with the sometimes large quantities of lava erupted

(Williams, 1970, 1972; Lippard, 1973), and with the possible difficulty of magma segregation. Metasomatism could also provide an explanation for the texture and mineralogy of hydrous ultramafic nodules commonly enclosed in the basalts. Numerous documentations of mantle source heterogenity have been made for various basalt types (e.g., Schilling, 1973; O'Nions et al., 1976; Langmuir et al., 1978; Frey et al., 1978; and others); where alkaline magmatism is concerned, heterogeneity is predominantly related to the presence of a fluid or melt phase which produces patchy distribution of enriched metasomatized mantle.

Enrichment of the mantle source is envisioned by many authors (Lloyd and Bailey, 1975; Sun and Hanson, 1975; Frey et al., 1978; Menzies and Murthy, 1980b; Boettcher and O'Neil, 1980; and others) to be either a fluid or melt phase originating in or below the LVZ. Most of these authors suggest the enrichment event to be recent in relation to magma production (but see Sun and Hanson, 1975); this is supported by isotopic evidence (Menzies and Murthy, 1980b). Generation of these mobile fluids or small partial melts is a totally reasonable process if the regional tectonic environment is considered. Bailey (1974, 1977) and Lloyd (1981) have pointed out the connection between continental rifting and alkaline magma generation; thinning and extension of the crust prior to rifting, or rifting alone will produce a depressurization of the underlying mantle, which is likely to result in the release and migration of volatile phases.

The Kula samples give abundant indication that they are derived from a recently enriched source region. High concentrations of incompatible trace elements, light rare earth elements, Na_2O, K_2O and P_2O_5 characterize both lavas and ultramafic nodules (although generally to a lesser extent in the ultramafic nodules). High Sr abundances are non-radiogenic, as shown by the low by variable $^{87}Sr/^{86}Sr$ ratios. A hydrous and/or volatile-rich phase, kaersutite, occurs in abundance as phenocrysts and megacrysts in the lavas, and is the dominant nodule phase, coexisting with apatite and micas. Samples $68C_3$, $68C_2$ and TM-9-57 contain no hornblende and have

high Mg numbers (67-66), which make them candidates for possible primary magmas, yet have incompatible element concentrations similar to hornblende-rich lavas (whch may also have high Mg numbers), suggesting that fractionation may not be the process relating these lavas.

Trace element variation diagrams (Fig. 51, after Sun and Hanson, 1975) illustrate similarities between the Kula basalts and primary alkali basalts and nephelinites from Ross Island, Antarctica and from oceanic islands. Although the Kula suite contains samples that are undoubtably not primary, Sun and Hanson (1975) point out that incompatible element ratios should not change significantly for fractionation of ferromagnesian phases, thus there is some justification for comparison. The remarkable similarities of the Kula data with the oceanic island data is evidence that the Kula lavas are derived from a geologically recently enriched source similar to that of most oceanic alkali-rich basalts (not crustally contaminated).

Further evidence for both an enriched source and for source heterogeneity comes from the work of Pearce and Norry (1979). These authors concluded from experimental and theoretical study of high field strength elements (Ti, Zr, Y and Nb) that source heterogeneity and processes such as fluid transfer are responsible for variation in the Zr/Nb and Zr/Y ratios of different basalts. Figure 52 shows Kula Zr/Nb and Zr/Y ratios plotted against Zr in ppm, along with the data of Pearce and Norry for various basalt suites. The similarity
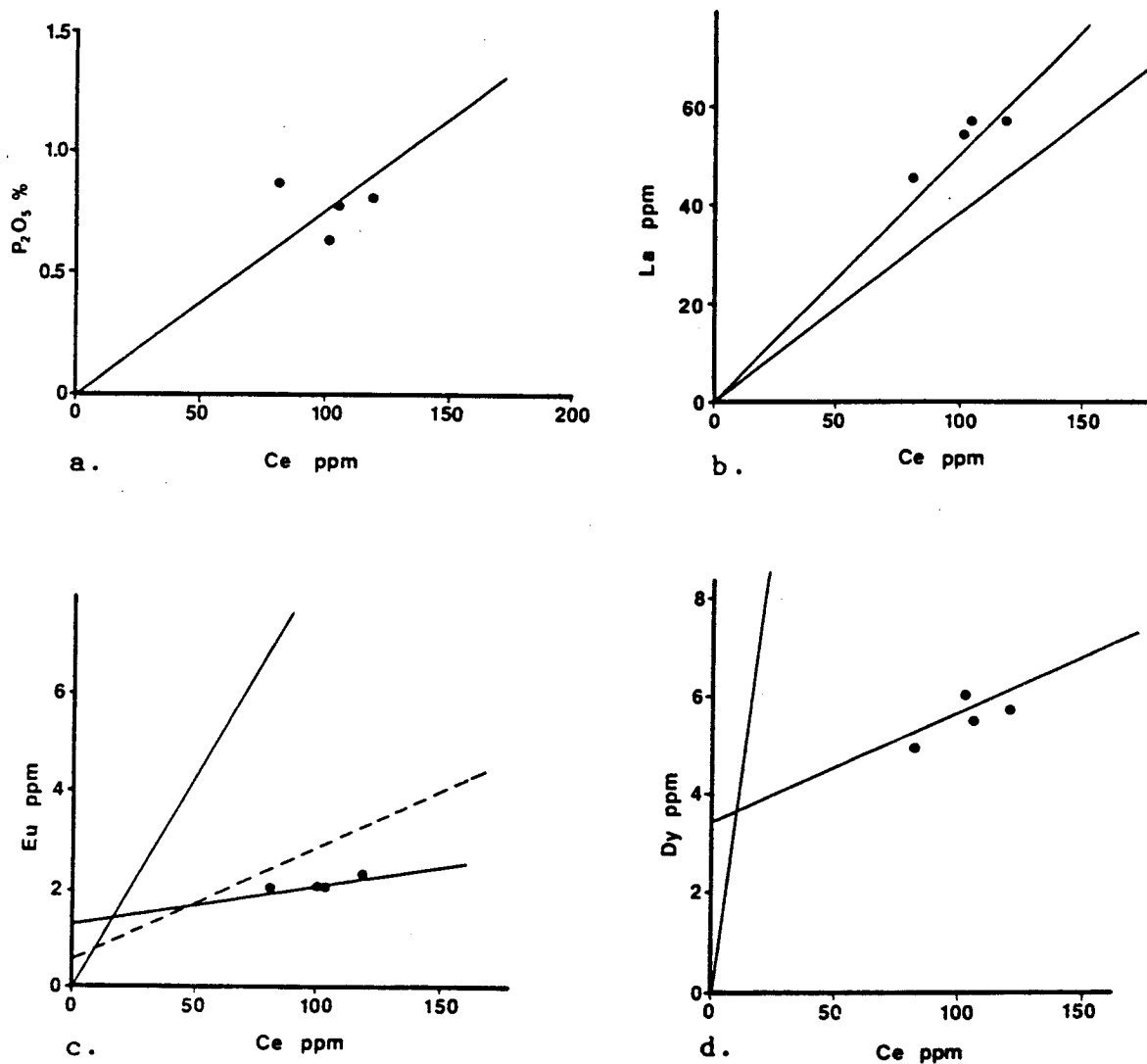
Figure 51a-d. Trace element variation diagrams after Sun and Hanson, 1975, with available Kula data for comparison. Although the sparse amount of data allows no earth-shattering conclusions, the volcanics seem to exhibit the same characteristics as suites of primary alkali basalts and nephelinites from oceanic islands. The collinearity of the La vs Ce data, which lie about a line extending through the origin suggests that these data are controlled exclusively by the extent of partial melting of a source with a La/Ce ratio slightly greater than chondritic. The other three plots either show no clear relation (P205 vs Ce), or lie about a line which does not intersect the origin, suggesting that D for Eu and Dy approaches or exceeds F for at least part of the partial melting sequence. Analyses are from lavas D1, D2, D4 and D5.

e.

f.
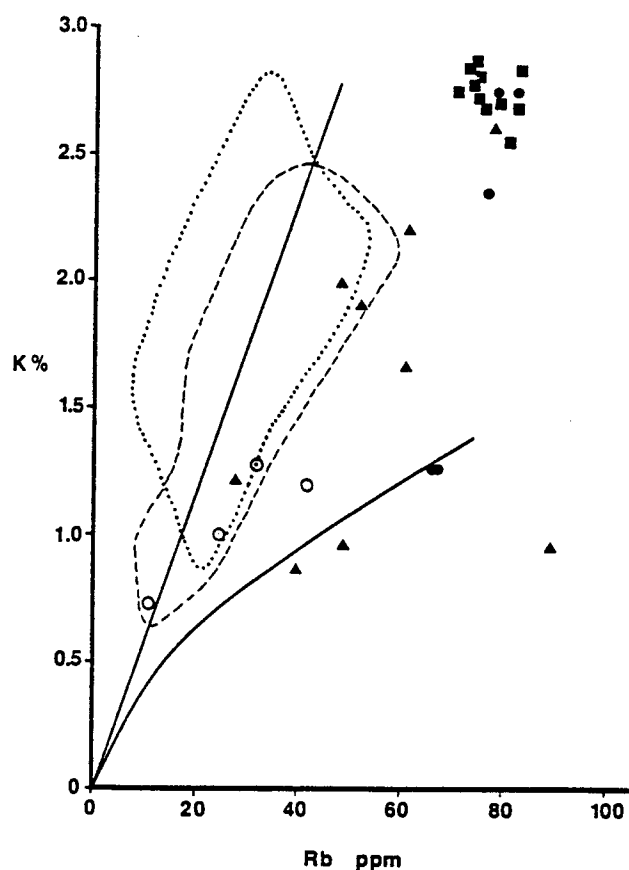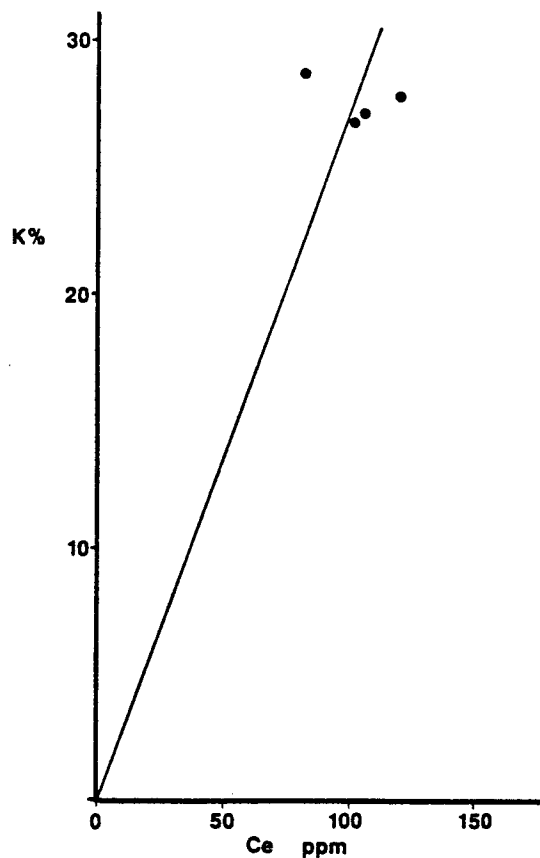
Figure 51e-f. K% vs Rb and Ce after Sun and Hanson, 1975,
with Kula data for comparison. Only three of the second
period volcanic samples plot in the primary alkali basalt
or nephelinite fields in Fig. 51e. This is not especially
surprising, since as mentioned in the text, most of the Kula
samples are probably not primary compositions. The lower
K/Rb of the Kula suite suggests that amphibole, not
phlogopite is present in the mantle residue. Also intriguing
is the position of four samples along the curve representing
a mantle source with 4% hornblende. 1st period=filled
circles, 2nd period=triangles, 3rd period=squares, nodules
=open circles.
Fig. 51f has little data, but the scatter of values may
suggest the presence of a K bearing phase in the residum.
Analyses are from lavas D1, D2, D4 and D5.
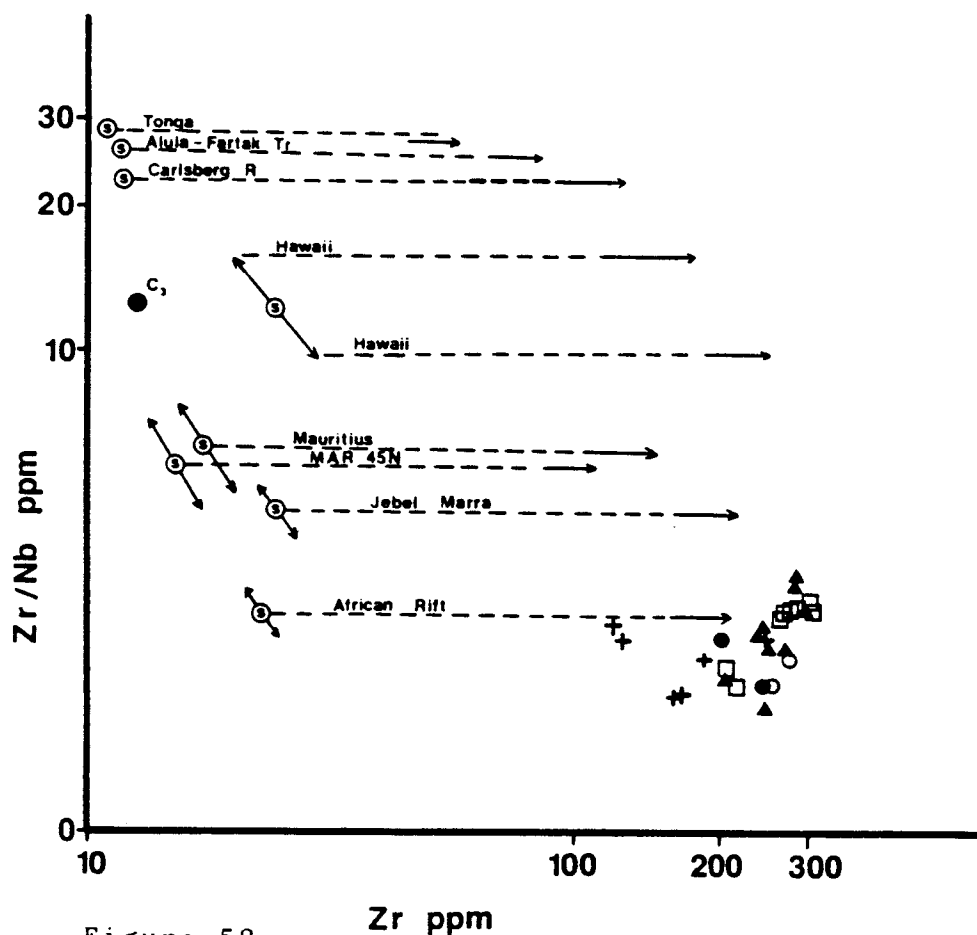
Figure 52a.

Figure 52a & b. Pearce and Norry's (1979) genetic interpretation of trace element variation in volcanic rock suites with Kula data superimposed. Viewed in light of their interpretations, the Kula volcanic suite data indicates that it may have been derived from a heterogeneous mantle source that has undergone an enrichment event. The position of the nodule analyses relative to the volcanic analyses suggests that they are related to the lavas, perhaps samples of less fractionated melts. 52a = Zr/Nb vs. Zr, 52b = Zr/Y vs Zr.
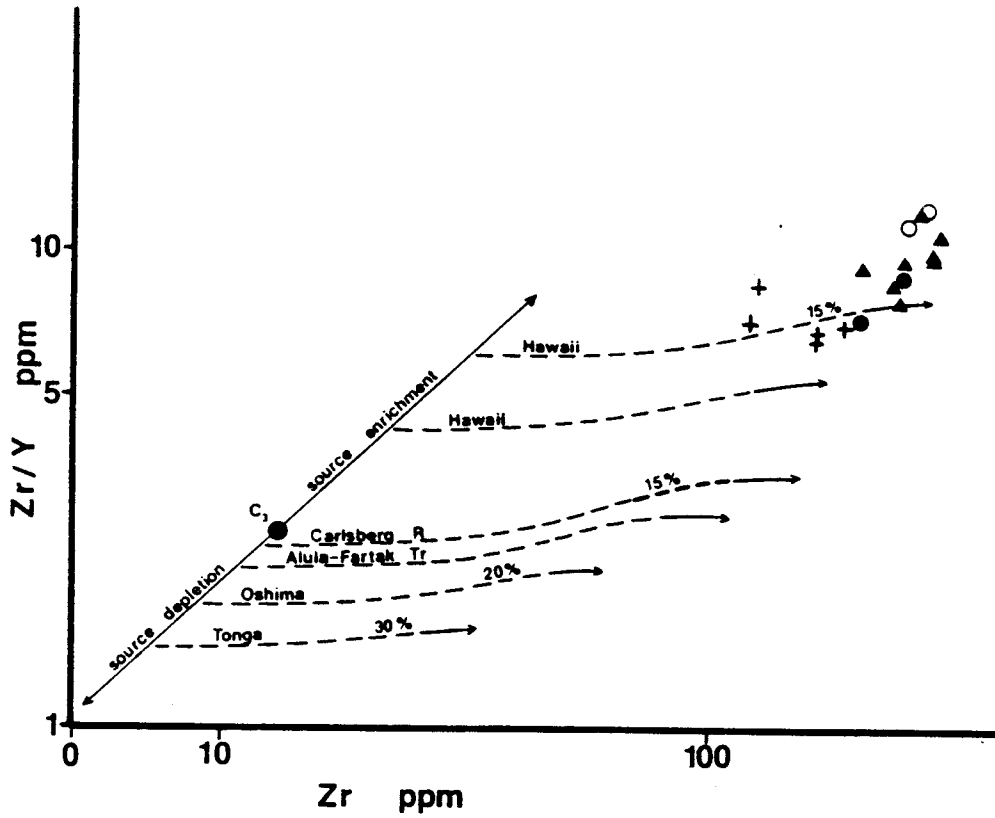
Figure 52b.

--- partial melting trend (and estimated degree of melting)
—·— open system fractionation
—— closed system fractionation
● C3 chondrite composition
   estimated source composition ranges (for Zr/Nb)

○● First period lavas ○ (Al ball mill) ● (W ball mill)
△ Second period lavas
□ Third period lavas
+ Nodules

in Zr/Nb versus Zr of Kula lavas and lavas of the East African Rift is not surprising. As was previously mentioned, variations in incompatible element ratios may be indicative of source region heterogeneities. Variations in the Zr content are indicative of either partial melting or fractional crystallization processes (Pearce and Norry, 1979). Kula basalt trends indicate that some of the suite variation might be best explained by source heterogeneity. The ultramafic nodules appear to have been derived from an identical source as the basalts, and Zr data suggest that they might be related to the basalts by fractionation processes, although closed system fractionation models did not indicate this relationship. It is interesting to note that Pearce and Norry maintain that high field strength elements are not transported in aqueous fluids (thus are useful in the study of weathered or metamorphosed igneous rocks), yet they resort to some mechanism of fluid transport to account for variation in Zr/Nb ratios, as well as for the alkaline undersaturated nature of magmas with extreme Zr/Nb ratios (both low and high). If these elements are not susceptable to fluid transport, then high concentrations of Nb and Zr in primitive magmas may indicate the presence of hydrous mobile partial melts instead of, or accompanying, fluids in the enriched source.

In an average unmetasomatized olivine dominated mantle source, with Ni abundances of approximately 2000-2500 ppm (Green and Ringwood, 1967; Cox et al., 1979) and a Ni bulk

distribution coefficient of 10, for a wide range of partial melts the primary Ni content of the magma will be > 200 ppm (Cox et al., 1979). Ni abundances this high are only found in nodule TM-9-69CG. To model Kula lavas as primary melts of this average mantle composition, Ni distribution coefficents would have to be in excess of any experimentally determined value (Irving, 1978; Banner, 1981). This implies that if the Kula magmas were derived from this source, none of them are near-primary.

A number of authors have identified primary alkali-rich magmas that have Ni abundances of approximately 100 ppm (e.g., Kesson, 1973). Experimental studies by Leeman (1973) also show a low permissible primary Ni content of 90 ppm for partial melts of lherzolite. The presence in the source of a variable percentage of enriched amphibole and/or phlogopite-bearing veins, perhaps together with metasomatized lherzolite resulting from mobile fluids filter pressed from the amphibole-rich veins (see Wilshire et al., 1980), could generate magmas with low concentrations of compatible elements such as Ni, Cr and Co. For this example, lavas such as TM-9-57, TM-9-70, $68C_2$ and $68C_3$ could represent near-primary liquid compositions. It is unfortunate that a model such as metasomatic enrichment, which seems to explain so much, has at present so few quantitatively testable constraints.

Origin of the Nodules

Petrographic observation, mineral chemistry, whole rock

chemistry, and isotopic data all suggest that TM-9-63N, TM-9-64N and TM-9-69FG are of igneous origin and are cognate to the Kula basalts. The enriched nature of these nodules suggests an origin as either samples of trapped magma, orthocumulates, or conduit-linings, that were broken up and incorporated in later eruptions. It is also possible that the enrichment is a late feature, resulting from processes similar to those that caused the enrichment of the source. The presence of oikocrystic plagioclase in TM-9-63N suggests that this nodule originated in an environment shallower and/or less volatile-rich than the plagioclase-free nodules. Rb and Sr abundances, when compared with the isotopic data, suggest that nodule TM-9-69FG (and possibly the others?) is depleted in Rb, possibly a result of fluid leaching. The fine-grained metamorphic textures of both TM-9-63N and TM-9-69FG indicate complex histories prior to their entrainment in the third period magmas.

TM-9-69CG has a mineral assemblage which differs from the other nodules because it contains olivine, its phase chemistry differs from both other nodules and the lavas but this nodule is also thought to be genetically related to the Kula magmas. Petrographic observations and whole rock chemistry suggest that this nodule, like the others, has an igneous origin. TM-9-69CG may represent a sample of high pressure orthocumulate of a Kula magma, a trapped sample of a primary Kula magma or a sample of an enriched hydrous basaltic vein in the mantle source region. I prefer the last

explanation, but further data (REE) are needed prior to evaluating these, or other, possibilities.

Model for Origin of the Magmas

The Kula lavas are believed to have been derived by partial melting of a source enriched in incompatible elements. This enrichment is believed to be a recent envent and a result of the regional post-middle Miocene extensional tectonic regime in western Anatolia (Dewey and Şengör, 1979; Şengör and Dyer, 1979). Crustal thinning resulted in depressurization of the subcontinental mantle and upward migration of incompatible element-enriched fluids or partial melts. Metasomatism of the Kula upper mantle source by these fluids and/or veining of the source with amphibole-and phlogopite-rich material (perhaps similar to nodule TM-9-69CG) must have occurred either simultaneously with, or shortly prior to, the partial melting event that generated the Kula basalts, because of the very low Sr isotopic ratios. Other authors (e.g., Menzies and Murthy, 1980a,b,c) have also argued for recent enrichment relative to magma generation based on isotopic data. Magma transport is envisioned to proceed along a propagating crack and conduit system as proposed by Spera (1980). Isotopic differences in essentially simultaneously erupting, crustally uncontaminated magmas, and the presence of both sodic and potassic trends in second period lavas, as well as other observations, suggest that any sort of large magma chamber under Kula is unlikely. Semi-isolated conduit systems better explain intra-period

variation by allowing preservation of local source heterogeneities. In this conduit system, both flow differentiation and assimilation may have been active processes. Dissolution of volatile phases at moderate to low pressure would act as the propellant for rapid transport of the magma to the surface. The highly vesicular nature of the lavas, abundant hydrous phenocryst phases, geomorphology of the flows (long and thin suggesting very low viscosity melts, thin and widespread first period plateau basalts), widespread ash deposits, and the abundance of angular crustal inclusions are evidence of both the volatile-rich and forceful nature of the eruption. Decompression melting (sieve texture), aluminous nature of the clinopyroxene (with a high proportion of Al^{VI}) and total lack of plagioclase phenocrysts (some calcic plagioclase megacrysts are probably related to the Kula magmas as crystallates of trapped magma under low pressure, < 10 kb) suggest rapid rise of the magma from subcrustal depth. The composition of the aluminous titaniferous augites is similar to experimentally produced high pressure clinopyroxenes (Green and Hibberson, 1970; Thompson, 1974), and suggests that the Kula clinopyroxenes may have crystallized at pressures of 14-20 km. These figures can be used as evidence of sub-crustal origin only, because of the uncertain effects of large concentrations of volatiles and bulk composition on clinopyroxene composition.

If nodule TM-9-69CG is representative of a recently enriched, hornblende-bearing source reservoir, this

constrains generation of partial melts to depths of less than 80 km (approximately 24 kb) from hornblende stability relations determined experimentally by Lambert and Wyllie (1968), although the metasomatizing fluids and/or hydrous melts may have been derived from substantially deeper (Boettcher and O'Neil, 1980; and others).

Relationship between Magmatism and Tectonics

Figure 53 shows the chemical character of volcanism as a function of time for dated Miocene to Recent volcanic rocks of western Anatolia. Early Miocene time was dominated by calc-alkaline volcanism; Burdigalian volcanic rocks change from dominantly andesitic in early Burdigalian to dacitic with aubundant tuffs and ignimbrites in late Burdigalian. Langhian is characterized by a hiatus in volcanic activity. When volcanism resumes in early Serravallian time, the chemistry of the lava has changed from silicic calc-alkalic to silicic alkalic (alkali rhyolites). From Serravalian to Recent, composition of the volcanic rocks has become progressively more basic and alkaline. In Figure 53 the Kula eruptions are represented by the last two squares. It is also evident from this Figure that post-Langhian volcanism has been less abundant (and more localized) than was early Miocene volcanism.

Variation in chemistry of the volcanic rocks closely parallels Miocene to Recent tectonic evolution as envisioned by Şengör and Yilmaz (1981). Subduction of the African plate under western Anatolia was responsible for the widespread

CHEMICAL CHARACTER OF NEOGENE TO RECENT VOLCANIC ROCKS OF WESTERN TURKEY

ALKALINE

CALC-ALKALINE

MIOCENE

PLIOCENE

22.5

AQUITANIAN

BURDIGALIAN

LANGHIAN | SERRAVALLIAN

TORTONIAN

MESSINIAN

5

1.8

0 m.y.b.p.
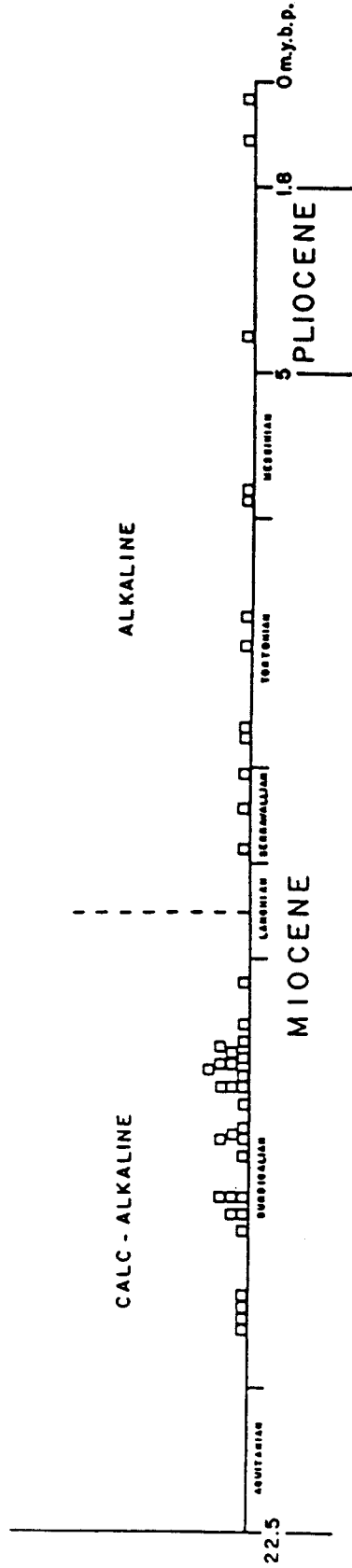
Figure 53. Dated Miocene-Recent volcanic rocks from western Anatolia. Dates and rock types taken from Ercan's compilation (unpublished M.T.A. report). The chemistry of the volcanism records the mid-Miocene transition from a compressional to an extensional tectonic environment within the Anatolian scholle.

Page 202 is missing from all copies of the submitted thesis; however no text material or figure appears to be absent, so this is probably just a pagination error.

andesitic volcanism of early Burdigalian time. The change of dominantly dacitic and ignimbrite eruptions may have been a result of continental crust input (J.F. Dewey, personal communication, 1980); not surprising, considering that this area was characterized at the time by an anomalously thick crust in north-south compression. The collision of the Arabian Platform with eastern Anatolia and Iran was immediately mirrored by a compositional change in western Anatolian volcanic rocks. An extensional environment replaced the prior compressional regime in western Anatolia as movement began along the north and east Anatolian transform faults. Magmas in this transitional period were most likely of highly complex origin, with both crust and mantle sources. Continued extension to the present time has created increasingly basic volcanism, with chemistry similar to some of the East African Rift volcanics (e.g., Brown and Carmichael, 1969). These young lavas seem to indicate derivation from an upper mantle source, probably a source enriched by metasomatic fluids or melts. Some of the fluids, or perhaps all of them, may have been derived from prior subduction. It is a bit surprising that such small and isolated centers of volcanic activity occur from late Miocene to Recent, considering the amount of extension proposed by Sengor (1978); however, the sub-continental mantle under the Kula region has had a long period of melt production. The amount of volcanism may be a direct function of available water to generate melts; therefore, volcanic activity would

have been more abundant during active subduction (or more rapid subduction), thus the more abundant early Miocene volcanism. Also, the development of the present horst and graben terrane, with lystric surfaced normal faults may have impeded magma migration through the crust. The occurrence of nearly all young volcanic centers and hot springs at the intersection of fault trends (usually faults with some strike-slip displacement) support this; these intersections may form the only avenue of escape for the magmas. Alternatively, the fault intersections may cause the concentration of sub-crustal mobile volatile phases, thereby creating a condusive site for both magma generation and transport through the crust.

This thesis presents a rough framework and generalized correlation supporting tectonic control of magmatism in western Anatolia. Although first-order relationships seem to support the models of tectonic evolution of the eastern Mediterranean region according to Şengör and his assorted co-authors, further detailed petrologic and field studies of the western Anatolian lavas are needed, which should provide important insights into progressive evolution of the sub-continental mantle, the role of the continental crust in magma genesis and the extent of mantle-crust interaction during production of magmas associated with orogenesis.

REFERENCES

Aoki, K-I and Kushiro, I., 1968, Some clinopyroxenes from
    ultramafic inclusions in Dreiser Weiher, Eifel. Contrib.
    Mineral. Petrol, v. 18, p. 326-337.

Arth, J.G., 1976, Behavior of trace elements during magmatic
    processes: a summary of theoretical models and their
    applications. Jour. Res. U.S. Geol. Sur., v. 4, p. 41-47.

Bailey, D.K., 1974, Continental rifting and alkaline
    magmatism. In: The Alkaline Rocks, H. Sorensen (ed.), J.
    Wiley and Sons, New York, p.148-159.

Baker, I., 1969, Petrology of the volcanic rocks of Saint
    Helena island, South Atlantic. Geol. Soc. Amer. Bull., v.
    80, p. 1283-1310.

Baker, P.E., Gass, I.G., Harris, P.G., and LeMaitre, R.W.,
    1964, The vulcanological report of the Royal Society
    expedition to Tristan da Cunha, 1962. Phil. Trans. R.
    Society London, A, v. 256, p. 439-578.

Banner, J.L., 1981, Lolobau Island, New Britain: Petrology of an
    island arc volcanic complex. Unpubl. M.S. Thesis, State
    University of New York at Stony Brook, 134 p.

Best, M.G., 1940, Kaersutite-peridotite inclusions and kindred
    megacrysts in basanitic lavas, Grand Canyon, Arizona. Contr.
    Mineral. Petrol., v. 27, p. 25-44.

Best, M.G., 1974, Mantle-derived amphibole within inclusions
    in alkalic- basaltic lavas. Jour. Geophys. Res., v. 79, p.
    2107-2113.

Binns, R.A., 1969, High-pressure megacrysts in basanitic
    lavas near Armidale, New South Wales. Amer. Jour. Sci., v.
    267-A, p. 33-49.

Binns, R.A., Duggan, M.B., and Wilkerson, J.F.G., 1970, High-
    pressure megacrysts in alkaline lavas from northeastern New
    South Wales, with chemical analyses by G.I.Z. Kalocsai. Amer.
    Jour. Sci., v. 269, p.132-168.

Boettcher, A.L. and O'Neil, J.R., 1980, Stable isotope,
    chemical and petrographic studies of high pressure amphiboles
    and micas: evidence for metasomatism in the mantle source
    regions of alkali basalts and kimberlites. Amer. Jour. Sci.,
    v. 280-A, p. 594-621.

Borsi, S., Ferrara, G., Innocenti, F., and Mazzuoli, 1973,
    Geochronology and petrology of Recent volcanics in the
    eastern Aegean Sea (West Anatolia and Lesvos Island). Bull.
    Volc., v.36, p. 473-496.

205

Bowen, N.L., 1928, The Evolution of the Igneous Rocks. Princeton University Press (1956 Dover ed.), 334 p.

Brinkmann, R., 1976, Geology of Turkey. Ferdinand Enke Verlag, Stuttgart, 158 p.

Brown, F.H. and Carmichael, I.S.E., 1969, Quaternary volcanoes of the Lake Rudolf region: 1. The basanite-tephrite series of the Korath range. Lithos, v. 2, p. 239-260.

Bryan, W.B., Finger, L.W., and Chayes, F., 1969, Estimating proportions in petrographic mixing equations by least-squares approximation. Science, v. 163, p. 926-297.

Buddington, A.F. and Lindsley, D.H., 1964, Iron-titanium oxide minerals and synthetic equivalents. Jour. Petrol., v. 5, p. 310-357.

Buerger, M.J., 1945, The genesis of twin crystals. Amer. Mineral., v.30, p. 469-482.

Carmichael, I.S.E. and Nicholls, J., 1967, Iron-titanium oxides and oxygen fugacities in volcanic rocks. Jour. Geophys. Res., v. 72, p. 4665-4687.

Carmichael, I.S.E., Turner, F.J., and Verhoogen, J., 1974, Igneous Petrology, McGraw-Hill, 739 p.

Cavet and Jaoul (1946), Unpublished M.T.A. Report. Ankara, Turkey.

Chinner, G.A. and Schairer, J.F., 1962, The join $Ca_3Al_2Si_3O_{12}$-$Mg_3Al_2Si_3O_{12}$ and its bearing on the system CaO-MgO-Al_2O_3-SiO_2 at atmospheric pressure. Amer. Jour. Sci., v. 260, p. 611-634.

Coombs, D.S. and Wilkerson, J.F.G., 1969, Lineages and fractionation trends in undersaturated volcanic rocks from the East Otago volcanic province (New Zealand) and related rocks. Jour. Petrol., v. 10, p.440-501.

Cox, K.G., Bell, J.D., and Pankhurst, R.J., 1979, The Interpretation of Igneous Rocks. George Allen and Unwin Ltd, London, 450 p.

Daly, R.A., 1910, Origin of the alkaline rocks. Geol. Soc. Amer. Bull., v. 21, p. 87-118.

Deer, W.A., Howie, R.A., and Zussman, J., 1966, An Introduction to the Rock-Forming Minerals. Longman Pub., London, 528 p.

Deer, W.A., Howie, R.A., and Zussman, J., 1978, Rock Forming Minerals, Vol. 2A: Single Chain Silicates (2nd Ed.). John Wiley and Sons, New York, 668 p.

Delaney, J.S., Smith, J.V., Carswell, D.A., and Dawson, J.B., 1980, Chemistry of micas from kimberlites and xenoliths - II. Primary-and secondary-textured micas from peridotite xenoliths. Geochim. Cosmochim. Acta, v. 44, p. 857-872.

Dewey, J.F., Pitman, W.C., III, Ryan, W.B.F., and Bonnin, J., 1973, Plate tectonics and the evolution of the Alpine System. Geol. Soc. Amer. Bull., v. 84, p. 3137-3180.

Dewey, J.F. and Şengör, A.M.C., 1979, Aegean and surrounding regions: Complex multiplate and continuum tectonics in a convergent zone. Geol. Soc. Amer. Bull., Pt. 1, v. 90, p. 84-92.

Dürr, S., 1975, Uber Alter und geotektonische Stellung des Menderes? Kristallins/SW-Anatolien und seine Aequivalente in der mittleren Aegaeis. Habilitations-Schrift, Marburge/Lahn, 107 p.

Dürr, S., Altherr, R., Keller, J., Okrusch, M., and Seidel, E., 1978, The median Aegean crystalline belt: Stratigraphy, structure, metamorphism, magmatism. In: Alps, Apennines, Hellenides, (eds.) H. Closs, D. Roeder and K. Schmidt; E. Schweizerbart'sche Verlagsbuchhandlung, Stuttgart, p. 455-476.

Ercan, T., Dincel, A., Metin, S., Turkecan, A., and Gunay, E., 1978, Usak Yoresindeki Neojen Havzalarinin Jeolojisi. Turkiye Jeoloji Kurumu Bulteni, v. 21, p. 97-106.

Erinç, S., 1955, Die morphologische entwicklungsstadien der Kucukmenderes-Masse: University of Istanbul Geographical Institute Reviews, No. 2, p. 93-95.

Erinç, S., 1970, Kula ve Adala arasinda genç volkan reliyefi. İstanbul Universitesi Cografya Enstitüsü Dergisi, v. 9, p. 7-31.

Evans, S.H., Jr. and Nash, W.P., 1979, Petrogenesis of xenolith-bearing basalts from SE Arizona. Amer. Mineral., v. 64, p. 249-267.

Faure, G., 1977, Principles of Isotope Geology, John Wiley and Sons, 464 p.

Faure, G., Bowman, J.R., Elliot, D., and Jones, L.M., 1974, Strontium isotope composition and petrogenesis of the Kirkpatrick basalt, Queen Alexandra Range, Antarctica. Contr. Mineral. Petrol., v. 48, p. 153-169.

Francis, D.M., 1976, The origin of amphibole in lherzolite xenoliths from Nunivak Island, Alaska. Jour. Petrol., v. 17, p. 357-378.

Frey, F.A. and Green, D.H., 1974, The mineralogy, geochemistry and origin of lherzolite inclusions in Victorian basanites. Geochim. Cosmochim. Acta, v. 38, p. 1023-1059.

Frey, F.A., Green, D.H., and Roy, S.D., 1978, Integrated models of basalt petrogenesis: A study of quartz tholeiites to olivine melilitites from southeastern Australia utilizing geochemical and experimental petrological data. Jour. Petrol., v. 19, Pt. 3, p. 463-513.

Garcia, M.O. and Jacobson, S.S., 1979, Crystal clots, amphibole fractionation and the evolution of calc-alkaline magmas. Contrib. Mineral. Petrol., v. 69, p. 319-327.

Green, D.H., 1971, Composition of basaltic magmas as indicators of conditions of origin: Application to oceanic volcanism. Roy. Soc. (London) Philos. Trans., v. 268, p. 707-722.

Green, D.H. and Hibberson, W., 1970, Experimental duplication of conditions of precipitation of high pressure phenocrysts in a basaltic magma. Phys. Earth Planet. Interiors, v. 3, p. 247-254.

Green, D.H. and Ringwood, A.E., 1967, The genesis of basaltic magmas. Contr. Mineral. Petrol., v. 15, p. 103-190.

Griffin, W. and Murthy, V.R., 1969, Distribution of K, Rb, Sr and Ba in some minerals relevant to basalt genesis. Geochim. Cosmochim. Acta, v. 33, p. 1389-1414.

Gutnic, M., Monod, O., Poisson, A., and Dumont, F.-D., 1979, Geologie des Taurides occidentales (Turquie). Mem. Soc. Geol. Fr., N.S., v. 58, 112 p.

Haggerty, S.E., 1978, Spinels in high pressure regimes. In: The Mantle Sample: Inclusions in Kimberlites and Other Volcanics, (eds.) F.R. Boyd and H.O.A. Meyer, Amer. Geophys. Union, p. 183-196.

Hamilton, W.J., 1842, Researches in Asia Minor, Pontus and Armenia. London.

Hamilton, W.J. and Strickland, H.E., 1841, On the geology of the western part of Asia Minor. Trans. Geol. Soc. London, Ser. VI, v. 2, 1.

Harker, A., 1954, Petrology for Students (8th Ed.). Cambridge University Press, 283 p.

Irving, A.J., 1974, Megacrysts from the Newer Basalts and other basaltic rocks of Southeastern Australia. Geol. Soc. Amer. Bull., v. 85, p. 1503-1514.

Irving, A.J., 1978, A review of experimental studies of crystal/liquid trace element partitioning.Geochim. Cosmochim. Acta, v. 42, p. 743-770.

Irving, A.J. and Green, D.H., 1976, Geochemistry and petro-genesis of the Newer Basalts of Victoria and South Australia. Geol. Soc. Australia Jour., v. 23, p. 45-66.

Kay, R.W. and Gast, P.W., 1973, The rare earth content and origin of alkali-rich basalts. Jour. Geol., v. 81, p. 653-682.

Kesson, S.E., 1973, The primary geochemstry of the Monaro alkaline volcanics, Southeastern Australia - evidence for upper mantle heterogeneity. Contr. Mineral. Petrol., v. 42, p. 93-108.

Ketin, I., 1959, Turkiye'nin orojenik gelismesi. Maden Tektik Arama Dergisi, v. 53, p. 78-86.

Ketin, I., 1966, Tectonic units of Anatolia. Bull. Mineral. Res. Expl.Inst. Turk., v. 66, p. 23-34.

Kuno, H., 1950, Petrology of Hakoko volcano and the adjacent areas. Geol. Soc. Amer. Bull., v. 61, p. 957-1020.

Kuno, H., 1964, Aluminum augite and bronzite in alkali olivine basalt from Taka-sima, north Kyusyu, Japan. In: Advancing Frontiers in Geology and Geophysics, volume dedicated to Dr. Krishnan, Osmania Univ. Press, Hyderabad, p. 205-220.

Kuno, H., 1968, Differentiation of basalt magmas. In: Basalts, vol. 2, Hess and Poldervaart (eds), Interscience Publ., p. 623-688.

Lambert, I.B. and Wyllie, P.J., 1968, Stability of hornblende and a model for the low velocity zone. Nature, v. 219, p. 1240-1241.

Leeman, W.P., 1973, Partitioning of Ni and Co between olivine and basaltic liquid (abs). EOS, v. 54, p. 1222.

Lindstrom, D.J., 1976, Experimental study of the partitioning of the transition metals between clinopyroxene and coexisting silicate liquids. Ph.D. Thesis, University of Oregon, 188 p.

Lippard, S., 1973, The petrology of phonolites from the Kenya Rift. Lithos, v. 6, p. 217-234.

Lloyd, F.E., 1981, Upper mantle metasomatism beneath a continental rift: Clinopyroxenes in alkali mafic lavas and nodules from South West Uganda. Mineral. Mag., v. 44, p. 315-323.

Lloyd, F.E. and Bailey, D.K., 1975, Light element metasomatism of the continental mantle: the evidence and the consequences. Phys. Chem. Earth, v. 9, p. 389-416.

MacDonald, G.A. and Katsura, T., 1964, Chemical composition of Hawaiian lavas. Jour. Petrol., v. 5, p. 82-133.

Masuda, A., Nakamura, N., and Tanaka, T., 1973, Fine structures of mutually normalized rare-earth patterns of chondrites. Geochim. Cosmochim. Acta, v. 37, p. 239-248.

McKenzie, D.P., 1973, Active tectonics of the Mediterranean Region. Geophys. Jour. Roy. Astron. Soc., v. 30, p. 109-185.

McKenzie, D.P., 1978, Active tectonics of the Alpide-Himalayan belt: the Aegean Sea and surrounding regions. Geophys. Jour., London (im Druck).

Menzies, M. and Murthy, V.R., 1980a, Enriched mantle: Nd and Sr isotopes in diopsides from kimberlite nodules. Nature, v. 283, p. 634-636.

Menzies, M. and Murthy, V.R., 1980b, Mantle metasomatism as a precursor to the genesis of alkaline magmas - isotopic evidence. Amer. Jour. Sci., v. 280-A, p. 622-638.

Menzies, M. and Murthy, V.R., 1980c, Nd and Sr isotope geochemistry of hydrous mantle nodules and their host alkali basalts: Implications for local heterogeneities in metasomatically veined mantle. Earth Planet. Sci. Lett., v. 46, p. 323-334.

Mitchell, R.H., 1973, Magnesian ilmenite and its role in kimberlite petrogenesis. Jour. Geol., v. 81, p. 301.

Nockolds, S.R., Knox, O.B., and Chinner, G.A., 1978, Petrology for Students, Cambridge University Press, 435 p.

O'Nions, R.K., Pankhurst, R.J., and Gronvold, K., 1976, Nature and development of basalt magma sources beneath Iceland and the Reykjanes Ridge. Jour. Petrol., v. 17, p. 315-338.

Oxburgh, E.R., 1964, Petrological evidence for the presence of amphibole in the upper mantle and its petrogenetic and geophysical implications. Geol. Mag., v. 101, p. 1.

Pearce, J.A. and Norry, M.J., 1979, Petrogenetic implications of Ti, Zr, Y and Nb variations in volcanic rocks. Contrib. Mineral. Petrol., v. 69, p. 33-47.

Philippson, A., 1913, Das Vulkangebeit von Kula in Lydien, die Katakaumene der Alten. Petermann's Mitteilunge, v. 118, p. 237-241.

Pushkar, P. and Stoeser, D.B., 1975, $^{87}Sr/^{86}Sr$ ratios in some volcanic rocks and some semifused inclusions of the San Francisco volcanic field. Geology, v. 3, p. 669-671.

Ringwood, A.E., 1975, Composition and Petrology of the Earth's Mantle. McGraw Hill, 618 p.

Saggerson, E.P. and Williams, L.A..J., 1964, Ngurumanite from southern Kenya and its bearing on the origin of the rocks in the northern Tanganyika alkaline district. Jour. Petrol., v. 5, p. 40-81.

Schairer, J.J. and Yoder, H.S., Jr., 1969, Critical planes and flow sheet for a portion of the system $CaO-MgO-Al_2O_3-SiO_2$ having petrological applications. Carnigie Inst. Yrbk, v. 68, p. 202-214.

Schilling, J.G., 1973, Iceland mantle plume: Geochemical study of Reykjanes Ridge. Nature, v. 242, p. 565-571.

Schroder, B., Thompson, G., Sulanowska, M., and Ludden, J.N., 1980, Analysis of geologic materials using an automated x-ray fluorescence system. X-Ray Spectro., v. 9, p. 198-205.

Şengör, A.M.C., 1978, Uber die angebliche primare Vertikaltektonik im Agaisraum. N. Jb. Geol. Palaont. Monatshefte, v. 11, p. 698-703.

Şengör, A.M.C. and Dyer, J.M.N., 1979, Neotectonic provinces of the Tethyan orogenic belt of the eastern Mediterranean: Variations in tectonic style and magmatism in a collision zone (abs). EOS, v. 60, p. 390.

Şengör, A.M.C. and Kidd, W.S.F., 1979, Post-collisional tectonics of the Turkish-Iranian Plateau and a comparison with Tibet. Tectonophysics, v. 55, p. 361-376.

Şengor, A.M.C. and Yilmaz, J., 1981, Tethyan evolution of Turkey: a plate tectonic approach. Tectonophysics, v. 75, p. 181-241.

Spera, F.J., 1980, Aspects of magma transport. In: Physics of Magmatic Processes, R.B. Hargraves (ed.), Princeton Univ. Press, p. 265-323.

Stormer, J.C., 1973, Calcium zoning in olivine and its relationship to silica activity and pressure. Geochim. Cosmochim. Acta, v. 37, p. 1815-1821.

Stuckless, J.S. and Irving, A.J., 1976, Strontium isotope geochemistry of megacrysts and host basalts of southeastern Australia. Geochim. Cosmochim. Acta, v. 40, p. 209-213.

Taylor, S.R., 1965, Application of trace elements to problems in petrology. Phys. Chem. Earth, v. 6, p. 133-213.

Taylor, S.R. and Gorton, M., 1977, Geochemical application of spark source mass spectrography, III. Element sensitivity, precision and accuracy. Geochim. Cosmochim. Acta, v. 41, p. 137

Tchihatcheff, P.de., 1867, Asie Mineure, Tome 4, Geologie, Paris, 211 p.

Texier,   1882, Asie Mineure, Paris, p. 272-275.

Thompson, R.N., 1974, Some high-pressure pyroxenes. Mineral. Mag., v.39, p. 768-787.

Tilley, C.E. and Harwood, H.F., 1931, The dolerite-chalk contact of Scawt Hill. Co. Antrim. Mineral. Mag., v. 22, p. 439-468.

Van der Molen, I. and Patterson, M.S., 1979, Experimental deformation of partially-melted granite. Contrib. Mineral. Petrol., v. 70, p.299-318.

Velde, D. and Yoder, H.S., Jr., 1976, The chemical compositions of melilite-bearing eruptive rocks. Carnegie Inst. Washington Yrbk, v. 75, p. 574-580.

Verhoogen, J., 1962, Distribution of titanium between silicates and oxides in igneous rocks. Amer. Jour. Sci., v. 260, p. 211-220.

Walker, D., Kirkpatrick, R.J., Longhi, J., and Hays, J.F., 1976, Crystal>lization history of lunar picritic basalt sample 12002: Phase equilibria and cooling rate studies. Geol. Sco. Amer. Bull., v. 87, p. 646-656.

Washington, H.S., 1893, The volcanoes of the Kula basin in Lydia. Ph.D. Thesis, University of Leipzig.

Washington, H.S., 1894a, The Volcanoes of the Kula Basin in Lydia. Drummond Publ., New York, 67 p.

Washington, H.S., 1894b, On the basalts of Kula. Amer. Jour. Sci., v.47, p. 114.

Washington, H.S., 1900, The composition of Kulaite. Jour. Geol., v. 8, p. 610-620.

Wass, S.Y., 1973, The origin and petrogenetic significance of hour-glass zoning in titaniferous clinopyroxenes. Mineral. Mag., v. 39, p. 133-144.

Wass, S.Y., 1979, Multiple origins of clinopyroxenes in alkalic basaltic rocks. Lithos, v. 12, p. 115-132.

Wass, S.Y., 1980, Geochemistry and origin of xenolith-bearing and related alkali basaltic rocks from the southern Highlands, New South Wales, Australia. Amer. Jour. Sci., v. 280-A, p. 639-666.

Watson, E.B., 1979, Calcium content of forsterite coexisting with silicate liquid in the system $Na_2O-CaO-MgO-Al_2O_3-SiO_2$. Amer. Mineral., v.64, p. 824-829.

Watson, E.B., 1980, Apatite and phosphorus in mantle source regions: An experimental study of apatite/melt equilibria at pressures to 25 kbar. Earth Planet. Sci. Lett., v. 51, p. 322-335.

Wilkinson, J.F.G., 1975, Ultramafic inclusions and high pressure megacrysts from a nephelinite sill, Nandewar Mountains, northeastern New South Wales, and their bearing on the origin of certain ultramafic inclusions in alkaline volcanic rocks. Contr. Mineral. Petrol., v. 51, p. 235-262.

Williams, L.A.J., 1970, The volcanics of the Gregory Rift Valley, East Africa. Bull. Volc., v. 34, p. 439-465.

Williams, L.A.J., 1972, The Kenya Rift volcanics: a note on volumes and chemical composition. In: East African Rifts, R.W. Girdler (ed.), Tectonophysics, v. 15, p. 83-96.

Wilshire, H.G., Nielson-Pike, J.E., Meyer, C.E., and Schwarzman, E.C., 1980, Amphibole-rich veins in lherzolite xenoliths, Dish Hill and Deadman Lake, California. Amer. Jour. Sci., v. 280-A, p. 576-593.

Wilshire, H.G. and Trask, N.J., 1971, Structural and textural relationships of amphibole and phlogopite in peridotite inclusions, Dish Hill, California. Amer. Mineral., v. 56, p. 240-255.

Windom, K.E. and Boettcher, A.L., 1980, Mantle metasomatism and the kimberlite-lamprophyre assocation: Evidence from an eclogite nodule from Roberts Victor Mine, South Africa. Jour. Geol., v. 88, p. 705-712.

Wright, T.L. and Doherty, P.C., 1970, A linear programming and least squares computer method for solving petrologic mixing problems. Geol. Soc. Amer. Bull., v. 81, p. 1995-2008.

Yagi, K., 1963, Liquidus data on the system acmite-nepheline-diopside at 1 atmosphere. Carnegie Inst. Washington Yrbk, v. 62, p. 133-134.

Yoder, H.S., Jr., 1979, Melilite-bearing rocks and related lamprophyres. In: The Evolution of the Igneous Rocks. H.S. Yoder, Jr. (ed.), Princeton Univ. Press, p. 391-411.

Yoder, H.S. and Tilley, C.E., 1962, Origin of basalt magmas:
    an experimental study of natural and synthetic rock systems.
    Jour. Petrol., v. 3, p. 342-532.

APPENDIX

MINERAL ANALYSIS

CLINOPYROXENE   (first period)

	1	2	3	4	5	6	7
SiO2	45.49	49.49	44.06	46.74	46.71	51.37	51.54
TiO2	2.94	1.45	3.82	2.58	2.67	0.51	0.54
Al2O3	8.65	6.38	11.60	6.96	6.91	3.09	3.52
Cr2O3	0.09	0.45	--	0.07	0.07	0.05	0.06
FeO*	6.54	4.80	7.68	6.84	6.80	10.82	10.68
MnO	0.15	0.11	0.19	0.14	0.14	0.56	0.46
MgO	11.84	14.32	9.21	12.50	12.34	10.16	9.95
CaO	23.59	22.79	21.04	23.08	22.99	20.68	20.06
Na2O	0.52	0.82	1.55	0.58	0.63	1.85	1.91
K2O	--	--	0.05	--	--	--	--
P2O5	0.02	0.01	0.16	0.06	0.07	0.05	0.07
F-	na	na	na	na	na	na	na
Cl-	na	na	na	na	na	na	na
total	99.84	100.63	99.30	99.55	99.33	99.14	98.79

	8	9	10	11	12	13	14
SiO2	50.10	46.84	51.08	48.03	44.92	47.99	48.01
TiO2	1.30	2.76	0.60	1.98	3.19	2.02	1.86
Al2O3	5.46	6.81	3.39	8.95	10.21	8.40	6.36
Cr2O3	0.41	--	0.07	0.30	0.03	0.50	0.02
FeO*	5.36	6.97	10.71	5.70	7.47	5.24	7.13
MnO	0.11	0.16	0.54	0.04	0.10	0.10	0.21
MgO	13.78	12.01	10.65	12.94	11.36	13.36	12.65
CaO	21.82	22.72	21.29	22.39	22.93	22.02	22.98
Na2O	0.73	0.57	1.96	0.87	0.61	0.98	0.60
K2O	--	--	--	--	--	--	--
P2O5	0.05	0.07	0.02	0.06	0.06	0.03	0.04
F-	na	na	na	na	na	na	na
Cl-	na	na	na	na	na	na	na
total	99.13	98.92	100.31	101.26	100.87	100.63	99.85

	15	16	17	18	19	20	21	22
SiO2	44.33	45.96	47.07	45.51	46.95	49.40	45.18	47.21
TiO2	3.05	2.06	2.27	1.73	0.40	1.75	3.08	3.09
Al2O3	8.68	6.83	7.01	7.73	7.49	6.09	8.90	6.32
Cr2O3	--	--	0.02	0.04	0.07	0.14	0.05	--
FeO*	8.32	7.73	7.45	7.88	11.83	5.50	6.32	7.48
MnO	0.19	0.23	0.23	0.19	0.14	0.12	0.14	0.15
MgO	10.91	8.26	12.28	6.66	9.12	13.86	11.32	11.76
CaO	22.93	22.84	22.22	22.41	23.46	22.04	22.00	22.30
Na2O	0.57	4.25	0.59	6.59	0.19	0.74	0.70	0.79
K2O	--	--	--	--	--	--	--	--
P2O5	0.04	0.06	0.05	0.07	0.04	--	0.03	0.03
F-	na	na	na	na	na	na	na	na
Cl-	na	na	na	na	na	na	na	na
total	99.03	98.25	99.19	98.81	99.68	99.64	97.72	99.13

1. Recrystallized titanaugite in sieve texture phenocryst core, TM-9-57.
2. Non-recrystallized titaniferous augite from phenocryst core of analysis 1.
3. Titanaugite rim of grain of analysis 1.
4. Titanaugite microlite, TM-9-57.
5. Groundmass titanaugite core, TM-9-57.
6. Sodic augite megacryst core, TM-9-57.
7. Outer edge of sodic augite core of analysis 6.
8. Titaniferous augite mantle on analysis 7.
9. Titanaugite rim around analysis 8.
10. Sodian augite core, TM-9-57.
11. Titaniferous augite mantle on analysis 10.
12. Titanaugite rim on analysis 11.
13. Titanaugite phenocryst core, TM-9-67I.
14. Outer mantle of titaniferous augite on analysis 13.
15. Titanaugite mantle on analysis 14.
16. Titanaugite outer rim on analysis 15.
17. Core analysis of groundmass titanaugite, TM-9-67I.
18. Titaniferous augite rim analysis of pyroxene of analysis 17.
19. Non-aluminous salite, TM-9-67I.
20. Titaniferous augite phenocryst core, TM-9-68.
21. Titanaugite rim of analysis 20.
22. Titanaugite in fine grain clot, TM-9-68.

OLIVINE (first period)

	1	2	3	4	5	6
SiO2	35.29	38.80	39.00	53.34	39.30	38.19
TiO2	0.41	--	0.01	0.16	0.04	0.06
Al2O3	0.41	--	--	27.81	0.00	0.00
Cr2O3	0.07	--	--	--	0.02	0.00
FeO*	41.30	19.47	19.84	0.67	16.03	22.66
MnO	1.05	0.34	0.39	0.02	0.20	0.53
MgO	24.86	39.18	39.09	0.02	43.80	38.68
CaO	0.72	0.24	0.24	0.23	0.20	0.00
Na2O	0.04	0.01	0.01	13.71	0.02	0.00
K2O	0.31	--	--	2.15	0.00	0.00
P2O5	0.32	0.03	0.02	--	0.02	0.00
total	104.79	98.07	98.60	98.10	99	64

	7	8	9	10	11
SiO2	37.63	36.82	39.80	39.87	36.75
TiO2	0.05	0.05	0.05	0.03	0.07
Al2O3	0.06	0.00	--	--	--
Cr2O3	0.02	0.02	0.01	--	0.02
FeO*	27.12	27.40	14.68	14.11	30.86
MnO	0.63	0.72	0.23	0.22	0.89
MgO	35.99	34.86	43.22	43.84	30.52
CaO	0.02	0.05	0.30	0.27	0.47
Na2O	0.00	0.00	0.04	0.04	0.05
K2O	0.00	0.00	--		--
P2O5	0.01	0.04	0.01	0.01	0.11
total	100.47	101.91	100.43	98.40	99.74

Olivine

1. Groundmass olivine, TM-9-57.
2. Chrysolite core (Fo78), TM-9-57.
3. Phenocryst core, TM-9-57.
4. Glass inclusion in olivine phenocryst, TM-9-57.
5. Chrysolite core (Fo79), TM-9-67I.
6. Chrysolite rim (Fo75) of analysis 5, bordering
   clinopyroxene.
7. Chrysolite rim (Fo70) of analysis 5, bordering
   mesostasis.
8. Hyalosiderite rim (Fo79) of analysis 5, bordering
   mesostasis.
9. Chrysolite core (Fo83), TM-9-68.
10. Chrysolite core (Fo84), Tm-9-68.
11. Groundmass hyalosiderite (Fo63), TM-9-68.

FELDSPAR AND FELDSPATHOIDS   (first period)

	1	2	3	4	5	6	7
SiO2	50.60	50.59	51.15	51.95	52.01	50.46	54.81
TiO2	0.16	0.10	0.15	0.07	0.14	0.13	0.50
Al2O3	31.25	31.26	30.78	31.11	30.24	30.01	26.38
Cr2O3	0.01	0.00	0.00	0.00	0.00	0.00	0.04
FeO*	0.57	0.50	0.50	0.61	0.46	0.49	1.53
MnO	0.02	0.00	0.02	0.02	0.00	0.00	0.01
MgO	0.04	0.00	0.03	0.04	0.03	--	1.04
CaO	14.24	0.64	13.01	0.33	12.29	0.34	9.00
Na2O	3.50	16.02	3.84	15.33	3.98	16.15	4.47
K2O	0.17	2.88	0.32	3.01	0.70	2.99	3.16
P2O5	0.01	0.00	0.00	0.00	0.03	--	0.03
total	100.57	102.00	99.80	102.47	99.87	100.58	100.97

	8	9	10	11	12	13	14	15
SiO2	50.71	49.56	44.55	53.34	56.91	53.77	54.52	57.50
TiO2	0.11	0.14	2.88	0.16	0.15	0.11	0.21	0.16
Al2O3	30.70	31.90	22.01	27.81	23.66	22.70	23.32	25.89
Cr2O3	0.00	0.00	0.02	0.00	0.01	0.00	0.01	0.00
FeO*	0.70	0.47	10.72	0.64	0.34	0.26	0.21	0.40
MnO	0.04	0.00	0.06	0.02	0.00	0.01	0.00	0.00
MgO	0.08	0.00	5.43	0.02	0.00	0.00	0.00	0.00
CaO	12.60	0.59	3.94	0.23	0.00	0.93	0.14	6.91
Na2O	4.11	16.80	7.89	13.71	0.12	0.18	0.18	6.50
K2O	0.40	2.54	1.44	2.15	13.02	20.42	20.83	2.61
P2O5	0.03	0.00	0.00	0.00	0.00	0.73	0.08	0.00
total	99.47	102.00	98.94	98.10	94.21	99.12	99.51	99.97

1. Labradorite (An69), microphenocryst core, TM-9-57.
2. Rim of grain from analysis 1.
3. Labroadorite (An64) microphenocryst rim of grain in analysis 1.
4. Nepheline glass, TM-9-57.
5. Labradorite glass (An60), TM-9-57.
6. Nepheline glass, TM-9-57.
7. Andesine groundmass lath, TM-9-57.
8. Labradorite groundmass lath, TM-9-57.
9. Nepheline, in fine grain clot, TM-9-68.
10. Anorthoclase(?) in fine grained clot, TM-9-68.
11. Nepheline glass inclusion in olivine, TM-9-57.
12. Leucite glass, TM-9-67I.
13. Leucite glass, TM-9-67I.
14. Leucite glass, TM-9-67I.
15. Feldspathic round blob, TM-9-67I.

OXIDES (first period)

	1	2	3	4	5	6	7
SiO2	0.14	0.22	0.24	0.52	1.14	3.14	0.27
TiO2	22.28	21.90	25.84	24.00	25.69	24.01	22.73
Al2O3	4.97	5.33	1.38	1.29	2.46	2.10	1.57
Cr2O3	0.08	0.15	0.08	--	0.06	0.05	0.04
FeO*	66.88	65.72	65.19	61.87	63.64	65.64	64.66
MnO	0.87	0.90	0.77	0.70	0.66	0.83	0.62
MgO	2.54	2.85	1.20	2.26	1.29	4.56	1.66
CaO	0.08	0.19	0.17	2.55	0.55	0.10	0.29
Na2O	--	--	0.04	--	0.02	--	--
K2O	--	--	0.10	--	0.07	--	--
P2O5	--	0.02	0.02	1.93	0.08	--	0.08
total	97.84	97.28	95.00	97.67	95.76	100.40	92.02

1. Titanomagnetite, TM-9-57.
2. Titanomagnetite, TM-9-57, same grain as analysis 1.
3. Titanomagnetite, TM-9-67I.
4. Titanomagnetite, TM-9-68.
5. Titanomagnetite, TM-9-68.
6. Titanomagnetite in fine grained clot, TM-9-68.
7. Titanomagnetite in fine grained clot, TM-9-68.

XENOLITH   Inclusions in TM-9-67I

	1	2	3	4	5
SiO2	0.04	0.27	45.88	51.21	45.16
TiO2	0.01	0.13	0.02	0.31	0.02
Al2O3	--	0.63	34.09	1.21	34.04
Cr2O3	--	0.12	--	0.22	--
FeO*	--	77.47	0.20	9.72	0.38
MnO	--	0.16	0.01	0.21	0.13
MgO	1.70	0.09	--	11.71	--
CaO	48.21	0.25	17.82	24.37	17.94
Na2O	--	0.05	1.55	0.26	1.24
K2O	--	0.07	--	--	--
P2O5	0.15	0.12	--	0.01	--
total	50.12	79.35	99.59	99.24	98.91

1. Carbonate which forms a discontinuous rim around xenolith.
2. Iron oxide(?) or sulfide (pyrrhotite?)
3. Bytownite feldspar.
4. Low-alumina salite.
5. Anorthite feldspar.

CLINOPYROXENE (second period)

	1	2	3	4	5	6	7	8
SiO2	47.69	43.85	43.87	45.11	47.97	47.05	44.27	47.63
TiO2	2.06	3.89	3.90	2.36	1.83	2.92	3.67	1.84
Al2O3	8.65	10.21	10.50	9.69	7.43	7.22	9.88	8.09
Cr2O3	--	0.01	0.04	0.03	0.04	0.04	0.09	0.01
FeO*	6.41	7.21	7.32	12.25	8.70	6.99	7.30	9.90
MnO	0.09	0.09	0.11	0.25	0.23	0.07	0.10	0.30
MgO	12.55	11.02	11.26	8.16	11.10	12.62	11.46	9.52
CaO	22.03	22.27	22.35	21.15	22.00	22.76	22.66	21.48
Na2O	0.90	0.61	0.61	1.67	1.22	0.57	0.66	2.00
P2O5	0.10	0.10	0.11	0.05	0.07	0.11	0.09	--
total	100.48	99.26	100.06	100.73	100.59	100.36	100.17	100.78

	9	10	11	12	13	14	15	16
SiO2	46.34	46.05	46.39	45.46	49.71	46.14	42.93	45.88
TiO2	2.40	1.50	2.69	2.48	1.61	2.00	3.45	2.81
Al2O3	9.34	12.77	9.17	9.27	5.47	8.74	11.78	9.23
Cr2O3	0.04	--	0.05	0.08	0.09	--	--	--
FeO*	6.60	2.87	7.00	6.68	5.98	8.08	8.66	6.91
MnO	0.10	0.07	0.13	0.11	0.12	0.11	0.12	0.11
MgO	12.13	12.43	11.87	11.99	14.01	11.08	9.45	12.13
CaO	22.48	24.68	22.49	21.97	22.14	23.17	22.29	22.23
Na2O	0.79	0.27	0.74	0.74	0.61	0.66	0.95	0.73
P2O5	0.04	0.06	0.09	0.07	0.09	0.10	0.11	0.09
total	100.27	100.71	100.63	98.86	99.82	100.09	99.74	100.11

	17	18	19	20	21	22	23
SiO2	43.70	46.11	46.14	46.91	46.16	46.70	1.34
TiO2	3.46	2.16	2.62	2.59	2.66	2.26	0.17
Al2O3	11.34	7.68	8.96	8.46	9.41	8.98	1.34
Cr2O3	0.04	--	--	--	0.06	0.19	0.13
FeO*	6.99	13.64	6.43	6.56	6.49	6.63	74.04
MnO	0.13	0.43	0.11	0.11	0.11	0.11	0.20
MgO	11.09	7.36	12.15	12.34	12.39	13.03	0.13
CaO	21.72	20.84	22.50	22.41	22.01	22.05	0.60
Na2O	0.71	1.77	0.73	0.77	0.82	0.73	0.08
P2O5	0.04	0.05	0.07	0.11	0.07	0.11	0.13
total	99.21	100.06	99.73	100.26	100.19	100.78	78.23

Clinopyroxene

1. Titanaugite phenocryst core, 68C3.
2. Titanaugite phenocryst rim of grain of analysis 1.
3. Titanaugite phenocryst rim of grain of analysis 1.
4. Sodian augite megacryst core, 68C3.
5. Titaniferous augite mantle on analysis 4.
6. Titanaugite rim on analysis 5.
7. Titanaugite groundmass grin, 68C3.
8. Sodian augite core, 53Cl.
9. Titanaugite rim of analysis 8.
10. Titaniferous augite core, 53Cl.
11. Titanaugite rim of analysis 10.
12. Titanaugite round microlite, 53Cl.
13. Titaniferous augite microlite, 53Cl.
14. Titanaugite core, 68Cl.
15. Titanaugite zonation mantling core in analysis 14.
16. Titanaugite rim mantling analysis 15.
17. Titanaugite overgrowth on kaersutite, 68Cl.
18. Sodian augite core, 68Cl.
19. Outer edge of sodian augite core from analysis 18, 68Cl.
20. Titanaugite rim on sodian augite from analysis 19.
21. Titanaugite core, 68Cl.
22. Titanaugite rim of analysis 21.
23. Oxide inclusion in core titanaugite (in analysis 21).

APATITE

	1
SiO_2	0.74
TiO_2	0.05
Al_2O_3	0.23
Cr_2O_3	--
$FeO*$	0.81
MnO	0.21
MgO	0.54
CaO	47.31
Na_2O	0.40
K_2O	
P_2O_5	40.19
$F-$	2.84
$Cl-$	1.31
total	94.62

1. Myrmekitic textured apatite groundmass grain, 68Cl.

OLIVINE (second period)

	1	2	3	4	5	6	7
SiO2	39.55	39.57	39.81	39.96	40.26	39.54	39.63
TiO2	0.03	0.04	0.10	0.07	--	0.04	0.02
Al2O3	--	--	--	--	--	--	--
Cr2O3	--	--	--	0.03	--	--	--
FeO*	17.57	17.68	16.07	15.93	16.74	17.03	17.24
MnO	0.35	0.33	0.27	0.30	0.31	0.36	0.36
MgO	42.55	42.46	44.34	44.20	43.58	43.58	42.59
CaO	0.21	0.21	0.25	0.25	0.28	0.32	0.27
Na2O	0.02	0.05	0.03	0.01	0.03	0.01	0.02
K2O	--	--	--	--	--	--	--
P2O5	0.07	0.01	0.13	0.02	0.02	0.03	0.07
total	100.35	100.37	100.99	100.75	101.23	100.89	100.22

1. Chrysolite (Fo81) core, 53C1.
2. Chrysolite (Fo81) rim of grain in analysis 1.
3. Chrysolite (Fo83) core, 68C3.
4. Chrysolite (Fo83) core, 68C3.
5. Chrysolite (Fo82) rim of grain in analysis 4.
6. Chrysolite (Fo82) core, 68C3.
7. Chrysolite (Fo81) core, 68C3.

AMPHIBOLE (second period)

	1	2	3	4	5	6	7
SiO2	39.34	39.34	39.53	40.16	39.30	40.79	40.79
TiO2	5.31	4.32	4.92	5.00	5.05	5.34	6.13
Al2O3	15.54	15.22	14.93	14.94	15.04	15.18	14.30
Cr2O3	0.01	0.02	0.03	0.04	0.02	0.07	0.05
FeO*	10.14	11.68	11.55	10.50	11.01	9.87	10.34
MnO	0.12	0.12	0.12	0.07	0.12	0.07	0.15
MgO	12.42	11.89	12.06	12.30	11.93	12.52	12.14
CaO	11.66	11.23	11.89	11.84	11.84	11.77	11.42
Na2O	2.81	2.72	2.78	2.61	2.59	2.46	2.80
K2O	1.39	1.45	1.41	1.45	1.45	1.50	1.39
P2O5	0.075	0.13	0.05	0.07	0.04	0.06	0.12
F-	0.29	0.38	0.16	--	0.22	0.85	1.30
Cl-	0.03	0.02	0.03	0.02	0.02	0.03	0.03
total	99.14	98.52	99.46	99.00	98.64	100.51	100.94

1. Core of zoned kaersutite, 53C1.
2. Intermediate zone of ferroan pargasite mantling core of grain in analysis 1.
3. Kaersutite rim of grain in analysis 1.
4. Kaersutite core, 68C1.
5. Kaersutite rim of grain in analysis 4.
6. Kaersutite core, 68C1.
7. Kaersutite rim of grain in analysis 6. This rim was further mantled by a titanaugite corona.

PLAGIOCLASE

	1	2	3	4
SiO2	50.64	52.03	51.63	57.59
TiO2	0.25	0.17	0.14	0.11
Al2O3	30.51	30.82	30.54	26.56
Cr2O3	--	0.03	--	0.02
FeO*	0.61	0.68	0.58	0.30
MnO	0.02	0.01	--	
MgO	0.09	0.04	0.07	0.08
CaO	13.75	12.96	12.88	8.79
Na2O	3.30	3.72	3.92	5.95
K2O	0.30	0.38	0.37	0.86
P2O5	0.05	0.01	0.09	0.05
total	99.53	100.87	100.22	100.32

1. Groundmass bytownite lath (An70), 68C3.
2. Groundmass labradorite lath (An64), 53C1.
3. Groundmass labradorite lath (An63), 68C1.
4. Andesine xenocryst (An43), 68C1.

ANALCITE AND GLASS (second period)

	1	2	3	4	5
SiO2	58.39	55.75	54.04	52.95	57.47
TiO2	0.13	0.23	1.05	0.85	0.16
Al2O3	23.83	24.89	22.46	22.86	23.86
Cr2O3	--	--	0.02	--	--
FeO*	0.65	0.77	4.60	4.62	0.54
MnO	0.02	--	0.12	0.13	--
MgO	0.33	0.18	1.00	0.98	0.05
CaO	1.07	2.90	1.43	2.31	1.63
Na2O	5.07	4.95	8.47	8.17	4.93
K2O	0.74	0.66	6.50	6.08	0.75
P2O5	0.17	0.42	0.37	0.39	0.49
F-	--	0.03	0.48	--	0.29
Cl-	--	0.02	0.25	0.24	0.05
total	90.40	90.81	100.77	99.59	90.20

Analcite and Glass

1. Circular analcite grain in groundmass, 68C3.
2. Circular analcite grain in groundmass, 68C3.
3. Pale brown glass, mesostasis, 68C3.
4. Pale brown glass, mesostasis, 68C3.
5. Circular analcite grain in groundmass, 68C3.

XENOLITHS/MEGACRYSTS (second period)

	1	2	3	4	5	6	7
SiO2	53.32	53.39	0.13	54.41	65.77	35.09	34.81
TiO2	0.43	0.30	60.82	0.04	0.03	0.14	0.04
Al2O3	6.44	1.47	--	0.85	18.66	19.39	21.20
Cr2O3	0.05	0.04	0.13	0.12	--	--	--
FeO*	18.84	19.48	30.50	3.56	--	4.59	4.07
MnO	0.67	0.79	0.63	0.06	--	0.08	0.07
MgO	21.62	21.06	6.23	16.16	--	2.72	2.39
CaO	1.51	1.51	0.02	25.25	--	35.00	35.01
Na2O	0.20	0.03	--	0.16	1.96	2.10	2.28
K2O	0.02	0.01	--	--	14.00	0.33	0.35
P2O5	0.05	0.03	0.01	0.03	--	0.05	0.04
F-	0.14	0.03	--	--	--	0.33	0.23
Cl-	0.02	0.02	--	--	0.02	0.01	--
total	103.33	98.16	98.47	100.63	100.43	99.84	100.48

	8	9	10	11	12	13	14
SiO2	43.03	48.63	30.23	43.64	47.07	44.95	45.18
TiO2	2.07	2.74	1.10	2.68	2.05	2.79	2.38
Al2O3	13.96	18.90	11.04	9.86	8.81	10.64	9.57
Cr2O3	0.03	--	--	--	0.01	0.17	--
FeO*	7.12	8.85	5.39	12.65	6.27	6.08	7.73
MnO	0.04	0.09	0.06	0.33	0.09	0.10	0.18
MgO	8.96	2.84	3.75	7.00	12.67	11.73	11.45
CaO	24.01	7.39	4.77	20.70	22.63	22.21	21.81
Na2O	0.27	7.18	3.55	1.80	0.84	0.90	0.88
K2O	--	3.29	0.63	--	--	--	--
P2O5	--	1.09	0.98	--	--	--	--
F-	0.10	0.25	-?-	--		0.02	--
Cl-	--	0.21	0.84				
total	99.59	101.46	62.34	98.66	100.44	99.59	99.18

1. Aluminous orthopyroxene from plagioclase rich xenolith, 68C1.
2. Aluminous orthopyroxene from plagioclase rich xenolith, 68C1.
3. Magnesium-rich titanomagnetite from plagioclase xenolith, 68C1.
4. Non-aluminous diopside, crustal xenolith, 68C1.
5. Potassium feldspar, crustal xenolith, 68C1.
6. Gehlenite, gehlenite-clinopyroxene megacryst in ash-filled vesicle, 53C1.
7. Gehlenite, same megacryst as in analysis 6.
8. Aluminous salite, same megacryst as in analysis 6.
9. Fine grain dark grunge, which forms a regular network in the gehlenite, same grain as in analysis 6.
10. Grungier grunge, same grain as in analysis 6.
11. Partially resorbed sodian augite in core, kaersutite-clinopyroxene xenolith, 68C2.
12. Titanaugite core, mantle on grain in analysis 11.
13. Titanaugite rim of grain in analysis 11.
14. Recrystallized(?) titanaugite, inclusion in grain.

RESORBED QUARTZ XENOCRYSTS(?) AND SURROUNDING QUENCH PHASES

	1	2	3	4	5	6	7
SiO_2	62.36	64.11	55.68	55.77	50.51	51.91	52.25
TiO_2	1.08	0.76	1.48	0.51	1.03	0.82	1.15
Al_2O_3	15.04	11.32	16.77	3.43	3.44	1.33	12.06
Cr_2O_3	--	--	--	0.01	0.01	--	0.06
FeO*	4.80	6.76	6.43	9.66	8.42	9.90	8.63
MnO	0.09	0.11	0.09	0.23	0.21	0.25	0.21
MgO	0.41	1.56	0.88	9.24	13.10	12.59	8.92
CaO	1.03	2.79	2.12	16.73	20.60	20.69	16.09
Na_2O	3.58	2.59	4.61	1.75	0.67	0.56	2.85
K_2O	7.34	6.82	7.10	1.80	--	--	1.80
P_2O_5	0.79	0.13	1.08	0.11	0.07	0.06	0.39
F54	0.34	0.05	0.49	0.11	0.18	0.24	0.34
Cl-	0.18	0.13	0.19	0.05	0.04	0.02	0.08
total	97.04	97.23	96.91	99.38	98.29	98.38	104.83

	8	9	10	11
SiO2	52.84	53.18	53.41	51.77
TiO2	1.40	0.27	0.20	1.51
Al2O3	21.49	0.63	0.08	6.29
Cr2O3	0.02	0.02	0.04	0.04
FeO*	5.93	10.02	12.48	6.43
MnO	0.12	0.23	0.30	0.16
MgO	0.98	12.26	17.15	13.62
CaO	2.17	21.10	15.51	20.53
Na2O	8.46	0.80	0.23	0.87
K2O	6.09	0.15	--	0.40
P2O5	0.60	0.05	0.10	0.17
F-	0.36	--	0.02	0.10
Cl-	0.18	0.03	0.01	0.05
total	100.66	98.73	99.52	101.93

1. Turbid pale brown glass, 68C1.
2. Turbid pale brown glass, 68C1, same grain as analysis 1.
3. Dark brown grunge which discontinuously surround the glass of analyses 1 and 2.
4. Microlite in glass of analyses 1 and 2.
5. Aluminous salite surrounding glass and grunge of analyses 1-4.
6. Low alumina salite surrounding analyses 1-4.
7. Heterogeneous glass, dark brown, 68C3.
8. Heterogeneous glass, light brown, same grain as analysis 7.
9. Heterogeneous glass, dark brown, same grain as analysis 7.
10. Non-aluminous salite microlite in glass, same grain as analysis 7.
11. Titaniferous augite microphenocysts surrounding grain in analyses 7-9.

CLINOPYROXENE (third period)

	1	2	3	4	5	6	7
SiO2	45.92	50.17	47.46	50.48	48.91	49.88	44.47
TiO2	2.79	1.52	2.30	1.64	1.86	1.59	3.80
Al2O3	9.25	5.00	8.21	4.66	6.05	5.02	11.19
Cr2O3	0.23	0.10	0.26	0.22	0.05	0.12	0.20
FeO*	5.13	5.05	4.91	5.09	5.96	5.46	6.04
MnO	0.12	0.16	0.12	0.12	0.12	0.11	0.07
MgO	12.54	14.47	13.07	15.31	14.33	14.88	12.28
CaO	21.70	22.59	22.21	22.80	22.11	22.25	22.23
Na2O	0.78	0.59	0.71	0.59	0.59	0.58	0.78
K2O	--	--	--	--	--	--	--
P2O5	0.06	0.07	0.07	0.06	0.13	0.07	0.05
total	98.52	99.72	99.32	100.96	100.12	99.96	101.11

	8	9	10.	11	12	13	14
SiO2	46.81	48.38	48.84	49.29	46.24	42.83	50.64
TiO2	2.68	1.71	1.86	1.69	2.81	4.41	0.30
Al2O3	8.84	6.99	7.21	6.53	8.93	11.81	0.70
Cr2O3	0.06	0.30	0.09	0.05	0.03	0.02	0.04
FeO*	6.14	4.50	5.24	5.72	6.51	7.05	18.37
MnO	0.13	0.09	0.10	0.14	0.16	0.12	0.90
MgO	12.70	14.16	14.00	14.05	12.16	10.70	7.04
CaO	22.40	21.74	21.10	21.55	21.40	21.45	21.95
Na2O	0.82	0.76	0.83	0.81	0.94	0.80	0.47
K2O	--	--	--	--	--	--	--
P2O5	0.04	0.01	0.01	0.03	0.15	0.11	0.03
total	100.63	98.64	99.26	99.87	99.31	99.29	100.43

	15	16	17	18	19	20
SiO2	45.34	48.98	49.42	47.46	47.98	49.50
TiO2	3.48	1.77	1.80	2.39	1.48	1.57
Al2O3	8.90	7.90	5.40	6.97	5.41	5.05
Cr2O3	--	0.30	0.17	--	--	--
FeO*	6.85	4.71	5.56	6.61	14.06	6.83
MnO	0.12	0.07	0.11	0.11	0.64	0.16
MgO	11.44	13.44	13.54	12.57	7.84	12.95
CaO	22.66	21.51	22.66	22.63	20.18	22.65
Na2O	0.52	0.86	0.63	0.88	1.96	0.56
K2O	--	--	--	--	--	--
P2O5	0.01	--	--	--	--	--
total	99.32	99.54	99.42	99.72	99.55	99.27

Clinopyroxene

1. Titanaugite core, V.
2. Titaniferous augite rim of grain in analysis 1.
3. Titanaugite core, V.
4. Titaniferous augite core, microphenocryst, V.
5. Titaniferous augite rim of grain in analysis 4.
6. Titaniferous augite core, V.
7. Titanaugite overgrowth on olivine, core of pyroxene, V.
8. Titanaugite rim on pyroxene of analysis 7.
9. Titaniferous augite core, K-1.
10. Titaniferous augite rim of grain in analysis 9.
11. Titaniferous augite rim of grain in analysis 9.
12. Titanaugite microphenocryst core, K-1.
13. Titanaugite microphenocryst, rim of grain in analysis 12.
14. Non-aluminous salite megacryst core, K-1.
15. Embayed titanaugite rim of grain in analysis 14.
16. Titaniferous augite core, D-2.
17. Titaniferous augite rim of grain in analysis 16.
18. Titanaugite core, D-2.
19. Sodian augite core, D-2
20. Titaniferous augite rim of grain in analysis 19.

OLIVINE (third period)

	1	2	3	4	5	6	7
SiO_2	40.35	40.39	40.03	40.49	39.97	40.37	40.15
TiO_2	0.04	0.04	0.05	0.01	0.04	0.04	0.05
Al_2O_3	--	--	--			--	--
Cr_2O_3	0.04	0.03	0.05	0.03	0.05	--	0.01
FeO*	13.23	13.52	14.05	14.51	15.20	14.05	14.39
MnO	0.23	0.25	0.27	0.30	0.30	0.23	0.25
MgO	46.72	46.66	45.79	45.70	44.63	46.07	45.66
CaO	0.20	0.22	0.27	0.25	0.33	0.23	0.36
Na_2O	--	--	0.01	0.01	0.02	0.03	--
K_2O	--	--	--	--	--	--	--
P_2O_5	0.02	0.01	0.01	0.04	0.07	0.01	0.01
total	100.84	101.11	100.52	101.36	100.62	101.02	100.88

	8	9	10	11	12	13	14
SiO2	40.02	39.72	39.84	39.81	38.84	39.98	39.16
TiO2	--	--	0.04	0.05	0.04	0.04	0.07
Al2O3	--	--	--	--	0.04	--	--
Cr2O3	0.02	0.05	--	0.01	0.04	--	--
FeO*	13.22	13.05	15.82	14.50	21.29	15.55	19.75
MnO	0.22	0.20	0.32	0.25	0.56	0.25	0.44
MgO	46.48	46.32	43.21	45.61	39.31	43.96	39.98
CaO	0.21	0.25	0.29	0.23	0.30	0.22	0.30
Na2O	0.02	--	0.05	--	--	0.03	0.03
K2O	--	--	--	--	--	--	--
P2O5	0.03	0.10	0.28				
total	100.23	99.70	99.85	100.45	100.42	100.03	99.74

1. Chrysolite, intermediate zone (Fo86), V.
2. Chrystoalite core (Fo86), same grain as in analysis 1.
3. Chrysolite rim (Fo85), same grain as in analysis 1.
4. Chrysolite core (Fo85), V.
5. Chrysolite rim (Fo84) of grain in analysis 4.
6. Chrysolite core (Fo85) of grain showing undulatory
    extinction and mantled by clinopyroxene, V.
7. Chrysolite rim (Fo85) of grain in analysis 6.
8. Chrysolite core (Fo86), K-1.
9. Chrysolite rim (Fo86) of grain in analysis 8.
10. Chrysolite (Fo82), K-1.
11. Chrysolite core (Fo85), D-2.
12. Chrysolite rim (Fo77) of grain in analysis 11.
13. Chrsyolite core (Fo83), D-2.
14. Chrysolite rim (Fo78) of grain in analysis 13.

AMPHIBOLE (third period)

	1	2	3	4	5	6	7
SiO2	39.16	40.27	39.54	38.35	39.75	38.91	39.78
TiO2	5.79	5.19	5.36	4.57	5.05	4.85	5.16
Al2O3	15.51	13.71	14.50	14.84	13.87	14.21	14.75
Cr2O3	0.01	0.02	0.02	0.03	0.04	--	0.01
FeO*	9.35	9.17	9.24	15.04	9.14	11.60	8.79
MnO	0.09	0.13	0.08	0.23	0.11	0.22	0.11
MgO	13.08	13.63	13.33	9.84	13.82	11.47	13.44
CaO	11.52	11.80	11.75	11.41	11.69	11.30	11.82
Na2O	2.46	2.65	2.45	2.53	2.62	2.38	2.35
K2O	1.71	1.57	1.61	1.56	1.54	1.70	1.75
P2O5	0.10	0.11	0.09	0.10	0.12	0.05	0.06
F-	0.30	0.39	0.45	0.25	1.27	0.63	0.37
Cl-	0.04	0.04	0.02	0.05	0.02	0.04	0.02
total	99.13	98.69	98.43	98.79	99.03	97.36	98.39

	8	9	10	11	12	13	14
SiO2	39.67	39.45	39.98	39.81	39.72	53.88	0.12
TiO2	5.16	4.21	5.01	5.81	5.54	1.16	13.32
Al2O3	15.02	15.58	14.73	15.00	15.09	22.13	9.32
Cr2O3	0.01	--	--	0.03	0.04	0.02	0.11
FeO*	10.29	18.23	10.66	8.64	8.99	5.35	67.35
MnO	0.12	0.30	0.11	0.13	0.12	0.11	0.59
MgO	12.55	7.08	12.69	13.35	13.15	0.86	5.23
CaO	11.77	13.13	11.77	11.55	11.60	1.87	--
Na2O	2.37	2.93	2.65	2.41	2.47	5.95	0.01
K2O	1.77	1.36	1.64	1.55	1.58	5.88	0.10
P2O5	0.09	0.11	0.10	0.06	0.07	0.21	0.08
F-	0.35	0.26	0.16	0.06	0.27	0.06	0.43
Cl-	0.02	0.08	0.03	0.03	0.03	0.23	0.06
total	99.19	102.72	99.54	98.43	98.67	97.70	96.70

	15	16
SiO2	39.69	39.19
TiO2	5.49	4.95
Al2O3	14.57	14.29
Cr2O3	0.04	--
FeO*	8.66	12.01
MnO	0.13	0.10
MgO	13.21	11.35
CaO	11.31	11.19
Na2O	2.29	2.40
K2O	1.73	1.67
P2O5	0.02	0.04
F-	0.30	0.44
Cl-	0.03	0.04
total	97.46	97.66

Amphibole

1. Optically unzoned kaersutite core, V.
2. Optically unzoned rim of grain in analysis 1.
3. Optically zoned kaersutite core, V.
4. Kaersutite intermediate zone, same grain as in analysis 3.
5. Kaersutite rim of grain in analysis 3.
6. Oxidized kaersutite with abundant oxide inclusions, V.
7. Kaersutite with heavy oxidized margin, core, V.
8. Kaersutite rim of grain in analysis 7.
9. Analysis of opaque oxidized margin of kaersutite in analysis 7.
10. Kaersutite microphenocrysts mantling olivine megacryst, V.
11. Optically unzoned kaersutite core, K-1.
12. Kaersutite rim of grain in analysis 11.
13. Pale tan glass surrounding gas bubble in core of kaersutite phenocryst, V.
14. Titanomagnetite mantle on glass inclusion in grain from analysis 13.
15. Optically zoned core of kaersutite, same grain as in analysis 13.
16. Rim of kaersutite, same grain as in analysis 13.

FELDSPAR AND FELDSPATHOIDS (third period)

	1	2	3	4	5	6
SiO2	52.70	52.63	56.73	53.45	55.95	52.22
TiO2	0.11	0.09	0.02	0.04	0.25	0.96
Al2O3	28.86	28.81	26.89	29.52	22.21	20.57
Cr2O3	0.02	--	--	--	--	--
FeO*	0.49	0.49	0.36	0.43	0.66	4.27
MnO	0.02	--	0.02	--	--	0.15
MgO	0.04	0.04	0.04	0.10	0.29	2.10
CaO	12.67	12.48	9.50	11.85	1.34	2.43
Na2O	4.06	4.11	5.53	4.42	0.88	0.94
K2O	0.34	0.41	0.64	0.43	16.61	15.27
P2O5	0.07		0.03	0.05	0.28	0.43
total	99.38	99.06	99.75	100.27	98.45	99.36

1. Labradorite (An62) groundmass grain, D-2.
2. Labradorite (An61) groundmass grain, D-2.
3. Andesine microlite (An47) core, V.
4. Labradorite microlite (An58), rim of grain in analysis 5.
5. Leucite groundmass grain, V.
6. Same leucite grain as in analysis 5, with defocused microprobe beam.

OPAQUE PHASES (Third period)

	1	2	3	4	5	6	7	8	9	10	11
SiO2	0.13	0.11	52.55	64.79	58.07	53.49	0.08	3.35	0.33	66.00	64.46
TiO2	0.30	0.20	0.80	0.05	0.07	0.42	23.00	0.02	0.01	--	--
Al2O3	63.14	62.87	22.88	21.66	26.59	26.84	3.30	1.00	--	21.97	22.42
Cr2O3	0.06	0.06	0.02	0.01	0.01	0.04	0.09	--	--	--	--
FeO*	22.22	24.96	6.86	0.14	0.30	0.54	65.93	0.55	0.43	0.08	0.12
MnO	0.13	0.12	0.20	--	--	--	0.81	0.05	0.07	--	--
MgO	13.75	11.52	2.29	--	--	--	2.68	0.30	0.14	--	--
CaO	0.01	0.01	3.63	2.47	8.26	10.66	0.08	47.81	49.72	3.14	3.55
Na2O	0.02	--	4.02	7.30	5.95	4.95	--	0.35	0.11	8.55	8.83
K2O	--	--	4.58	3.72	1.04	0.69	--	0.12	--	1.33	1.34
P2O5	--	0.02	0.99	--	--	0.12		38.59	40.95	--	--
F-			0.30					2.52	5.15		
Cl-			0.22					0.23	0.37		
total	99.76	99.87	99.34	100.14	100.29	97.74	95.98	94.89	97.29	101.09	100.74

Xenocrysts/Megacrysts

1. Purple rounded pleonaste spinel megacryst, V.
2. Purple rounded pleonaste spinel megacryst, V.
3. Inclusion in spinel of analyses 1 and 2.
4. Anorthoclase megacryst, V.
5. Andesine megacryst (An40), K-1.
6. Labradorite rim (An53) of grain in analysis 5.
7. Titanomagnetite, D-2.
8. Rounded apatite megacryst core with opaque inclusions, D-2.
9. Rim of grain in analysis 8.
10. Oligoclase xenocryst (An15) core, V.
11. Oligoclase xenocryst (An17) rim, V.

RESORBED QUARTZ XENOCRYSTS AND ASSOCIATED PHASES (third period)

	1	2	3	4	5	6	7
SiO2	54.21	53.18	50.30	100.22	74.74	60.00	75.25
TiO2	1.20	0.22	1.31	0.04	0.67	1.32	0.69
Al2O3	20.29	1.41	4.49	--	8.04	18.99	7.82
Cr2O3	--	0.04	0.04	--	0.07	--	0.07
FeO*	5.45	11.17	5.93	--	5.38	4.50	6.63
MnO	0.11	0.27	0.16	--	0.13	0.11	0.15
MgO	1.07	11.77	14.20	--	0.89	0.67	0.75
CaO	1.32	21.73	21.96	--	1.19	1.08	1.03
Na2O	7.24	0.66	0.55	0.02	4.03	7.46	1.39
K2O	6.24	0.03	--	--	5.43	5.76	4.68
P2O5	0.46	0.09	0.10	0.02	0.17	0.41	0.16
F-	0.22	0.60	0.56				
Cl-	0.22	0.03	0.02				
total	98.09	101.17	99.62	100.29	100.72	100.31	98.62

1. Dark brown glass, K-1.
2. Non-aluminous salite microlite in glass, same grain as in analysis 1.
3. Titaniferous augite rim around phases in analyses 1 and 2.
4. Embayed quartz xenocryst, K-1.
5. Low index of refraction material surrounding quartz grain in analysis 4.
6. Low index of refraction material surrounding quartz grain in analysis 4.
7. Microlite on edge of material in analyses 5 and 6.

APATITE (third period)

	1
SiO2	0.38
TiO2	--
Al2O3	0.05
Cr2O3	0.01
FeO*	--
MnO	--
MgO	0.21
CaO	47.63
Na2O	0.14
K2O	--
P2O5	40.52
F-	3.52
Cl-	0.48
total	92.93

1. Myrmekitic-textured groundmass apatite, V.

NODULES- CLINOPYROXENE

	1	2	3	4	5	6	7
SiO2	47.05	46.14	42.28	42.59	49.60	49.24	48.20
TiO2	2.62	2.88	5.15	4.89	1.42	1.50	1.82
Al2O3	7.60	8.78	13.75	10.93	5.65	6.21	6.46
Cr2O3	0.01	0.00	0.04	0.02	0.04	0.02	0.00
FeO*	5.77	6.27	6.26	6.14	8.58	8.44	7.94
MnO	0.16	0.14	0.16	0.14	0.20	0.22	0.21
MgO	11.32	11.38	10.50	10.86	10.52	10.40	10.58
CaO	23.04	22.98	22.80	23.15	22.44	22.57	22.43
Na2O	0.98	0.99	0.64	0.63	1.47	1.55	1.58
K2O	0.00	0.00	0.01	0.00	0.00	0.00	0.00
P2O5	0.07	0.16	0.13	0.09	0.02	0.01	0.07
total	98.62	99.75	101.70	99.44	99.95	100.16	99.29

	8	9	10	11	12	13	14
SiO2	48.36	48.09	47.84	44.74	48.74	45.34	45.15
TiO2	1.98	2.38	2.47	3.75	2.02	2.86	3.10
Al2O3	7.67	7.93	8.63	10.44	7.96	10.48	10.11
Cr2O3	0.02	0.01	0.00	0.04	0.01	0.00	0.00
FeO*	7.96	8.24	8.41	7.27	8.18	8.24	8.62
MnO	0.15	0.19	0.16	0.09	0.17	0.13	0.14
MgO	10.46	10.39	10.10	10.29	10.55	9.46	9.64
CaO	21.68	21.71	21.77	22.87	21.79	22.18	22.53
Na2O	2.03	1.96	1.98	1.13	1.82	1.42	1.19
K2O	0.00	0.00	0.00	0.00	0.00	0.00	0.00
P2O5	0.01	0.05	0.03	0.01	0.02	0.02	0.03
total	100.32	100.96	101.40	100.63	101.27	100.13	100.52

	15	16	17	18	19	20
SiO2	48.94	51.02	50.53	50.60	50.50	48.71
TiO2	1.64	0.86	0.93	0.89	0.96	1.55
Al2O3	6.95	4.45	4.77	4.78	4.64	7.39
Cr2O3	0.04	0.06	0.05	0.04	0.10	0.06
FeO*	5.68	5.13	5.24	5.46	5.49	5.20
MnO	0.13	0.12	0.13	0.09	0.08	0.12
MgO	12.79	13.95	13.73	13.99	13.75	13.35
CaO	22.73	23.25	22.73	23.06	22.87	23.85
Na2O	0.66	0.63	0.66	0.63	0.64	0.48
K2O	0.00	0.00	0.00	0.00	0.00	0.00
P2O5	0.01	0.01	0.00	0.03	0.03	0.03
total	99.58	99.47	98.77	99.57	99.07	100.74

1. Titanaugite microphenocryst core, pyroxene mantling zoned kaersutite, TM-9-64N.
2. Titanaugite microphenocryst core, pyroxene mantling zoned kaersutite, TM-9-64N.
3. Titanaugite rim (note high TiO2) of grain in analysis 2.
4. Titanaugite rim (note high TiO2) of grain in analysis 1.
5. Sodian augite, TM-9-64N.
6. Rim of grain in analysis 5.
7. Titaniferous augite, TM-9-63N.
8. Sodian titaniferous augite, edge of nodule, TM-9-69FG.
9. Sodian titanaugite, 0.9 mm from nodule edge, TM-9-69FG.
10. Sodian titanaugite, 3.05 mm from nodule edge, TM-9-69FG.
11. Sodian titanaugite, 6.75 mm from nodule edge, TM-9-69FG.
12. Sodian titanaugite, nodule interior, TM-9-69FG.
13. Sodian titanaugite, nodule interior, TM-9-69FG.
14. Sodian titanaugite, nodule interior, TM-9-69FG.
15. titaniferous augite with phlogopite overgrowth, TM-9-69CG.
16. Aluminous salite, same grain as analysis 15, in an area free of mica overgrowths.
17. Aluminous salite, analysis near adjoining ferroan pargasite grain, TM-9-69CG.
18. Aluminous salite, TM-9-69CG.
19. Aluminous salite core, TM-9-69CG.
20. Titaniferous augite which looks optically similar to ferroan pargasite, TM-9-69CG.

NODULES- OLIVINE

1	2	3	4
39.24	39.07	33.26	38.16
0.04	0.10	2.71	0.05
0.00	0.00	4.07	0.00
0.01	0.00	0.23	0.03
19.11	18.88	26.38	16.63
0.36	0.42	0.38	0.34
40.46	40.95	35.86	39.95
0.07	0.08	1.52	0.09
0.00	0.04	0.04	0.00
0.00	0.00	0.00	0.00
0.02	0.03	0.03	0.00
99.32	99.58	104.48	95.24

1. Chrysolite core (Fo79), TM-9-69CG.
2. Chrysolite rim (Fo79), TM-9-69CG.
3. Olivine, TM-9-69CG.
4. Chrysolite (Fo81), altered olivine, TM-9-69CG.

NODULES- AMPHIBOLE

	1	2	3	4	5	6	7
SiO2	39.32	39.11	38.58	39.14	39.68	38.54	40.30
TiO2	3.09	3.16	4.58	5.00	5.57	4.91	4.11
Al2O3	14.32	14.25	14.42	14.53	14.94	15.02	14.43
Cr2O3	0.04	0.03	0.02	0.04	0.03	0.01	0.00
FeO*	15.35	15.23	12.73	10.73	7.93	10.91	12.86
MnO	0.32	0.33	0.16	0.13	0.13	0.09	0.21
MgO	9.70	9.84	11.09	11.81	13.08	12.33	11.16
CaO	11.28	11.27	12.02	11.98	12.16	12.30	11.79
Na2O	3.06	2.96	2.50	2.40	2.95	2.37	2.18
K2O	1.71	1.73	1.66	1.72	1.48	1.83	1.89
P2O5	0.00	0.00	0.05	0.03	0.06	0.01	0.00
total	98.19	97.91	97.83	97.51	98.00	98.32	98.92

	8	9	10	11	12	13	14
SiO2	40.86	40.37	40.72	39.61	40.71	40.14	40.12
TiO2	3.54	3.38	3.35	3.32	3.22	3.34	3.33
Al2O3	14.45	13.93	14.52	15.29	14.33	14.39	14.79
Cr2O3	0.00	0.00	0.00	0.00	0.04	0.00	0.00
FeO*	13.05	12.66	13.06	13.21	12.77	13.25	12.99
MnO	0.20	0.20	0.20	0.21	0.22	0.20	0.22
MgO	11.39	11.63	11.46	11.33	11.48	11.34	11.36
CaO	11.50	11.69	11.61	11.59	11.44	11.50	11.47
Na2O	2.91	2.75	2.77	2.61	2.83	2.72	2.77
K2O	1.80	1.81	1.84	1.91	1.84	1.88	1.85
P2O5	0.04	0.01	0.05	0.02	0.02	0.01	0.00
total	99.72	98.43	99.57	99.11	99.11	98.89	98.78

	15	16	17	18	19	20	21	22
SiO2	39.60	41.16	40.24	39.85	40.55	38.70	39.46	38.43
TiO2	3.71	2.95	3.02	3.15	3.49	4.61	5.02	4.66
Al2O3	15.13	14.25	13.90	14.54	15.21	15.12	14.68	14.57
Cr2O3	0.00	0.04	0.07	0.06	0.10	0.00	·0.00	0.00
FeO*	12.27	8.90	8.75	8.52	8.56	12.14	8.96	13.76
MnO	0.22	0.05	0.10	0.11	0.11	0.15	0.09	0.27
MgO	10.99	14.47	13.99	14.57	13.96	11.26	13.06	10.52
CaO	11.62	11.64	11.55	12.33	12.41	11.31	11.77	11.31
Na2O	2.76	2.77	2.56	2.51	2.37	2.81	2.82	2.81
K2O	1.77	1.59	1.58	1.89	2.07	1.74	1.70	1.69
P2O5	0.00	0.05	0.05	0.06	0.03			
total	98.89	98.05	97.86	95.81	97.59	98.86	97.59	98.06

238

1. Ferroan pargasite rim, zoned grain, analysis adjacent to titanaugite microphenocryst mantle, TM-9-64N.
2. Ferroan pargasite intermediate zone of grain in analysis 1.
3. Kaersutite core of grain in analysis 1.
4. Kaersutite core, TM-9-64N.
5. Kaersutite, TM-9-63N.
6. Kaersutite, 0.1 mm from nodule edge, TM-9-69FG.
7. Ferroan pargasite, 0.5 mm from edge, TM-9-69FG.
8. Ferroan pargasite, 0.7 mm from edge, TM-9-69FG.
9. Ferroan pargasite, 1.1 mm from edge, TM-9-69FG.
10. Ferroan pargasite, 1.5 mm from edge, TM-9-69FG.
11. Ferroan pargasite, 1.7 mm from edge, TM-9-69FG.
12. Ferroan pargasite, 1.9 mm from edge, TM-9-69FG.
13. Ferroan pargasite, 3.8 mm from edge, TM-9-69FG.
14. Ferroan pargasite, 5.3 mm from edge, TM-9-69FG.
15. Ferroan pargasite, 6.05 mm from edge, TM-9-69FG.
16. Ferroan pargasite oikocryst, thin strip between phlogopite and clinopyroxene, TM-9-69CG.
17. Ferroan pargasite oikocryst, border, TM-9-69CG.
18. Ferroan pargasite oikocryst near apatite grain, TM-9-69CG.
19. Ferroan pargasite oikocryst, analysis away from other phases, TM-9-69CG.
20. Zoned kaersutite, core analysis, TM-9-64N.
21. Kaersutite intermediate zone, same grain as in analysis 20.
22. Kaersutite, same grain as in analysis 20, near titanferous biotite.

NODULES- FELDSPAR

1	2
55.52	56.70
0.07	0.06
27.32	26.32
0.01	0.01
0.20	0.25
0.01	0.00
0.00	0.00
9.61	9.11
5.80	5.87
0.52	0.62
0.02	0.04
99.08	98.97

1. Andesine (An46) interstitial to mafic phases, TM-9-63N.
2. Andesine (An44) interstitial to mafic phases, TM-9-63N.

NODULES- OXIDE (OPAQUES)

	1	2	3	4	5	6	7	8
SiO2	12.86	9.59	0.21	0.27	5.16	0.10	19.09	0.08
TiO2	0.19	0.88	0.32	0.20	1.55	48.84	8.21	0.07
Al2O3	9.29	5.44	1.72	2.29	10.96	0.75	11.88	0.00
Cr2O3	0.02	0.07	0.08	0.06	0.05	0.03	0.70	0.00
FeO*	77.37	76.78	87.69	87.40	78.48	44.39	33.05	75.09
MnO	0.00	0.20	0.16	0.34	0.88	0.86	0.34	0.01
MgO	0.18	0.56	0.23	1.32	0.81	3.62	21.74	0.00
CaO	0.35	0.66	0.36	0.30	0.52	0.07	5.31	0.08
Na2O	0.12	0.80	0.05	0.11	0.17	0.04	0.11	0.00
K2O	0.00	0.17	0.11	0.07	0.04	0.01	0.00	0.00
P2O5	0.01	0.15	0.11	0.09	0.18	0.07	0.07	0.00
total	100.38	95.30	91.03	92.45	98.80	98.81	100.50	75.33

1. Rod-shaped opaque in glass, TM-9-64N.
2. Magnetite inclusion in kaersutite, TM-9-63N.
3. Magnetite, TM-9-63N.
4. Magnetite, 0.3 mm from nodule edge, TM-9-69FG.
5. Magnetite(?), 2.3 mm from nodule edge, TM-9-69FG.
6. Magnesian ilmenite, TM-9-69FG.
7. Yellow-orange (reflected light) opaque inclusion in olivine, TM-9-69CG.
8. Yellow-orange euhedral opaque, TM-9-69CG.

NODULES- APATITE

	1	2	3
SiO2	0.36	0.39	0.41
TiO2	0.03	0.01	0.00
Al2O3	0.00	0.00	0.00
Cr2O3	0.01	0.02	0.00
FeO*	0.18	1.88	7.61
MnO	0.04	0.02	0.05
MgO	0.12	0.17	0.15
CaO	52.52	50.01	46.00
Na2O	0.00	0.00	0.00
K2O	0.00	0.00	0.00
P2O5	39.11	36.68	36.73
total	92.38	89.18	90.98

1. Large apatite with opaque inclusions, TM-9-69CG.
2. Large apatite with opaque inclusions, attempt to identify opaque phase, TM-9-69CG.
3. Large apatite with opaque inclusions, attempt to identify opaque phase, TM-9-69GC.

NODULES — GLASS

	1	2	3	4	5	6	7
SiO2	50.09	50.98	44.84	49.58	49.91	49.16	56.43
TiO2	1.71	1.80	1.68	1.66	1.96	1.91	1.43
Al2O3	20.96	21.68	23.55	20.53	20.75	20.28	22.99
Cr2O3	0.00	0.04	0.00	0.00	0.02	0.02	0.01
FeO*	6.61	6.83	6.48	6.39	6.14	6.70	3.14
MnO	0.13	0.15	0.12	0.11	0.13	0.09	0.09
MgO	2.54	2.44	2.36	2.66	2.68	2.75	2.08
CaO	6.65	4.36	3.94	6.44	6.66	7.04	3.44
Na2O	5.77	5.98	5.28	7.16	7.34	6.83	2.36
K2O	4.16	4.64	2.86	4.20	4.19	4.16	5.05
P2O5	0.61	0.75	0.60	0.70	0.61	0.69	0.48
total	99.23	99.64	92.71	99.51	100.39	99.61	97.50

	8	9
SiO2	55.63	47.09
TiO2	1.23	2.01
Al2O3	22.95	20.44
Cr2O3	0.04	0.00
FeO*	4.44	9.98
MnO	0.11	0.23
MgO	2.09	2.38
CaO	4.84	4.68
Na2O	2.27	1.83
K2O	4.64	2.67
P2O5	0.53	1.16
total	98.76	92.47

1. Brown glass near titanaugite microphenocrysts, TM-9-64N.
2. Brown glass near amphibole, TM-9-64N.
3. Brown glass off rim of sodian titaniferous augite, TM-9-64N.
4. Brown-white glass, TM-9-64N.
5. Brown-white glass, TM-9-64N.
6. Brown-white glass near apatite, TM-9-64N.
7. Pale orange glass at 120o grain boundaries, TM-9-63N.
8. Pale orange glass at 120o grain boundaries, TM-9-63N.
9. Orange glass at 120o grain boundaries, TM-9-69FG.

NODULES- MICAS

	1	2	3	4
SiO2	35.63	36.07	36.79	34.20
TiO2	5.13	4.61	4.07	3.50
Al2O3	16.33	16.54	17.29	15.47
Cr2O3	0.01	0.00	0.01	0.07
FeO*	14.91	15.26	8.79	7.30
MnO	0.16	0.22	0.05	0.02
MgO	13.28	13.39	18.68	16.35
CaO	0.00	0.00	0.00	0.00
Na2O	0.75	0.69	0.79	0.82
K2O	9.00	8.93	9.05	7.29
P2O5	0.00	0.00	0.01	0.11
total	95.20	95.71	95.53	85.13

1. Titaniferous biotite, patches and rims in and mantling
    kaersutite, TM-9-64N.
2. Titaniferous biotite mantling kaersutite, TM-9-64N.
3. Titaniferous phlogopite oikocryst, TM-9-69CG.
4. Titaniferous phlogopite oikocryst, TM-9-69CG.

NODULES- SPHENE

	1	2
SiO2	31.25	38.60
TiO2	37.08	20.32
Al2O3	1.43	5.89
Cr2O3	0.01	0.00
FeO*	0.79	4.85
MnO	0.04	0.09
MgO	0.02	4.44
CaO	26.52	23.96
Na2O	0.06	0.96
K2O	0.00	0.00
P2O5	0.22	0.13
total	97.41	99.24

1. Sphene mantling kaersutite, TM-9-64N.
2. Sphene inclusion in kaersutite, TM-9-64N.